UV Laser Direct Writing Technology for the Fabrication of Flexible Sensors

Wang, S.

Important note
To cite this publication, please use the final published version (if applicable).
Please check the document version above.

UV LASER DIRECT WRITING TECHNOLOGY FOR THE FABRICATION OF FLEXIBLE SENSORS

UV Laser Direct Writing Technology for the Fabrication of Flexible Sensors

Dissertation

for the purpose of obtaining the degree of doctor
at Delft University of Technology
by the authority of the Rector Magnificus Prof.dr.ir. T.H.J.J. van der Hagen
chair of the Board for Doctorates
to be defended publicly on
Monday, 17 March 2025 at 10:00

by

Shaogang WANG

Master of Engineering in Mechanical Engineering,
Guilin University of Electronic Technology, Guilin, China,

This dissertation has been approved by the promotors.

Composition of the doctoral committee:

Rector Magnificus, Chairperson
Prof. dr. P. J. French, Delft University of Technology, promotor
Prof. dr. H. Ye, Delft University of Technology, copromotor

Independent members:
Prof. dr. ir. G. J. M. Krijnen, University of Twente
Prof. dr. Y. Li, Southern University of Science and Technology, China
Em. Prof. dr. ir. P. M. Sarro, Delft University of Technology
Prof. dr. ir. F. P. Widdershoven, Delft University of Technology
Prof. dr. G. Q. Zhang, Delft University of Technology

To my parents

CONTENTS

SUMMARY

WITH the rapid development of science and technology, the Internet of Things and big data have become important forces driving the progress of modern technology. The evolution of these technologies has spurred the widespread application of smart devices and services, bringing revolutionary changes to various industries. In this context, flexible sensors have become a key bridge between the physical and digital worlds because of their unique bendability and high adaptability. They not only provide real-time data collection and transmission, but also serve a crucial role in health monitoring and environmental detection due to their lightweight and flexible characteristics.

As fabrication technologies continue to innovate, flexible sensors are evolving towards miniaturization, integration, and customization. Although flexible sensors based on a variety of micro- and nanostructures and innovative materials have made significant progress in recent years, challenges still exist in terms of sensor performance, integration capability, and fabrication efficiency. To address these challenges, we utilized ultraviolet (UV) laser direct writing technology to efficiently achieve the microstructure fabrication and material modification required for the sensing capabilities of flexible sensors by precisely controlling the time, space, and energy of the laser. Correspondingly, we developed innovative fabrication technologies based on UV laser direct writing for different types of flexible sensors, including pressure sensors, strain sensors, gas sensors, and temperature sensors. The application of these technologies not only improves the fabrication efficiency but also enhances the sensor performance to meet the demands for customization and miniaturization. This thesis primarily focuses on the following contents:

Chapter 1 introduced the importance of flexible sensors in the field of flexible electronics. It explored the classification, mechanism, and development trends of flexible sensors. Subsequently, the application and classification of laser direct writing (LDW) technology in the development of flexible sensors were thoroughly discussed. Finally, the research motivation and outline of this thesis were summarized.

Chapter 2 developed a laser pyrolysis direct writing (LPDW) technology for the fabrication of high-performance flexible pressure sensors with a PDMS micro-pyramid array structure. This chapter investigated the mechanism of continuous laser pyrolysis of Polydimethylsiloxane (PDMS) surfaces under precise UV-LDW through experiments and simulations. The effects of laser parameters on the performance of the sensor and its working mechanism were explained in detail. The fabricated sensors exhibited remarkable sensitivities of $3132.0 \, \text{kPa}^{-1}$, $322.5 \, \text{kPa}^{-1}$, and $27.8 \, \text{kPa}^{-1}$ in the pressure ranges of 0-0.5 kPa, 0.5-3.5 kPa, and 3.5-10 kPa, respectively. The sensors demonstrated fast response times (loading 22 ms and unloading 18 ms) and excellent repeatability and durability over 3000 cycles. Additionally, the sensors demonstrated the ability to detect micro and low pressures, such as mobile phone vibrations, airflow impacts, and finger touches. Moreover, these sensors exhibited excellent array integration capabilities for

spatial pressure distribution detection.

Chapter 3 introduced a laser transmission pyrolysis (LTP) technology for fabricating flexible strain sensors based on metal (Au) cracks with microchannel arrays. This chapter explored the mechanism of efficient fabrication of PDMS surface microchannels by TLP technology through experiments and simulations. It revealed the stress redistribution of the PDMS surface with the microchannel array under stretching. The fabricated sensors exhibited high sensitivity (GF = 1718.5), excellent strain resolution (0.1%), wide detection range (59%), fast response and recovery times (69 ms and 141 ms, respectively), and robust durability (over 3000 cycles). Additionally, the sensors proved capable of accurately monitoring not only subtle physiological signals such as pulse and swallowing but also large-scale motion signals such as knee flexion and finger bending.

Chapter 4 developed a selective reduction laser sintering (SRLS) technology for fabricating flexible nitrogen dioxide (NO_2) gas sensors based on indium oxide (In_2O_3) nanoparticles (NPs). This chapter investigated the mechanism of oxygen vacancy defect formation under UV laser sintering of In_2O_3 NPs through experiments and simulations. The effects of differences in laser scanning intervals on sintering temperature, oxygen vacancies, and sensor performance were further explored. The mechanism of oxygen vacancy defects in In_2O_3 for the enhanced adsorption performance of the NO_2 molecule was explained by density functional theory (DFT) simulation. The fabricated sensor demonstrated excellent response at room temperature (S = 460.9 at 10 ppm), fast response/recovery time (τ_{resp}/τ_{reco} = 27/570 s), and superior selectivity (response ratio > 400). Additionally, these sensors exhibited good light and humidity resistance, with faster recovery under light-assisted conditions.

Chapter 5 introduced a UV laser direct writing technique (UV-LDW) for fabricating flexible temperature sensors based on nickel oxide and laser-induced graphene (NiO-LIG) nanocomposites (NPs). This chapter investigated the mechanisms underlying the fabrication of NiO-LIG via UV laser direct writing on NiO-PI films, focusing on the partial reduction of NiO to metallic Ni and the formation of oxygen vacancy defects. The mechanism of performance enhancement of NiO-LIG temperature sensors after NiO NP compositing was further revealed. The fabricated sensor exhibited excellent sensitivity ($-0.075\%\,°C^{-1}$) and outstanding linear response (R^2 = 0.999) over the temperature range of 30 to 100 °C. By incorporating PDMS packaging technology, these sensors not only exhibited exceptional humidity resistance and waterproof capabilities but also rapidly responded to sudden temperature changes and continuously monitored long-term temperature variations.

Chapter 6 summarized the research findings, highlighted advancements achieved through the development of innovative laser direct writing technology in the fabrication of flexible sensors, and discussed potential directions for future research utilizing this technology.

SAMENVATTING

MET de snelle ontwikkeling van wetenschap en technologie zijn het Internet der Dingen en big data belangrijke krachten geworden die de vooruitgang van de moderne technologie stimuleren. De evolutie van deze technologieën heeft geleid tot de wijdverspreide toepassing van slimme apparaten en diensten, wat revolutionaire veranderingen teweegbrengt in verschillende industrieën. In deze context zijn flexibele sensoren een cruciale brug geworden tussen de fysieke en digitale werelden vanwege hun unieke buigzaamheid en hoge aanpasbaarheid. Ze bieden niet alleen realtime gegevensverzameling en -overdracht, maar spelen ook een cruciale rol in gezondheidsmonitoring en milieudetectie vanwege hun lichtgewicht en flexibele eigenschappen.

Naarmate de fabricagetechnologieën blijven innoveren, evolueren flexibele sensoren naar miniaturisatie, integratie en maatwerk. Hoewel flexibele sensoren op basis van een verscheidenheid aan micro- en nanostructuren en innovatieve materialen de afgelopen jaren aanzienlijke vooruitgang hebben geboekt, bestaan er nog steeds uitdagingen op het gebied van sensorprestaties, integratievermogen en fabricage-efficiëntie. Om deze uitdagingen aan te pakken, hebben we gebruik gemaakt van ultraviolet (UV) laser direct schrijftechnologie om efficiënt de microstructuurfabricage en materiaalmodificatie te bereiken die nodig zijn voor de sensoreigenschappen van flexibele sensoren door de tijd, ruimte en energie van de laser nauwkeurig te regelen. Overeenkomstig hebben we innovatieve fabricagetechnologieën ontwikkeld op basis van UV-laser direct schrijven voor verschillende soorten flexibele sensoren, waaronder druksensoren, rekstrooksensoren, gassensoren en temperatuursensoren. De toepassing van deze technologieën verbetert niet alleen de fabricage-efficiëntie maar verhoogt ook de sensorprestaties om te voldoen aan de eisen voor maatwerk en miniaturisatie. Deze scriptie richt zich primair op de volgende inhouden:

Hoofdstuk 1 introduceerde het belang van flexibele sensoren in het veld van flexibele elektronica. Het verkende de classificatie, mechanismen en ontwikkelingstrends van flexibele sensoren. Vervolgens werd de toepassing en classificatie van laser direct writing (LDW) technologie in de ontwikkeling van flexibele sensoren uitvoerig besproken. Tot slot werd de onderzoeksmotivatie en de opzet van deze scriptie samengevat.

Hoofdstuk 2 ontwikkelde een laserpyrolyse direct writing (LPDW) technologie voor de fabricage van hoogwaardige flexibele druksensoren met een Polydimethylsiloxaan (PDMS) micro-piramide-arraystructuur. Dit hoofdstuk onderzocht het mechanisme van continue laserpyrolyse van PDMS-oppervlakken onder nauwkeurige UV-LDW door middel van experimenten en simulaties. De effecten van lasereigenschappen op de prestaties van de sensor en het werkingsmechanisme werden in detail uitgelegd. De vervaardigde sensoren toonden opmerkelijke gevoeligheden van 3132,0 kPa^{-1}, 322,5 kPa^{-1} en 27,8 kPa^{-1} in de drukbereiken van 0-0,5 kPa, 0,5-3,5 kPa en 3,5-10 kPa respectievelijk. De sensoren toonden snelle reactietijden (laden 22 ms en lossen 18 ms) en uitstekende herhaalbaarheid en duurzaamheid over 3000 cycli. Bovendien toonden de sensoren het

vermogen om micro en lage drukken te detecteren, zoals mobiele telefoontrillingen, luchtstroomimpacts en vingeraanrakingen. Bovendien vertoonden deze sensoren uitstekende arrayintegratiecapaciteiten voor ruimtelijke drukverdelingsdetectie.

Hoofdstuk 3 introduceerde een laser transmissive pyrolyse (LTP) technologie voor het fabriceren van flexibele rekstrooksensoren op basis van metaal (Au) scheuren met microkanaalarrays. Dit hoofdstuk verkende het mechanisme van efficiënte fabricage van PDMS-oppervlak microkanalen door TLP-technologie door middel van experimenten en simulaties. Het onthulde de stressherverdeling van het PDMS-oppervlak met de microkanaalarray onder rekking. De vervaardigde sensoren vertoonden hoge gevoeligheid (GF = 1718,5), uitstekende rekresolutie (0,1%), breed detectiebereik (59%), snelle respons- en hersteltijden (69 ms en 141 ms respectievelijk), en robuuste duurzaamheid (meer dan 3000 cycli). Bovendien bewezen de sensoren in staat te zijn om niet alleen subtiele fysiologische signalen zoals pols en slikken nauwkeurig te monitoren, maar ook grootschalige bewegingssignalen zoals knieflexie en vingerbuiging.

Hoofdstuk 4 ontwikkelde een selectieve reductie laser sintering (SRLS) technologie voor het fabriceren van flexibele stikstofdioxide (NO_2) gasensors op basis van indiumoxide (In_2O_3) nanopartikels (NPs). Dit hoofdstuk onderzocht het mechanisme van zuurstofvacaturedefectvorming onder UV-laser sintering van In_2O_3 NPs door middel van experimenten en simulaties. De effecten van verschillen in laserscaninterval op sintertemperatuur, zuurstofvacatures en sensorprestaties werden verder verkend. Het mechanisme van zuurstofvacaturedefecten in In_2O_3 voor de verbeterde adsorptieprestatie van het NO_2-molecuul werd uitgelegd door density functional theory (DFT) simulatie. De vervaardigde sensor toonde uitstekende respons bij kamertemperatuur (S = 460,9 bij 10 ppm), snelle respons-/hersteltijd (τ_{resp}/τ_{reco} = 27/570 s), en superieure selectiviteit (responsverhouding > 400). Bovendien vertoonden deze sensoren goede licht- en vochtbestendigheid, met snellere herstel onder lichtondersteunde omstandigheden.

Hoofdstuk 5 ontwikkelde een UV-laser direct writing techniek (UV-LDW) voor het fabriceren van flexibele temperatuursensoren op basis van nikkeloxide en lasergeïnduceerd grafiet (NiO-LIG) nanocomposieten (NPs). Dit hoofdstuk onderzocht de mechanismen die ten grondslag liggen aan de fabricage van NiO-LIG via UV-laser direct writing op NiO-PI films, met focus op de gedeeltelijke reductie van NiO tot metallisch Ni en de vorming van zuurstofvacaturedefecten. Het mechanisme van prestatieverbetering van NiO-LIG temperatuursensoren na NiO NP-samenstelling werd verder onthuld. De vervaardigde sensor vertoonde uitstekende gevoeligheid (−0,075% °C^{-1}) en een uitstekende lineaire respons (R^2 = 0,999) over het temperatuurbereik van 30 tot 100 °C. Door het opnemen van PDMS-verpakkingstechnologie, vertoonden deze sensoren niet alleen uitzonderlijke vochtbestendigheid en waterdichte capaciteiten maar reageerden ook snel op plotselinge temperatuurveranderingen en monitorden continu lange-termijn temperatuurvariaties.

Hoofdstuk 6 vat de onderzoeksbevindingen samen, benadrukt de vooruitgang die is geboekt door de ontwikkeling van innovatieve laser direct writing technologie bij de fabricage van flexibele sensoren, en bespreekt potentiële richtingen voor toekomstig onderzoek met deze technologie.

1

INTRODUCTION

Laser direct writing (LDW) technology, particularly ultraviolet (UV) laser-based direct writing technology, plays an important role in the field of flexible sensor fabrication. This technology can achieve precise material modification and microstructure fabrication at the microscale. In particular, LDW technology achieves physical and chemical effects such as melting, sintering, pyrolysis, and surface modification through the precise control of the laser in time, space, and energy for precise device fabrication. UV lasers, characterized by their short wavelengths and high energy density, are especially suitable for applications that require high-precision surface treatments. These features enable LDW technology to offer high efficiency, cost-effectiveness, strong controllability, and flexible customization capabilities in the fabrication of flexible electronic devices. During the fabrication of flexible sensors, UV laser direct writing technology can effectively perform fine processing on a diverse range of materials, including polymers, metals, oxides, and their composites. This not only enhances the efficiency and precision of sensor fabrication but also improves sensor performance through laser-induced material modifications, such as enhanced sensitivity, expanded sensing range, and improved reliability. Therefore, LDW technology provides an innovative design and fabrication pathway for multi-scale fabrication, multi-dimensional design, and multi-material integration of flexible sensors.

1

1.1. BACKGROUND

WITH the rapid advancement of science and technology, flexible electronics have become an essential component of both modern technology and everyday life [1]. These devices not only retain the core functions of traditional electronics but also exhibit unique application value and broad application prospects in various fields due to their excellent flexibility and adaptability, as illustrated in Figure 1.1. Particularly in wearable devices, medical monitoring, energy harvesting and storage, display technology, and sensor technology, flexible electronics are driving scientific and technological advancements and enhancing human life with their superior performance [2–4].
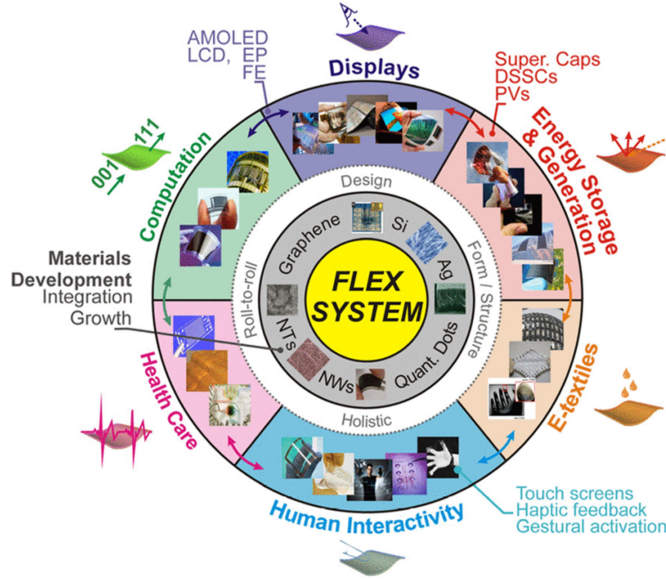
Figure 1.1: Materials, fabrication, and applications of flexible electronics [1].

Flexible sensors, core components of flexible electronics, have successfully overcome the limitations of traditional rigid sensors, demonstrating excellent application prospects in health monitoring and environmental detection [5]. These sensors enable real-time, continuous, and accurate monitoring of human physiological indicators and environmental quality parameters such as pressure, strain, humidity, temperature, and gas concentration, providing crucial hardware support for health management [6] and environmental monitoring [7].

With the rapid advancement of manufacturing technology and increasing demands from various applications, sensors are evolving towards miniaturization, customization, integration, and intelligence, as shown in Figure 1.2. To adapt to these trends, stricter performance standards have been established for flexible sensors, which include expanding the sensing range, increasing sensitivity, and enhancing reliability [8]. These trends place more significant requirements on material selection, technological innovation, cost-effectiveness, and performance optimization in the manufacturing of flexible sensors [9].
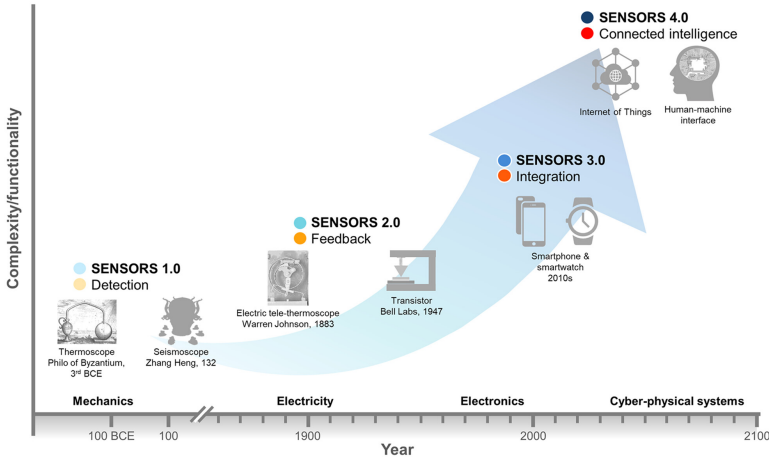
Figure 1.2: Evolution of sensor technology. Sensors 1.0: Basic detection; Sensors 2.0: Incorporation of electrical feedback; Sensors 3.0: Integrated miniaturization in devices; Sensors 4.0: Improve perception capabilities based on networks and algorithms [2].

In this context, laser direct writing (LDW) technology, renowned for its exceptional precision, flexibility, and adaptability, has paved the way for the innovative design and fabrication processes of flexible sensors [10]. LDW technology, in combination with additive, subtractive, and hybrid fabrication methods, effectively addresses the complex fabrication requirements for multi-scale fabrication, multi-dimensional design, and multi-material integration in various types of flexible sensors [11]. This technology provides diverse design options and high-precision fabrication processes for the development of flexible sensors, simultaneously improving the fabrication efficiency and precision of sensors at various scales and with different materials.

Specifically, LDW technology enables material modification and structural fabrication of flexible sensors from micro to macro scales. It precisely controls the time, space, and energy of the laser to induce physical and chemical effects on the target material, including melt sintering, pyrolytic ablation, and surface modification [12]. LDW technology offers numerous advantages, such as high efficiency, low cost, robust controllability, customization capabilities, and environmental sustainability [13–17]. These characteristics make LDW technology exceptionally suitable for the fabrication of multifunctional flexible sensors and open up new opportunities for sensor fabrication.

1.2. OVERVIEW OF FLEXIBLE SENSORS

1.2.1. DEVELOPMENT AND TREND OF FLEXIBLE SENSORS

Over the past few decades, flexible sensors have emerged as a transformative technology driving traditional electronics towards greater adaptability and flexibility [18]. Compared with traditional rigid sensors, flexible sensors mainly composed of flexible substrates can not only fit closely to human skin and biological tissues but also easily adapt to extreme or complex environments. This capability makes flexible sensors valuable

1

for the continuous and accurate monitoring of signals from both the human body and external environments [19, 20]. Therefore, in applications ranging from health monitoring to environmental detection and even human-computer interaction, flexible sensors have demonstrated their significant value, becoming an essential research direction in the field of flexible electronics [21].

Figure 1.3: A brief chronology of the development of flexible sensors.

Since the beginning of the 21st century, the field of flexible sensors has experienced significant developments driven by rapid technological advances. These advances have been propelled by innovations in materials, structures, and fabrication processes,

alongside a growing demand for multifunctionality, biocompatibility, and wireless, self-powered capabilities in sensors designed for emerging markets [5, 22].

The major milestones in the development of flexible sensors from 2000 to 2024 are illustrated in Figure 1.3, providing a brief chronology by timeline. In 2000, Jiang et al. [23] introduced flexible skin technology compatible with integrated circuit (IC) processes and successfully applied it to shear stress sensor arrays. By 2002, Nilsson et al. [24] proposed a humidity sensor utilizing Nafion film as a proton conductor combined with the concept of the organic electrochemical transducer. In 2004, Someya et al. [25] developed a large-area flexible pressure sensor matrix incorporating organic field-effect transistors (OFETs) for artificial skin applications. In 2006, Yoon et al. [26] developed a modular and scalable capacitive tactile sensor using elastic PDMS for large-area applications. In 2008, Lee et al. [27] designed and fabricated a flexible temperature and humidity sensor on a perylene substrate using a micro-electro-mechanical-systems (MEMS) process. In 2010, Mannsfeld et al. [28] employed micro-structuring technology and PDMS material to fabricate a highly sensitive flexible capacitive pressure sensor.

As time progresses, advancements in the field of flexible sensors are increasingly driven by material innovation. By 2011, Yamada et al. [29] developed a wearable flexible strain sensor based on single-walled carbon nanotube (SWCNT) films to detect human body movements. In 2012, Pang et al. [30] introduced a flexible sensor using reversible interlocking of nanofibers capable of detecting various mechanical loads, including pressure, shear, and torsion. In 2013, Schwartz et al. [31] developed a flexible pressure sensor based on organic thin-film transistors (OTFTs), utilizing micro-structured PDMS as the dielectric material. In 2014, Gong et al. [32] presented a simple and efficient strategy to fabricate a wearable, highly sensitive pressure sensor using ultrathin gold nanowires. By 2015, Joo et al. [33] engineered a flexible pressure sensor using the principle of spontaneous wrinkle formation in pre-stretched PDMS treated with UV/ozone combined with silver nanowire embedding technology. In 2016, Yamamoto et al. [34] developed a multifunctional flexible sensor based on carbon nanotube (CNT) thin-film transistors for healthcare monitoring fabricated using a novel printing technology. In 2017, Matsuhisa et al. [35] used printing technology to prepare elastic conductors using in-situ generated silver nanoparticles (AgNPs), enabling the fabrication of flexible sensors with both pressure and temperature detection capabilities.

Recent developments in flexible sensors are increasingly focusing on functional diversity. In 2018, An et al. [36] reported a transparent and flexible fingerprint sensor using a hybrid structure of ultralong metal nanofibers and fine nanowires, which realized multifunctional detection of fingerprint identification, tactile pressure, and skin temperature. In 2019, Boutry et al. [37] developed a biodegradable pressure sensor using fringe field capacitance technology, achieving wireless operation through inductive coupling. By 2020, Song et al. [38] proposed a fully self-powered wearable system with a triboelectric nanogenerator, a low-power wireless sensor circuit, and a microfluidic sweat sensor patch for dynamic biomarker monitoring. In 2021, Zhu et al. [39] introduced a flexible photosensor array for neuromorphic vision systems, combining carbon nanotubes and perovskite quantum dots as functional materials. In 2022, Yu et al. [40] utilized custom-developed nanomaterial inks for the scalable inkjet printing of flexible physicochemical sensor arrays, enabling the detection of various hazardous substances and pathogens.

In 2023, Yang et al. [41] reported a multifunctional flexible sensor using vanadium oxide (VO_X)-doped laser-induced graphene (LIG) to detect nitrogen oxides (NO_X) and temperature in soil. By 2024, Yu et al. [42] introduced a flexible temperature-pressure dual sensor based on a 3D spiral thermoelectric Bi_2Te_3 film.

1.2.2. CLASSIFICATION AND MECHANISM OF FLEXIBLE SENSORS

With the rapid development of the Internet of Things (IoT), sensors, as a critical technical component, serve as a vital bridge between the real world and the digital world. A sensor is defined as a device that detects a specific measured value and converts this signal into a usable output based on predefined rules [43]. Technological advancements in materials science and electronic engineering are gradually transforming traditional rigid sensors into flexible sensors [44]. This transformation significantly enhances sensor adaptability in various applications, improving their comfort and convenience. Particularly in the fields of health monitoring and environmental detection, the use of flexible sensors has become increasingly widespread, as shown in Figure 1.4.

Figure 1.4: Classification of flexible sensors in the fields of health monitoring and environmental detection.

In the field of health monitoring, flexible sensors can be classified into several types based on pressure [45, 46], strain [47, 48], temperature [48, 49], biological [50, 51], and chemical signals [52, 53], according to the difference in the signal being detected. These sensors provide accurate data support for medical and healthcare applications through real-time monitoring of vital physiological parameters such as heart rate, blood pressure, and body temperature, greatly enhancing the development of intelligent medical and

remote diagnostic technologies [54, 55].

In the field of environmental detection, flexible sensors primarily detect and record different types of environmental parameters, including light [56, 57], temperature [58, 59], humidity [60, 61], gas [62, 63], and pH [64, 65] indicators.

These sensors not only monitor critical parameters and track environmental changes but also play a crucial role in fields such as water management, agricultural production, and urban planning, providing a scientific basis for effective environmental management [66–68].

These flexible sensors can be further classified according to their working mechanisms, each offering distinct advantages and applications, as illustrated in Figure 1.5.
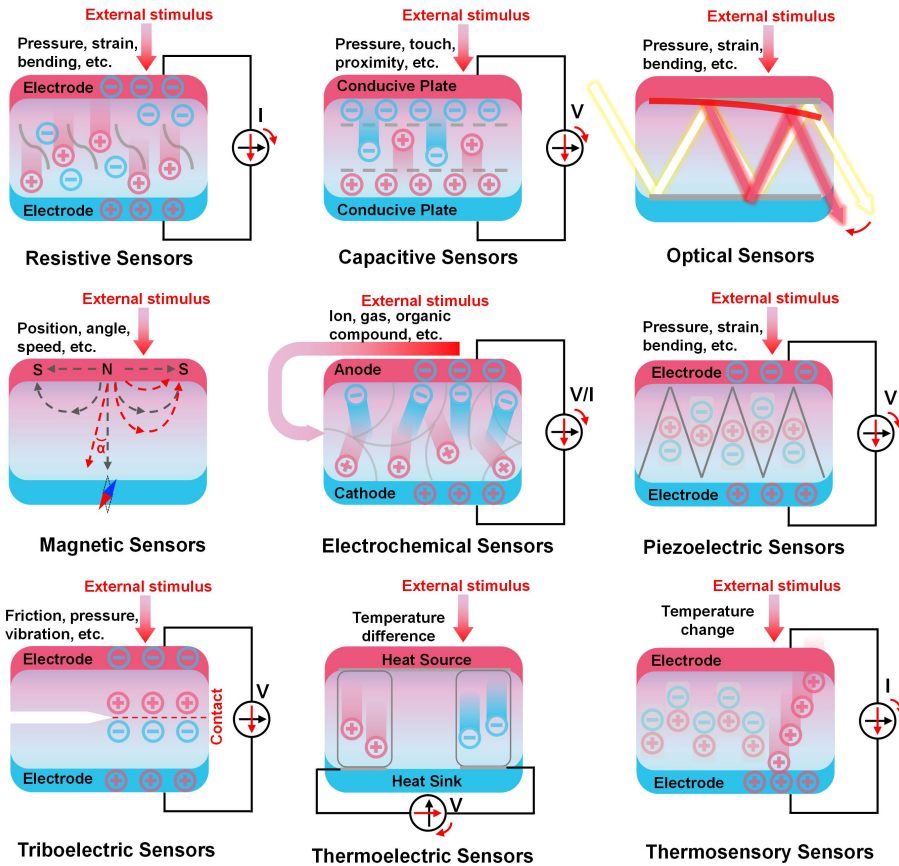
Figure 1.5: Schematic diagram of the sensing mechanism of different types of flexible sensors

Resistive flexible sensors operate by detecting changes in resistance caused by external stimuli such as pressure, stretching, or bending [69, 70]. These sensors are extensively used in wearable devices, robotics, and health monitoring systems, attributed to their simple construction, low cost, and ease of integration.

1

Capacitive flexible sensors utilize capacitive responses to detect various physical stimuli, including pressure, distance, and humidity [71, 72]. Owing to their high sensitivity, good stability, and low energy consumption, these sensors are widely used in wearable devices, touchscreen technology, and environmental monitoring.

Optical flexible sensors utilize the propagation, absorption, reflection, or emission properties of light to detect and quantify environmental changes or changes in the physical state [73, 74]. With their high sensitivity and non-contact measurement capabilities, these sensors show potential for a wide range of applications in fields such as medical diagnostics, environmental monitoring, and robotics.

Magnetic flexible sensors employ the response of the material to a magnetic field to detect the strength, direction, or change in the magnetic field [75, 76]. Owing to their flexibility and high sensitivity to magnetic fields, these sensors are critically important in applications such as wearable devices, location tracking, traffic monitoring, and industrial automation.

Electrochemical flexible sensors, a class of devices, utilize electrochemical principles to detect the presence, concentration, or activity of chemical components [77, 78]. These sensors are extensively used in fields including medical and health monitoring, environmental monitoring, and industrial process control, owing to their high sensitivity, low cost, and capability to analyze complex biological or environmental samples directly.

Piezoelectric and triboelectric flexible sensors utilize the conversion of mechanical energy into electrical energy, serving a wide range of applications in energy harvesting and sensing [79, 80]. These sensors are particularly suited for wearable devices, smart interfaces, and environmental monitoring due to their ability to convert mechanical pressure, vibration, or motion directly into electrical signals. These capabilities position these sensors as key components in the development of self-powered devices and systems, which operate independently of external power sources and contribute to sustainability.

Thermoelectric and thermosensory flexible sensors utilize the response of materials to temperature changes to convert and detect thermal energy [81, 82]. These sensors are used in diverse applications, including energy recovery, environmental monitoring, and medical monitoring, as they can directly convert thermal energy into electrical energy or generate electrical signals by sensing temperature. Thermoelectric sensors are crucial for precision temperature control systems, capturing slight temperature changes in the environment and converting them into voltage. Meanwhile, thermosensory sensors are well suited for temperature monitoring and dynamic thermal event tracking due to their rapid response and high sensitivity.

1.2.3. MATERIAL AND TECHNOLOGY INNOVATION OF FLEXIBLE SENSORS

Compared to traditional rigid sensors, flexible sensors exhibit similar performance indicators such as sensitivity [83, 84], linearity [85, 86], detection range [87, 88], response time [89, 90], hysteresis [91, 92], and durability [93, 94]. These performance indicators not only determine the potential application of the sensor but also directly influence the selection of materials and technologies in the sensor fabrication process.

Benefiting from advances in materials science, the range of applications for flexible

sensors has dramatically expanded. Consequently, the selection of materials for flexible sensors is pivotal, significantly influencing their functionality, flexibility, stability, compatibility, and cost-effectiveness [95]. Typically, materials used in flexible sensors are classified into three main types: substrate materials, functional materials, and functional substrate materials. Each of these three types of materials has unique properties, and their selection and combination further extend the diversity of flexible sensors, as shown in Figure 1.6.
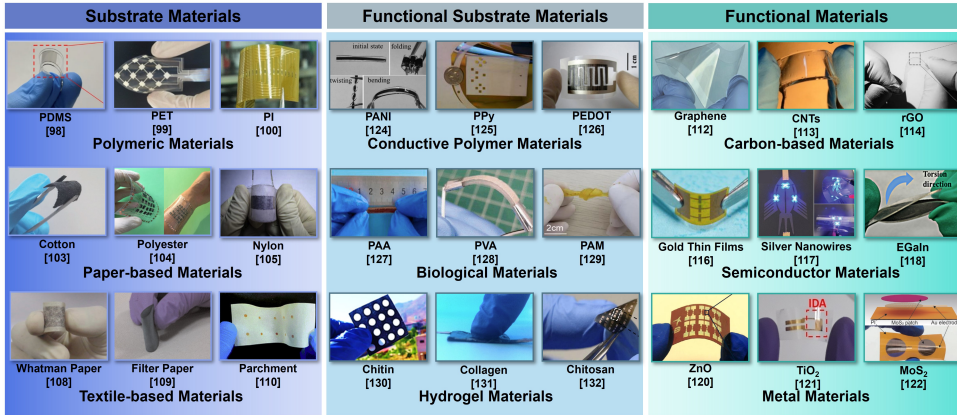
Figure 1.6: Substrate materials, functional materials, and functional substrate materials for the fabrication of flexible sensors.

Substrate materials serve as the support structure for the flexible sensor, providing necessary mechanical strength and flexibility properties. These materials are able to withstand the environmental stresses of the application while remaining flexible enough to adapt to various shapes and surfaces.

Polymeric materials, including polydimethylsiloxane (PDMS), polyester (PET), and polyimide (PI), play a crucial role in flexible sensor development due to their superior flexibility, lightweight characteristics, and ease of processing [96, 97]. PDMS, a silicon-based organic polymer, is renowned for its excellent elasticity and biocompatibility, making it widely used in biomedical sensor applications [98]. PET, valued for its mechanical properties and cost-effectiveness, is commonly employed in mechanical sensor applications [99]. PI, distinguished by its outstanding thermal stability and electrical insulation, is ideal for temperature sensor applications [100].

Textile-based materials such as cotton, polyester, and nylon are essential as substrate materials for flexible sensors due to their softness and excellent adaptability to skin [101, 102]. These fibers not only ensure a comfortable wearing experience but also enable the integration of advanced functionalities through textile technologies. Cotton, in particular, is suitable for wearable sensor applications involving direct skin contact due to its inherent comfort and superior breathability [103]. Polyester and nylon, with their durability, heat resistance, and chemical stability, are particularly suitable for mechanical sensing applications [104, 105].

Paper-based materials, including Whatman paper, filter paper, and parchment, play

a pivotal role in the field of flexible sensors, offering distinct advantages such as low cost, ease of processing, and biodegradability [106, 107]. Whatman paper, characterized by its uniform pore size and chemical stability, is extensively employed in laboratory analyses and biochemical sensing, particularly in microfluidics and biodiagnostic sensor applications [108]. Filter paper, known for its excellent liquid absorption and capillary action, is commonly utilized in the fabrication of low-cost biomedical sensors for analyzing blood and other biofluids [109]. Parchment, noted for its high temperature and oil resistance, is particularly suitable for use in chemical sensors that detect specific chemicals or solvents [110].

Functional materials are the critical components of flexible sensors, which are directly involved in the sensing process by converting external stimuli into measurable electrical signals. The selection and application of these materials directly determine the type and performance of the sensor.

Carbon-based materials, including graphene, carbon nanotubes (CNTs), and reduced graphene oxide (rGO), are particularly suitable for constructing flexible sensors due to their superior electrical conductivity and mechanical strength [111]. Graphene is favored for its outstanding electrical properties, mechanical strength, and surface characteristics and is widely considered ideal for fabricating flexible biochemical and mechanical sensors [112]. CNTs, characterized by their unique one-dimensional structure and inherent elasticity, provide exceptional strength and flexibility, making them ideally suited for high-sensitivity mechanical sensing applications [113]. rGO is utilized in biological and chemical sensing applications due to its high specific surface area and excellent dispersibility [114].

Metal materials, such as gold thin films, silver nanowires, and gallium-based liquid metals, are key components in the design of flexible sensors, valued for their excellent electrical conductivity and unique physical properties [115]. Gold thin films, owing to their exceptional chemical stability and biocompatibility, are widely used in medical monitoring sensors that require long-term contact with the human body [116]. Silver nanowires, known for their excellent electrical and optical properties, are extensively used in the fabrication of wearable flexible electronics and optoelectronic sensors [117]. Eutectic gallium-indium (EGaIn), a representative liquid metal that remains liquid at room temperature, offers significant advantages in developing flexible mechanical sensors due to its ductility and self-healing properties [118].

Semiconductor materials, including zinc oxide (ZnO), titanium dioxide (TiO$_2$), and molybdenum disulfide (MoS$_2$), are essential in the field of flexible sensors due to their distinct electronic and photoelectric properties [119]. ZnO, owing to its excellent optoelectronic and semiconductor properties, is commonly used in flexible photodetectors and gas sensors [120]. TiO$_2$ is noted for its outstanding chemical stability and efficient photocatalytic properties, making it particularly well-suited for applications including flexible gas monitoring and light detection [121]. MoS$_2$, a two-dimensional semiconductor material, exhibits excellent electrical, optoelectronic, and mechanical properties, making it suitable for both flexible optoelectronic and mechanical sensor applications [122].

Functional substrate materials are pivotal in the advancement of modern flexible sensors. These materials provide not only physical support but also directly endow the

sensors with the required electrical, chemical, or biological functionality.

Conductive polymer materials, such as polyaniline (PANI), polypyrrole (PPy), and polythiophene (PEDOT), have shown exceptional performance in the field of flexible sensors, primarily due to their conductivity, flexibility, and ease of processing [123]. PANI is extensively utilized in high-performance mechanical sensing because of its excellent environmental stability and tunable conductivity [124]. PPy is commonly used in biomedical sensors, particularly in neuroscience and tissue engineering, due to its good biocompatibility and electrochemical stability [125]. PEDOT, known for its outstanding electrical conductivity and biocompatibility, is extensively utilized in the detection of gases and specific chemicals, making it the preferred choice for biological and chemical sensor applications [126].

Hydrogel materials, including sodium polyacrylate (PAA), polyvinyl alcohol (PVA), and polyacrylamide (PAM), exhibit significant potential in flexible sensor technology due to their high-water content, excellent biocompatibility, and mechanical elasticity. PAA hydrogels are ideal for designing and fabricating mechanical sensors due to their reversible swelling and responsiveness [127]. PVA hydrogels are commonly used in wearable sensors and flexible chemical sensors for wound therapy monitoring owing to their film-forming and biodegradable properties [128]. PAM hydrogels are extensively utilized in flexible bioassay and environmental monitoring sensors due to their excellent mechanical stability and controllable pore structure [129].

Biological materials, such as chitin, collagen, and chitosan, exhibit significant potential in flexible sensors due to their biodegradability and excellent biocompatibility. Chitin, a natural polysaccharide derived from crustaceans, is particularly suitable for biomedical applications in flexible sensors due to its outstanding biocompatibility and biodegradability [130]. Collagen and chitosan are both natural materials that have proven valuable in medical devices, demonstrating their effectiveness as functionalized substrate materials for flexible sensors. These materials are particularly valuable in medical monitoring devices requiring long-term interaction with the human body [131, 132].

The selection of appropriate fabrication technologies is crucial for the efficient fabrication of high-performance flexible sensors. The right fabrication technology not only ensures the functionality and stability of the sensors in specific environments but also directly impacts their scalability and cost-effectiveness for commercialization. As shown in Figure 1.7, the fabrication techniques for flexible sensors are classified into two main types: micro-nano structures fabrication technologies and functional material fabrication technologies.

Micro-nanostructure fabrication technologies focus on designing and constructing high-precision micro- and nanostructures essential for flexible sensors. These technologies include photolithography, electron beam lithography, nanoimprint lithography, 3D printing, inkjet printing, and laser ablation.

Photolithography (PL) is a fundamental technology in microelectronic manufacturing, and its applications have extended to the development of flexible sensors. This technology primarily involves coating a photosensitive material (photoresist), selectively exposing the photoresist through a mask, and then developing the exposed photoresist to remove excess material and form the desired pattern [133]. Meanwhile, lithography has evolved into soft lithography, which utilizes stencils to transfer patterns, and rolling

1

lithography, designed for large-area flexible electronic devices [134].

Electron beam lithography (EBL) is a high-precision micro- and nanofabrication technique utilized in the preparation of semiconductors, microelectronics, and flexible sensors. This technology employs a high-energy electron beam to directly write onto a substrate coated with an electron-sensitive resist (EBL photoresist), precisely controlling the path of the beam to create the desired micro- and nanostructures [135]. EBL can fabricate fine electrodes and sensing structures and is also used for patterning nanomaterials in flexible biochemical sensors, highlighting its potential for nanoscale applications [136].

Nanoimprint lithography (NIL) is a technology used to replicate nanoscale structures, and it is widely applied in semiconductors, optical components, and flexible sensor fabrication. This technique transfers micro- and nanostructures from a template (mold) onto a substrate through mechanical deformation [137]. This technology can produce substrates with specific nanoscale patterns for flexible biosensors based on Surface-Enhanced Raman Scattering (SERS) [138]. Additionally, NIL can create nanoscale structures on flexible transparent conductive films to enable optical sensing functions [139].

3D printing provides a unique method for directly constructing complex three-dimensional structures in the fabrication of flexible sensors. This technology integrates multiple materials and functionalities into a single manufacturing step, significantly expanding design and functional possibilities [140]. This technology enables the integrated printing of both structural and functional sensor components, allowing for seamless integration of substrate structures and functional materials. Meanwhile, it can customize and print various complex geometries on flexible surfaces to meet specific application requirements[141].

Inkjet printing, a precise material deposition method, is widely used in the fabrication of flexible sensors. This technology allows for the direct printing of functional materials onto various flexible substrates, streamlining the production of flexible electronic devices with complex patterns [142]. It further enhances the flexibility in the design and fabrication of multifunctional flexible sensors by directly printing electrodes, along with photosensitive, thermosensitive, and chemically sensitive materials, onto flexible substrates [143].

Laser ablation is a precise material removal technology that selectively removes substrates or functional materials to form desired microstructures or patterns. This method is particularly well-suited for preparing fine electrodes, microchannels, and other functional structures [144]. It enables the precise fabrication of microelectrodes or conductive paths on flexible substrates like polymer films, making it ideal for producing flexible electrochemical and resistive sensors [145]. Additionally, laser ablation can create minute fluidic channels, crucial for the development of flexible biosensors that analyze biological samples [146].

Functional material fabrication technologies focus on developing and processing materials applied in flexible sensors that respond specifically to external stimuli. These technologies include vapor deposition, electrodeposition, solution treatment, material composite, self-assembly, and laser modification.

Vapor deposition, including chemical vapor deposition (CVD) and physical vapor
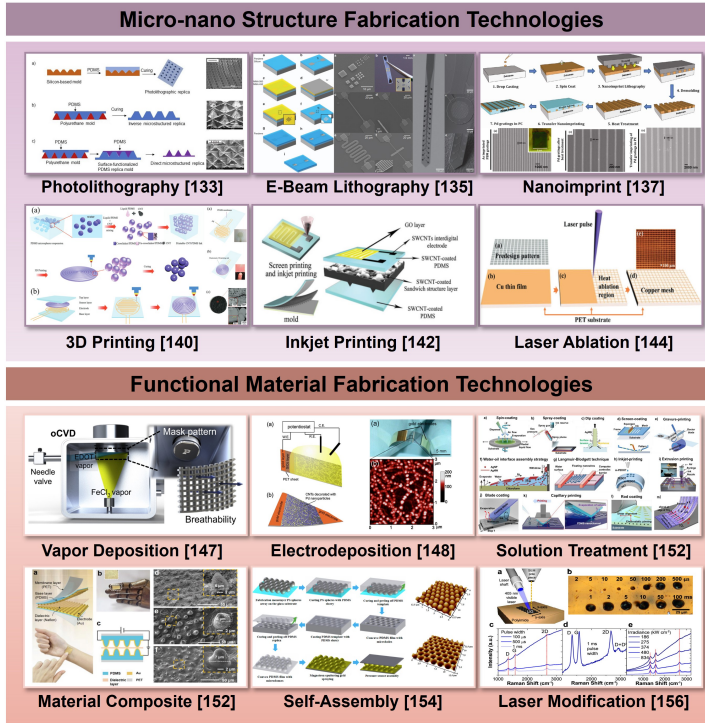
Figure 1.7: Substrate materials, functional materials, and functional substrate materials for the fabrication of flexible sensors.

deposition (PVD), is a commonly used method for depositing materials in the fabrication of flexible sensors. These technologies prepare thin film layers on flexible substrates through a gas-to-solid phase transition [147]. This process not only imparts specific chemical and physical properties to the surface, allowing the sensor to respond to certain chemicals or biomolecules, but it also deposits a protective layer that enhances the stability and reliability of the sensor in harsh environments.

Electrodeposition is a method that forms thin films or coatings on substrates through electrochemical reactions and is widely used in the fabrication of conductive films, metallic structures, and other functional coatings [148]. This technology enables the direct formation of conductive paths and electrodes on flexible substrates, specifically for electrochemical sensors. By adjusting electrochemical parameters, electrodeposition can also prepare nanoscale functional structures, thereby enhancing the sensitivity and selectivity of the sensors [149].

Solution treatment is a common and effective method in the fabricating of flexible sensors, primarily involving the use of chemical solvents and solutes to synthesize, modify, or deposit functional materials. This technology is widely used to fabricate conductive pathways and electrodes on flexible substrates for resistive, capacitive, and electrochemical sensors [150]. Meanwhile, it allows for the fabrication of specific chemical

or biological recognition layers on the sensor surface, thus enabling the detection of specific chemicals or biomolecules [151].

Material composite involves the physical or chemical combination of two or more different materials to create composites with novel properties and enhanced performance. This technology enables the integration of conductive nanomaterials, such as silver nanoparticles, carbon nanotubes, and metal-organic frameworks, with polymer substrates to produce flexible and highly conductive mechanical sensors [152]. Additionally, it facilitates the formation of specific composite detection materials on sensor surfaces, enabling biomolecular detection or chemical composition analysis [153].

Self-assembly is driven by the strategic design of molecules with specific affinities or functionalities, which spontaneously organize through non-covalent interactions such as hydrogen bonding, van der Waals forces, and electrostatic interactions [154]. This technology facilitates highly ordered nanostructures that allow for precise molecular-level control, thereby enhancing the electrical performance and sensitivity of sensors. Meanwhile, it enables the formation of functional self-assembled monolayers (SAMs) on the sensor surfaces, providing specific biorecognition or chemical selectivity [155].

Laser modification utilizes the high energy density of lasers to locally alter the structure and properties of materials, thereby imparting specific functionalities. This technology is used to create micro- and nano-scale surface textures, enhancing the specific surface area and improving the sensitivity or hydrophobicity of sensors [156]. Additionally, laser modification can introduce specific chemical groups onto the sensor surface to enhance the adsorption and recognition capabilities of biomolecules [157].

1.3. OVERVIEW OF LDW IN THE DEVELOPMENT OF FLEXIBLE SENSORS

1.3.1. APPLICATION AND CLASSIFICATION OF LASER TECHNOLOGY

A laser is a highly concentrated coherent beam of light that is passed through an excitation medium and amplified with the aid of special optical components such as mirrors and lenses to produce a single wavelength of light [158]. The extreme directionality of this beam and the high concentration of energy make the laser a very precise and efficient light source. In industrial production, lasers are widely used in a variety of applications, such as cutting, welding, and material processing, and are capable of achieving high-precision processing results [159]. In the field of scientific research, lasers are used for precise measurements and experimental operations, for example, in physics experiments by laser cooling technology to achieve near absolute zero temperature [160]. In the medical field, laser technology is widely used in minimally invasive procedures, such as eye surgery and tumor removal, providing non-invasive and precisely controlled treatments [161].

The foundation of laser applications across various fields is based on the interaction between lasers and materials, primarily determined by the laser wavelength and power, as well as the absorption characteristics and chemical composition of the materials. Among these parameters, wavelength is a key factor in determining the efficiency of the laser interaction with the material, the precision of the process, the depth of penetration, and the type of material to which it is applied. Shorter wavelength lasers (e.g.,

ultraviolet) generally have a stronger effect on the surface of the material and are suitable for applications that require high-precision surface treatment. In contrast, longer wavelength lasers (e.g., infrared) are able to penetrate deeper into the material and are suitable for applications requiring deeper processing. The classification of lasers corresponding to different wavelengths is shown in Table 1.1 [162, 163].

Table 1.1: Classification and summary of laser types, wavelengths, emission modes and gain media.

Number	Wavelength	Types	Emission Mode	Typical Gain Media
1	193 nm	ArF	Pulsed	Gas
2	248 nm	KrF	Pulsed	Gas
3	266 nm	Nd: YAG (FH)	Pulsed	Solid State
4	343 nm	Yb: YAG (TH)	Pulsed	Solid State
5	355 nm	Nd: YAG (TH)	Pulsed	Solid State
6	405 nm	InGaN	CW & Pulsed	Semiconductor
7	488 nm	Argon	CW & Pulsed	Gas
8	532 nm	Nd: YAG (SH)	Pulsed	Solid State
9	632.8 nm	HeNe	Pulsed	Gas
10	635 nm	AlGaInP	CW & Pulsed	Semiconductor
11	694 nm	Ruby	Pulsed	Solid State
12	755 nm	Alexandrite	CW & Pulsed	Solid State
13	785 nm	GaAlAs	CW & Pulsed	Semiconductor
14	700 - 1000 nm	Ti: Sapphire	Pulsed	Solid State
15	980 nm	InGaAs	CW & Pulsed	Semiconductor
16	1030 nm	Yb: YAG	Pulsed	Solid State
17	1064 nm	Nd: YAG	Pulsed	Solid State
18	1080 nm	Nd: YAP	CW & Pulsed	Solid State
19	1550 nm	InGaAsP	CW & Pulsed	Semiconductor
20	2080 nm	Tm Fiber	CW & Pulsed	Solid State
21	2100 nm	He Fiber	CW & Pulsed	Solid State
22	2940 nm	Er: YAG	CW & Pulsed	Solid State
23	2.7 - 11.2 μm	ICL	CW & Pulsed	Solid State
24	2.63 - 15.0 μm	QCL	CW & Pulsed	Solid State
25	10.6 μm	CO_2	CW & Pulsed	Gas

Note: CW - Continuous Wave; YAG - Yttrium Aluminum Garnet; SH - Second Harmonic; TH - Third Harmonic ; FH - Fourth Harmonic; ICL - Interband Cascade Laser; QCL - Quantum Cascade Laser.

Deep ultraviolet lasers such as ArF and KrF (wavelengths 193 nm and 248 nm) are primarily used in semiconductor manufacturing for photolithography to create precise chip circuits [164]. These lasers are also extensively used in material science for fine surface processing and modification and in chemical and physical research for analyzing molecular structures [165]. Lasers in the ultraviolet to near-ultraviolet range (wavelengths 343 nm to 488 nm), such as Yb: YAG and Nd: YAG, are employed in material science and biomedical research for precision machining, photochemical reaction acti-

vation, and biological marking [166–168]. Argon-ion lasers (488 nm), in particular, play a crucial role in spectroscopy and flow cytometry for molecular and cellular level analysis [169]. In the visible spectrum (wavelengths 488 nm to 694 nm), lasers like HeNe and AlGaInP are used for interferometric measurements, spectral analysis, and precision alignment systems [170–172] . Ruby lasers (694 nm) are particularly suited for cutting and engraving non-metallic materials [173]. Near-infrared lasers (wavelengths 700 nm to 1064 nm), such as Ti: Sapphire and InGaAs, are widely used in industrial automation, machine vision systems, and fiber optic communications [174, 175]. Nd: YAG lasers (1064 nm) are the go-to choice for industrial laser cutting and welding, while Ti: Sapphire lasers, known for their tunability, are frequently utilized in spectroscopy and ultrafast optical experiments [176, 177]. Mid-infrared to far-infrared lasers (wavelengths 1080 nm to 15.0 μm), like Er: YAG and CO_2, are applied in material processing, including cutting, welding, and surface treatment of metals and non-metals [178]. Quantum cascade lasers (QCL) are used for gas detection and environmental monitoring due to their high-power output, especially proving advantageous in detecting specific chemicals and pollutants [179].

1.3.2. DEVELOPMENT OF LDW TECHNOLOGY IN FLEXIBLE SENSORS

Recent advances in laser direct writing (LDW) technology have significantly advanced micro- and nano-fabrication.

This technology enables the synthesis and preparation of materials from the micron to the nanometer scale through laser-material interactions, effectively controlling the morphology and properties of the materials. Specifically, the LDW process involves both physical and chemical changes. The physical changes, represented by material ablation, are triggered by intense laser-induced lattice vibrations [180]. The chemical changes, represented by laser etching, result from the extensive breakage of valence bonds directly caused by the laser [181]. LDW technology has the advantages of high energy density, wide operating range, and high writing speed. Compared to conventional fabrication methods, it enables precise fabrication of complex structures and diverse preparation of functionalized materials. Additionally, LDW technology excels in micro- and nanofabrication due to its efficiency, precision, controllability, ease of integration, and compatibility with various materials. This technology has a wide range of applications in fields as diverse as supercapacitors [182, 183], nanogenerators [184, 185], actuators [186, 187], bioengineering [188, 189], and microfluidic devices [190, 191], providing tailored solutions to advanced manufacturing challenges.

In the field of fabrication of flexible sensors, LDW technology has been widely applied to a variety of sensor types, as shown in Figure 1.8. These sensors include flexible physical sensors for pressure, strain, and temperature [192–194]; flexible chemical sensors for analyzing saliva, sweat, and breath gases [195–197]; flexible biosensors for monitoring electrocardiograms (ECGs), electromyograms (EMGs), and electroencephalograms (EEGs) [198–200]; and flexible multimodal sensors that combine several sensing capabilities [201–203].

In terms of flexible physical sensors, Gopalakrishnan et al. [181] demonstrate a cost-effective method for creating wireless humidity sensors on metalized paper via laser direct writing. This approach utilizes Al_2O_3 nanostructures to enhance sensitivity to hu-
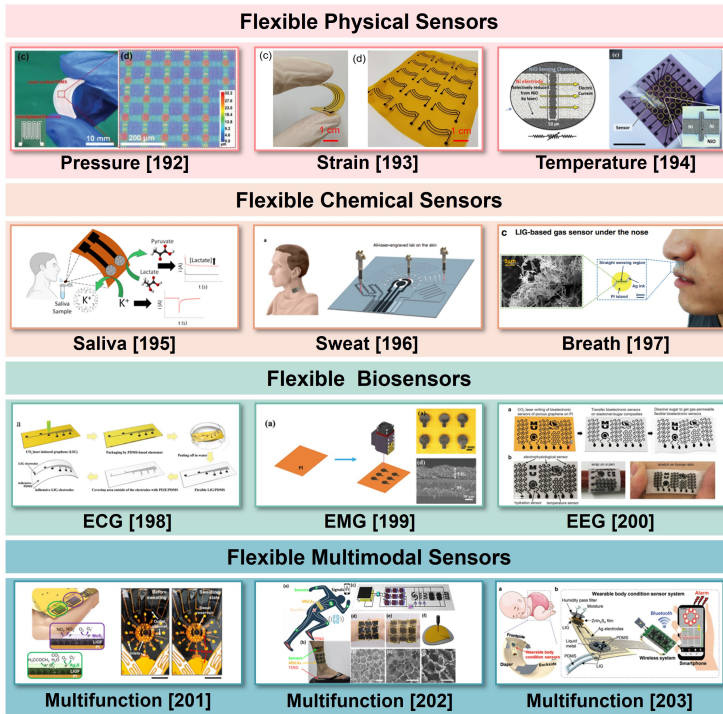
Figure 1.8: Classification of flexible sensors fabricated by laser direct writing (LDW)-based micro-nano fabrication technology.

midity changes, ideal for food packaging quality monitoring. For the flexible chemical sensors, Yang et al. [41] introduce a highly sensitive sensor for selective NO_2 gas detection using laser-induced graphene doped with vanadium oxide. This sensor, with its dual gas and temperature measurement capabilities, shows great potential for applications in precision agriculture and environmental monitoring. In the biosensor domain, Gandla et al. [182] create a large-area, stretchable electronic system through laser ablation, which is soft, adhesive, breathable, and suitable for continuous physiological monitoring, showing robust performance in robotic interactions. For the flexible multimodal sensors, Wang et al. [183] introduce a novel method for producing freestanding graphene papers using laser-induced techniques, allowing scalable fabrication with customizable properties, ideal for flexible electronics and smart structures with tailored mechanical, electrical, and superhydrophobic features for diverse applications.

1.3.3. MECHANISM CLASSIFICATION OF LDW TECHNOLOGY IN FLEXIBLE SENSORS

In LDW processing, the adjustment of laser parameters, such as wavelength, power, frequency, time, pulse width, scanning speed, etc., is crucial for achieving specific processing effects, which are usually produced by the synergistic action of several laser pa-

rameters. Based on their mechanism of action, LDW technologies can be classified into three main categories: laser additive manufacturing, laser subtractive manufacturing, and laser transformative manufacturing, as shown in Figure 1.9.
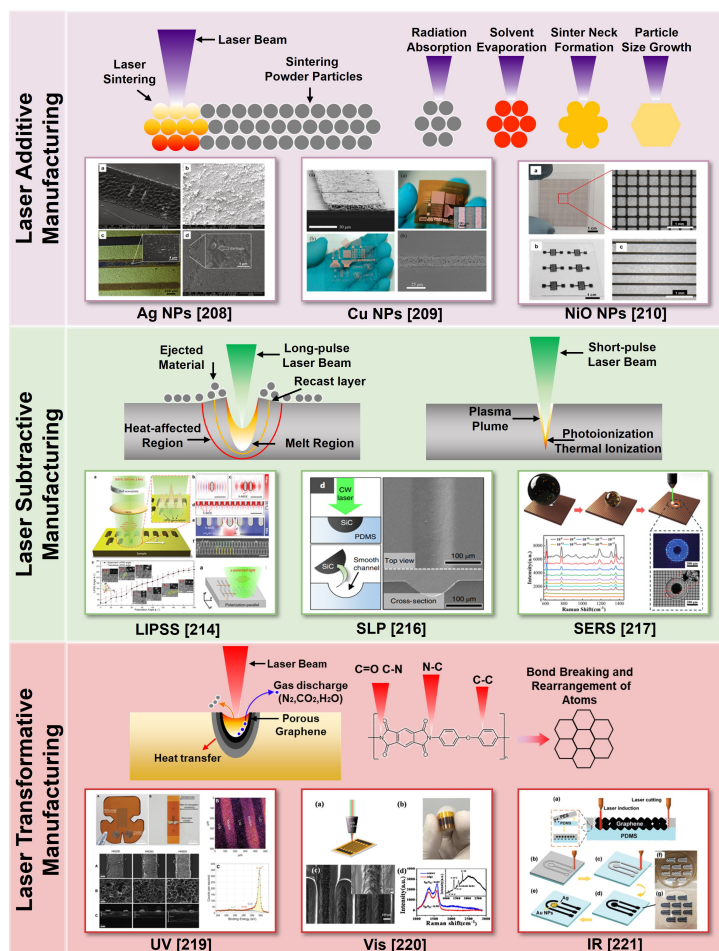
Figure 1.9: Mechanisms for fabricating flexible sensors using LDW technology are categorized as laser additive manufacturing, laser subtractive manufacturing, and laser transformative manufacturing.

Laser additive manufacturing (LAM) utilizes lasers as an energy source to melt or sinter materials to build three-dimensional structures layer by layer. This technology is compatible with a wide range of nanomaterials, including nanoparticles, nanowires, nanotubes, and nanorods [204], and is extensively employed in the fabrication of flexible circuits [205], flexible sensors [206], and flexible heaters [207]. Particularly on flexible and stretchable substrates, laser sintered nano precursor inks enable the rapid formation of continuous conductive structures [208–210]. During the laser sintering process, the metal nanoparticles first absorb the laser energy and rapidly heat up to the melt-

ing point. Then the heat spreads to the surrounding area, prompting the evaporation of solvents and the decomposition of organic additives within the film [211]. Under the action of a high-energy laser, the molten metal nanoparticles form sintered necks due to the surface plasmon resonance effect and gradually agglomerate into larger particles. Through laser scanning, these particles repeatedly melt and solidify to form uniform conductive paths. Furthermore, the laser promotes the decomposition of organic reducing agents and the reduction of metal ions in metal oxide nano-inks to prepare functionalized materials. The high positioning accuracy and rapid thermal effect of laser sintering prevent extensive damage to the substrate over a long period, making it ideal for flexible polymer substrates. Simultaneously, the laser heat creates a strong interfacial bond between the conductive metal matrix and the substrate [212]. With the continuous optimization of the laser system, the precision and application range of this technology continues to expand, effectively breaking through the limitations of traditional flexible sensor manufacturing.

Laser subtractive manufacturing (LSM) technology utilizes the precisely controlled thermal effects of lasers to facilitate the patterning, cutting, and ablation of materials and the fine preparation of micro- and nano-structures [213]. The technology is particularly well suited to the precise fabrication of shape-specific patterns and microdevices, showing unique advantages, especially in the manufacture of micro-sized devices. In laser micro- and nano-subtractive fabrication techniques, the laser-induced periodic surface structuring (LIPSS) method is the most advanced [214]. This technology allows the creation of composite structures at different scales, dynamically tuning the interfacial properties of the material and generating complex nanostructures [215]. In addition, successive laser pyrolysis (SLP) has been applied to the development of biosensor materials and the fabrication of microchannels, thus pioneering the precise three-dimensional processing of PDMS [216]. Furthermore, laser ablation has also shown its unique advantages in the fabrication of functional surfaces (e.g., super hydrophilic or hydrophobic surfaces) and the preparation of surface-enhanced Raman scattering (SERS) sensors [217]. Overall, by fine-tuning parameters such as laser power and laser scanning speed, laser subtractive manufacturing technology simplifies the process and improves processing quality and efficiency. The technology has the potential to replace traditional multi-step, time-consuming, and expensive manufacturing processes and shows great potential for application, especially in the development of flexible sensors.

Laser transformative manufacturing (LTM) technology is widely used to modify carbon-based precursor materials by improving and optimizing the properties of the target material through laser-induced physical or chemical reactions. The most famous application example is laser-induced graphene (LIG), a carbon-based material with excellent mechanical and electrochemical properties, which is widely used to prepare flexible functional devices [218]. The preparation of LIG involves different types of lasers, including ultraviolet (UV) laser [219], visible (Vis) laser [220], and infrared (IR) lasers [221]. These different wavelengths of laser light can promote the modification of carbon-based polymers through photochemical or photothermal effects [222, 223]. For instance, under UV laser irradiation, high-energy photons directly break low-energy chemical bonds in carbon-based precursors to form dense graphene structures [219]. In contrast, under the action of infrared laser, high temperature induces the breaking of chemical bonds,

1

such as C-O, C=O, and C-N, mainly through photothermal reactions, which promotes the carbonization and graphitization processes, thus generating graphene network structures with high porosity [221]. Typically, lasers with long pulse widths (e.g., continuous wave, millisecond, microsecond, and nanosecond lasers) are used to process LIG and its derivatives by gathering a large amount of energy in a short period through the photothermal effect [224]. This type of processing not only breaks the material bonding at localized high temperatures but also inhibits the decomposition of carbon precursors and induces the aggregation of small carbon clusters into large graphene clusters while reducing oxidation [225]. To obtain high-precision graphene patterning, ultrafast lasers (e.g., picosecond and femtosecond lasers) are usually employed, whose high instantaneous output power induces nonlinear interactions with carbon-based precursors [226]. This technology provides a flexible, customizable, and scalable solution for the preparation of flexible sensors.

1.4. MOTIVATION AND OUTLINE OF THIS THESIS

1.4.1. MOTIVATION

With the rapid development of science and technology, flexible electronic devices, especially flexible sensors, have shown great application potential and practical value in several fields. These sensors are widely used in health monitoring and environmental detection due to their excellent adaptability, compatibility, and flexibility. Although flexible sensors based on various micro-nanostructures and innovative materials have made significant progress in recent years, challenges remain in terms of sensor performance, integration capability, and manufacturing efficiency. This thesis is dedicated to exploring and addressing the core technological and material challenges that hinder the further development of flexible sensors. Through an in-depth study of the mechanisms, advantages, and potential applications of UV pulsed laser direct writing (LDW) technology in sensor fabrication, this research overcomes the limitations of traditional fabrication technologies and systematically introduces innovations in the following areas:

High-Performance Flexible Pressure Sensors:

1. Developed Laser Pyrolysis Direct Writing (LPDW) technology for the rapid fabrication of flexible pressure sensors with microstructures (micro-truncated pyramid).

2. Explained the mechanism of continuous laser pyrolysis (CLP) of PDMS via UV lasers.

3. Investigated the impact of different UV laser parameters on the performance of flexible pressure sensors with PDMS microstructures.

High-Performance Flexible Strain Sensors:

1. Developed Laser Transmission Pyrolysis (LTP) technology for the rapid fabrication of strain sensors with microstructures (microchannel).

2. Explained the working mechanism of flexible strain sensors based on metal (Au) cracking.

3. Analyzed the mechanical performance and deformation response of flexible sensors with PDMS substrates under different laser scanning intervals.

High-Performance Flexible Gas Sensors:

1. Developed Selective Reduction Laser Sintering (SRLS) technology to fabricate

highly sensitive and selective flexible nitrogen dioxide (NO_2) gas sensors.

2. Developed a method to fabricate and modulate oxygen vacancy (OV) defects in In2O3 nanoparticles through laser sintering, significantly enhancing the performance of the sensor.

3. Explored the effects of laser parameters on gas sensor performance, offering a technological route for scalable sensor production.

High-Performance Flexible Temperature Sensors:

1. Developed Ultraviolet-Laser Direct Writing (UV-LDW) technology for the fabrication of flexible temperature sensors based on NiO-LIG nanocomposites.

2. Revealed the reduction mechanism of NiO via ultraviolet laser direct writing and its role in enhancing the performance of NiO-LIG flexible temperature sensors.

3. Explored the effects of different scanning intervals on the performance of NiO-LIG temperature sensors, demonstrating their potential applications.

These technologies fully demonstrate the diverse applications of UV laser technology in manufacturing high-performance flexible sensors. By optimizing each technology for specific material and application requirements, they not only significantly enhance the sensing performance and application potential of the sensors but also promote the widespread use of new materials and manufacturing technologies in the fields of flexible sensors and rapid laser manufacturing, thereby significantly upgrading the state of the art in these fields.

1.4.2. Outline

This thesis is organized into 6 chapters, introducing in detail the sensor design, fabrication process, sensor mechanism, performance testing, and potential applications of flexible sensors fabricated using laser direct writing (LDW) technology. The thesis outline is shown in Figure 1.10.
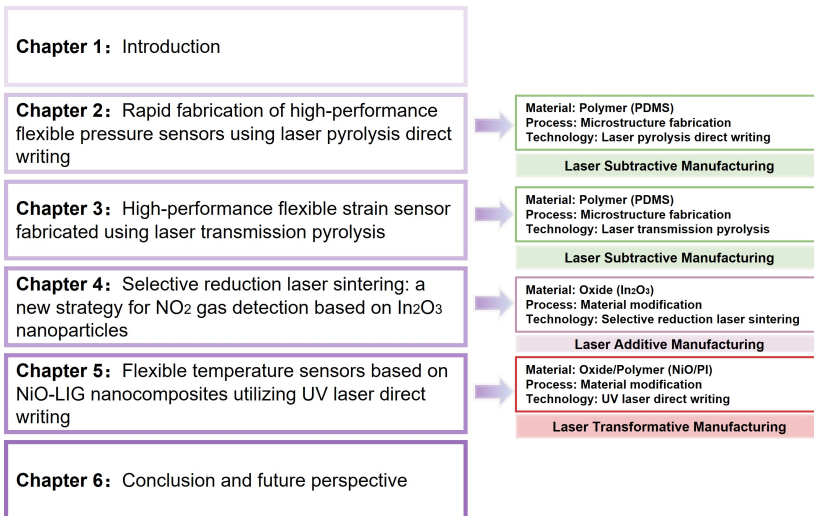
Figure 1.10: The outline of the thesis.

1

Chapter 1 introduces the background and importance of flexible sensors in modern technology. It further discusses the classification, mechanisms, and development trends of flexible sensors. Additionally, this chapter provides an in-depth discussion on the application and classification of laser direct writing (LDW) technology in the development of flexible sensors, along with the motivation and outline of this thesis.

Chapter 2 describes in detail the conditions, mechanisms, thermal effects, and processes for fabricating flexible pressure sensors using laser pyrolysis direct writing (LPDW) technology. The chapter also explores the performance and potential applications of these sensors.

Chapter 3 discusses the methods and techniques used to design and fabricate flexible strain sensors with laser transport pyrolysis (LTP) technology. Additionally, it details the design and fabrication processes, performance testing, mechanism analysis, and practical applications of the sensors.

Chapter 4 presents the development process of a NO_2 gas sensor using In_2O_3 nanoparticles and the selective reduction laser sintering (SRLS) technique. This includes investigations of the SRLS process, defect characterization, sensor performance testing, and analysis of the sensing mechanism.

Chapter 5 details the fabrication of flexible temperature sensors using NiO-LIG nanocomposites with the ultraviolet (UV) laser direct writing technique. The chapter discusses the preparation process, surface and material properties, performance characterization of the sensors, and their application demonstrations.

Chapter 6 summarizes the entire research work, highlights key findings, and suggests directions for future research.

References

[1]   A. Nathan *et al.*, "Flexible electronics: The next ubiquitous platform", *Proceedings of the IEEE*, vol. 100, no. Special Centennial Issue, pp. 1486–1517, 2012.

[2]   B. Zong, S. Wu, Y. Yang, Q. Li, T. Tao, and S. Mao, "Smart gas sensors: Recent developments and future prospective", *Nano-Micro Letters*, vol. 17, no. 1, p. 54, 2025.

[3]   P. Wang *et al.*, "The evolution of flexible electronics: From nature, beyond nature, and to nature", *Advanced Science*, vol. 7, no. 20, p. 2 001 116, 2020.

[4]   Y. Khan *et al.*, "Flexible hybrid electronics: Direct interfacing of soft and hard electronics for wearable health monitoring", *Advanced Functional Materials*, vol. 26, no. 47, pp. 8764–8775, 2016.

[5]   W. Yang, Y. Qin, Z. Wang, T. Yu, and Z. Ge, "Recent advances in the development of flexible sensors: Mechanisms, materials, performance optimization, and applications", *Journal of Electronic Materials*, vol. 51, no. 12, pp. 6735–6769, 2022.

[6]   T. Q. Trung and N.-E. Lee, "Flexible and stretchable physical sensor integrated platforms for wearable human-activity monitoringand personal healthcare", *Advanced materials*, vol. 28, no. 22, pp. 4338–4372, 2016.

[7]   Y. Yang and Z. D. Deng, "Stretchable sensors for environmental monitoring", *Applied Physics Reviews*, vol. 6, no. 1, 2019.

[8] B. Zazoum, K. M. Batoo, and M. A. A. Khan, "Recent advances in flexible sensors and their applications", *Sensors*, vol. 22, no. 12, p. 4653, 2022.

[9] Y. Luo *et al.*, "Technology roadmap for flexible sensors", *ACS nano*, vol. 17, no. 6, pp. 5211–5295, 2023.

[10] Y. Zhang, X. Wang, K. Yan, H. Zhu, B. Wang, and B. Zou, "Laser micro/nano-structuring pushes forward smart sensing: Opportunities and challenges", *Advanced Functional Materials*, vol. 33, no. 8, p. 2 211 272, 2023.

[11] Z. Huang, G. Shao, and L. Li, "Micro/nano functional devices fabricated by additive manufacturing", *Progress in Materials Science*, vol. 131, p. 101 020, 2023.

[12] D. J. Joe *et al.*, "Laser–material interactions for flexible applications", *Advanced materials*, vol. 29, no. 26, p. 1 606 586, 2017.

[13] M. Cui *et al.*, "High-efficiency and low-intensity threshold femtosecond laser direct writing of precise metallic micropatterns on transparent substrate", *Advanced Materials Technologies*, vol. 8, no. 8, p. 2 201 610, 2023.

[14] Z.-L. Wu *et al.*, "Polymer-based device fabrication and applications using direct laser writing technology", *Polymers*, vol. 11, no. 3, p. 553, 2019.

[15] C. Zhang *et al.*, "Laser direct writing of highly ordered two-level hierarchical microstructures for flexible piezoresistive sensor with enhanced sensitivity", *Advanced Materials Interfaces*, vol. 9, no. 1, p. 2 101 596, 2022.

[16] J. Maciulaitis *et al.*, "Customization of direct laser lithography-based 3d scaffolds for optimized in vivo outcome", *Applied Surface Science*, vol. 487, pp. 692–702, 2019.

[17] L. Shen, S. Zhou, B. Gu, S. Wang, and S. Wang, "Highly sensitive strain sensor fabricated by direct laser writing on lignin paper with strain engineering", *Advanced Engineering Materials*, vol. 25, no. 14, p. 2 201 882, 2023.

[18] Y. Yin, C. Guo, H. Li, H. Yang, F. Xiong, and D. Chen, "The progress of research into flexible sensors in the field of smart wearables", *Sensors*, vol. 22, no. 14, p. 5089, 2022.

[19] Y. Gao, L. Yu, J. C. Yeo, and C. T. Lim, "Flexible hybrid sensors for health monitoring: Materials and mechanisms to render wearability", *Advanced Materials*, vol. 32, no. 15, p. 1 902 133, 2020.

[20] M. A. A. Mamun and M. R. Yuce, "Recent progress in nanomaterial enabled chemical sensors for wearable environmental monitoring applications", *Advanced Functional Materials*, vol. 30, no. 51, p. 2 005 703, 2020.

[21] R. Yin, D. Wang, S. Zhao, Z. Lou, and G. Shen, "Wearable sensors-enabled human–machine interaction systems: From design to application", *Advanced Functional Materials*, vol. 31, no. 11, p. 2 008 936, 2021.

[22] Y. S. Rim, S.-H. Bae, H. Chen, N. De Marco, and Y. Yang, "Recent progress in materials and devices toward printable and flexible sensors", *Advanced Materials*, vol. 28, no. 22, pp. 4415–4440, 2016.

1

[23] F. Jiang, G.-B. Lee, Y.-C. Tai, and C.-M. Ho, "A flexible micromachine-based shear-stress sensor array and its application to separation-point detection", *Sensors and Actuators A: Physical*, vol. 79, no. 3, pp. 194–203, 2000.

[24] D. Nilsson, T. Kugler, P.-O. Svensson, and M. Berggren, "An all-organic sensor–transistor based on a novel electrochemical transducer concept printed electrochemical sensors on paper", *Sensors and Actuators B: Chemical*, vol. 86, no. 2-3, pp. 193–197, 2002.

[25] T. Someya, T. Sekitani, S. Iba, Y. Kato, H. Kawaguchi, and T. Sakurai, "A large-area, flexible pressure sensor matrix with organic field-effect transistors for artificial skin applications", *Proceedings of the National Academy of Sciences*, vol. 101, no. 27, pp. 9966–9970, 2004.

[26] H.-K. Lee, S.-I. Chang, and E. Yoon, "A flexible polymer tactile sensor: Fabrication and modular expandability for large area deployment", *Journal of microelectromechanical systems*, vol. 15, no. 6, pp. 1681–1686, 2006.

[27] C.-Y. Lee, G.-W. Wu, and W.-J. Hsieh, "Fabrication of micro sensors on a flexible substrate", *Sensors and Actuators A: Physical*, vol. 147, no. 1, pp. 173–176, 2008.

[28] S. C. Mannsfeld *et al.*, "Highly sensitive flexible pressure sensors with microstructured rubber dielectric layers", *Nature materials*, vol. 9, no. 10, pp. 859–864, 2010.

[29] T. Yamada *et al.*, "A stretchable carbon nanotube strain sensor for human-motion detection", *Nature nanotechnology*, vol. 6, no. 5, pp. 296–301, 2011.

[30] C. Pang *et al.*, "A flexible and highly sensitive strain-gauge sensor using reversible interlocking of nanofibres", *Nature materials*, vol. 11, no. 9, pp. 795–801, 2012.

[31] G. Schwartz *et al.*, "Flexible polymer transistors with high pressure sensitivity for application in electronic skin and health monitoring", *Nature communications*, vol. 4, no. 1, p. 1859, 2013.

[32] S. Gong *et al.*, "A wearable and highly sensitive pressure sensor with ultrathin gold nanowires", *Nature communications*, vol. 5, no. 1, p. 3132, 2014.

[33] Y. Joo *et al.*, "Silver nanowire-embedded pdms with a multiscale structure for a highly sensitive and robust flexible pressure sensor", *Nanoscale*, vol. 7, no. 14, pp. 6208–6215, 2015.

[34] Y. Yamamoto *et al.*, "Printed multifunctional flexible device with an integrated motion sensor for health care monitoring", *Science advances*, vol. 2, no. 11, e1601473, 2016.

[35] N. Matsuhisa *et al.*, "Printable elastic conductors by in situ formation of silver nanoparticles from silver flakes", *Nature materials*, vol. 16, no. 8, pp. 834–840, 2017.

[36] B. W. An, S. Heo, S. Ji, F. Bien, and J.-U. Park, "Transparent and flexible fingerprint sensor array with multiplexed detection of tactile pressure and skin temperature", *Nature communications*, vol. 9, no. 1, p. 2458, 2018.

[37] C. M. Boutry *et al.*, "Biodegradable and flexible arterial-pulse sensor for the wireless monitoring of blood flow", *Nature biomedical engineering*, vol. 3, no. 1, pp. 47–57, 2019.

[38] Y. Song *et al.*, "Wireless battery-free wearable sweat sensor powered by human motion", *Science advances*, vol. 6, no. 40, eaay9842, 2020.

[39] Q.-B. Zhu *et al.*, "A flexible ultrasensitive optoelectronic sensor array for neuromorphic vision systems", *Nature communications*, vol. 12, no. 1, p. 1798, 2021.

[40] Y. Yu *et al.*, "All-printed soft human-machine interface for robotic physicochemical sensing", *Science robotics*, vol. 7, no. 67, eabn0495, 2022.

[41] L. Yang *et al.*, "Vanadium oxide-doped laser-induced graphene multi-parameter sensor to decouple soil nitrogen loss and temperature", *Advanced Materials*, vol. 35, no. 14, p. 2 210 322, 2023.

[42] H. Yu *et al.*, "Flexible temperature-pressure dual sensor based on 3D spiral thermoelectric Bi2Te3 films", *Nature Communications*, vol. 15, no. 1, p. 2521, 2024.

[43] M. J. McGrath and C. N. Scanaill, *Sensor technologies: healthcare, wellness, and environmental applications*. Springer Nature, 2013.

[44] T. Yang, D. Xie, Z. Li, and H. Zhu, "Recent advances in wearable tactile sensors: Materials, sensing mechanisms, and device performance", *Materials Science and Engineering: R: Reports*, vol. 115, pp. 1–37, 2017.

[45] M. Zhong *et al.*, "Wide linear range and highly sensitive flexible pressure sensor based on multistage sensing process for health monitoring and human-machine interfaces", *Chemical Engineering Journal*, vol. 412, p. 128 649, 2021.

[46] J. Wang *et al.*, "Wearable multichannel pulse condition monitoring system based on flexible pressure sensor arrays", *Microsystems & Nanoengineering*, vol. 8, no. 1, p. 16, 2022.

[47] S. Baloda, Z. A. Ansari, S. Singh, and N. Gupta, "Development and analysis of graphene nanoplatelets (GNPs)-based flexible strain sensor for health monitoring applications", *IEEE Sensors Journal*, vol. 20, no. 22, pp. 13 302–13 309, 2020.

[48] H. Tian *et al.*, "Scalable fabrication of high-performance and flexible graphene strain sensors", *Nanoscale*, vol. 6, no. 2, pp. 699–705, 2014.

[49] Y.-F. Wang *et al.*, "Fully printed PEDOT: PSS-based temperature sensor with high humidity stability for wireless healthcare monitoring", *Scientific reports*, vol. 10, no. 1, p. 2467, 2020.

[50] C. Zhao *et al.*, "Biological hair-inspired AgNWs@ au-embedded nafion electrodes with high stability for self-powered ionic flexible sensors", *ACS Applied Materials & Interfaces*, vol. 14, no. 40, pp. 46 023–46 031, 2022.

[51] L. Manjakkal, S. Dervin, and R. Dahiya, "Flexible potentiometric pH sensors for wearable systems", *RSC advances*, vol. 10, no. 15, pp. 8594–8617, 2020.

[52] W. Gao *et al.*, "Fully integrated wearable sensor arrays for multiplexed in situ perspiration analysis", *Nature*, vol. 529, no. 7587, pp. 509–514, 2016.

[53] W. Ling *et al.*, "Materials and techniques for implantable nutrient sensing using flexible sensors integrated with metal–organic frameworks", *Advanced materials*, vol. 30, no. 23, p. 1 800 917, 2018.

1

[54]   F. Zhang *et al.*, "A highly accurate flexible sensor system for human blood pressure and heart rate monitoring based on graphene/sponge", *RSC advances*, vol. 12, no. 4, pp. 2391–2398, 2022.

[55]   Y. Su *et al.*, "Printable, highly sensitive flexible temperature sensors for human body temperature monitoring: A review", *Nanoscale Research Letters*, vol. 15, pp. 1–34, 2020.

[56]   Y. Zhou *et al.*, "Halide-exchanged perovskite photodetectors for wearable visible-blind ultraviolet monitoring", *Nano Energy*, vol. 100, p. 107 516, 2022.

[57]   W. Peng and H. Wu, "Flexible and stretchable photonic sensors based on modulation of light transmission", *Advanced Optical Materials*, vol. 7, no. 12, p. 1 900 329, 2019.

[58]   F. Zhang, Y. Zang, D. Huang, C.-a. Di, and D. Zhu, "Flexible and self-powered temperature–pressure dual-parameter sensors using microstructure-frame-supported organic thermoelectric materials", *Nature communications*, vol. 6, no. 1, p. 8356, 2015.

[59]   P. Escobedo, M. Bhattacharjee, F. Nikbakhtnasrabadi, and R. Dahiya, "Flexible strain and temperature sensing NFC tag for smart food packaging applications", *IEEE Sensors Journal*, vol. 21, no. 23, pp. 26 406–26 414, 2021.

[60]   Z. Duan *et al.*, "Facile, flexible, cost-saving, and environment-friendly paper-based humidity sensor for multifunctional applications", *ACS applied materials & interfaces*, vol. 11, no. 24, pp. 21 840–21 849, 2019.

[61]   P. Zhu *et al.*, "Flexible and highly sensitive humidity sensor based on cellulose nanofibers and carbon nanotube composite film", *Langmuir*, vol. 35, no. 14, pp. 4834–4842, 2019.

[62]   S. Pandey, G. K. Goswami, and K. K. Nanda, "Nanocomposite based flexible ultrasensitive resistive gas sensor for chemical reactions studies", *Scientific reports*, vol. 3, no. 1, p. 2082, 2013.

[63]   H.-Y. Li, C.-S. Lee, D. H. Kim, and J.-H. Lee, "Flexible room-temperature nh3 sensor for ultrasensitive, selective, and humidity-independent gas detection", *ACS applied materials & interfaces*, vol. 10, no. 33, pp. 27 858–27 867, 2018.

[64]   S. Honda *et al.*, "Detachable flexible ISFET-based pH sensor array with a flexible connector", *Advanced Electronic Materials*, vol. 6, no. 10, p. 2 000 583, 2020.

[65]   Y. Li, Y. Mao, C. Xiao, X. Xu, and X. Li, "Flexible pH sensor based on a conductive PANI membrane for pH monitoring", *RSC advances*, vol. 10, no. 1, pp. 21–28, 2020.

[66]   Z. Xu *et al.*, "Flat flexible thin milli-electrode array for real-time in situ water quality monitoring in distribution systems", *Environmental Science: Water Research & Technology*, vol. 3, no. 5, pp. 865–874, 2017.

[67]   D. Wang, S. Luo, and K.-D. Xu, "A flexible terahertz metamaterial sensor for pesticide sensing and detection", *ACS Applied Materials & Interfaces*, 2024.

[68] D. Čygas*, A. Laurinavičius, M. Paliukaitė, A. Motiejūnas, L. Žiliūtė, and A. Vaitkus, "Monitoring the mechanical and structural behavior of the pavement structure using electronic sensors", *Computer-Aided Civil and Infrastructure Engineering*, vol. 30, no. 4, pp. 317–328, 2015.

[69] J. Wu *et al.*, "Highly sensitive temperature–pressure bimodal aerogel with stimulus discriminability for human physiological monitoring", *Nano Letters*, vol. 22, no. 11, pp. 4459–4467, 2022.

[70] S. Mousavi, D. Howard, F. Zhang, J. Leng, and C. H. Wang, "Direct 3D printing of highly anisotropic, flexible, constriction-resistive sensors for multidirectional proprioception in soft robots", *ACS applied materials & interfaces*, vol. 12, no. 13, pp. 15 631–15 643, 2020.

[71] M. B. Durukan, M. O. Cicek, D. Doganay, M. C. Gorur, S. Çınar, and H. E. Unalan, "Multifunctional and physically transient supercapacitors, triboelectric nanogenerators, and capacitive sensors", *Advanced Functional Materials*, vol. 32, no. 1, p. 2 106 066, 2022.

[72] C. Zhang, S. Liu, X. Huang, W. Guo, Y. Li, and H. Wu, "A stretchable dual-mode sensor array for multifunctional robotic electronic skin", *Nano Energy*, vol. 62, pp. 164–170, 2019.

[73] J. Pan, Z. Zhang, C. Jiang, L. Zhang, and L. Tong, "A multifunctional skin-like wearable optical sensor based on an optical micro-/nanofibre", *Nanoscale*, vol. 12, no. 33, pp. 17 538–17 544, 2020.

[74] D. Lei *et al.*, "An ion channel-induced self-powered flexible pressure sensor based on potentiometric transduction mechanism", *Advanced Functional Materials*, vol. 32, no. 5, p. 2 108 856, 2022.

[75] L. Pan *et al.*, "Flexible magnetic sensors", *Sensors*, vol. 23, no. 8, p. 4083, 2023.

[76] M. Melzer *et al.*, "Wearable magnetic field sensors for flexible electronics", *Advanced Materials*, vol. 27, no. 7, pp. 1274–1280, 2015.

[77] L. Manjakkal, B. Sakthivel, N. Gopalakrishnan, and R. Dahiya, "Printed flexible electrochemical pH sensors based on CuO nanorods", *Sensors and Actuators B: Chemical*, vol. 263, pp. 50–58, 2018.

[78] Q. Chen, D. Liu, L. Lin, and J. Wu, "Bridging interdigitated electrodes by electrochemical-assisted deposition of graphene oxide for constructing flexible gas sensor", *Sensors and Actuators B: Chemical*, vol. 286, pp. 591–599, 2019.

[79] Y. Wang, Y. Yu, X. Wei, and F. Narita, "Self-powered wearable piezoelectric monitoring of human motion and physiological signals for the postpandemic era: A review", *Advanced Materials Technologies*, vol. 7, no. 12, p. 2 200 318, 2022.

[80] D.-L. Wen *et al.*, "Printed silk-fibroin-based triboelectric nanogenerators for multi-functional wearable sensing", *Nano Energy*, vol. 66, p. 104 123, 2019.

[81] Y. Chen *et al.*, "Energy autonomous electronic skin with direct temperature-pressure perception", *Nano Energy*, vol. 98, p. 107 273, 2022.

[82]   Y. Lee *et al.*, "Flexible pyroresistive graphene composites for artificial thermosensation differentiating materials and solvent types", *ACS nano*, vol. 16, no. 1, pp. 1208–1219, 2022.

[83]   Z. Wang *et al.*, "The semiconductor/conductor interface piezoresistive effect in an organic transistor for highly sensitive pressure sensors", *Advanced Materials*, vol. 31, no. 6, p. 1 805 630, 2019.

[84]   S. Sharma *et al.*, "Hydrogen-bond-triggered hybrid nanofibrous membrane-based wearable pressure sensor with ultrahigh sensitivity over a broad pressure range", *ACS nano*, vol. 15, no. 3, pp. 4380–4393, 2021.

[85]   G. Y. Bae, S. W. Pak, D. Kim, G. Lee, Y Chung, K Cho, *et al.*, "Linearly and highly pressure-sensitive electronic skin based on a bioinspired hierarchical structural array.", *Advanced Materials (Deerfield Beach, Fla.)*, vol. 28, no. 26, pp. 5300–5306, 2016.

[86]   C. Jeong, J. S. Lee, B. Park, C. S. Hong, J. U. Kim, and T.-i. Kim, "Controllable configuration of sensing band in a pressure sensor by lenticular pattern deformation on designated electrodes", *Advanced Materials*, vol. 31, no. 36, p. 1 902 689, 2019.

[87]   Y. Ye and F. Jiang, "Highly stretchable, durable, and transient conductive hydrogel for multi-functional sensor and signal transmission applications", *Nano Energy*, vol. 99, p. 107 374, 2022.

[88]   X. Liao *et al.*, "An artificial peripheral neural system based on highly stretchable and integrated multifunctional sensors", *Advanced Functional Materials*, vol. 31, no. 24, p. 2 101 107, 2021.

[89]   J. Choi *et al.*, "Synergetic effect of porous elastomer and percolation of carbon nanotube filler toward high performance capacitive pressure sensors", *ACS applied materials & interfaces*, vol. 12, no. 1, pp. 1698–1706, 2019.

[90]   S. Chun *et al.*, "A highly sensitive force sensor with fast response based on interlocked arrays of indium tin oxide nanosprings toward human tactile perception", *Advanced Functional Materials*, vol. 28, no. 42, p. 1 804 132, 2018.

[91]   J. Oh *et al.*, "Highly uniform and low hysteresis piezoresistive pressure sensors based on chemical grafting of polypyrrole on elastomer template with uniform pore size", *Small*, vol. 15, no. 33, p. 1 901 744, 2019.

[92]   X. Guo *et al.*, "Biologically emulated flexible sensors with high sensitivity and low hysteresis: Toward electronic skin to a sense of touch", *Small*, vol. 18, no. 32, p. 2 203 044, 2022.

[93]   T. Yang *et al.*, "Tactile sensing system based on arrays of graphene woven microfabrics: Electromechanical behavior and electronic skin application", *ACS nano*, vol. 9, no. 11, pp. 10 867–10 875, 2015.

[94]   D. Kang *et al.*, "Ultrasensitive mechanical crack-based sensor inspired by the spider sensory system", *Nature*, vol. 516, no. 7530, pp. 222–226, 2014.

[95]   H. Niu *et al.*, "Advances in flexible sensors for intelligent perception system enhanced by artificial intelligence", *InfoMat*, vol. 5, no. 5, e12412, 2023.

[96] S. Y. Kwon *et al.*, "On-skin and tele-haptic application of mechanically decoupled taxel array on dynamically moving and soft surfaces", *npj Flexible Electronics*, vol. 6, no. 1, p. 98, 2022.

[97] A. Malik and B. Kandasubramanian, "Flexible polymeric substrates for electronic applications", *Polymer Reviews*, vol. 58, no. 4, pp. 630–667, 2018.

[98] X. Wang, Y. Deng, P. Jiang, X. Chen, and H. Yu, "Low-hysteresis, pressure-insensitive, and transparent capacitive strain sensor for human activity monitoring", *Microsystems & Nanoengineering*, vol. 8, no. 1, p. 113, 2022.

[99] S. Emamian, B. B. Narakathu, A. A. Chlaihawi, B. J. Bazuin, and M. Z. Atashbar, "Screen printing of flexible piezoelectric based device on polyethylene terephthalate (PET) and paper for touch and force sensing applications", *Sensors and Actuators A: Physical*, vol. 263, pp. 639–647, 2017.

[100] B. Ma, J. Ren, J. Deng, and W. Yuan, "Flexible thermal sensor array on PI film substrate for underwater applications", in *2010 IEEE 23rd International Conference on Micro Electro Mechanical Systems (MEMS)*, IEEE, 2010, pp. 679–682.

[101] R. Wu *et al.*, "Silk composite electronic textile sensor for high space precision 2D combo temperature–pressure sensing", *Small*, vol. 15, no. 31, p. 1 901 558, 2019.

[102] J.-w. Zhang, Y. Zhang, Y.-y. Li, and P. Wang, "Textile-based flexible pressure sensors: A review", *Polymer Reviews*, vol. 62, no. 1, pp. 65–94, 2022.

[103] F. Yin *et al.*, "A waterproof and breathable Cotton/rGO/CNT composite for constructing a layer-by-layer structured multifunctional flexible sensor", *Nano Research*, vol. 15, no. 10, pp. 9341–9351, 2022.

[104] L. Zhang, H. Li, X. Lai, T. Gao, J. Yang, and X. Zeng, "Thiolated graphene@ polyester fabric-based multilayer piezoresistive pressure sensors for detecting human motion", *ACS applied materials & interfaces*, vol. 10, no. 48, pp. 41 784–41 792, 2018.

[105] S. Lu *et al.*, "Wearable graphene film strain sensors encapsulated with nylon fabric for human motion monitoring", *Sensors and Actuators A: Physical*, vol. 295, pp. 200–209, 2019.

[106] Z. Dong *et al.*, "Facile fabrication of paper-based flexible thermoelectric generator", *npj Flexible Electronics*, vol. 5, no. 1, p. 6, 2021.

[107] S. K. Mahadeva, K. Walus, and B. Stoeber, "Paper as a platform for sensing applications and other devices: A review", *ACS applied materials & interfaces*, vol. 7, no. 16, pp. 8345–8362, 2015.

[108] L. R. Shobin and S. Manivannan, "Carbon nanotubes on paper: Flexible and disposable chemiresistors", *Sensors and Actuators B: Chemical*, vol. 220, pp. 1178–1185, 2015.

[109] S. Kumar *et al.*, "Reduced graphene oxide modified smart conducting paper for cancer biosensor", *Biosensors and Bioelectronics*, vol. 73, pp. 114–122, 2015.

[110] D. Maddipatla *et al.*, "Rapid prototyping of a novel and flexible paper based oxygen sensing patch via additive inkjet printing process", *RSC advances*, vol. 9, no. 39, pp. 22 695–22 704, 2019.

1

[111] Y. Guo, X. Wei, S. Gao, W. Yue, Y. Li, and G. Shen, "Recent advances in carbon material-based multifunctional sensors and their applications in electronic skin systems", *Advanced Functional Materials*, vol. 31, no. 40, p. 2 104 288, 2021.

[112] H. Jang, Y. J. Park, X. Chen, T. Das, M.-S. Kim, and J.-H. Ahn, "Graphene-based flexible and stretchable electronics", *Advanced Materials*, vol. 28, no. 22, pp. 4184–4202, 2016.

[113] J. Lee *et al.*, "Transparent, flexible strain sensor based on a solution-processed carbon nanotube network", *ACS applied materials & interfaces*, vol. 9, no. 31, pp. 26 279–26 285, 2017.

[114] L. T. Duy *et al.*, "Flexible transparent reduced graphene oxide sensor coupled with organic dye molecules for rapid dual-mode ammonia gas detection", *Advanced Functional Materials*, vol. 26, no. 24, pp. 4329–4338, 2016.

[115] D. Shukla, H. Wang, O. Awartani, M. D. Dickey, and Y. Zhu, "Surface embedded metal nanowire–liquid metal–elastomer hybrid composites for stretchable electronics", *ACS Applied Materials & Interfaces*, vol. 16, no. 11, pp. 14 183–14 197, 2024.

[116] Y. Ren, X. Yang, Y. Chang, J. Shu, and K. Luo, "Highly sensitive and flexible strain sensor based on Au thin film", *Journal of Micromechanics and Microengineering*, vol. 29, no. 1, p. 015 001, 2018.

[117] S.-H. Ke *et al.*, "Screen-printed flexible strain sensors with Ag nanowires for intelligent and tamper-evident packaging applications", *Advanced Materials Technologies*, vol. 5, no. 5, p. 1 901 097, 2020.

[118] Y. Guan *et al.*, "A novel composite material for flexible wearable devices based on eutectic gallium indium (EGaIn), multi-walled carbon nanotubes (MWCNTs) and polydimethylsiloxane (PDMS)", *Composite Structures*, vol. 291, p. 115 653, 2022.

[119] M. V. Nikolic, V. Milovanovic, Z. Z. Vasiljevic, and Z. Stamenkovic, "Semiconductor gas sensors: Materials, technology, design, and application", *Sensors*, vol. 20, no. 22, p. 6694, 2020.

[120] X. Liu, L. Gu, Q. Zhang, J. Wu, Y. Long, and Z. Fan, "All-printable band-edge modulated ZnO nanowire photodetectors with ultra-high detectivity", *Nature communications*, vol. 5, no. 1, p. 4007, 2014.

[121] A. V. Raghu, K. K. Karuppanan, J. Nampoothiri, and B. Pullithadathil, "Wearable, flexible ethanol gas sensor based on TiO2 nanoparticles-grafted 2D-titanium carbide nanosheets", *ACS Applied Nano Materials*, vol. 2, no. 3, pp. 1152–1163, 2019.

[122] W. Wu *et al.*, "Piezophototronic effect in single-atomic-layer MoS2 for strain-gated flexible optoelectronics", *Adv. Mater*, vol. 28, no. 38, pp. 8463–8468, 2016.

[123] I.-A. Pavel, S. Lakard, and B. Lakard, "Flexible sensors based on conductive polymers", *Chemosensors*, vol. 10, no. 3, p. 97, 2022.

[124] X. X. Gong *et al.*, "Flexible strain sensor with high performance based on PANI/PDMS films", *Organic Electronics*, vol. 47, pp. 51–56, 2017.

[125] L. Y. Zheng *et al.*, "Electrochemical measurements of biofilm development using polypyrrole enhanced flexible sensors", *Sensors and Actuators B: Chemical*, vol. 182, pp. 725–732, 2013.

[126] Y. Seekaew, S. Lokavee, D. Phokharatkul, A. Wisitsoraat, T. Kerdcharoen, and C. Wongchoosuk, "Low-cost and flexible printed graphene–PEDOT: PSS gas sensor for ammonia detection", *Organic Electronics*, vol. 15, no. 11, pp. 2971–2981, 2014.

[127] R. Liu, J. Chen, Z. Luo, X. Zhang, W. Chen, and Z. Niu, "Stretchable, self-adhesive, conductive, anti-freezing sodium polyacrylate-based composite hydrogels for wearable flexible strain sensors", *Reactive and Functional Polymers*, vol. 172, p. 105 197, 2022.

[128] S. Azadi *et al.*, "Biocompatible and highly stretchable PVA/AgNWs hydrogel strain sensors for human motion detection", *Advanced Materials Technologies*, vol. 5, no. 11, p. 2 000 426, 2020.

[129] S. Sun and X. Maimaitiyiming, "Silver nanowire/polyacrylamide/gelatin flexible stress, strain and temperature sensor", *Colloids and Surfaces A: Physicochemical and Engineering Aspects*, vol. 675, p. 131 919, 2023.

[130] T. Naghdi *et al.*, "Chitin nanofiber paper toward optical (bio) sensing applications", *ACS applied materials & interfaces*, vol. 12, no. 13, pp. 15 538–15 552, 2020.

[131] X. Wang, O. Yue, X. Liu, M. Hou, and M. Zheng, "A novel bio-inspired multifunctional collagen aggregate based flexible sensor with multi-layer and internal 3D network structure", *Chemical Engineering Journal*, vol. 392, p. 123 672, 2020.

[132] M. A. Kafi, A. Paul, A. Vilouras, E. S. Hosseini, and R. S. Dahiya, "Chitosan-graphene oxide-based ultra-thin and flexible sensor for diabetic wound monitoring", *IEEE Sensors Journal*, vol. 20, no. 13, pp. 6794–6801, 2019.

[133] J. Pignanelli, K. Schlingman, T. B. Carmichael, S. Rondeau-Gagné, and M. J. Ahamed, "A comparative analysis of capacitive-based flexible PDMS pressure sensors", *Sensors and Actuators A: Physical*, vol. 285, pp. 427–436, 2019.

[134] D. Ma *et al.*, "A novel photolithographic method for fabrication of flexible micro-patterned glucose sensors", *Journal of Electroanalytical Chemistry*, vol. 876, p. 114 720, 2020.

[135] K. Scholten and E. Meng, "Electron-beam lithography for polymer bioMEMS with submicron features", *Microsystems & nanoengineering*, vol. 2, no. 1, pp. 1–7, 2016.

[136] Y. Chuo, D. Hohertz, C. Landrock, B. Omrane, K. L. Kavanagh, and B. Kaminska, "Large-area low-cost flexible plastic nanohole arrays for integrated bio-chemical sensing", *Ieee Sensors Journal*, vol. 13, no. 10, pp. 3982–3990, 2013.

[137] S. H. Lim, B. Radha, J. Y. Chan, M. S. Saifullah, G. U. Kulkarni, and G. W. Ho, "Flexible palladium-based H2 sensor with fast response and low leakage detection by nanoimprint lithography", *ACS applied materials & interfaces*, vol. 5, no. 15, pp. 7274–7281, 2013.

[138] V. Suresh, L. Ding, A. B. Chew, and F. L. Yap, "Fabrication of large-area flexi-
       ble SERS substrates by nanoimprint lithography", *ACS Applied Nano Materials*,
       vol. 1, no. 2, pp. 886–893, 2018.

[139] D. Wan, H.-L. Chen, Y.-T. Lai, C.-C. Yu, and K.-F. Lin, "Use of reversal nanoim-
       printing of nanoparticles to prepare flexible waveguide sensors exhibiting en-
       hanced scattering of the surface plasmon resonance", *Advanced Functional Ma-
       terials*, vol. 20, no. 11, pp. 1742–1749, 2010.

[140] H. Wang, H. Yang, S. Zhang, L. Zhang, J. Li, and X. Zeng, "3D-printed flexible tac-
       tile sensor mimicking the texture and sensitivity of human skin", *Advanced Ma-
       terials Technologies*, vol. 4, no. 9, p. 1 900 147, 2019.

[141] Z. Tang, S. Jia, C. Zhou, and B. Li, "3D printing of highly sensitive and large-
       measurement-range flexible pressure sensors with a positive piezoresistive ef-
       fect", *ACS applied materials & interfaces*, vol. 12, no. 25, pp. 28 669–28 680, 2020.

[142] C. Yang, A. Abodurexiti, and X. Maimaitiyiming, "Flexible humidity and pressure
       sensors realized by molding and inkjet printing processes with sandwich struc-
       ture", *Macromolecular Materials and Engineering*, vol. 305, no. 8, p. 2 000 287,
       2020.

[143] S. Ma *et al.*, "Fabrication of novel transparent touch sensing device via drop-on-
       demand inkjet printing technique", *ACS applied materials & interfaces*, vol. 7,
       no. 39, pp. 21 628–21 633, 2015.

[144] R. Qin *et al.*, "Flexible fabrication of flexible electronics: A general laser ablation
       strategy for robust large-area copper-based electronics", *Advanced Electronic
       Materials*, vol. 5, no. 10, p. 1 900 365, 2019.

[145] P. S. Das, A. Chhetry, P. Maharjan, M. S. Rasel, and J. Y. Park, "A laser ablated
       graphene-based flexible self-powered pressure sensor for human gestures and
       finger pulse monitoring", *Nano Research*, vol. 12, pp. 1789–1795, 2019.

[146] K. Huang *et al.*, "Ultrasensitive MWCNT/PDMS composite strain sensor fabri-
       cated by laser ablation process", *Composites Science and Technology*, vol. 192,
       p. 108 105, 2020.

[147] M. Clevenger, H. Kim, H. W. Song, K. No, and S. Lee, "Binder-free printed PE-
       DOT wearable sensors on everyday fabrics using oxidative chemical vapor depo-
       sition", *Science Advances*, vol. 7, no. 42, eabj8958, 2021.

[148] S. Wu, Z. Yin, Q. He, X. Huang, X. Zhou, and H. Zhang, "Electrochemical depo-
       sition of semiconductor oxides on reduced graphene oxide-based flexible, trans-
       parent, and conductive electrodes", *The Journal of Physical Chemistry C*, vol. 114,
       no. 27, pp. 11 816–11 821, 2010.

[149] E. Erçarıkcı, Z. Aksu, K. D. Kıranşan, and E. Topçu, "Graphene paper with elec-
       trodeposited NiCo2S4 nanoparticles as a novel flexible sensor for simultane-
       ous detection of folic acid and ascorbic acid", *Diamond and Related Materials*,
       vol. 121, p. 108 713, 2022.

[150] L. Meng, W. Wang, B. Xu, J. Qin, K. Zhang, and H. Liu, "Solution-processed flexible transparent electrodes for printable electronics", *ACS nano*, vol. 17, no. 5, pp. 4180–4192, 2023.

[151] L. Wang, J. A. Jackman, W. B. Ng, and N.-J. Cho, "Flexible, graphene-coated biocomposite for highly sensitive, real-time molecular detection", *Advanced Functional Materials*, vol. 26, no. 47, pp. 8623–8630, 2016.

[152] M. Wang *et al.*, "Composite flexible sensor based on bionic microstructure to simultaneously monitor pressure and strain", *Advanced Healthcare Materials*, vol. 12, no. 27, p. 2 301 005, 2023.

[153] P. Q. Nguyen *et al.*, "Wearable materials with embedded synthetic biology sensors for biomolecule detection", *Nature Biotechnology*, vol. 39, no. 11, pp. 1366–1374, 2021.

[154] Y. Zhang *et al.*, "Flexible and highly sensitive pressure sensor based on microdome-patterned pdms forming with assistance of colloid self-assembly and replica technique for wearable electronics", *ACS applied materials & interfaces*, vol. 9, no. 41, pp. 35 968–35 976, 2017.

[155] P. Zhu *et al.*, "Electrostatic self-assembly enabled flexible paper-based humidity sensor with high sensitivity and superior durability", *Chemical Engineering Journal*, vol. 404, p. 127 105, 2021.

[156] M. G. Stanford *et al.*, "High-resolution laser-induced graphene. flexible electronics beyond the visible limit", *ACS applied materials & interfaces*, vol. 12, no. 9, pp. 10 902–10 907, 2020.

[157] T.-S. D. Le *et al.*, "Recent advances in laser-induced graphene: Mechanism, fabrication, properties, and applications in flexible electronics", *Advanced Functional Materials*, vol. 32, no. 48, p. 2 205 158, 2022.

[158] T. H. Maiman *et al.*, "Stimulated optical radiation in ruby", 1960.

[159] C. Bader and I. Krejci, "Indications and limitations of Er: YAG laser applications in dentistry", *American journal of dentistry*, vol. 19, no. 3, p. 178, 2006.

[160] D. V. Seletskiy, R. Epstein, and M. Sheik-Bahae, "Laser cooling in solids: Advances and prospects", *Reports on Progress in Physics*, vol. 79, no. 9, p. 096 401, 2016.

[161] W. Gesierich, "Diagnostic and therapeutic laser applications in pulmonary medicine–A review", *Medical Laser Application*, vol. 25, no. 1, pp. 5–13, 2010.

[162] R. Photonics, "Encyclopedia of laser physics and technology", *Thermal Lensing*, 2013.

[163] M. J. Weber, *Handbook of laser wavelengths*. CRC press, 2018.

[164] R. F. Pease and S. Y. Chou, "Lithography and other patterning techniques for future electronics", *Proceedings of the IEEE*, vol. 96, no. 2, pp. 248–270, 2008.

[165] M. Wisniewski, A. Sionkowska, H. Kaczmarek, S. Lazare, V. Tokarev, and C. Belin, "Spectroscopic study of a KrF excimer laser treated surface of the thin collagen films", *Journal of Photochemistry and Photobiology A: Chemistry*, vol. 188, no. 2-3, pp. 192–199, 2007.

1

[166]   S. Mishra and V. Yadava, "Laser beam micromachining (LBMM)–a review", *Optics and lasers in engineering*, vol. 73, pp. 89–122, 2015.

[167]   P. M. Donaldson *et al.*, "Breaking barriers in ultrafast spectroscopy and imaging using 100 kHz amplified Yb-laser systems", *Accounts of Chemical Research*, vol. 56, no. 15, pp. 2062–2071, 2023.

[168]   C. Lin, C. Mertz, H. Bitting, and M. El-Sayed, "Fluorescence anisotropy studies of dibucaine· HCl in micelles and bacteriorhodopsin", *Journal of Photochemistry and Photobiology B: Biology*, vol. 13, no. 2, pp. 169–185, 1992.

[169]   W. G. Telford, "Lasers in flow cytometry", *Methods in cell biology*, vol. 102, pp. 373–409, 2011.

[170]   J Schmit, K Creath, and J. Wyant, "Surface profilers, multiple wavelength, and white light interferometry", *Optical shop testing*, vol. 667755, 2007.

[171]   M. A. Calin, M. R. Calin, and R. Savastru, "Spectral analysis of methylene blue–mediated photodynamic inactivation of bacteria using a 635-nm diode laser system", *Spectroscopy Letters*, vol. 46, no. 5, pp. 327–333, 2013.

[172]   M. A. Johnson, C. C. Kankelborg, R. Meuchel, and R. Smart, "Confocal microscopy for high-precision non-contact optical measurements", in *Optical System Alignment, Tolerancing, and Verification XII*, SPIE, vol. 10747, 2018, pp. 69–79.

[173]   S. Fukuta, M. Nomura, T. Ikeda, M. Yoshizawa, M. Yamasaki, and Y. Sasaki, "Wavelength dependence of machining performance in UV-, VIS-and NIR-laser cutting of wood", *Journal of Wood Science*, vol. 62, pp. 316–323, 2016.

[174]   M Stecher *et al.*, "Towards industrial inspection with THz systems", *Ultrashort Pulse Laser Technology: Laser Sources and Applications*, pp. 311–335, 2016.

[175]   K. Nagarathnam and K. M. Taminger, "Technology assessment of laser-assisted materials processing in space", in *AIP Conference Proceedings*, American Institute of Physics, vol. 552, 2001, pp. 153–160.

[176]   J. P. Bergmann, M. Bielenin, and T. Feustel, "Aluminum welding by combining a diode laser with a pulsed nd: Yag laser", *Welding in the World*, vol. 59, pp. 307–315, 2015.

[177]   J. Dong and P. Deng, "Ti: sapphire crystal used in ultrafast lasers and amplifiers", *Journal of crystal growth*, vol. 261, no. 4, pp. 514–519, 2004.

[178]   F. Olsen and L Alting, "Pulsed laser materials processing, ND-YAG versus CO2 lasers", *CIRP annals*, vol. 44, no. 1, pp. 141–145, 1995.

[179]   A Kosterev *et al.*, "Application of quantum cascade lasers to trace gas analysis", *Applied Physics B*, vol. 90, pp. 165–176, 2008.

[180]   Y. L. Yao, H. Chen, and W. Zhang, "Time scale effects in laser material removal: A review", *The International Journal of Advanced Manufacturing Technology*, vol. 26, pp. 598–608, 2005.

[181]   A. Labunet, A. Tonea, A. Kui, and S. Sava, "The use of laser energy for etching enamel surfaces in dentistry—A scoping review", *Materials*, vol. 15, no. 6, p. 1988, 2022.

[182] J. Gao *et al.*, "Laser-assisted large-scale fabrication of all-solid-state asymmetrical micro-supercapacitor array", *Small*, vol. 14, no. 37, p. 1 801 809, 2018.

[183] J. Gao *et al.*, "Laser-assisted multiscale fabrication of configuration-editable supercapacitors with high energy density", *ACS nano*, vol. 13, no. 7, pp. 7463–7470, 2019.

[184] D. Kim *et al.*, "Direct-laser-patterned friction layer for the output enhancement of a triboelectric nanogenerator", *Nano Energy*, vol. 35, pp. 379–386, 2017.

[185] M. G. Stanford, J. T. Li, Y. Chyan, Z. Wang, W. Wang, and J. M. Tour, "Laser-induced graphene triboelectric nanogenerators", *ACS nano*, vol. 13, no. 6, pp. 7166–7174, 2019.

[186] H. Cheng *et al.*, "Graphene fibers with predetermined deformation as moisture-triggered actuators and robots", *Angewandte Chemie International Edition*, vol. 52, no. 40, pp. 10 482–10 486, 2013.

[187] D. Jin, Q. Chen, T.-Y. Huang, J. Huang, L. Zhang, and H. Duan, "Four-dimensional direct laser writing of reconfigurable compound micromachines", *Materials Today*, vol. 32, pp. 19–25, 2020.

[188] P Pou *et al.*, "Laser surface texturing of Titanium for bioengineering applications", *Procedia Manufacturing*, vol. 13, pp. 694–701, 2017.

[189] A. Mazzoli, "Selective laser sintering in biomedical engineering", *Medical & biological engineering & computing*, vol. 51, pp. 245–256, 2013.

[190] J. Kim and X. Xu, "Excimer laser fabrication of polymer microfluidic devices", *Journal of Laser Applications*, vol. 15, no. 4, pp. 255–260, 2003.

[191] K. Sugioka *et al.*, "Femtosecond laser 3D micromachining: A powerful tool for the fabrication of microfluidic, optofluidic, and electrofluidic devices based on glass", *Lab on a Chip*, vol. 14, no. 18, pp. 3447–3458, 2014.

[192] Q. Du *et al.*, "High-performance flexible pressure sensor based on controllable hierarchical microstructures by laser scribing for wearable electronics", *Advanced Materials Technologies*, vol. 6, no. 9, p. 2 100 122, 2021.

[193] J. Wang *et al.*, "Programmed ultrafast scan welding of Cu nanowire networks with a pulsed ultraviolet laser beam for transparent conductive electrodes and flexible circuits", *ACS applied materials & interfaces*, vol. 12, no. 31, pp. 35 211–35 221, 2020.

[194] J. Shin *et al.*, "Sensitive wearable temperature sensor with seamless monolithic integration", *Advanced Materials*, vol. 32, no. 2, p. 1 905 527, 2020.

[195] R. G. Hjort *et al.*, "Laser-induced graphene decorated with platinum nanoparticles for electrochemical analysis of saliva", *ACS Applied Nano Materials*, vol. 6, no. 22, pp. 20 801–20 811, 2023.

[196] Y. Yang *et al.*, "A laser-engraved wearable sensor for sensitive detection of uric acid and tyrosine in sweat", *Nature biotechnology*, vol. 38, no. 2, pp. 217–224, 2020.

[197]   L. Yang *et al.*, "Moisture-resistant, stretchable NOx gas sensors based on laser-induced graphene for environmental monitoring and breath analysis", *Microsystems & nanoengineering*, vol. 8, no. 1, p. 78, 2022.

[198]   J. Yang *et al.*, "Facile fabrication of robust and reusable PDMS supported graphene dry electrodes for wearable electrocardiogram monitoring", *Advanced Materials Technologies*, vol. 6, no. 9, p. 2 100 262, 2021.

[199]   Q. Zhang *et al.*, "Three-in-one portable electronic sensory system based on low-impedance laser-induced graphene on-skin electrode sensors for electrophysiological signal monitoring", *Advanced Materials Interfaces*, vol. 10, no. 3, p. 2 201 735, 2023.

[200]   B. Sun *et al.*, "Gas-permeable, multifunctional on-skin electronics based on laser-induced porous graphene and sugar-templated elastomer sponges", *Advanced Materials*, vol. 30, no. 50, p. 1 804 327, 2018.

[201]   H. Wang *et al.*, "Double-sided wearable multifunctional sensing system with anti-interference design for human–ambience interface", *ACS nano*, vol. 16, no. 9, pp. 14 679–14 692, 2022.

[202]   C. Zhang *et al.*, "Human motion-driven self-powered stretchable sensing platform based on laser-induced graphene foams", *Applied Physics Reviews*, vol. 9, no. 1, 2022.

[203]   K. Xu *et al.*, "A wearable body condition sensor system with wireless feedback alarm functions", *Advanced Materials*, vol. 33, no. 18, p. 2 008 701, 2021.

[204]   E. Hwang, J. Hong, J. Yoon, and S. Hong, "Direct writing of functional layer by selective laser sintering of nanoparticles for emerging applications: A review", *Materials*, vol. 15, no. 17, p. 6006, 2022.

[205]   Y. D. Suh *et al.*, "Maskless fabrication of highly robust, flexible transparent cu conductor by random crack network assisted cu nanoparticle patterning and laser sintering", *Advanced Electronic Materials*, vol. 2, no. 12, p. 1 600 277, 2016.

[206]   V. B. Nam and D. Lee, "Evaluation of Ni-based flexible resistance temperature detectors fabricated by laser digital pattering", *Nanomaterials*, vol. 11, no. 3, p. 576, 2021.

[207]   S.-Y. Lin *et al.*, "High-performance graphene-based flexible heater for wearable applications", *Rsc Advances*, vol. 7, no. 43, pp. 27 001–27 006, 2017.

[208]   . I. Zergioti, F. Zacharatos, R. Geremia, and D. Karnakis], "Selective laser sintering of Ag nanoparticles ink for applications in flexible electronics", *Applied Surface Science*, 2015.

[209]   B. Kang, S. Han, J. Kim, S. Ko, and M. Yang, "One-step fabrication of copper electrode by laser-induced direct local reduction and agglomeration of copper oxide nanoparticle", *The Journal of Physical Chemistry C*, vol. 115, no. 48, pp. 23 664–23 670, 2011.

[210]   Y. Rho, K. T. Kang, and D. Lee, "Highly crystalline Ni/NiO hybrid electrodes processed by inkjet printing and laser-induced reductive sintering under ambient conditions", *Nanoscale*, pp. 8976–8985, 2016.

[211] D. Lee, D. Paeng, H. K. Park, and C. P. Grigoropoulos, "Vacuum-free, maskless patterning of Ni electrodes by laser reductive sintering of NiO nanoparticle ink and its application to transparent conductors", *ACS nano*, vol. 8, no. 10, pp. 9807–9814, 2014.

[212] C. SHEN, P. WENG, Z. WANG, W. WU, and X. XIE, "Research progress in laser direct writing of flexible circuit", *Scientia Sinica Physica, Mechanica & Astronomica*, vol. 51, no. 8, p. 084 201, 2021.

[213] S. Jiang, Q. Chen, J. Lin, G. Liao, T. Shi, and L. Qian, "Thermal stress-induced fabrication of carbon micro/nanostructures and the application in high-performance enzyme-free glucose sensors", *Sensors and Actuators B: Chemical*, vol. 345, p. 130 364, 2021.

[214] K. Min *et al.*, "Fabrication of perforated pdms microchannel by successive laser pyrolysis", *Materials*, vol. 14, no. 23, p. 7275, 2021.

[215] J. Huang, K. Xu, S. Xu, X. Li, and Q.-H. Wei, "Self-aligned laser-induced periodic surface structures for large-area controllable nanopatterning", *Laser & Photonics Reviews*, vol. 16, no. 8, p. 2 200 093, 2022.

[216] J. Shin *et al.*, "Monolithic digital patterning of polydimethylsiloxane with successive laser pyrolysis", *Nature Materials*, vol. 20, no. 1, pp. 100–107, 2021.

[217] J. Yu *et al.*, "Extremely sensitive sers sensors based on a femtosecond laser-fabricated superhydrophobic/-philic microporous platform", *ACS Applied Materials & Interfaces*, vol. 14, no. 38, pp. 43 877–43 885, 2022.

[218] R. Ye, D. K. James, and J. M. Tour, "Laser-induced graphene", *Accounts of chemical research*, vol. 51, no. 7, pp. 1609–1620, 2018.

[219] A. F. Carvalho *et al.*, "Laser-induced graphene strain sensors produced by ultraviolet irradiation of polyimide", *Advanced Functional Materials*, vol. 28, no. 52, p. 1 805 271, 2018.

[220] C. Cheng *et al.*, "Bisphenol a sensors on polyimide fabricated by laser direct writing for onsite river water monitoring at attomolar concentration", *ACS applied materials & interfaces*, vol. 8, no. 28, pp. 17 784–17 792, 2016.

[221] Y. Luo *et al.*, "Stretchable and flexible non-enzymatic glucose sensor based on poly (ether sulfone)-derived laser-induced graphene for wearable skin diagnostics", *Advanced Materials Technologies*, vol. 7, no. 9, p. 2 101 571, 2022.

[222] R. You, Y.-Q. Liu, Y.-L. Hao, D.-D. Han, Y.-L. Zhang, and Z. You, "Laser fabrication of graphene-based flexible electronics", *Advanced Materials*, vol. 32, no. 15, p. 1 901 981, 2020.

[223] H. Wang, Z. Zhao, P. Liu, and X. Guo, "Laser-induced graphene based flexible electronic devices", *Biosensors*, vol. 12, no. 2, p. 55, 2022.

[224] L. Wang, K. Yin, Q. Deng, Q. Huang, and C. J. Arnusch, "Multiscale hybrid-structured femtosecond laser-induced graphene with outstanding photo-electro-thermal effects for all-day anti-icing/deicing", *Carbon*, vol. 219, p. 118 824, 2024.

1

[225]   Z. Wan, N.-T. Nguyen, Y. Gao, and Q. Li, "Laser induced graphene for biosensors", *Sustainable Materials and Technologies*, vol. 25, e00205, 2020.

[226]   Z. Zhai, N. Wu, Z. Wang, Y. Zhang, D. Song, and Y. Cui, "Fabrication of LIG coating on SiC/SiC composites with femtosecond laser", *Optik*, vol. 245, p. 167 628, 2021.

2

RAPID FABRICATION OF HIGH-PERFORMANCE FLEXIBLE PRESSURE SENSORS USING LASER PYROLYSIS DIRECT WRITING

The fabrication of flexible pressure sensors with low cost, high scalability, and easy fabrication is an essential driving force in developing flexible electronics, especially for high-performance sensors that require precise surface microstructures. However, optimizing complex fabrication processes and expensive microfabrication methods remains a significant challenge. In this chapter, we introduce a laser pyrolysis direct writing technology that enables rapid and efficient fabrication of high-performance flexible pressure sensors with a micro-truncated pyramid array. The pressure sensor demonstrates exceptional sensitivities, with values of 3132.0 kPa^{-1}, 322.5 kPa^{-1}, and 27.8 kPa^{-1} in the pressure ranges of 0-0.5 kPa, 0.5-3.5 kPa, and 3.5-10 kPa, respectively. Furthermore, the sensor exhibits rapid response times (loading: 22 ms, unloading: 18 ms) and exceptional reliability, enduring over 3000 pressure loading and unloading cycles. Moreover, the pressure sensor can be easily integrated into a sensor array for spatial pressure distribution detection. The laser pyrolysis direct writing technology introduced in this study presents a highly efficient and promising approach to designing and fabricating high-performance flexible pressure sensors utilizing micro-structured polymer substrates.

2.1. INTRODUCTION

WITH the rapid development of the Internet of Things (IoT), more and more sensors are being integrated into daily life and industrial production as an important sensing medium. Flexible pressure sensors have gained considerable attention due to their potential applications in health monitoring [2], human-machine interaction [3], electronic skin [4], soft robotic [5], etc. To satisfy the demands of these applications, flexible pressure sensors should not only possess high sensitivity, wide detection range, fast response time, excellent repeatability, and robust reliability but also offer the advantages of low cost, high scalability, and easy fabrication. Flexible pressure sensors are generally categorized into four types based on their sensing mechanism and signal transmission mode: piezoresistive [6–8], piezoelectric [9–11], capacitive [12, 13], and triboelectric [14, 15]. In the case of piezoresistive flexible sensors, applying external forces to their sensing material and device structure induces local strain in the force-bearing area. Consequently, the resistance network, consisting of material resistance and contact resistance within the sensor, changes with the localized strain, enabling the detection and identification of pressure [16, 17].

Advanced materials, including carbon nanotubes [18], carbon nanofibers [19], graphene [20, 21], MXene [22, 23], metal nanowires [24], and nanoparticles [25], have been widely applied as sensing elements to create electrical percolation pathways. In addition, flexible materials such as polydimethylsiloxane (PDMS) [26][25], polyimide (PI)[27], polyethylene terephthalate (PET) [28], polyethylene (PE) [29], and polyurethane (PU) [30] serve not only as flexible substrates for active materials but also as flexible electrodes, which can be fabricated through methods like infilling [31], coating [32], and modification [33]. Therefore, introducing advanced sensing materials or constructing effective microstructures has been considered in numerous reports as two comprehensive strategies to obtain high-performance flexible sensors [34, 35]. Especially using PDMS as a substrate material for creating surface microstructures is widely regarded as a promising strategy for fabricating flexible pressure sensors due to its exceptional flexibility, transparency, and biocompatibility [36–38].

For the fabrication of flexible sensors with various microstructures, the template method is a widely adopted manufacturing technology. This method involves casting or coating uncured elastic materials onto molds, such as silicon wafers [39], abrasive paper[40], natural leaves [41], silk [42], etc., to transfer patterned microstructures. In particular, traditional photolithography has been widely employed as a precise and efficient method for fabricating well-design silicon molds used in the production of high-performance flexible pressure sensors. However, this method requires a strictly controlled fabrication environment, precise equipment, and complex processes to maintain fabrication accuracy. Hence, it is still a significant challenge to design and fabricate flexible pressure sensors that combine high sensitivity and wide detection range with low cost and simple process. To date, the potential applications of laser direct writing (LDW) technology in surface modification [43, 44], nanomaterial synthesis [45, 46], and microfluidic device design [47, 48] have attracted considerable interest. Laser direct writing enables the fabrication of diverse functional devices without requiring photomasks. Particularly in the field of microstructure fabrication, it allows for the creation of not only two-dimensional surface microstructures [49, 50] but also three-dimensional mi-

crostructures [51, 52]. Compared to traditional physical and chemical fabrication methods, laser direct writing technology has significant advantages in terms of efficiency, precision, controllability, and flexibility.

Herein, we develop an efficient and promising approach for designing and fabricating flexible pressure sensors with a micro-truncated pyramid array using laser pyrolysis direct writing (LPDW) technology. To optimize the fabrication parameters, we summarized the realization conditions for continuous laser pyrolysis, such as the average laser power, pulse repetition frequency, and laser focal distance. The mechanism of continuous laser pyrolysis was then explored and investigated through experimental characterization and finite element simulation. On this basis, micro-truncated pyramid structures were fabricated on the surface of a PDMS film by LPDW technology. Subsequently, a thin layer of gold was magnetron sputtered on the surface of the PDMS film with a micro-truncated pyramid array to impart piezoresistive capability. Finally, the PDMS conductive film (Au/PDMS) was assembled with a film consisting of indium tin oxide and polyethylene terephthalate (ITO/PET) to produce the flexible pressure sensor. Performance testing revealed that the pressure sensor exhibited high sensitivity, wide detection range, fast response time, and long-term mechanical durability. Furthermore, the pressure sensor responded quickly to micro-pressure and small-pressure external signals involved in various applications. As a proof-of-concept, the potential application of the sensor array in real-time detection of spatial pressure distribution was demonstrated.

2.2. EXPERIMENTAL SECTION

2.2.1. FABRICATION OF THE PDMS FILM

The liquid mixture of PDMS precursors (Sylgard 184, Dow Corning, mixture ratio: 10:1) was poured onto a smooth plastic template and placed inside a vacuum chamber for degassing. The mixture was then cured at 80 °C for 2 hours to form a 2 mm thick transparent PDMS film.

2.2.2. FABRICATION OF THE MICROSTRUCTURE ARRAYS

The micro-truncated pyramid arrays were fabricated using laser pyrolysis direct writing technology on the PDMS surface. This was achieved by using an ultraviolet (UV) pulsed laser system (Grace X 355-3A, Han's Laser Technology Industry Group Co., Ltd., wavelength: 355 nm, spot size: 30 μm) operating at a fixed scanning speed (V_{ss}) of 10 mm/s, a laser average power (P_{avg}) of 1.5 W, and a pulse repetition frequency (F_{pr}) of 40 kHz. SiC nanoparticles (Bide Pharmatech Co., Ltd., particle size: 0.5-0.7 μm) were coated at the initial point of the scan path to induce the continuous laser pyrolysis reaction. After fabrication, the pyrolysis products (3C-SiC) on the PDMS surface were cleaned with an ultrasonic cleaner using anhydrous ethanol and dried with nitrogen gas. A 150 nm thick gold conductive layer was deposited onto the PDMS film (12 × 12 mm) with micro-truncated pyramid arrays using magnetron sputtering equipment (KT-Z1650PVD, Zhengzhou Ketan Instrument Equipment Co., Ltd.)

2.2.3. Packaging of the flexible pressure sensors

The commercial single-sided conductive tapes (3M7766-50, 3M Company) were utilized as lead wires to connect the ITO/PET electrode (South China Xiangcheng Technology Co., Ltd, thickness: 125 μm, resistance: ≤10 Ω/sq) and Au/PDMS electrode, respectively. Liquid metal (Alfa Aesar Chemical Co., Ltd., metal basis: 99.99 % Ga-In-Sn) was coated on the conductive tapes. Subsequently, the ITO/PET electrode and Au/PDMS electrode were aligned and assembled by heating a heat-shrinkable tube at 100 °C to complete the final packaging of the flexible pressure sensor.

2.2.4. Characterization and measurement

The morphology of the PDMS film with micro-truncated pyramid arrays was characterized using a scanning electron microscope (SEM, Gemini 300, ZEISS) and a 3D laser scanning microscope (VK-X1000, KEYENCE). Thermal gravimetric analysis (TGA, STA 449C, NETZSCH) was employed to investigate the changes in gravimetric components during the pyrolysis of PDMS. The samples were heated from 27 °C to 1400 °C at a ramp rate of 20 °C/min in air. The pyrolysis products were characterized using X-ray diffraction (XRD, Rigaku Smartlab) with a scanning rate of 10 °/min. The mechanical performance of the flexible pressure sensor was evaluated using a universal testing machine (TSE503A, Wance Testing Machine Co., Ltd.). The corresponding electrical signals were measured using a digital source meter (2450, Keithley), and the response time was recorded using an oscilloscope (TBS2104B, Tektronix).

2.3. Results and discussion

2.3.1. Realization conditions of LPDW technology

It is widely acknowledged that PDMS is a transparent polymer. When a laser is irradiated perpendicularly to its surface, a portion of the laser power is reflected. Moreover, due to the low absorption coefficient of PDMS for ultraviolet (UV) laser light, most of the laser energy passes through the PDMS film without inducing any physical or chemical reactions. However, when opaque 6H-SiC nanoparticles (NPs) are coated at the initial point of the UV pulsed laser scanning path, the photothermal effect of the laser on the 6H-SiC NPs initiates a pyrolysis reaction on the PDMS surface (Figure 2.1(a)). This initial laser pyrolysis (ILP) reaction generates 3C-SiC on the PDMS surface, triggering a continuous laser pyrolysis (CLP) phenomenon. To maintain a continuous impact of the pulsed laser on the PDMS surface, the pulse repetition frequency must be sufficiently high to ensure the new laser pulse overlaps with the region where the 3C-SiC pyrolysis products are present. In other words, the occurrence of CLP reactions is dependent on the inherent properties of pulsed lasers and takes place iteratively with each pulsed laser irradiation, as illustrated in Figure A.1. With a higher pulse repetition frequency at a constant laser scanning speed, the density of overlap between individual circular pyrolysis regions formed by each pulse increases, resulting in a continuous pyrolysis region that approximates a straight line more closely.

When combined with advanced laser control software, the laser pyrolysis direct writing (LPDW) technology provides an efficient method for fabricating PDMS surface microstructures. Significantly, we found that the laser pyrolysis products of PDMS exhib-
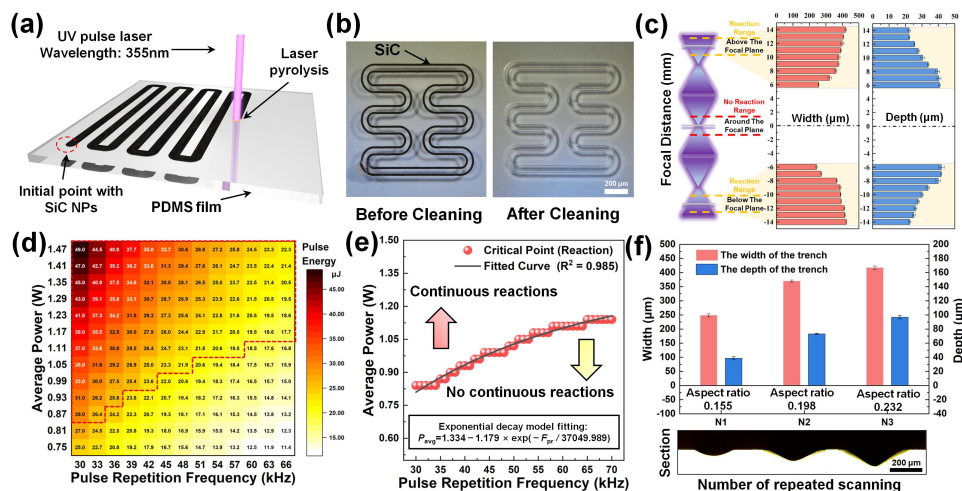
Figure 2.1: (a) Schematic illustration of the continuous laser pyrolysis (CLP) process. (b) Optical microscope images of the serpentine pattern written by LPDW technology before and after cleaning treatment. (c) Comparison data on microchannel width and depth prepared by LPDW technology at different focal distances (V_{ss} = 10 mm/s, P_{avg} = 1.5W, and F_{pr} = 40 kHz). (d) The critical realization conditions distribution heatmap for CLP reaction (D_{def} = −6 mm). (e) The critical reaction boundary fitting curve of CLP reaction under different F_{pr} and P_{avg}. (f) Comparison of microchannel aspect ratio and cross-sectional morphology under different numbers of laser scans.

ited minimal adhesion to the PDMS surface and could be easily removed through ultrasonic cleaning. Figure 2.1(b) shows the serpentine pattern written using laser pyrolysis direct writing technology before and after cleaning. Interestingly, we observed that the initiation of CLP reaction on the PDMS surface was restricted to the regions situated significantly above and below the laser focal plane (Figure 2.1(c)). In contrast, the regions near the laser focal plane exhibited extremely low sensitivity to the CLP reaction. As a result, within the focal plane range of (−6 mm, 6 mm), the laser failed to induce CLP reactions. This phenomenon can be attributed to the pressure waves generated by the rapid evaporation or melting of the material induced by the high heating temperature gradient of the laser (See Supporting Information Section A.1). However, upon further defocusing, the CLP reaction was smoothly induced by laser, following the heat flow distribution of the Gaussian heat source. Meanwhile, within the focal plane range of [−6 mm, −14 mm] and [6 mm, 14 mm], the width and depth of the PDMS microchannel increased and decreased, respectively, with increasing defocus. Additionally, at positions distant from the focal plane, the temperature and temperature gradient generated by the laser photothermal effect were insufficient to reach the critical pyrolysis condition of PDMS. Correspondingly, the 3D laser confocal images of the microchannel structure on the PDMS surface at various focal distances are illustrated in Figure A.2.

Based on the above phenomenon, we investigated the critical conditions of CLP reaction at different laser average powers (P_{avg}) and pulse repetition frequencies (F_{pr}) while maintaining a fixed scanning speed (V_{ss} = 10 mm/s). Figure 2.1(d) illustrates the reaction conditions under which CLP reaction can occur smoothly, as shown in the area

marked with the red dotted line. Under the condition of fixed V_{ss}, we observed that as F_{pr} increases, the P_{avg} required to induce the CLP reaction gradually levels off. This phenomenon reflects the influence of F_{pr} and P_{avg} on the behavior of continuous laser pyrolysis and can be explained through the physical mechanisms of pulsed lasers. Under low F_{pr} conditions, the peak power of a single pulse is higher due to the longer pulse interval. However, the spot spacing (D_{ss}) between the centers of two consecutive pulse spots increases significantly with decreasing frequency. The relationship can be calculated using the following formula:

$$D_{ss} = \frac{V_{ss}}{F_{pr}} \tag{2.1}$$

This increase in D_{ss} may lead to discontinuities in the pyrolysis reaction, as the heat from adjacent spots may not overlap effectively, thus weakening the driving effect of heat accumulation on the pyrolysis reaction. Therefore, even if a single pulse has a higher peak power, maintaining continuous pyrolysis at a low frequency remains challenging. As F_{pr} increases, the D_{ss} gradually decreases, and the heat accumulation effect increases, thereby improving the continuity of pyrolysis. However, when F_{pr} increases to a specific range, the average power curve of the laser begins to show a flattening characteristic, and the occurrence of the pyrolysis reaction depends only on the magnitude of the average laser power. Furthermore, when the defocusing distance ($D_{def} = -6$ mm) is fixed, the relationship between the critical P_{avg} and F_{pr} that determines whether a CLP reaction is triggered can be described using the exponential decay model:

$$P_{avg} = 1.334 - 1.179 \times \exp\left(-\frac{F_{pr}}{37049.989}\right) \tag{2.2}$$

where 1.334 represents the asymptotic value of P_{avg} at high F_{pr} conditions, -1.179 denotes the reduction in P_{avg} under low F_{pr} conditions caused by the longer intervals between pulses, and 37049.989 (about 37 kHz) reflects the characteristic range over which the F_{pr} influences the contribution to the P_{avg}. Correspondingly, Figure 2.1(e) shows the relationship between the critical P_{avg} and F_{pr} required to sustain CLP reactions. Detailed experimental data are presented in Figure A.4.

Surprisingly, after determining the F_{pr} and D_{def} of the laser, we found that increasing the laser power did not lead to a significant enhancement in the aspect ratio of the microchannel. However, increasing the number of laser scans proved to be an effective approach for improving the aspect ratio of the microchannel (Figure 2.1(f)). As the number of laser scans increased from 1 to 2 and 3 (N1, N2, and N3), the aspect ratio of the microchannel increased from 0.155 to 0.198 and 0.233, respectively. Moreover, both the width and depth of the microchannels increased with the number of scans. Cross-sectional optical microscope images of the PDMS revealed that after a single laser scan, the cross-section of the PDMS microchannel exhibited a tendency towards a semi-elliptical distribution. However, as the number of scans increased to 2 and 3, the cross-section of the PDMS microchannel approached a two-dimensional Gaussian distribution. We attribute this phenomenon to the isotropic extension of the pyrolysis temperature during the CLP reaction. The corresponding scanning electron microscopy (SEM) images of the surface topography after the different number of laser scans are shown in

Figure A.5. Furthermore, the roughness results for the sidewalls of the microchannel are shown in Figure A.6 and Figure A.7, which are discussed in detail in Supporting Information Section A.1.

2.3.2. MECHANISM ANALYSIS OF LPDW TECHNOLOGY

The CLP reaction, being the primary process in LPDW technology, can be defined as the heat transfer and diffusion process resulting from the photothermal effect of the moving laser source on the material surface. To gain insight into the CLP reaction mechanism, we conducted an X-ray powder diffraction analysis on the pyrolysis products with varying average power (Figure 2.2(a)). The red spectrum exhibited three peaks at 34.9°, 35.5°, and 38.0°, which clearly indicated the presence of 6H-SiC NPs that were coated at the initial position on the PDMS surface. In contrast, the blue spectrum displayed three peaks at 35.2°, 59.6°, and 71.7°, which corresponded perfectly to the 3C-SiC product resulting from the CLP reaction. As the laser power was gradually increased from 1.5 W to 2.1 W, the peak intensity of the XRD pattern for the 3C-SiC product intensified due to the higher reaction temperature. These results provide further confirmation that the CLP reaction becomes more pronounced and thorough as the temperature at the center of the laser beam spot increases.
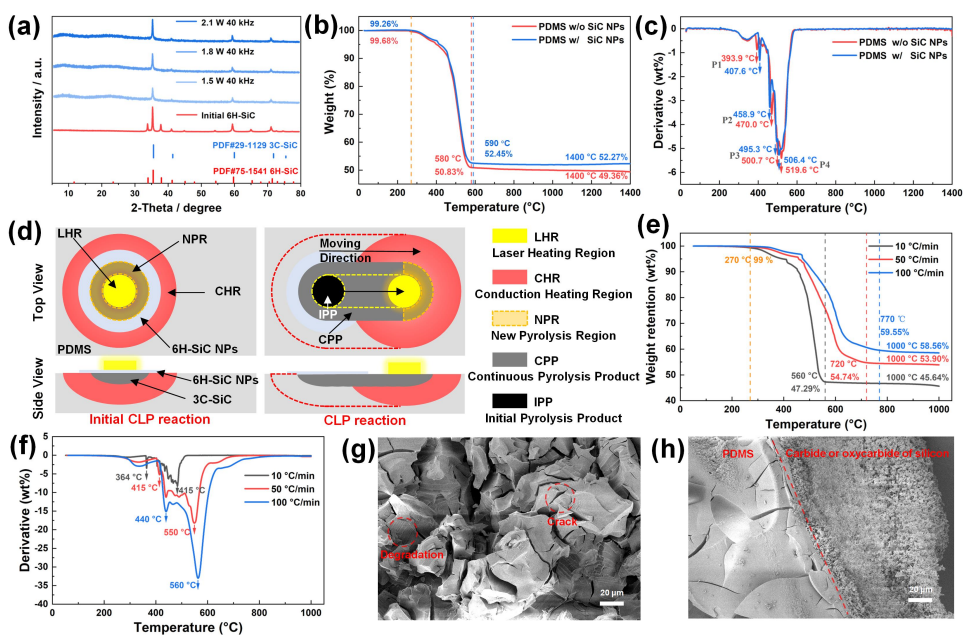
Figure 2.2: (a) XRD patterns of initial 6H-SiC NPs and 3C-SiC pyrolysis products with different laser average power (1.5, 1.8, and 2.1 W). (b) TG curves and (c) DTG curves of pristine PDMS and PDMS coated with 6H-SiC NPs. (d) Schematic illustration of initial laser pyrolysis (ILP) reaction and continuous laser pyrolysis (CLP) reaction mechanisms. (e) TG and (f) DTG curves of pristine PDMS samples at different heating rates. (g) and (h) SEM images of PDMS pyrolysis prod samples at heating rates of 10 °C/min and 100 °C/min.

To explore the role of 6H-SiC NPs in laser pyrolysis, we performed thermal gravimet-

ric (TG) analysis on PDMS samples with and without 6H-SiC NPs coating (Figure 2.2(b)). The samples, weighing 5 mg and with a mixture ratio of 10:1, were heated under an air atmosphere from 27 °C to 1700 °C at a rate of 20 °C/min. The weight loss percentage was recorded in the TG curves. Both pristine PDMS (without SiC NPs) and PDMS coated with 6H-SiC NPs (PDMS with SiC NPs) exhibited rapid weight loss at 300 °C, followed by a relatively stable weight loss curve until 600 °C. Specifically, the weight loss of PDMS with SiC NPs decreased from 99.26% to 52.45% at around 600 °C, while the weight loss of PDMS without SiC NPs decreased from 99.68% to 50.83%.

At 1400 °C, the difference in mass percentage between the two samples was only 2.91%, equivalent to approximately 0.146 mg. Considering the mass difference caused by the presence of 6H-SiC NPs on the PDMS surface, the difference in mass percentage between the two samples is negligible. The corresponding DTG curves revealed that the prominent peaks of the weight loss rate (Derivative) curves for both samples (PDMS with and without SiC NPs) appeared around 400 °C, 460 °C, 500 °C, and 510 °C, respectively (Figure 2.2(c)). Although there are some subtle differences in the weight loss rate curves between the two samples from 300 °C to 600 °C, the overall trend is similar. These results essentially indicate that the 6H-SiC NPs do not participate in the laser pyrolysis reaction of PDMS but rather serve as endothermic sources for inducing the photothermal effect by absorbing laser energy. Figure 2.2(d) provides a detailed illustration of the ILP and CLP processes. The ILP reaction is triggered by the absorption of laser energy at the initial point of the 6H-SiC NPs. The resulting laser heating region acts as the pyrolysis center, with heat diffusing downward through the PDMS surface, generating opaque initial and continuous pyrolysis products (3C-SiC) in the conduction heating region. With a slight movement of the laser, the laser heating region overlaps with the new pyrolysis region, causing the conduction heating region to move along with the laser, re-forming a new pyrolysis region and continuous pyrolysis products. Finally, the CLP pyrolysis reaction completes the iteration. Although several experiments and calculations have investigated the pyrolysis mechanism of PDMS, a comprehensive analysis of the pyrolysis process and products is still lacking [48, 53–55]. To address this gap, we summarize the differences between the pyrolysis mechanism of PDMS at low and high heating rates in Figure A.8(a), discussed in Supporting Information Section A.2.

To further confirm the difference in the pyrolysis mechanism of pristine PDMS at different heating rates, TG and DTG analyses were conducted to investigate the conversion process of PDMS to 3C-SiC under various heating rates (Figure 2.2(e) and Figure 2.2(f)). By comparing the results, we observed that the remaining weights of the three PDMS samples started to decrease at the same temperature of 270 °C, and the weights remained relatively stable at around 560 °C, 720 °C, and 770 °C, respectively. At 1000 °C, the remaining weights of the three samples were 45.64%, 53.90%, and 58.56%, respectively. The corresponding DTG curves indicated that the three PDMS samples reached the first peak weight loss rate at 364 °C, 439 °C, and 440 °C, respectively. As the temperature increased, the second peak of weight loss rate for the three PDMS samples appeared at 484 °C, 550 °C, and 570 °C, respectively. It is evident from the DTG curve that the peak weight loss rate of the PDMS samples increased with the heating rate, indicating a more intense pyrolysis process. Interestingly, the TG curves revealed that the weight loss of PDMS samples decreased with the heating rate. To explain this phenomenon, we utilized scan-

2

ning electron microscopy (SEM) to characterize the pyrolysis products of PDMS under heating rates of 10 °C/min and 100 °C/min (Figure 2.2(g) and Figure 2.2(h)). At a heating rate of 10 °C/min, PDMS undergoes low-heating-rate pyrolysis, leading to the breaking and reformation of Si-O bonds in the PDMS chain, ultimately forming cyclic oligomers. This thermal degradation process results in random cracks within the PDMS, promoting further pyrolysis of cyclic oligomers to 3C-SiC at high temperatures. In contrast, at a heating rate of 100 °C/min, PDMS undergoes high-heating-rate pyrolysis, resulting in the formation of silicon oxides on the PDMS surface through the breaking and reformation of Si-CH3 bonds. These silicon oxides create an oxygen-deficient environment within the PDMS, inhibiting further thermal degradation and direct reduction to 3C-SiC by pyrolytic carbon at high temperatures.

In the laser pyrolysis process, the heating rate is extremely high, far exceeding the critical conditions of the PDMS pyrolysis mechanism. Consequently, considering the pyrolysis mechanism of PDMS, we can infer that PDMS undergoes a direct transformation into 3C-SiC through laser pyrolysis.

2.3.3. THERMAL EFFECT OF LPDW TECHNOLOGY

Considering the extreme temperatures involved in the laser pyrolysis process, it becomes challenging to experimentally monitor the heating rate and temperature. To tackle this issue, we employed the finite element method (FEM) to investigate the initial and continuous laser pyrolysis processes based on the previous mechanisms. The physical models and parameter settings are discussed in Supporting Information Section A.3.

To validate the heating rate during the CLP process, we constructed a model that aligns with the experimental conditions ($10 \times 10 \times 2$ mm). The 3D isothermal surface distribution revealed the temperature distribution and heat transfer of the PDMS substrate and SiC pyrolysis product during the CLP process (Figure 2.3(a)). The high temperature was primarily concentrated at the laser spot and moved along with it as the laser scanned the surface. Accordingly, the heat was predominantly concentrated in the SiC pyrolysis product and slightly extended into the PDMS through the interface between SiC and PDMS. Additionally, the cross-sectional isothermal surface distributions illustrated that the new pyrolysis product in the heat conduction region played a significant role in the CLP process. Based on this observation, we extracted the maximum temperature and maximum temperature change rate of the entire simulation model under different laser power and scanning time (Figure 2.3(b) and Figure 2.3(c)). It was observed that the maximum temperature curves of PDMS and SiC exhibited three stages over time. Initially, from 0.0 s to 0.1 s, the temperature increased rapidly due to laser irradiation. During this stage, heat generation dominates over heat dissipation (heat conduction, heat radiation, and heat convection), leading to the rapid accumulation of heat in the SiC pyrolysis products. In the subsequent stage, from 0.1 s to 0.9 s, the maximum temperature curves remained stable. This phenomenon can be attributed to the dynamic balance between heat generation and heat dissipation during the CLP process. In the final stage, from 0.9 s to 1.0 s, the maximum temperature curve showed a sudden increase. This can be attributed to heat losing its primary heat conduction path as the laser moved to the edge of the model.

Furthermore, as the laser power increased from 1.5 W to 1.8 W and 2.1 W, the max-
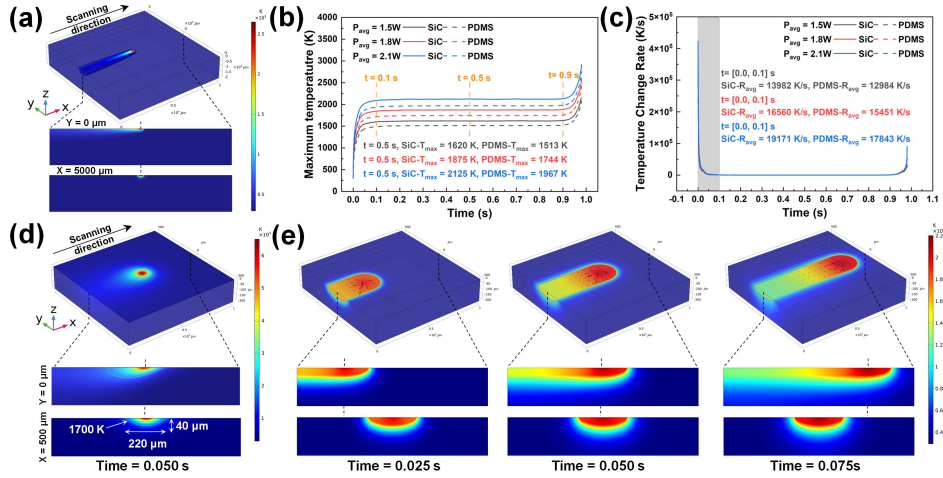
2

Figure 2.3: (a) 3D and cross-sectional isothermal surface distributions of PDMS and SiC during CLP reaction (P_{avg} = 1.5 W, V_{ss} = 10 mm/s, and Time = 0.5 s). (b) and (c) maximum temperature and maximum temperature change rate curves of PDMS and SiC with time under different laser average powers (1.5, 1.8, and 2.1 W). (d) 3D and cross-sectional temperature distributions of PDMS and SiC during ILP reaction (Time = 0.050 s). (e) 3D and cross-sectional temperature evolution distributions of the PDMS and SiC during CLP reaction (Time = 0.025, 0.050, and 0.075 s).

imum temperature of PDMS and SiC rose from 1513 K to 1744 K and 1967 K, and from 1620 K to 1875 K and 2125 K at 0.5s, respectively. It is important to note that during laser pyrolysis, the SiC pyrolysis products conduct most of the heat due to their excellent thermal conductivity. The curve of the highest temperature change rate further supports the temperature trend during the CLP reaction. At a P_{avg} of 1.5 W, the average maximum temperature change rates (R_{avg}) for PDMS and SiC were 12984 K/s and 13982 K/s from 0 to 0.1 s, respectively. With the increase in P_{avg}, the average maximum temperature change rates of PDMS and SiC increased to 15451 K/s and 16560 K/s at 1.8 W, and 17843 K/s and 19171 K/s at 2.1 W, respectively. Such a high-temperature change rate exceeds the critical heating rate in the high-heating-rate pyrolysis route of PDMS, further confirming that PDMS is directly converted into 3C-SiC pyrolysis products during the CLP reaction.

To investigate the temperature and temperature change rate during the laser pyrolysis in detail, we further optimized the simulation model to improve the simulation accuracy ($1000 \times 1000 \times 200$ µm). Moreover, considering the distinctions between the ILP and CLP processes, we initially examined the 3D and cross-sectional temperature distributions at the intermediate stage of the ILP process (Figure 2.3(d)). It was evident that the 6H-SiC layer absorbed the laser energy and reached the maximum temperature of 6409.10 K, leading to heat spreading in all directions. In the section parallel to the scanning direction (Y = 0 µm), the temperature distribution within the PDMS substrate closely resembled the shape of a wing section. In the section perpendicular to the scanning direction (X = 500 µm), the temperature distribution exhibited a semi-elliptical

pattern consistent with the morphology of the PDMS microchannel. Although there are
slight discrepancies compared to the experimental results (124 µm and 38 µm in Figure 2.1(c)), this temperature can largely serve as a reference for the critical temperature
required for PDMS conversion into 3C-SiC. The 3D isothermal surface distributions of
the initial pyrolysis process, along with the corresponding top view and cross-sectional
views, are illustrated in Figure A.11.

The temperature evolution distributions in 3D and cross-sections during the CLP
process were also investigated (Figure 2.3(e)). It was observed that the high-temperature
region was concentrated around the 3C-SiC pyrolysis products directly exposed to the
laser, with maximum temperatures recorded at different time points: 2054.64 K, 2137.67
K, and 2177.76 K. The disparity in heat capacity and thermal conductivity of the PDMS
substrate and 3C-SiC pyrolysis products resulted in heat accumulation within the 3C-
SiC and a limited amount of heat conduction into the PDMS during the CLP process. In
the section parallel to the scanning direction (Y = 0 µm), the temperature distribution
exhibited significant heat accumulation on the same side as the laser motion, attributed
to the conduction limitation of PDMS. Conversely, on the opposite side, the heat was
conducted through the 3C-SiC pyrolysis products. The black arrow indicated the thermal conduction direction corresponding to the 3C-SiC pyrolysis product. In the section
perpendicular to the scanning direction (X = 500 µm), the temperature distribution revealed that the 3C-SiC pyrolysis product primarily absorbed and conducted heat, which
was then transferred to the PDMS substrate.

These results align with the roles of the laser heating region and heat conduction
region in the previously discussed laser pyrolysis mechanism, providing a clear depiction
of the laser pyrolysis process of PDMS. Furthermore, in addition to the heating rate and
temperature, the deformation and stress involved in the CLP process are illustrated in
Figure A.12 and Figure A.13, and are further discussed in Supporting Information Section
A.3.

2.3.4. DESIGN AND FABRICATION OF FLEXIBLE PRESSURE SENSORS

To assess the potential application of LPDW technology in creating PDMS microarrays,
we designed and fabricated flexible pressure sensors featuring truncated pyramid microarray structures of varying pitches. After determining the optimal parameters (P_{avg}
= 1.5 W, F_{pr} = 40 kHz, V_{ss} = 10 mm/s, and D_{def} = −6 mm), we conducted laser scanning
on a square area (12 × 12 mm) of the PDMS surface at equidistant intervals in both horizontal and vertical directions, forming a number sign (#) pattern. Due to the inherent
limitations of the laser spot size, we adjusted the scanning pitch to control the size of
the micro-truncated pyramids. The resulting microstructure arrays with different laser
scanning pitches (#12×12, #16×16, and #20×20) were characterized using scanning electron microscopy (Figure 2.4(a)-(c)). These results demonstrate remarkable consistency
and reproducibility in the geometric shapes of micro-truncated pyramids.

Subsequently, we designed and fabricated flexible pressure sensors incorporating
micro-truncated pyramid arrays (Figure 2.4(d)). The fabrication process involved mixing
a cross-linking agent with the PDMS base, which was then poured into a meticulously
flat acrylic template. Following curing, a smooth PDMS film was obtained and patterned
using LPDW technology. The PDMS film was subsequently cleaned and subjected to
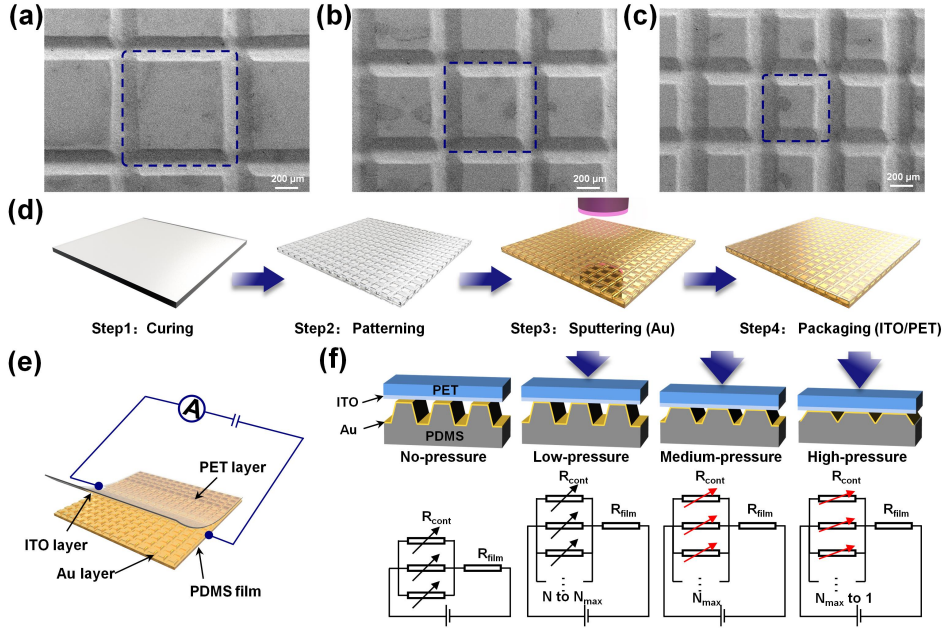
2

Figure 2.4: Surface topography of PDMS micro-truncated pyramid arrays with different scanning pitches (#12×12, #16×16, and #20×20) fabricated using continuous laser direct writing technology. (d) Schematic illustration of the fabrication process for flexible pressure sensors with micro-truncated pyramid array structure. (e) Simplified circuit schematic for testing the performance of the flexible pressure sensor. (f) 3D cross-sectional schematics and equivalent circuit diagrams of the sensor under different pressure conditions.

magnetron sputtering with a conductive metal layer (Au). Finally, the PDMS film with a micro-truncated pyramid array was electrically connected to a PET film with an ITO (Indium Tin Oxide) layer using conductive tape and liquid metal, and then packaged with heat-shrinkable tubes.

To ensure the accurate testing of the flexible pressure sensor, we employed a universal testing machine and a digital source meter to establish a test platform for measuring the sensitivity of the sensors. Specifically, we applied a constant voltage of 1.0 V between the ITO/PET and Au/PDMS electrodes and monitored the current change under various pressure levels. To aid in comprehending the testing process, we provided a simplified circuit model (Figure 2.4(e)). The equation for the corresponding mechanism of the sensor can be calculated as follows:

$$R_{total} = R_{cont} + R_{film} = \frac{R_{mtp}}{N} + R_{film} = \left(\frac{\rho_{eff}}{2A}\right)\frac{1}{N} + R_{film} \qquad (2.3)$$

Among them, the variable R_{total} represents the total resistance of the sensor, which consists of resistance R_{cont} and film resistance R_{film}. R_{cont} represents the contact resistance between the ITO/PET and Au/PDMS electrodes through the micro-truncated pyramid structures. R_{film} represents the additional uncontacted resistance in the ITO/PET and Au/PDMS electrodes, respectively. Accordingly, R_{cont} is determined by

the contact resistance of an individual micro-truncated pyramid (R_{mtp}) and the number of parallel connections of micro-truncated pyramid structures (N). According to the Holm contact resistance model, ρ_{eff} describes the effective resistivity of the contact pair formed between the ITO/PET and Au/PDMS electrodes based on the micro-truncated pyramid structure, while A represents the effective contact area of the contact pair. When external pressure is applied, the performance of the flexible pressure sensor, which is driven by resistance changes, is primarily determined by the parameters A and N.

To enhance understanding of this mechanism, we presented 3D cross-sectional schematics and equivalent circuit diagrams of the pressure sensor under different pressure conditions (Figure 2.4(f)). At low external pressure, the resistance value of the sensor is influenced by the number of contact pairs (N) between the electrodes. As external pressure increases, the contact area (A) between the electrodes expands, resulting in a change in contact resistance. At high external pressure, adjacent micro-truncated pyramid structures contact each other, reducing the number of contact pairs (N) and increasing the contact area (A). However, in a parallel circuit, the total resistance is lower than the smallest individual resistances. At this stage, the contact pairs of the micro-truncated pyramid array form a large contact block, and the minimum resistance of the contact block determines the final resistance of the sensor.

2.3.5. SENSING PERFORMANCE OF FLEXIBLE PRESSURE SENSORS

To assess the sensing performance of the flexible pressure sensor based on micro-truncated pyramid arrays, we conducted various characterizations on sensors with different laser scanning pitches (#12×12, #16×16, and #20×20). The sensor characteristics can be categorized into three main aspects: sensing characteristics, mechanical characteristics, and reliability characteristics. The sensitivity of the pressure sensor, a crucial sensing characteristic, is determined by the slope of the current change rate curve under different external pressure loads. Accordingly, the sensitivity (S) of the piezoresistive sensor is defined as:

$$S = \frac{\Delta I / I_0}{P} \tag{2.4}$$

where I_0 represents the initial current without external pressure, ΔI denotes the change in real-time current (I) under different pressures, and δP represents the variation of the external pressure [56]. Figure 2.5(a) and (b) illustrate the overall and local relationship between relative current ($\Delta I / I_0$) and external pressure (P) for three flexible pressure sensors with different scanning pitches. As the laser scanning pitch increased, the saturation current of the device noticeably notably increased. This observation aligns with the mechanism described earlier for the pressure sensor. For further studies, we selected the most sensitive device (#20 × 20) as the exemplar. It is evident that the response curves of current to external pressure could be divided into four distinct parts based on their slopes in different pressure ranges. In the pressure range of 0-0.5 kPa, the sensitivity of the sensor was 3132.0 kPa^{-1}. In the pressure ranges of 0.5-3.5 kPa and 3.5-10 kPa, the sensitivity was 322.5 kPa^{-1} and 27.8 kPa^{-1}, respectively. In the pressure range of 10-20 kPa, the sensitivity decreased to 0.94 kPa^{-1} while maintaining excellent linearity. These re-

sults demonstrate the excellent sensing performance of the pressure sensor at different pressure levels, particularly its high sensitivity in the micro-pressure and low-pressure ranges.
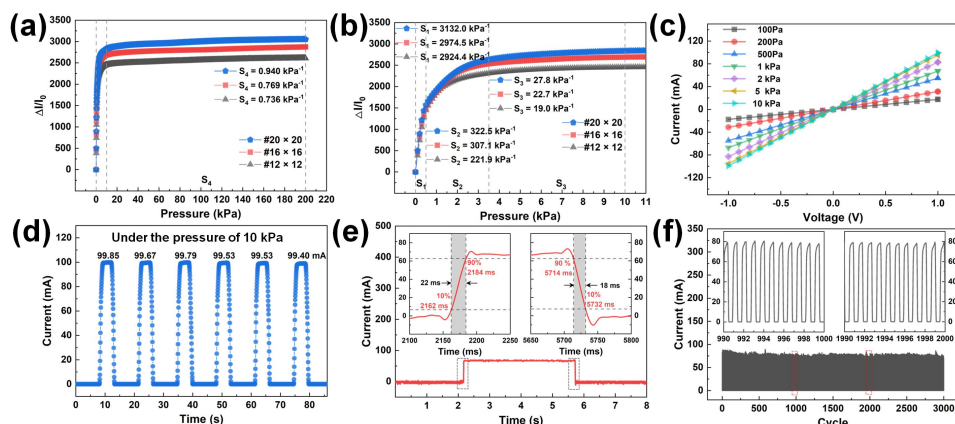

Figure 2.5: (a) and (b) Sensitivity comparison of pressure sensors with different scanning pitches (#12 × 12, #16 × 16, and #20 × 20). (c) Current-voltage (I-V) curves of the pressure sensor (#20 × 20) under different external pressures. (d) Current changes in the pressure sensor (#20 × 20) under steady and repeated external pressure (10 kPa). (e) Response time of the pressure sensor (#20 × 20) with an external pressure of 1 kPa. The insets show the response processes of loading and unloading, respectively. (f) Current changes in the pressure sensor (#20 × 20) during 3000 repeated loading/unloading cycles (frequency of about 1.0 Hz, applied pressure of 2 kPa). The insets show the detailed current change curves from 990-1000 s and 1990-2000 s.

To comprehensively analyze the electrical properties of the flexible pressure sensor, we investigated the current-voltage (I-V) characteristics and response time characteristics of the device. Figure 2.5(c) shows the current-voltage curves of the pressure sensor under different constant external pressure conditions. We observed that the slope of the I-V curve gradually increased with higher external pressure as the voltage was swept from $-1.0\,\mathrm{V}$ to $1.0\,\mathrm{V}$. Furthermore, the device strictly obeyed Ohm's law, and each voltage-current curve exhibited exceptional linearity.

This result indicates that the device maintains stable electrical characteristics under fixed pressure, which is crucial for its practical application in various scenarios.

Repeatability is also a vital aspect of sensing characteristics. It ensures that the sensor provides a consistent and stable output over time, even under challenging conditions of high pressure and repeated deformation. Figure 2.5(d) illustrates the current response curve of the device during the repeatability test. When the device underwent 6 cycles of repeated loading and unloading at 10 kPa, the peak current of the device remained stable at approximately 99.63 mA. The device exhibits a fast and accurate current response, maintaining a consistent peak shape and value for the response current profile across each cycle. This result suggests that the device exhibits promising consistency and repeatability, which are key factors for achieving accurate sensing in various applications.

Figure 2.5(e) illustrates the response time curve of the flexible pressure sensor during loading and unloading. The response time for pressure loading and unloading was defined as the time required for the maximum current to increase from 10% to 90% and

decrease from 90% to 10%, respectively [57]. The sampling frequency was set to 100 kHz with a 1.0 ms sampling interval. The device exhibited a remarkably rapid response speed during pressure loading and unloading, with response times of 22 ms and 18 ms, respectively. Although a slight overshoot was observed in its response, the sensor exhibited reliable dynamic response capabilities to a certain extent.

To assess the mechanical reliability of the flexible pressure sensor, we subjected the device to 3000 cycles of loading and unloading with an external pressure of 2 kPa and a frequency of approximately 1.0 Hz. Figure 2.5(f) illustrates the current output curve of the device during the cycles. While the peak value of the current output curve fluctuated in some cycles, the overall current output remained consistent, indicating the high mechanical stability of the flexible pressure sensor. Even after 1000 and 2000 cycles, the current output of the device remained consistently stable, suggesting the reliability of the conductive metal layer on the surface of the micro-truncated pyramid structures.

2.3.6. POTENTIAL APPLICATIONS OF FLEXIBLE PRESSURE SENSORS

To demonstrate the potential applications of the flexible pressure sensor, we conducted a series of sensor tests that encompassed different pressure ranges. Firstly, we utilized the flexible pressure sensor to detect micro-pressure fluctuations caused by vibrations from a smartphone (Figure 2.6(a)). The real-time current response curve of the sensor exhibited precise and periodic changes with the vibration of the smartphone, with the magnitude of the response current corresponding to the intensity of the vibration. This result demonstrates that the flexible pressure sensors can not only detect simple vibrations in acoustic scenarios but also micro-pressure on the surface of various equipment. Furthermore, we employed the flexible pressure sensor to detect real-time responses to airflow (Figure 2.6(b)). By adjusting the compression strength of the ear bulb syringe, airflow of different intensities was generated to act on the surface of the sensor. The flexible pressure sensor exhibited distinct response peaks for each airflow impact, demonstrating its high-resolution capability in detecting micro-pressure changes. This result indicates the potential application of pressure sensors in high-resolution micro-pressure detection. Additionally, we recorded the real-time response curve while tapping the International Morse Code for the letters T, U, and D, where long presses and short taps corresponded to the dash and dot signals, respectively (Figure 2.6(c)). These results highlight the potential of pressure sensors for detecting human motion, particularly in enabling precise and accurate motion signal detection.
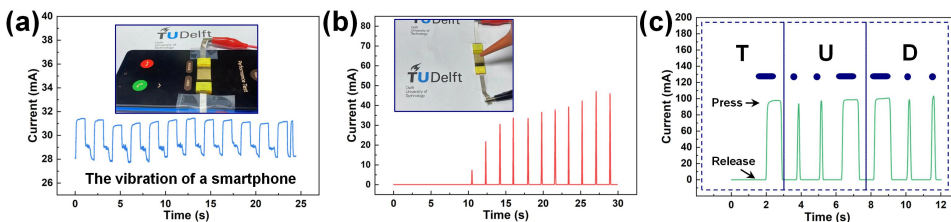

Figure 2.6: (a) Real-time detection of the vibration of a mobile phone during incoming calls. (b) Real-time detection of the impact of different intensities of airflow by squeezing a rubber suction ball. (c) Real-time detection of Morse Code by tapping the three letters of TUD with a finger.

To validate the LPDW technology, we successfully fabricated and integrated a proof-of-concept piezoresistive flexible pressure sensor array (5 × 5) consisting of 25 individual sensors based on the micro-truncated pyramid array (Figure 2.7). To assess its performance, we applied three different mass weights (10 g, 20 g, and 50 g) onto the surface of the sensor array, generating distinct pressure distributions across its surface.
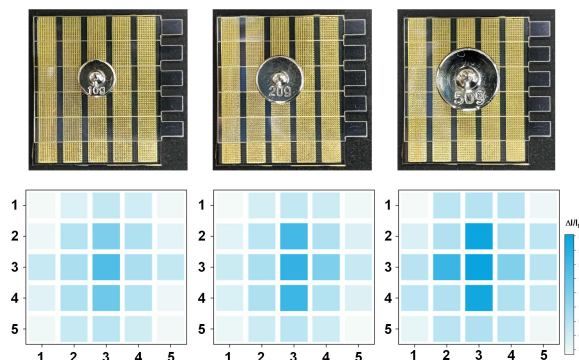

Figure 2.7: The detection of spatial pressure distribution capabilities on a 5 × 5 sensor array using weights of different masses (10 g, 20 g, and 50 g).

It was evident that the area beneath the weight appeared darker in color compared to the unloaded region, indicating a significant increase in current flow. Furthermore, as the amount of weight magnitude increased, the color corresponding to the loaded area exhibited a darker shade overall. Moreover, owing to the inherent rigidity of the PET/ITO material, the pressure applied at the center of the weight was extended and gradually decreased towards the edges of the sensor array, thereby causing the corresponding area to appear brighter. These results suggest that the integrated pressure sensor array has the potential for application in mapping spatial pressure detection.

2.4. Conclusion

In summary, we have developed a laser pyrolysis direct writing (LPDW) technology for fabricating high-performance flexible pressure sensors with a micro-pyramid array. Through extensive experiments and simulations, we reveal the optimal condition and mechanism for continuous laser pyrolysis (CLP). Using this technology, we designed and fabricated resistive flexible pressure sensors with a micro-truncated pyramid array using conductive PDMS film. The fabricated sensor exhibited remarkable sensitivities of 3132.0 kPa^{-1}, 322.5 kPa^{-1}, and 27.8 kPa^{-1} in the pressure ranges of 0-0.5 kPa, 0.5-3.5 kPa, and 3.5-10 kPa, respectively. The sensor had a fast response time (loading 22 ms and unloading 18 ms) and demonstrated excellent repeatability and durability over 3000 cycles. Furthermore, the sensor could detect micro and low pressures such as mobile phone vibrations, airflow impacts, and finger touches. It could also be easily integrated into sensor arrays to map the spatial distribution of non-uniform pressure fields. In addition to its outstanding performance, the flexible pressure sensor with a micro-truncated pyramid array fabricated using LPDW technology exhibited the advantages of

low cost, high scalability, and easy fabrication. Compared with traditional complex micro/nanofabrication processes, this study has provided a new route for designing and fabricating high-performance flexible pressure sensors.

REFERENCES

2

[1] S. Wang *et al.*, "Rapid fabrication of high-performance flexible pressure sensors using laser pyrolysis direct writing", *ACS applied materials & interfaces*, vol. 15, no. 34, pp. 41 055–41 066, 2023.

[2] S. Mishra, S. Mohanty, and A. Ramadoss, "Functionality of flexible pressure sensors in cardiovascular health monitoring: A review", *ACS sensors*, vol. 7, no. 9, pp. 2495–2520, 2022.

[3] F. He, X. You, W. Wang, T. Bai, G. Xue, and M. Ye, "Recent progress in flexible microstructural pressure sensors toward human–machine interaction and healthcare applications", *Small Methods*, vol. 5, no. 3, p. 2 001 041, 2021.

[4] U. Pierre Claver and G. Zhao, "Recent progress in flexible pressure sensors based electronic skin", *Advanced Engineering Materials*, vol. 23, no. 5, p. 2 001 187, 2021.

[5] A. M. Soomro *et al.*, "Flexible fluidic-type strain sensors for wearable and robotic applications fabricated with novel conductive liquids: A review", *Electronics*, vol. 11, no. 18, p. 2903, 2022.

[6] X. Song *et al.*, "Direct growth of graphene films on 3D grating structural quartz substrates for high-performance pressure-sensitive sensors", *ACS Applied Materials & Interfaces*, vol. 8, no. 26, pp. 16 869–16 875, 2016.

[7] Q. Zhang *et al.*, "A zinc-ion battery-type self-powered pressure sensor with long service life", *Advanced Materials*, vol. 34, no. 40, p. 2 205 369, 2022.

[8] T. Yin *et al.*, "3D porous structure in MXene/PANI foam for a high-performance flexible pressure sensor", *Small*, vol. 18, no. 48, p. 2 204 806, 2022.

[9] S.-I. Jeong *et al.*, "Three-dimensional multistack-printed, self-powered flexible pressure sensor arrays: Piezoelectric composites with chemically anchored heterogeneous interfaces", *ACS omega*, vol. 5, no. 4, pp. 1956–1965, 2020.

[10] Z. Ren *et al.*, "Self-powered 2D nanofluidic graphene pressure sensor with serosa-mimetic structure", *EcoMat*, vol. 5, no. 3, e12299, 2023.

[11] Y. Yang *et al.*, "Flexible piezoelectric pressure sensor based on polydopamine-modified BaTiO3/PVDF composite film for human motion monitoring", *Sensors and Actuators A: Physical*, vol. 301, p. 111 789, 2020.

[12] M. Zammali, S. Liu, and W. Yu, "A flexible, transparent, ultralow detection limit capacitive pressure sensor", *Advanced Materials Interfaces*, vol. 9, no. 17, p. 2 200 015, 2022.

[13] H. Wang *et al.*, "Flexible capacitive pressure sensors for wearable electronics", *Journal of Materials Chemistry C*, vol. 10, no. 5, pp. 1594–1605, 2022.

[14]   D. Yang *et al.*, "A flexible and wide pressure range triboelectric sensor array for real-time pressure detection and distribution mapping", *Journal of Materials Chemistry A*, vol. 8, no. 45, pp. 23 827–23 833, 2020.

[15]   X. Pu *et al.*, "Flexible triboelectric 3D touch pad with unit subdivision structure for effective XY positioning and pressure sensing", *Nano Energy*, vol. 76, p. 105 047, 2020.

[16]   W.-D. Li *et al.*, "Recent advances in multiresponsive flexible sensors towards E-skin: A delicate design for versatile sensing", *Small*, vol. 18, no. 7, p. 2 103 734, 2022.

[17]   S. Yao *et al.*, "Nanomaterial-enabled flexible and stretchable sensing systems: Processing, integration, and applications", *Advanced materials*, vol. 32, no. 15, p. 1 902 343, 2020.

[18]   M. Wang *et al.*, "Gesture recognition using a bioinspired learning architecture that integrates visual data with somatosensory data from stretchable sensors", *Nature Electronics*, vol. 3, no. 9, pp. 563–570, 2020.

[19]   C. Cai *et al.*, "A flexible and highly sensitive pressure sensor based on three-dimensional electrospun carbon nanofibers", *RSC advances*, vol. 11, no. 23, pp. 13 898–13 905, 2021.

[20]   X. Tang *et al.*, "Controllable graphene wrinkle for a high-performance flexible pressure sensor", *ACS applied materials & interfaces*, vol. 13, no. 17, pp. 20 448–20 458, 2021.

[21]   J. Yang *et al.*, "Flexible, tunable, and ultrasensitive capacitive pressure sensor with microconformal graphene electrodes", *ACS applied materials & interfaces*, vol. 11, no. 16, pp. 14 997–15 006, 2019.

[22]   Y. Ma *et al.*, "A highly flexible and sensitive piezoresistive sensor based on MXene with greatly changed interlayer distances", *Nature communications*, vol. 8, no. 1, p. 1207, 2017.

[23]   M. Zhu *et al.*, "Hollow MXene sphere/reduced graphene aerogel composites for piezoresistive sensor with ultra-high sensitivity", *Advanced electronic materials*, vol. 6, no. 2, p. 1 901 064, 2020.

[24]   M. Ha, S. Lim, J. Park, D.-S. Um, Y. Lee, and H. Ko, "Bioinspired interlocked and hierarchical design of zno nanowire arrays for static and dynamic pressure-sensitive electronic skins", *Advanced Functional Materials*, vol. 25, no. 19, pp. 2841–2849, 2015.

[25]   B. Chen *et al.*, "High-performance and superhydrophobic piezoresistive pressure sensor based on mountain ridge-like microstructure by silver nanoparticles and reduced graphene oxide", *Composites Part A: Applied Science and Manufacturing*, vol. 162, p. 107 171, 2022.

[26]   W. Li *et al.*, "Flexible and high performance piezoresistive pressure sensors based on hierarchical flower-shaped SnSe2 nanoplates", *ACS Applied Energy Materials*, vol. 2, no. 4, pp. 2803–2809, 2019.

[27] L. Yang *et al.*, "Wearable pressure sensors based on MXene/tissue papers for wireless human health monitoring", *ACS Applied Materials & Interfaces*, vol. 13, no. 50, pp. 60 531–60 543, 2021.

[28] A. You, X. Zhang, X. Peng, K. Dong, Y. Lu, and Q. Zhang, "A skin-inspired triboelectric nanogenerator with an interpenetrating structure for motion sensing and energy harvesting", *Macromolecular Materials and Engineering*, vol. 306, no. 8, p. 2 100 147, 2021.

[29] G. Wu, M. Panahi-Sarmad, X. Xiao, F. Ding, K. Dong, and X. Hou, "Fabrication of capacitive pressure sensor with extraordinary sensitivity and wide sensing range using PAM/BIS/GO nanocomposite hydrogel and conductive fabric", *Composites Part A: Applied Science and Manufacturing*, vol. 145, p. 106 373, 2021.

[30] X.-P. Li *et al.*, "Highly sensitive, reliable and flexible piezoresistive pressure sensors featuring polyurethane sponge coated with MXene sheets", *Journal of colloid and interface science*, vol. 542, pp. 54–62, 2019.

[31] Y. Jung *et al.*, "Flexible and highly sensitive three-axis pressure sensors based on carbon nanotube/polydimethylsiloxane composite pyramid arrays", *Sensors and Actuators A: Physical*, vol. 331, p. 113 034, 2021.

[32] Z. Wang *et al.*, "High sensitivity, wearable, piezoresistive pressure sensors based on irregular microhump structures and its applications in body motion sensing", *Small*, vol. 12, no. 28, pp. 3827–3836, 2016.

[33] C.-Y. Li and Y.-C. Liao, "Adhesive stretchable printed conductive thin film patterns on PDMS surface with an atmospheric plasma treatment", *ACS applied materials & interfaces*, vol. 8, no. 18, pp. 11 868–11 874, 2016.

[34] M. Guo *et al.*, "Low-temperature ppm-level H2S flexible gas sensor on the basis of Ag-modified ZnO", *Materials Science in Semiconductor Processing*, vol. 185, p. 108 944, 2025.

[35] Z. Shi *et al.*, "Morphological engineering of sensing materials for flexible pressure sensors and artificial intelligence applications", *Nano-micro letters*, vol. 14, no. 1, p. 141, 2022.

[36] R. G. Ferreira, A. P. Silva, and J. Nunes-Pereira, "Current on-skin flexible sensors, materials, manufacturing approaches, and study trends for health monitoring: A review", *ACS sensors*, vol. 9, no. 3, pp. 1104–1133, 2024.

[37] D.-Y. Khang, H. Jiang, Y. Huang, and J. A. Rogers, "A stretchable form of single-crystal silicon for high-performance electronics on rubber substrates", *Science*, vol. 311, no. 5758, pp. 208–212, 2006.

[38] C. Lee, L. Jug, and E. Meng, "High strain biocompatible polydimethylsiloxane-based conductive graphene and multiwalled carbon nanotube nanocomposite strain sensors", *Applied Physics Letters*, vol. 102, no. 18, 2013.

[39] B. Zhu *et al.*, "Microstructured graphene arrays for highly sensitive flexible tactile sensors.", *Small (Weinheim an der Bergstrasse, Germany)*, vol. 10, no. 18, pp. 3625–3631, 2014.

2

[40]   Y. Zhang *et al.*, "Highly stable flexible pressure sensors with a quasi-homogeneous composition and interlinked interfaces", *Nature communications*, vol. 13, no. 1, p. 1317, 2022.

[41]   M.-L. Seol, J.-H. Woo, D.-I. Lee, H. Im, J. Hur, and Y.-K. Choi, "Nature-replicated nano-in-micro structures for triboelectric energy harvesting", *Small*, vol. 10, no. 19, pp. 3887–3894, 2014.

[42]   X. Wang, Y. Gu, Z. Xiong, Z. Cui, and T. Zhang, "Silk-molded flexible, ultrasensitive, and highly stable electronic skin for monitoring human physiological signals.", *Advanced materials (Deerfield Beach, Fla.)*, vol. 26, no. 9, pp. 1336–1342, 2013.

[43]   H. Yang *et al.*, "Femtosecond laser patterned superhydrophobic/hydrophobic SERS sensors for rapid positioning ultratrace detection", *Optics Express*, vol. 29, no. 11, pp. 16 904–16 913, 2021.

[44]   B. Farshchian, J. R. Gatabi, S. M. Bernick, G.-H. Lee, R. Droopad, and N. Kim, "Scaling and mechanism of droplet array formation on a laser-ablated superhydrophobic grid", *Colloids and Surfaces A: Physicochemical and Engineering Aspects*, vol. 547, pp. 49–55, 2018.

[45]   S. Liang, Y. Dai, G. Wang, H. Xia, and J. Zhao, "Room-temperature fabrication of SiC microwire photodetectors on rigid and flexible substrates via femtosecond laser direct writing", *Nanoscale*, vol. 12, no. 45, pp. 23 200–23 205, 2020.

[46]   Z. Wan, N.-T. Nguyen, Y. Gao, and Q. Li, "Laser induced graphene for biosensors", *Sustainable Materials and Technologies*, vol. 25, e00205, 2020.

[47]   B.-B. Xu, Y.-L. Zhang, H. Xia, W.-F. Dong, H. Ding, and H.-B. Sun, "Fabrication and multifunction integration of microfluidic chips by femtosecond laser direct writing", *Lab on a Chip*, vol. 13, no. 9, pp. 1677–1690, 2013.

[48]   J. Shin *et al.*, "Monolithic digital patterning of polydimethylsiloxane with successive laser pyrolysis", *Nature Materials*, vol. 20, no. 1, pp. 100–107, 2021.

[49]   M. F. Jensen, M. Noerholm, L. H. Christensen, and O. Geschke, "Microstructure fabrication with a CO2 laser system: Characterization and fabrication of cavities produced by raster scanning of the laser beam", *Lab on a Chip*, vol. 3, no. 4, pp. 302–307, 2003.

[50]   J. Li, Y. Wu, Y. Pan, W. Liu, L. Huang, and J. Guo, "Fabrication, microstructure and properties of highly transparent Nd: YAG laser ceramics", *Optical Materials*, vol. 31, no. 1, pp. 6–17, 2008.

[51]   D. Jin, Q. Chen, T.-Y. Huang, J. Huang, L. Zhang, and H. Duan, "Four-dimensional direct laser writing of reconfigurable compound micromachines", *Materials Today*, vol. 32, pp. 19–25, 2020.

[52]   W. Ouyang, X. Xu, W. Lu, N. Zhao, F. Han, and S.-C. Chen, "Ultrafast 3D nanofabrication via digital holography", *Nature Communications*, vol. 14, no. 1, p. 1716, 2023.

[53] G. T. Burns, R. B. Taylor, Y. Xu, A. Zangvil, and G. A. Zank, "High-temperature chemistry of the conversion of siloxanes to silicon carbide", *Chemistry of materials*, vol. 4, no. 6, pp. 1313–1323, 1992.

[54] G. Camino, S. Lomakin, and M. Lazzari, "Polydimethylsiloxane thermal degradation Part 1. Kinetic aspects", *Polymer*, vol. 42, no. 6, pp. 2395–2402, 2001.

[55] G. Camino, S. Lomakin, and M Lageard, "Thermal polydimethylsiloxane degradation. Part 2. The degradation mechanisms", *Polymer*, vol. 43, no. 7, pp. 2011–2015, 2002.

[56] G. Li, D. Chen, C. Li, W. Liu, and H. Liu, "Engineered microstructure derived hierarchical deformation of flexible pressure sensor induces a supersensitive piezoresistive property in broad pressure range", *Advanced Science*, vol. 7, no. 18, p. 2 000 154, 2020.

[57] Y. Jung, J. Choi, W. Lee, J. S. Ko, I. Park, and H. Cho, "Irregular microdome structure-based sensitive pressure sensor using internal popping of microspheres", *Advanced Functional Materials*, vol. 32, no. 27, p. 2 201 147, 2022.

2

3

HIGH-PERFORMANCE FLEXIBLE STRAIN SENSOR FABRICATED USING LASER TRANSMISSION PYROLYSIS

In recent years, metal crack-based stretchable flexible strain sensors have attracted tremendous attention in wearable device applications due to their extremely high sensitivity. However, the trade-off between sensitivity and detection range has been an intractable dilemma, severely limiting their practical applications. In this chapter, we propose a laser transmission pyrolysis technology for fabricating high-performance flexible strain sensors based on (Au) metal cracks with the microchannel array on the polydimethylsiloxane (PDMS) surface. The fabricated flexible strain sensors exhibit high sensitivity (gauge factor of 1718.5), wide detection range (59% for tensile strain), precise strain resolution (0.1%), fast response and recovery times (69 ms and 141 ms), and robust durability (over 3000 cycles). In addition, experiment and simulation results reveal that introducing a microchannel array enables the stress redistribution strategy on the sensor surface, which significantly improves the sensing sensitivity compared to conventional flat surface sensors. Based on the outstanding performance, the sensors are applied to detect subtle physiological signals such as pulse and swallowing, as well as to monitor large-scale motion signals such as knee flexion and finger bending, demonstrating their potential applications in health monitoring, human-machine interactions, and electronic skin.

3.1. INTRODUCTION

IN recent years, the rapid advancement of flexible electronics technology has provided revolutionary impetus to various industries such as health monitoring [3], human-machine interaction [4], and electronic skin [5]. Flexible strain sensors, as a vital component in the field of flexible electronics, have attracted tremendous attention due to their excellent sensing performance of high sensitivity, wide detection range, fast response time, and robust durability [6]. Generally, according to the signal transmission mechanism, flexible strain sensors can be classified into resistive [7], capacitive [8], piezoelectric [9], and triboelectric [10]. Among them, resistive flexible strain sensors are not only superior to traditional metal conductor [11] and semiconductor [12] sensors in terms of sensing performance but also have the advantages of easy fabrication, low cost, and high plasticity [13, 14]. Typically, resistive strain sensors consist of sensing materials paired with elastic substrates. Conductive materials, such as metal nanomaterials (nanoparticles, nanowires, and nanoplates) [15–17] and low-dimensional materials (carbon blacks, carbon nanotubes, and graphene) [18–20] are commonly used as sensing materials for detecting strain changes. Elastic substrates, such as silicone-based substrates (PDMS, Ecoflex, and Dagon-skin) [21–23], and rubber-based substrates (natural rubber, styrene-butadiene rubber, and polyurethane rubber) [24–26] provide flexibility to sensors and ensure the stability and reliability of the sensing materials. In terms of the fabrication of strain sensors, the strategies can be categorized into two main types: embedding conductive materials within elastic substrates or attaching conductive materials onto the elastic substrates.

The high sensitivity of strain sensors usually stems from significant structural changes during strain, which lead to drastic changes in conductivity. For example, crack-based strain sensors achieve sensitive strain detection by taking advantage of the formation and expansion of cracks, coupled with their disconnection and reconnection properties. As reported, Kang et al. designed a crack-based resistive sensor composed of platinum (Pt) and polyurethane acrylate (PUA), which exhibited an ultrahigh sensitivity of 2000 over a sensing range of 0-2% [27]. Subsequently, Lee et al. fabricated a crack-based flexible strain sensor consisting of a gold (Au) layer and polyethylene terephthalate (PET), which demonstrated a sensitivity of about 1600 in a 2% strain field [28]. These pioneering studies proved that introducing cracks into metal film-based strain sensors is an effective strategy to improve their performance. However, due to the trade-off between sensitivity and detection range, high sensitivity inevitably leads to a narrow detection range, which severely limits the practical application of flexible strain sensors. Therefore, in addition to material innovation, many studies focused on improving the sensing performance of devices by modifying the crack structure [29], such as crack density [30], crack spacing [31], crack depth [32], and crack connectivity [33].

Herein, we designed and fabricated a flexible strain sensor based on (Au) metal cracks with microchannel arrays to overcome this limitation. To achieve these microchannel arrays rapidly and efficiently, we developed a promising novel technology for patterning the polydimethylsiloxane (PDMS) substrate: the laser transmission pyrolysis (LTP) method. We also summarized the realization conditions and pyrolysis mechanism of the laser transmission pyrolysis. After the microchannel arrays were fabricated on the PDMS surface, an Au film was deposited using magnetron sputtering to endow

resistive properties. Finally, the PDMS substrate with microchannel arrays and an Au film was sliced and packaged into individual flexible strain sensors. By introducing the microchannel array, a stress redistribution strategy was implemented on the PDMS surface, resulting in a significant resistance change in the Au film under the influence of external stress. These flexible strain sensors were characterized by high sensitivity (maximum gauge factor of 2448), wide detection range (maximum detection range of 59%), precise detection resolution (0.1%), fast response and recovery times (69 ms and 141 ms), and robust durability (over 3000 cycles). Building on this, we further demonstrated its practical application in detecting both subtle physiological signals (e.g., pulses and swallowing) and large-scale motions (e.g., knee flexion and finger bending).

3.2. Experimental section

3.2.1. Materials and equipment

During the experimental process, all chemicals were obtained from commercial sources and used without further purification. Polydimethylsiloxane (PDMS, Sylgard 184) was purchased from Dow Corning. The film ink type was chosen as Epson BK-T8231. Polyvinyl pyrrolidone (PVP, $(C_6H_9NO)_n$, Mw = 220000) and anhydrous ethanol (CH_3CH_2OH, 99.5%) were procured from Shanghai Macklin Biochemical Co., Ltd. The liquid metal (metal basis: 99.99% Ga-In-Sn) and single-sided conductive tape (3M7766-50) used in the packaging process were procured from Alfa Aesar Chemical Co., Ltd. and 3M Company, respectively. The PDMS with microchannel arrays was fabricated using an ultraviolet (UV) pulsed laser system (Grace X 355-3A, Han's Laser Technology Industry Group Co., Ltd., wavelength: 355 nm). The laser scan speed was set at 10 mm/s, and the motion in the X-Y direction was precisely controlled by software. The distance between the field lens and the sample was adjusted using the vertical Z-direction translation stage. To achieve laser transmission pyrolysis, the laser repetition frequency and laser power were set at 200 kHz and 1.8 W. The laser single pulse energy (E_{sp}) was calculated using the formula $E_{sp} = P_{avg}/F_{pr}$. The PDMS substrate patterned using LTP technology required further cleaning with an ultrasonic constant temperature cleaning machine (Ningbo Scientz Biotechnology Co., Ltd, SBL-15DT). To effectively remove the pyrolysis products, the ultrasonic power was set to 480 W, and the cleaning time was set to 20 min. The deposition of the (Au) metal film on the PDMS surface was carried out using a magnetron sputtering coating machine (T-Z1650PVD, Zhengzhou Ketan Instrument Equipment Co., Ltd.). The sputtering power was set at 55 W, the chamber was filled with argon (Ar) gas, and the vacuum level was maintained at 4 Pa. In the sensor packaging process, commercial single-sided conductive tapes were used as connecting wires. To ensure the reliability of the sensor during its application, liquid metal was coated onto these tapes. Subsequently, two heat-shrink tubes were heated at 130 °C for 20 seconds to protect and secure both ends of the sensor.

3.2.2. Characterization and testing

The morphology of the PDMS substrate with microchannel arrays was characterized using a scanning electron microscope (SEM, Gemini 300, ZEISS) and a 3D laser scanning microscope (VK-X1000, KEYENCE). The UV-Vis absorption spectra of the light-

absorbing coatings were characterized with a microvolume UV-Vis spectrophotometer (NanoDrop™ One, Thermo Fisher Scientific Inc.). The pyrolysis products were characterized with an X-ray diffraction instrument (XRD, Rigaku Smartlab) at a scanning rate of 10 °/min. The mechanical properties of the flexible strain sensor were assessed using a universal testing machine (TSE503A, Wance Testing Machine Co., Ltd.). The corresponding electrical signals were captured with a data acquisition and logging system (DAQ6510, Keithley), and the response time was monitored with an oscilloscope (TBS2104B, Tektronix).

Flexible tensile strain sensors are widely used to measure minute physical deformations. Their sensitivity is typically evaluated using the gauge factor (GF), which is determined by the structure and material of the sensor. In the context of this study, the GF value of the resistance-based flexible strain sensor can be calculated using the formula:

$$\text{GF} = \frac{\Delta R / R_0}{\epsilon} = \frac{\Delta R}{R_0 \cdot \epsilon} \tag{3.1}$$

In this formula, ϵ represents strain, R_0 denotes the initial resistance of the sensor in its stable state, and ΔR is the change in resistance of the sensor due to external strain ϵ.

3.3. Results and discussion

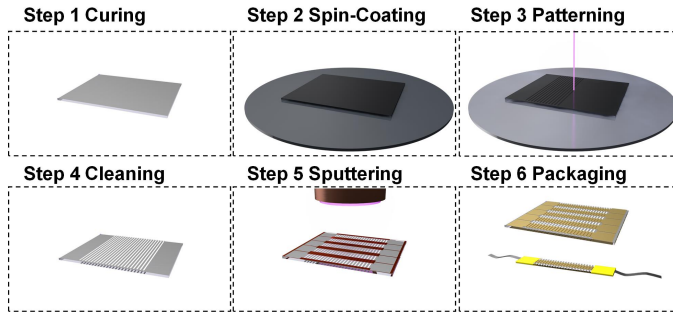### 3.3.1. Design and fabrication of flexible strain sensors

Figure 3.1: Schematic illustration of the fabrication process for the flexible strain sensor based on Au microcracks with a microchannel array.

Figure 3.1 illustrates the schematic diagram outlining the design and fabrication process for the flexible strain sensors with microchannel arrays using PDMS as a flexible substrate. The process involves 6 distinct steps. In Step 1, the PDMS elastomer base and curing agent were meticulously mixed in a proportion of 10:1 and degassed. This mixture was poured into a customized acrylic mold with a thickness of 1.0 mm and cured at a temperature of 80 °C for 2 h. In Step 2, the cut rectangular PDMS film (50 mm × 42 mm × 1 mm) was attached to a 4-inch quartz glass wafer. The film ink was dispersed within a solution containing 10 wt% PVP and ethanol, serving as the light-absorbing material. It was then spin-coated onto the PDMS film at 2000 rpm for 20 seconds. In Step 3, after the ethanol had evaporated, a UV laser was used to perform the laser transmission pyrolysis reaction on the PDMS substrate with a light-absorbing layer to create a microchannel

pattern. In Step 4, a high-power ultrasonic cleanser was employed to remove the laser transmission pyrolysis product and light-absorbing layer from the surface of the PDMS substrate. In Step 5, a partially hollowed polyimide (PI) film was placed over the PDMS film to define the effective area for the metal deposition layer. Then, magnetron sputtering equipment was used to deposit an Au film on the exposed areas of the photomask. In Step 6, the PDMS film with microchannel arrays and a gold coating was segmented and packaged using liquid metal and shrinkable tubes.

3.3.2. LASER TRANSMISSION PYROLYSIS TECHNOLOGY

It is well known that PDMS is a transparent polymer material that is used in numerous fields due to its excellent properties such as flexibility, elasticity, and biocompatibility. To fabricate microstructures on the PDMS surface, a series of innovative fabrication technologies have been developed [34, 35]. Compared to the traditional template method, which imposes strict requirements on fabrication environments, equipment, and processes, laser direct pyrolysis technology stands out due to its effectiveness, precision, controllability, and flexibility [36].

Unlike the continuous laser pyrolysis described in our previous work [37], laser transmission pyrolysis ensures the continuity of the photothermal effect by introducing a semi-transparent light-absorbing layer. Specifically, as shown in Figure 3.2(a), when the laser is vertically irradiated onto the light-absorbing layer covering the PDMS surface, most of the laser energy passes through the light-absorbing layer and PDMS substrate. Only a small portion of the energy is absorbed, leading to the formation of a laser heating region (LHR). Owing to the photothermal effect, the absorbed energy creates an ultra-high temperature gradient, subsequently triggering the laser pyrolysis reaction within the PDMS. Simultaneously, this process leads to the formation of a hemispherical pyrolysis product in the PDMS, facilitating heat transfer and forming a heat conduction region (HCR). Finally, the LTP reaction occurs iteratively as the laser moves, as shown in Figure B.1. In particular, the semi-transparent film ink layer effectively regulates the influence of high temperature on the continuity of pyrolysis during the laser pyrolysis process, which effectively improves the preparation quality.

On this basis, we investigated the effects of different laser average powers (P_{avg}) and pulse repetition frequencies (F_{pr}) on the morphology of the microchannels after laser transmission pyrolysis. Correspondingly, Figure 3.2(b) shows the 3D laser confocal images of the PDMS microchannels after LTP treatment in the defocused state ($D_{\mathrm{def}} = -1.0$ mm). Apparently, the LTP reaction achieved deeper microchannel depths under $P_{\mathrm{avg}} =$ 2.4 W and $F_{\mathrm{pr}} = 100$ kHz ($E_{\mathrm{sp}} = 24$ μJ). Correspondingly, owing to the strong photothermal effect, the sidewalls of the microchannels exhibited a relatively rough morphology. In contrast, under $P_{\mathrm{avg}} = 1.2$ W and $F_{\mathrm{pr}} = 150$ kHz ($E_{\mathrm{sp}} = 6$ μJ), the intensity of the LTP reaction was notably weak, resulting in shallower microchannel depths and inconsistent morphologies. Considering the operating mechanism of the pulsed laser, the single pulse energy (E_{sp}) determines the threshold of a single laser spot triggering the pyrolysis reaction, while the pulse repetition frequency (F_{pr}) affects the forming quality of continuous morphology during laser pyrolysis. On the premise that the single pulse energy reaches the pyrolysis energy threshold, increasing the pulse repetition frequency can significantly optimize the quality of the pyrolysis morphology. This is also the main

3

Figure 3.2: (a) Schematic diagram of the reaction mechanism of laser transmission pyrolysis (LTP). (b) 3D laser confocal images of PDMS microchannel morphology under different laser average powers and laser repetition frequencies (P, M, and G represent poor, medium, and good morphological quality, respectively). (c) The depth, width, and quality of the microchannel under different light-absorbing layers (wt%) and defocus distances (D_{def}). (d) Ultraviolet-visible (UV-Vis) absorption spectra of PVP absolute ethanol solutions with film inks of different mass percentages (0%, 5%, 10%, and 15%). (e) X-ray diffraction (XRD) pattern of products resulting from the LTP process, accompanied by a schematic diagram of the reaction mechanism. (f) SEM image of PDMS surface after LTP reaction (scale bar: 20 μm).

criterion for selecting the process conditions (P_{avg} = 1.8 W and F_{pr} = 200 kHz) for the fabrication of the flexible strain sensors.

To investigate the effects of different light-absorbing layers (wt%) and defocus distances (D_{def}) on the microchannel fabrication, we analyzed the depth, width, and quality of the microchannels under different conditions, as shown in Figure 3.2(c). The corresponding samples were labeled as S-5%, S-10%, and S-15%, respectively. We observed that as the mass percentage (wt%) of the film ink increased, the capacity of the light-absorbing layer to absorb UV laser increased, resulting in a corresponding increase in both the depth and width of the microchannels. This observation confirms that manipulating the light-absorbing layer can effectively control the reaction intensity of LTP. Interestingly, within the range of −0.5 mm and 0.5 mm around the focal plane, the quality of microchannels formed by the LTP reaction on the PDMS surface was poor. In con-

trast, optimal microchannel quality was realized at defocus distances farther from the focal plane (D_{def} = −1 mm and 1 mm). This observation further confirms that the LTP reaction near the focal plane is unstable due to factors such as the accumulation and convergence of laser energy [38].

Correspondingly, Figure 3.2(d) shows the ultraviolet-visible (UV-Vis) light absorption spectra of PVP absolute ethanol solutions of film inks with different mass percentages (5, 10, and 15 wt%). It was obvious that the absorption percentages of samples S-5%, S-10%, and S-15% at a wavelength of 355 nm were 10.56%, 17.47%, and 25.21%, respectively, showing clear differences. Meanwhile, we found that the uniformity of the light-absorbing layer on the PDMS surface was crucial for the morphology of the microchannels. This is also the primary reason for introducing the anhydrous ethanol solution of PVP as the dispersant and thickener of the film inks. Moreover, this approach effectively eliminates uncontrollable variables introduced by surface modification methods, such as ultraviolet or plasma treatment [39].

To explain the reaction mechanism of LTP further, we employed X-ray diffraction (XRD) to analyze the pyrolysis products, as shown in Figure 3.2(e). The purple spectrum exhibited three main peaks at 35.6°, 60.0°, and 71.8°, unmistakably indicating the 3C-SiC products generated during the LTP reaction. In the specific reaction process, PDMS undergoes pyrolysis due to the laser energy absorbed by the light-absorbing layer, experiencing a high heating rate. In the initial stage of the LTP reaction, the high temperature induces the breaking and reforming of Si-CH$_3$ bonds on PDMS chains, thereby further enhancing the cross-linking of PDMS and generating silicon oxide and pyrolytic carbon on the PDMS surface. With increasing temperature, the silicon oxides in PDMS are directly reduced to 3C-SiC by the pyrolytic carbon in an oxygen-deficient environment [40].

Figure 3.2(f) shows the SEM image of the PDMS surface after the LTP reaction. The morphology of the sample distinctly delineated both the laser heating and heat conduction regions. Within the laser heating region, porous pyrolysis products (3C-SiC) were clearly observed. Meanwhile, at the edge of the laser heating region, a clear boundary existed between the pyrolysis products and the light-absorbing layer. This indicates that the light-absorbing layer, besides inducing the LTP reaction, does not further exacerbate the spread of pyrolysis. Additionally, significant delamination was observed between the pyrolysis products and the PDMS substrate. This phenomenon is mainly attributed to the differences in the thermal expansion coefficients of the various materials.

3.3.3. PERFORMANCE TEST OF THE STRAIN SENSOR

After thoroughly understanding the LTP mechanism, it is possible to create customized microchannel patterns of various shapes on the PDMS surface. The fabrication parameters selected for the flexible strain sensor in terms of the UV laser were as follows: laser average power (P_{avg}) of 1.8 W, laser repetition frequency (F_{pr}) of 200 kHz, and laser defocus distance (D_{def}) of 1.0 mm. Building on this foundation, we designed and fabricated flexible strain sensors with the microchannel array at different LTP scanning intervals. In addition, the influence of different metal film thicknesses on the surface of the microchannel array was explored by controlling the sputtering time. The process of magnetron sputtering of metal layers is shown in Figure B.2. As shown in Figure 3.3

3

(a), the intervals for LTP scanning, from top to bottom, before sensor packaging were individually set to 1000 μm, 600 μm, and 200 μm (labeled as *I*-1000, *I*-600, and *I*-200). Concurrently, the flat surface PDMS substrate served as a control group to validate the performance enhancement of the flexible strain sensor (labeled as *I*-Flat). From left to right, the magnetron sputtering deposition times for the samples were set as 10 s, 20 s, and 30 s (labeled as *T*-10, *T*-20, and *T*-30). Apparently, samples with shorter sputtering times exhibit noticeable translucency. As the sputtering time increases, the transparency diminishes, and the sample eventually becomes opaque. From the SEM image of the sample (*I*-200&*T*-20), the laser scanning intervals were 200 μm, which contained a microchannel with a size of 60 μm, maintaining good structural consistency. The tiny cracks observed on the (Au) metal film are attributed to thermal stresses caused by the heating process of ion evaporation before the SEM imaging.

The metal-sputtered (Au) samples with microchannel arrays were sliced into specific sizes (length of 50 mm, width of 8.4 mm, and height of 1 mm) and subsequently packaged into individual flexible strain sensors (sensor effective area: length 30 mm, width 5 mm). The sensitivity and detection range of different sensors were evaluated as the vital performance indicators for flexible strain sensors. Figure 3.3(b) shows the relative resistance changes ($\Delta R/R_0$) of different flexible strain sensors, with the microchannel array and the flat surface, under various strains (ϵ) during the stretching process. The corresponding sensor performance test platform is shown in Figure B.3. Compared to the flexible strain sensor with a flat surface, the introduction of microchannels significantly enhances the sensitivity of the flexible strain sensor.
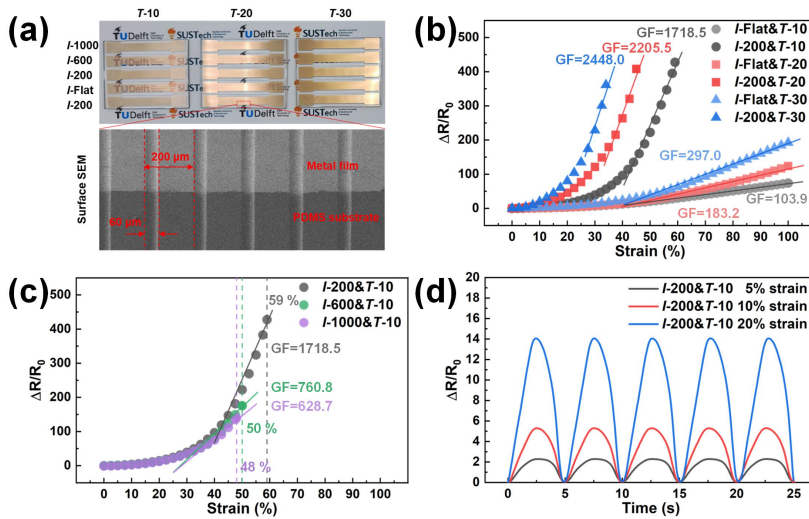

Figure 3.3: (a) Optical images of different scanning intervals and Au sputtering times, and the SEM image of local microchannel array. (b) Relative resistance changes of strain sensors based on different microchannel arrays and flat-surface under different strains. (c) Relative resistance changes of strain sensors based on different scanning intervals. (d) Relative resistance response curve of the sensor under large strain conditions (5%, 10%, and 20%).

Taking the *I*-Flat&*T*-10 and *I*-200&*T*-10 sensors as typical examples, on the flat-

surface PDMS substrate, after 10 seconds of metal sputtering, the GF value of the sensor (I-Flat&T-10) reached 103.9 after linear fitting within the 40-100% strain range. Notedly, after introducing the microchannel array (channel width = 60 μm, scanning interval = 200 μm), the GF value of the sensor (I-200&T-10) increased to an ultra-high 1718.5, with the performance increased by nearly 16 times. Correspondingly, due to the trade-off relationship between sensitivity and detection range, the inherent detection range of the strain sensor with the microchannel array decreased to 59%. Furthermore, for the flexible strain sensors based on metal cracks, the thickness of the metal sputtering significantly affects their performance [18]. Evidently, as the metal sputtering time increased from 10 s to 20 s and then to 30 s, the GF value of sensors with a flat surface rose from 103.9 to 183.2, finally reaching 297.0. Concurrently, the GF value of sensors with the microchannel array also climbed from 1718.5 to 2205.5 and further to 2448.0, while their detection range decreased from 59% to 45% and finally to 34%.

Additionally, the performance of flexible strain sensors with different scanning intervals is shown in Figure 3.3(c). It can be clearly observed that as the laser scanning interval increased from 200 μm to 600 μm and subsequently to 1000 μm, the GF value of the sensor dropped from 1718.5 to 760.8 and further down to 628.7. Meanwhile, the detection range of the sensor also diminished from 59% to 50% and then down to 48%. The detailed sensing performances of various sensor types are outlined in Table 3.1. Importantly, the detection range limit for the sensors with the flat surface was set at 100% and not the limit of its detection range.

Table 3.1: Sensing performance of flexible strain sensors

Sensor Type	Detection Range (ϵ)	Fitting Interval (ϵ)	Gauge Factor (GF)	Linearity (R^2)
I-200&T-10	0-59%	40-59%	1718.5	0.98
I-NLT&T-10	0-100%	40-100%	103.9	0.99
I-200&T-20	0-45%	35-45%	2205.5	0.98
I-NLT&T-20	0-100%	40-100%	183.2	0.99
I-200&T-30	0-34%	25-34%	2448.0	0.98
I-NLT&T-30	0-100%	29-100%	297.0	0.99

Among them, the device I-200&T-10 stood out with its extensive detection range coupled with exceptional sensitivity. Therefore, it was selected to further evaluate the performance of the flexible strain sensor. As shown in Figure 3.3(d), when subjected to strains of 5%, 10%, and 20%, the sensor consistently showed a clear and stable response to 5 consecutive triangle wave strains, operating at a steady frequency of 0.2 Hz. Clearly, the sensor has a distinct response to large strains. The asymmetry of the response peak is attributed to the hysteresis effect caused by the viscoelasticity of the PDMS material, leading to delayed strain recovery during loading and unloading cycles.

As shown in Figure 3.4(a), when the sensor is subjected to 4 consecutive small strains of 0.1%, its relative resistance precisely corresponds to the externally applied strain. This further demonstrates the consistency of the sensor response under small strain conditions and achieves a strain resolution of 0.1%.

To verify the response speed of the sensor, we measured its response time (stretch time, t_S) and recovery time (release time, t_R) under different stretch and release acceler-
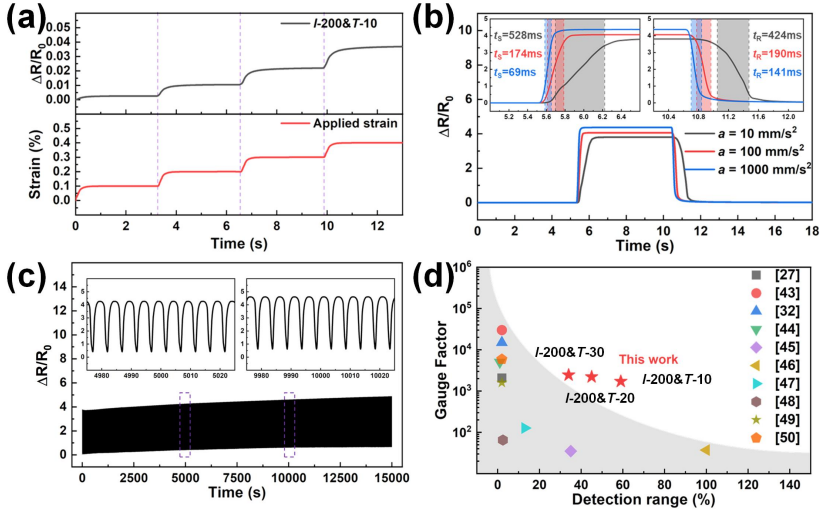
Figure 3.4: (a) Relative resistance response curve of the sensor under small strain conditions (0.1%, 0.2%, 0.3%, and 0.4%,). (b) The response time and recovery time of the sensor under different stretch and release accelerations. (c) Relative resistance response curve of the sensor for 3000 stretch-release cycles at 10% strain. (d) Comparison of sensing range and gauge factor with other reports.

ations (10, 100, and 1000 mm/s^2). As shown in Figure 3.4(b), with the increase in stretch and release acceleration, both the response and recovery times decreased significantly. It is worth noting that in all stretching and releasing accelerations, the recovery time is always slower than the response time, which is attributed to the intrinsic viscoelasticity of the PDMS material [41]. Specifically, at the maximum acceleration, the response and recovery times were 69 ms and 141 ms, respectively. These times are are comparable to the requirements of flexible strain sensors for various applications [6]. The response and recovery times were defined as the time corresponding to the relative resistance change of the sensor from 10% to 90% [42].

To evaluate the long-term reliability of the flexible strain sensor, a Periodic strain of 10% was applied to the sensor over 3,000 cycles at a 0.2 Hz frequency. As shown in Figure 3.4(c), despite slight degradation during the stretching and releasing phases, the sensor with the microchannel array demonstrated long-term reliability without any significant failures.

As summarized in Figure 3.4(d), the development of crack-based flexible strain sensors with high sensitivity and wide detection range is still challenging [27, 32, 43–50]. However, utilizing laser transmission pyrolysis technology to design a flexible strain sensor with a microchannel array based on Au metal cracks is expected to provide a comprehensive solution to this challenge.

3.3.4. Mechanism Analysis of the Strain Sensor
To investigate the sensing mechanism, we conducted a systematic analysis comparing the distribution of Au cracks under different strain conditions between the sensor with

the flat surface and the sensor with the microchannel array. Figure 3.5(a) shows the optical microscopy (OM) images of *I*-Flat&*T*-10 and *I*-200&*T*-10 under the tensile strain conditions of 10%, 30%, and 50%. The corresponding test platform for metal crack generation and extension is shown in Figure B.4. Under external strain, the surface Au film of the sensor developed elongated and random cracks perpendicular to the stretching direction. This crack propagation trend is consistent with previously reported studies on strain sensors based on metallic cracks [27, 32]. Specifically, for the *I*-Flat&*T*-10 sensor, the crack density was significantly lower under a 10% strain condition. In the flat region (R-1) of the PDMS substrate, surface stress induced fractures in the adhering Au film, resulting in crack formation and the release of energy from stretching [6]. As the strain increased to 30%, the number of cracks on the Au film rose noticeably, leading to a significant increase in micro-crack density. At a strain of 50%, the micro-crack density of the Au film reached saturation, and the micro-crack spacing further expanded. In comparison, for the *I*-200&*T*-10 sensor, the crack propagation models of the Au film in the channel and mesa regions (R-2 and R-3) of the PDMS substrate exhibited distinct differences. Under 10% strain, the Au cracks in the mesa region (R-3) were basically consistent with the flat region of *I*-Flat&*T*-10. However, the Au cracks in the channel region (R-2) showed a lower crack density and a higher crack spacing. Similarly, as the strain increased to 30%, the crack density in the mesa region further increased. Notably, the crack density in the channel region remained largely stable, but the crack spacing further expanded. Under a strain of 50%, the crack densities in both the mesa and channel regions reached a steady state. However, with increasing external stretching, the crack spacing in the channel region expanded significantly. This is also the primary reason for the significant change in the relative resistance of the flexible strain sensor with microchannel arrays.

To further investigate the effect of the microchannel array on the crack generation mechanism during the stretching of flexible sensors, we employed the finite element method (FEM) to simulate the deformation and strain distribution in the PDMS substrate. Figure 3.5(b) and (c) show the deformation and stress distributions of the PDMS substrates with the flat surface and the microchannel array under different strain conditions (10%, 30%, and 50%). Based on the simulation results, the PDMS substrates with the flat surface and the microchannel array (*I*-Flat&*T*-10 and *I*-200&*T*-10) exhibited uniform deformation in the primary regions under different tensile strains. However, owing to the Poisson's ratio of the PDMS material, a contraction occurred perpendicular to the stretch direction. This leads to an evident dumbbell-shaped morphology, particularly under large strain conditions (50%), potentially compromising the reliability of the strain sensor. Meanwhile, for the stress distribution, PDMS substrates with the flat surface and the microchannel array (*I*-Flat&*T*-10 and *I*-200&*T*-10) exhibited consistent stress distribution under the small strain conditions (10%), with a negligible difference. Nevertheless, as the strain increased to 30% and 50%, both substrates revealed stress concentrations at their fixed boundaries. In contrast, the primary regions of the substrates sustained a fairly uniform and periodic stress distribution. Notably, under a large strain of 50%, the channel region (R-2) of the PDMS substrate with the microchannel arrays exhibited significantly higher stress compared to the adjacent mesa region (R-3), as shown in Figure 3.6(a).
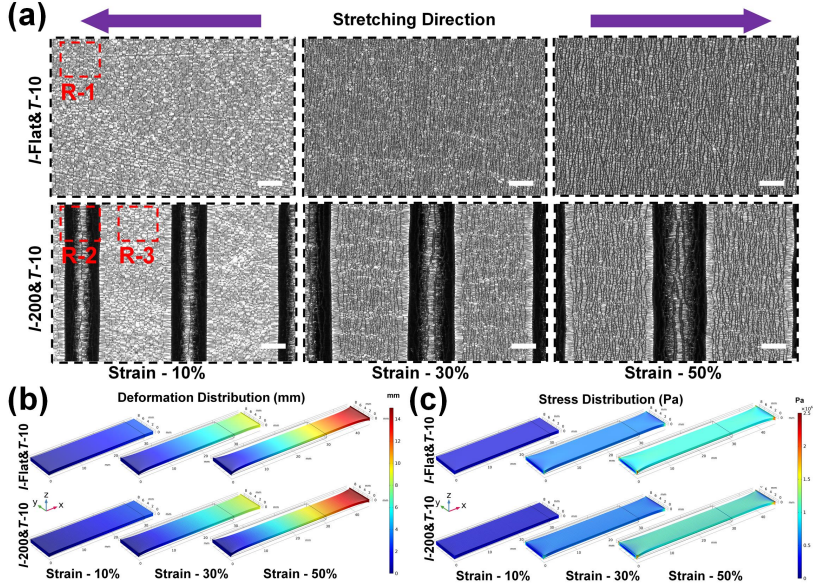
Figure 3.5: (a) Optical microscope (OM) images of surface Au microcracks distribution of *I*-Flat&*T*-10 and *I*-200&*T*-10 under 10%, 30%, and 50% tensile strain conditions (Scale bar: 10 µm). (b) and (c) Deformation and strain distribution of PDMS substrates with the flat surface and the microchannel array under different strain conditions (10%, 30%, and 50%).
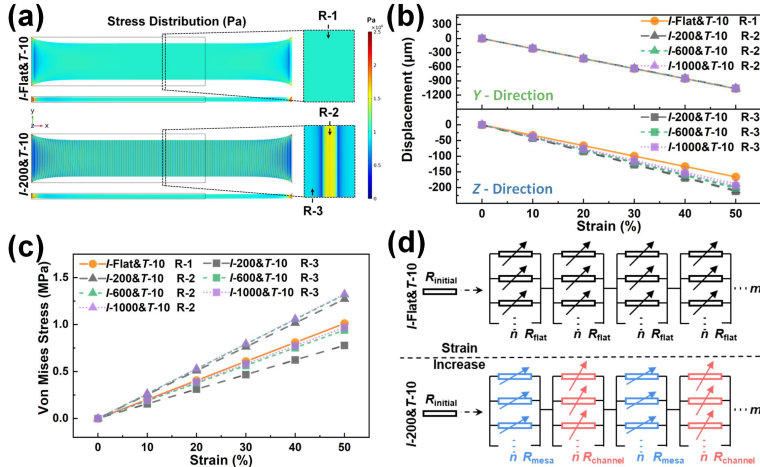

Figure 3.6: (a) Strain distribution of PDMS substrates with smooth surface and microchannel array under 50% strain state. (b) and (c) The changing trends of deformation and stress with different strains in different regions of PDMS substrates with smooth surfaces and microchannel arrays, respectively. (d) Equivalent circuit diagrams corresponding to PDMS substrates with the flat surface and the microchannel array.

To systematically analyze the changing trends, we evaluated the maximum deformation and average stress distribution in different regions (R-1, R-2, and R-3) under different tensile strain conditions for all types of PDMS substrates, as shown in Figure 3.6(b) and (c). In the Y-direction, the maximum surface deformation of different PDMS substrates remained relatively consistent. Conversely, in the Z-direction, PDMS substrates with low microchannel array density (I-1000&T-10) exhibited larger surface deformation as the strain increased. As the strain increased, the average surface stress in different regions of the PDMS substrates increased linearly. In PDMS substrates with microchannel arrays, the average surface stress in channel regions (R-2) was significantly higher than that in mesa regions (R-3). Meanwhile, for PDMS substrates with a flat surface, the average surface stress in the flat regions remained in an intermediate position. In fact, the above-mentioned deformation and stress distributions are in good agreement with the Au crack morphology as well as the measured performances of the sensors. Higher stress leads to significant changes in the relative resistance of the sensor, further proving that the introduction of microchannels improves the sensitivity of metal crack-based strain sensors. However, this stress redistribution strategy still cannot break the trade-off relationship between sensor sensitivity and detection range. In addition, a longer metal sputtering time will cause Au cracks on the surface of the sensor to more easily reach the fracture limit during the stretching process, resulting in a narrowing of the detection range. Counterintuitively, the lower the microchannel density, the higher the average surface stress in the channel area, which makes it easier for the Au cracks on the surface to reach the fracture limit, thus reducing the detection range of the sensor.

According to the conductive grid formed by the propagation of metal cracks, we define the sensor as a resistor network composed of m columns, each consisting of n resistors in parallel. Therefore, the total resistance of the sensor with a flat surface (R_{FS}) can be defined as:

$$R_{\text{FS}} = \frac{m}{n} R_{\text{flat}} \tag{3.2}$$

where the R_{flat} represents the crack gap resistance of the sensor with the flat surface. Correspondingly, the total resistance of the flexible strain sensor with a microchannel array (R_{MA}) is defined as:

$$R_{\text{MA}} = \frac{m}{2n} \left(R_{\text{channel}} + R_{\text{mesa}} \right) \tag{3.3}$$

where the R_{channel} and R_{mesa} indicate the crack gap resistance of the sensor with the microchannel array, respectively. The corresponding equivalent circuit diagrams are shown in Figure 3.6(d). For sensors with a flat surface, under small strain, crack generation is the dominant process, leading to increases in both m and n in the resistor network. During this stage (crack generation stage), since the crack growth direction is perpendicular to the tensile direction, m increases at a much faster rate than n. However, as the strain further increases, crack expansion becomes the dominant process, and both m and n in the resistor network reach saturation. During this stage (crack expansion stage), the expanding crack spacing causes a significant increase in the crack gap resistance (R_{flat}) in the network, becoming the main factor affecting the relative resistance change. For sensors with the microchannel array, the introduction of the microchan-

nel array effectively redistributes the stress distribution on the PDMS surface, resulting in different crack propagation models. The stress is significantly more concentrated in the microchannel region compared to the mesa region. Under the same strain conditions, the crack density in the microchannel region saturates more quickly. As the strain increases further, the crack gap resistance in the channel region (R_{channel}) exceeds that in the mesa region (R_{mesa}). Although the sensor with the microchannel array has lower crack density when saturated compared to the sensor with the flat surface, the notable change in relative resistance due to crack spacing leads to greater sensitivity.

Analysis of the above simulation results shows that the introduction of the microchannel array leads to uneven stress distribution on the sensor surface, which provides a theoretical basis for the strain redistribution strategy. This uneven distribution potentially affects the generation and expansion of metal cracks, thereby enhancing the sensitivity of strain sensors based on metal cracks.

3.3.5. Practical applications of the strain sensor

Benefiting from the high sensitivity and wide detection range of the designed flexible strain sensor, we extensively explored its capability to monitor signals for potential applications in health monitoring, human motion detection, and postoperative rehabilitation tracking. For monitoring subtle physiological signals, pulse signals serve as effective indicators of heart function and blood circulation, playing a crucial role in the prevention, diagnosis, and management of cardiovascular conditions. As shown in Figure 3.7(a), the flexible strain sensor was affixed to the radial artery side of the wrist, capturing the slight strain of the skin induced by pulse beats. Under standard conditions, the sensor identified the typical wrist pulse curve, where its relative resistance change exhibited periodic fluctuations and clear peaks synchronized with each heartbeat. The magnified relative resistance responses distinctly revealed the percussion wave, tidal wave, and diastolic waves (P-wave, T-wave, and D-wave) characteristic of the human pulse. Moreover, monitoring the swallowing process is essential for assessing swallowing disorders and valuable for daily observations of abnormal behaviors. As shown in Figure 3.7(b), the flexible sensor was attached to the throat to detect the subtle strains generated by the swallowing action. The relative resistance change of the sensor exhibited swift and periodic responses consistent with the swallowing action, generating a corresponding swallowing curve. This enlarged swallowing curve clearly illustrated the processes of larynx elevation (LE) and larynx anterior movement (LAM) during swallowing. These results further verify the potential application of the sensor in the field of small strain detection.

For large-scale motion signals, assessing the range of motion in the knee joint after total knee arthroplasty (TKA) is critical for postoperative rehabilitation tracking and recovery evaluation. As shown in Figure 3.7(c), the flexible strain sensor was secured to the surface of the quadriceps muscle on a knee joint model, aiming to monitor the flexion of the knee joint. The relative resistance change consistently fluctuated during the continuous 45° bending motion, and notably, the sensor met a strain threshold of 50% [51]. Furthermore, evaluations of finger bending serve as valuable tools for medical professionals, enabling them to accurately determine both the range of motion and the severity of impairment in patients with rheumatoid arthritis, osteoarthritis, or other forms of arthritis. As shown in Figure 3.7(d), the flexible sensor was attached between the
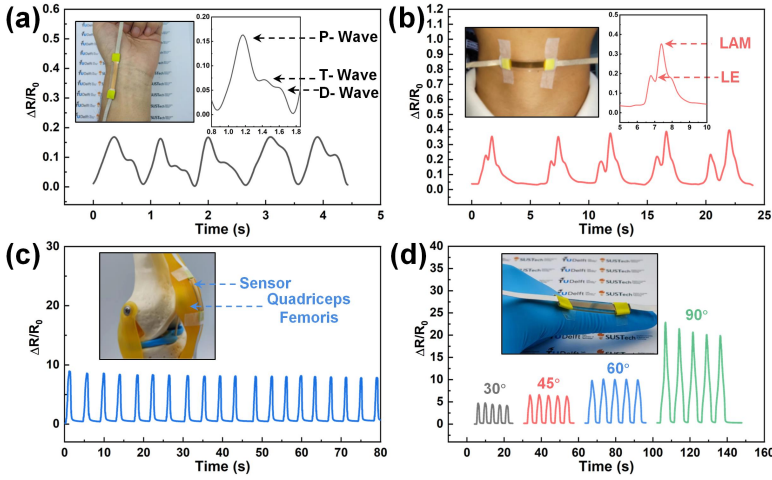
Figure 3.7: (a) Relative resistance responses of the flexible strain sensor for monitoring pulse beats. (b) Relative resistance responses of the sensor for detecting pharyngeal swallowing. (c) Relative resistance responses of the sensor for monitoring knee flexion. (d) Relative resistance responses of the sensor for detecting different finger bending angles (30°,45°, 60°, and 90°).

proximal and middle phalanges to detect finger bending. With increasing finger bending angles (30°, 45°, 60°, and 90°), the relative resistance change of the sensor exhibited significant proportional changes. These results further demonstrate the potential application of the sensor in the field of large strain detection.

3.4. CONCLUSION

In summary, we successfully developed a flexible strain sensor based on gold (Au) cracks with a microchannel array fabricated by the laser transmission pyrolysis technology. Through extensive experiments, we revealed its operating conditions and pyrolysis mechanism. Using this technology, we realized a surface stress redistribution strategy for microchannel arrays on PDMS surfaces, resulting in a significant increase in the sensitivity of sensors with microchannel arrays compared to conventional flat surface sensors. The sensor exhibited high sensitivity (GF = 1718.5), precise strain resolution (0.1%), wide detection range (59%), fast response and recovery times (69 ms and 141 ms, respectively), and robust durability (over 3000 cycles). Notably, the sensor could not only precisely detect subtle physiological signals such as pulse and swallowing but also monitor large-scale motion signals such as knee flexion and finger bending. This study provides a promising technology platform for designing and fabricating high-performance flexible strain sensors based on metal cracks and opens up vast possibilities for their application in the field of health monitoring, human-machine interactions, and electronic skin.

References

[1] S. Wang, Q. Zong, H. Yang, Q. Huang, H. Ye, and P. French, "Flexible high-sensitivity strain sensor fabricated with PDMS micro-channel array using laser transmission pyrolysis technology", in *2024 IEEE 37th International Conference on Micro Electro Mechanical Systems (MEMS)*, IEEE, 2024, pp. 367–370.

[2] S. Wang *et al.*, "High-performance flexible strain sensor fabricated using laser transmission pyrolysis", *IEEE Sensors Journal*, 2023.

[3] J. Huang *et al.*, "Wrinkle-enabled highly stretchable strain sensors for wide-range health monitoring with a big data cloud platform", *ACS Applied Materials & Interfaces*, vol. 12, no. 38, pp. 43 009–43 017, 2020.

[4] H. Zhang *et al.*, "A flexible wearable strain sensor for human-motion detection and a human–machine interface", *Journal of Materials Chemistry C*, vol. 10, no. 41, pp. 15 554–15 564, 2022.

[5] J. Zhou *et al.*, "Highly sensitive and stretchable strain sensors based on serpentine-shaped composite films for flexible electronic skin applications", *Composites Science and Technology*, vol. 197, p. 108 215, 2020.

[6] M. Amjadi, K.-U. Kyung, I. Park, and M. Sitti, "Stretchable, skin-mountable, and wearable strain sensors and their potential applications: A review", *Advanced Functional Materials*, vol. 26, no. 11, pp. 1678–1698, 2016.

[7] L. Duan, D. R. D'hooge, and L. Cardon, "Recent progress on flexible and stretchable piezoresistive strain sensors: From design to application", *Progress in Materials Science*, vol. 114, p. 100 617, 2020.

[8] H. Xu, Y. Lv, D. Qiu, Y. Zhou, H. Zeng, and Y. Chu, "An ultra-stretchable, highly sensitive and biocompatible capacitive strain sensor from an ionic nanocomposite for on-skin monitoring", *Nanoscale*, vol. 11, no. 4, pp. 1570–1578, 2019.

[9] M. Bobinger *et al.*, "Light and pressure sensors based on PVDF with sprayed and transparent electrodes for self-powered wireless sensor nodes", *IEEE Sensors Journal*, vol. 19, no. 3, pp. 1114–1126, 2018.

[10] J. Liu, L. Zhang, N. Wang, and C. Li, "Highly stretchable and transparent triboelectric nanogenerator based on multilayer structured stable electrode for self-powered wearable sensor", *Nano Energy*, vol. 78, p. 105 385, 2020.

[11] A. Fiorillo, C. Critello, and S. Pullano, "Theory, technology and applications of piezoresistive sensors: A review", *Sensors and Actuators A: Physical*, vol. 281, pp. 156–175, 2018.

[12] A. A. Barlian, W.-T. Park, J. R. Mallon, A. J. Rastegar, and B. L. Pruitt, "Semiconductor piezoresistance for microsystems", *Proceedings of the IEEE*, vol. 97, no. 3, pp. 513–552, 2009.

[13] Z. Duan *et al.*, "Inspiration from daily goods: A low-cost, facilely fabricated, and environment-friendly strain sensor based on common carbon ink and elastic core-spun yarn", *ACS Sustainable Chemistry & Engineering*, vol. 7, no. 20, pp. 17 474–17 481, 2019.

[14] J. Chen, Y. Zhu, and W. Jiang, "A stretchable and transparent strain sensor based on sandwich-like PDMS/CNTs/PDMS composite containing an ultrathin conductive CNT layer", *Composites Science and Technology*, vol. 186, p. 107 938, 2020.

[15] J. Lee *et al.*, "A stretchable strain sensor based on a metal nanoparticle thin film for human motion detection", *Nanoscale*, vol. 6, no. 20, pp. 11 932–11 939, 2014.

[16] M.-S. Lee *et al.*, "High-performance, transparent, and stretchable electrodes using graphene–metal nanowire hybrid structures", *Nano letters*, vol. 13, no. 6, pp. 2814–2821, 2013.

[17] J. Kim, S. W. Lee, M. H. Kim, and O. O. Park, "Zigzag-shaped silver nanoplates: Synthesis via ostwald ripening and their application in highly sensitive strain sensors", *ACS applied materials & interfaces*, vol. 10, no. 45, pp. 39 134–39 143, 2018.

[18] R. Zhou *et al.*, "Hierarchical synergistic structure for high resolution strain sensor with wide working range", *Small*, vol. 19, no. 34, p. 2 301 544, 2023.

[19] J. Lee *et al.*, "Transparent, flexible strain sensor based on a solution-processed carbon nanotube network", *ACS applied materials & interfaces*, vol. 9, no. 31, pp. 26 279–26 285, 2017.

[20] Y.-C. Qiao *et al.*, "Graphene devices based on laser scribing technology", *Japanese Journal of Applied Physics*, vol. 57, no. 4S, 04FA01, 2018.

[21] T. Li *et al.*, "A flexible strain sensor based on CNTs/PDMS microspheres for human motion detection", *Sensors and Actuators A: Physical*, vol. 306, p. 111 959, 2020.

[22] M. Li, S. Chen, B. Fan, B. Wu, and X. Guo, "Printed flexible strain sensor array for bendable interactive surface", *Advanced Functional Materials*, vol. 30, no. 34, p. 2 003 214, 2020.

[23] Y. Li, T. He, L. Shi, R. Wang, and J. Sun, "Strain sensor with both a wide sensing range and high sensitivity based on braided graphene belts", *ACS applied materials & interfaces*, vol. 12, no. 15, pp. 17 691–17 698, 2020.

[24] S. Tadakaluru, W. Thongsuwan, and P. Singjai, "Stretchable and flexible high-strain sensors made using carbon nanotubes and graphite films on natural rubber", *Sensors*, vol. 14, no. 1, pp. 868–876, 2014.

[25] P. Costa, C Silvia, J. Viana, and S. L. Mendez, "Extruded thermoplastic elastomers styrene–butadiene–styrene/carbon nanotubes composites for strain sensor applications", *Composites Part B: Engineering*, vol. 57, pp. 242–249, 2014.

[26] X. Wu, Y. Han, X. Zhang, and C. Lu, "Highly sensitive, stretchable, and wash-durable strain sensor based on ultrathin conductive layer@ polyurethane yarn for tiny motion monitoring", *ACS applied materials & interfaces*, vol. 8, no. 15, pp. 9936–9945, 2016.

[27] D. Kang *et al.*, "Ultrasensitive mechanical crack-based sensor inspired by the spider sensory system", *Nature*, vol. 516, no. 7530, pp. 222–226, 2014.

[28]   T. Lee, Y. W. Choi, G. Lee, S. M. Kim, D. Kang, and M. Choi, "Crack-based strain sensor with diverse metal films by inserting an inter-layer", *RSC advances*, vol. 7, no. 55, pp. 34 810–34 815, 2017.

[29]   D. Qi, K. Zhang, G. Tian, B. Jiang, and Y. Huang, "Stretchable electronics based on pdms substrates", *Advanced Materials*, vol. 33, no. 6, p. 2 003 155, 2021.

[30]   M. Amjadi, M. Turan, C. P. Clementson, and M. Sitti, "Parallel microcracks-based ultrasensitive and highly stretchable strain sensors", *ACS applied materials & interfaces*, vol. 8, no. 8, pp. 5618–5626, 2016.

[31]   Z. Chu, W. Jiao, Y. Huang, Y. Zheng, R. Wang, and X. He, "Superhydrophobic gradient wrinkle strain sensor with ultra-high sensitivity and broad strain range for motion monitoring", *Journal of Materials Chemistry A*, vol. 9, no. 15, pp. 9634–9643, 2021.

[32]   B. Park *et al.*, "Dramatically enhanced mechanosensitivity and signal-to-noise ratio of nanoscale crack-based sensors: Effect of crack depth.", *Advanced Materials (Deerfield Beach, Fla.)*, vol. 28, no. 37, pp. 8130–8137, 2016.

[33]   T. Yang *et al.*, "Structural engineering of gold thin films with channel cracks for ultrasensitive strain sensing", *Materials Horizons*, vol. 3, no. 3, pp. 248–255, 2016.

[34]   J. Shin *et al.*, "Monolithic digital patterning of polydimethylsiloxane with successive laser pyrolysis", *Nature Materials*, vol. 20, no. 1, pp. 100–107, 2021.

[35]   Z. Ji, D. Jiang, X. Zhang, Y. Guo, and X. Wang, "Facile photo and thermal two-stage curing for high-performance 3D printing of poly (dimethylsiloxane)", *Macromolecular rapid communications*, vol. 41, no. 10, p. 2 000 064, 2020.

[36]   K. Min *et al.*, "Fabrication of perforated PDMS microchannel by successive laser pyrolysis", *Materials*, vol. 14, no. 23, p. 7275, 2021.

[37]   S. Wang *et al.*, "Rapid fabrication of high-performance flexible pressure sensors using laser pyrolysis direct writing", *ACS applied materials & interfaces*, vol. 15, no. 34, pp. 41 055–41 066, 2023.

[38]   T. A. Meinhold and N. Kumar, "Radiation pressure acceleration of protons from structured thin-foil targets", *Journal of Plasma Physics*, vol. 87, no. 6, p. 905 870 607, 2021.

[39]   J. Zhu, X. Wu, J. Jan, S. Du, J. Evans, and A. C. Arias, "Tuning strain sensor performance via programmed thin-film crack evolution", *ACS applied materials & interfaces*, vol. 13, no. 32, pp. 38 105–38 113, 2021.

[40]   G. Camino, S. Lomakin, and M Lageard, "Thermal polydimethylsiloxane degradation. Part 2. The degradation mechanisms", *Polymer*, vol. 43, no. 7, pp. 2011–2015, 2002.

[41]   E. K. Dimitriadis, F. Horkay, J. Maresca, B. Kachar, and R. S. Chadwick, "Determination of elastic moduli of thin layers of soft material using the atomic force microscope", *Biophysical journal*, vol. 82, no. 5, pp. 2798–2810, 2002.

[42] Y. X. Song, W. M. Xu, M. Z. Rong, and M. Q. Zhang, "A sunlight self-healable transparent strain sensor with high sensitivity and durability based on a silver nanowire/polyurethane composite film", *Journal of Materials Chemistry A*, vol. 7, no. 5, pp. 2315–2325, 2019.

[43] T. Kim *et al.*, "Spider-inspired tunable mechanosensor for biomedical applications", *npj Flexible Electronics*, vol. 7, no. 1, p. 12, 2023.

[44] H. A. Mahmoud, H. Nesser, A. Wagih, and G. Lubineau, "Optimizing fragmentation of metallic film for cracked-based strain sensor", *ACS Applied Electronic Materials*, vol. 6, no. 7, pp. 5359–5370, 2024.

[45] Y. Hu *et al.*, "Highly sensitive omnidirectional signal manipulation from a flexible anisotropic strain sensor based on aligned carbon hybrid nanofibers", *Journal of Materials Chemistry A*, vol. 10, no. 2, pp. 928–938, 2022.

[46] S. Zhu *et al.*, "Inherently conductive poly (dimethylsiloxane) elastomers synergistically mediated by nanocellulose/carbon nanotube nanohybrids toward highly sensitive, stretchable, and durable strain sensors", *ACS Applied Materials & Interfaces*, vol. 13, no. 49, pp. 59 142–59 153, 2021.

[47] D. Zhao *et al.*, "Highly sensitive and flexible strain sensor based on AuNPs/CNTs' synergic conductive network", *Applied Nanoscience*, vol. 9, pp. 1469–1478, 2019.

[48] L. Zhao *et al.*, "Laser-patterned hierarchical aligned micro-/nanowire network for highly sensitive multidimensional strain sensor", *ACS Applied Materials & Interfaces*, vol. 14, no. 42, pp. 48 276–48 284, 2022.

[49] S. I. Badrudin, M. M. Noor, M. I. Abd Samad, N. S. N. Zakaria, J. Yunas, and R. Latif, "Eliminating surface cracks in metal film-polymer substrate for reliable flexible piezoelectric devices", *Engineering Science and Technology, an International Journal*, vol. 50, p. 101 617, 2024.

[50] Z. Han *et al.*, "High-performance flexible strain sensor with bio-inspired crack arrays", *Nanoscale*, vol. 10, no. 32, pp. 15 178–15 186, 2018.

[51] S. Li *et al.*, "Contact-resistance-free stretchable strain sensors with high repeatability and linearity", *ACS nano*, vol. 16, no. 1, pp. 541–553, 2021.

4

Selective Reduction Laser Sintering: A New Strategy for NO$_2$ Gas Detection Based on In$_2$O$_3$ Nanoparticles

This chapter introduces a novel strategy for fabricating flexible nitrogen dioxide (NO$_2$) gas sensors based on Indium Oxide (In$_2$O$_3$) nanoparticles (NPs) employing selective reduction laser sintering (SRLS) technology. The SRSL technology utilizes ultraviolet (UV) laser selective reduction sintering to precisely and rapidly create oxygen vacancy (OV) defects in In$_2$O$_3$ NPs. These oxygen vacancies (OVs) enhance the active adsorption sites and contribute additional free electrons, significantly improving sensor performance at room temperature. The sensors exhibit excellent response (S = 460.9 at 10 ppm), rapid response/recovery (τ_{resp}/τ_{reco} = 27/570 s), and superior selectivity (response ratio > 400), in addition to robust light and humidity resistance. Moreover, under photo-assisted conditions, the recovery speed of the sensors is further improved. This technology not only provides an innovative strategy for the development of high-performance flexible NO$_2$ gas sensors but also broadens the application potential of laser direct writing (LDW) technology in advanced materials and sensor fabrications.

4.1. Introduction

THE rapid advancement of flexible sensors has surpassed the constraints of tradi-
tional sensors, becoming increasingly vital in both industrial production and daily
life [3]. In addition to their applications in mechanical, thermoelectric, chemical, neuro-
electric, and electrochemical signal processing, flexible sensors are increasingly empha-
sized for the precise and continuous detection of gas signals [4–8]. Considering power
consumption and operational safety, the development of room temperature (RT) flexi-
ble gas sensors has emerged as a significant trend [9]. The detection of nitrogen dioxide
(NO$_2$) has become critical, reflecting its significant role in environmental health mon-
itoring (EHM). As a major by-product of fossil fuel combustion, NO$_2$ causes acid rain,
photochemical smog, and ozone layer depletion, posing severe environmental risks [10,
11]. Additionally, exposure to NO$_2$ at levels above the 3-ppm threshold is associated
with severe health issues, including lung cancer, stroke, and asthma [12–14]. Therefore,
the development of advanced RT flexible NO$_2$ sensors with excellent response, rapid re-
sponse/recovery, and superior selectivity is an urgent priority.

To enhance the performance of NO$_2$ gas sensors, researchers have explored vari-
ous advanced materials such as metal oxide, conductive polymers, and carbon nano-
materials [15–17]. However, the synthesis of these materials typically involves energy-
intensive, costly, and complex processes such as chemical vapor deposition, chemical
polymerization, and arc discharge [18–20]. In addition, the fabrication of sensors based
on these materials typically requires precisely engineered interdigitated electrodes made
of precious metals such as platinum (Pt), gold (Au), and silver (Ag) [21–23].Indium ox-
ide (In$_2$O$_3$) stands out in applications such as solar cells, photocatalysis, and gas sens-
ing due to its exceptional physical and chemical properties [24–26]. Notably, as an N-
type semiconductor metal oxide, In$_2$O$_3$ exhibits high sensitivity and selectivity for de-
tecting NO$_2$ gas [27]. To further enhance the performance of In$_2$O$_3$-based NO$_2$ sensors,
nanomorphology controls such as nanofibers, nanosheets, and nanoparticles have been
utilized to increase the surface activity of In$_2$O$_3$ [28–30]. Additionally, functional modi-
fications such as constructing heterostructures, nanocomposite, and defect engineering
have been applied to enhance the electronic structures of In$_2$O$_3$ [31–33]. Despite these
advancements, In$_2$O$_3$-based gas sensors still face challenges such as limited gas selec-
tivity, high operating temperature requirements, and performance degradation under
humid conditions, which restrict their broader application [34].

In response to these challenges, laser direct writing (LDW) technology has revolu-
tionized the fabrication of flexible gas sensors with its excellent processing accuracy and
control capability [35]. This technology utilizes a laser beam to precisely remove, add, or
modify both the surface and interior of target materials, achieving high-resolution heat
treatments at the micron or submicron level [36]. Selective laser sintering (SLS), a sub-
set of LDW technology, is widely used for the sintering and modifying of metal, ceramic,
and metal oxide nanoparticles, attributed to its low heat input and high thermal gradi-
ent [37–39]. Meanwhile, this technology allows maskless and customized rapid sintering
processes on various substrates controlled by computer software [40]. Defect engineer-
ing, an effective material modification method, plays a crucial role in optimizing the
properties of sensor materials [41]. For In$_2$O$_3$ nanoparticles, the introduction of oxygen
vacancy (OV) defects not only increases the number of adsorption sites but also modu-

lates the electronic structure, which significantly improves the sensitivity and selectivity of the sensor [42]. However, the efficient fabrication of In_2O_3 NPs with OV defects for flexible NO_2 gas sensing using SLS technology continues to pose a significant challenge.

In this study, we report the development of the flexible NO_2 gas sensor using selective reduction laser sintering (SRLS) technology. This technology selectively reduces polyvinyl pyrrolidone (PVP) coated In_2O_3 nanoparticles (NPs) by controlling the key parameters of an ultraviolet (UV) pulse laser, thereby enabling the formation of OV defects in In_2O_3 NPs. Owing to the introduction of oxygen vacancies (OVs), the sensors demonstrate excellent response (S = 460.9 at 10 ppm), rapid response/recovery (τ_{resp}/τ_{reco} = 27/570 s), and superior selectivity (response ratio > 400) at RT (25 °C). Furthermore, the sensors exhibit robust resistance to light and humidity and an even faster recovery speed under the photo-assisted condition. Through experimental verification and material characterization, the impact of varying laser scanning intervals on the OV defects and sensing performance was further explored. Additionally, the adsorption mechanism of the NO_2 molecule on In_2O_3 with OV was investigated through theoretical calculations. This technology not only provides a new strategy for the fabrication of flexible NO_2 sensors based on In_2O_3 with OVs but also further expands the application prospects of LDW technology in material science and device fabrication.

4.2. EXPERIMENTAL SECTION

Preparation of In_2O_3 NP Paste: Initially, under a constant-temperature (60 °C) ultrasonic environment, 0.1 g of ethylcellulose (EC), 0.1 g cetyltrimethylammonium bromide (CTAB), and 0.9 g of polyvinylpyrrolidone (PVP) were completely dissolved in 7.41 mL of 1-pentanol. Subsequently, 4.9 g of In_2O_3 Nanoparticles (NPs) (particle size < 50 nm) were added to the mixture and mixed using a planetary gravity mixer at 1200 rpm for 60 s. The mixture was then subjected to ultrasonic dispersion at 60 °C for 30 min to ensure complete dispersion of the nanoparticles.

Coating of In_2O_3 NP Paste: PET films (250 μm) were washed sequentially with ethanol and deionized water and blown dry with nitrogen gas. Subsequently, more than 2.5 mL of In_2O_3 NP paste was applied to a 5 cm × 5 cm PET substrate and evenly coated using a four-sided scraper. The coated substrate was then dried at room temperature (25 °C) for 2 h to achieve a uniform In_2O_3 NP layer with a thickness of 30 μm.

Sensor Fabrication: Flexible NO_2 gas sensors were fabricated using selective reduction laser sintering (SRLS) technology with a UV pulse laser system. The system consists of a computer-aided design module, a 355 nm UV laser source (3 W), a galvanometer system, and an F-theta lens (f = 103 mm). The laser scanning speed (V_{ss}) was set to 10 mm/s, the average laser power (P_{avg}) to 0.27 W, the pulse repetition frequency (F_{pr}) to 200 kHz, and the defocus distance (D_{def}) to 0 mm. During the sensor fabrication process, the laser scanning interval was set to 70 μm, the number of laser linear scans was 2 times, and the corresponding effective adsorption area of the sensor region was about 0.4 cm^2. After sintering, the sensor was cleaned in deionized water to remove unsintered paste and dried in an oven at 60 °C for 10 minutes. Sensor electrodes were screen printed using low-temperature silver paste and cured at 60 °C for 15 min.

Sensor Testing: The target NO_2 gas concentration was achieved by diluting a 100 ppm NO_2 commercial calibration gas with dry air in an 8 L mixing chamber. All gas-sensing

tests were carried out at room temperature (RT) and standard atmospheric pressure. The sensor was tested by passing dry air, target concentration of NO$_2$ gas, and dry air sequentially through the test chamber to evaluate its gas sensing response. Real-time response data were collected using a Keithley 2450 source meter, and ambient relative humidity (RH) was monitored with a commercial humidity sensor (SHT3x-DIS, Sensirion).

Material Characterization: Particle size and crystalline phase of In$_2$O$_3$ NPs were analyzed using transmission electron microscopy (TEM, JEM-2100Plus, JEOL). The morphology of the sensing region was evaluated using scanning electron microscopy (SEM, ZEISS Gemini 300, and Regulus 8100) and 3D laser confocal microscopy (VK-X1000, KEYENCE). Thermogravimetric/differential thermogravimetry (TG/DTG) analysis was carried out in an air atmosphere using a simultaneous thermal analyzer (TGA, STA 449C, NETZSCH), with a heating rate of 10 °C /min from 25 to 1000 °C. Differential scanning calorimetry (DSC) analysis was conducted in both air and vacuum environments using a differential scanning calorimeter (HDSC PT1600-Linseis), employing varying heating rates of 10, 20, and 50 °C/min from 25 to 800 °C. Raman spectroscopy was conducted using a 532 nm laser (Raman, LabRAM HR Evolution, HORIBA), and X-ray photoelectron spectroscopy (XPS, Thermo Scientific K-Alpha) analyzed the surface composition and valence state. Electron paramagnetic resonance (EPR, EMX-PLUS, Bruker) was used to characterize the defect state of the material within the sensing region at room temperature with a modulation frequency of 100 kHz and a power of 1 mW. The sensor photoresponse characteristics were evaluated using an adjustable monochromatic light source (TLS130B-300X).

Computational Method: All calculations of structural relaxations and electronic properties in this work were performed using the density functional theory (DFT) based on the DMol^3 package in Materials Studio. The exchange-related energy was calculated using the generalized approximate gradient (GGA) and Perdew-Burke-Ernzerhof (PBE) functions. Double numerical polarization (DNP) was chosen as the basis group function of the linear combination of atomic orbitals. The convergence tolerances for optimization were 1×10^{-5} Ha/atom (energy), 2×10^{-3} Ha/Å (gradient), and 5×10^{-3} Å (displacement). A grid of $3 \times 3 \times 1$ Monkhorst-Pack k-point was applied throughout the calculations. To obtain correct total energy values in static electronic structure simulations, a global orbital cutoff of 5.0 Å was assigned. For the In$_2$O$_3$ bulk, an In$_2$O$_3$ with five atomic layers and 1×1 unit cells was used as the model system, where three atomic layers were kept constrained during optimizations. A vacuum layer of 30 Å was added to separate neighboring bulks to avoid possible interaction. Meanwhile, the initial adsorption distance before the optimization was set to 2 Å.

To more reliably analyze the adsorption stability of NO$_2$ gas molecules on In$_2$O$_3$, the adsorption energy (E_{ad}) is calculated by the equation:

$$E_{ad} = E_{gas/substrate} - E_{gas} - E_{substrate} \tag{4.1}$$

where E_{gas}, $E_{substrate}$, and $E_{gas/substrate}$ are the total energy of the gas (NO$_2$), substrate (In$_2$O$_3$ with and without OV), and gas/substrate (the system after adsorption), respectively. To understand the electronic interaction and quantify the amount of charge transfer between NO$_2$ and In$_2$O$_3$ bulk, the charge density difference is calculated the equation:

$$\Delta\rho = \rho_{\text{gas/substrate}} - \rho_{\text{gas}} - \rho_{\text{substrate}} \qquad (4.2)$$

where $\rho_{\text{gas/substrate}}$, ρ_{gas}, and $\rho_{\text{substrate}}$ are the total charge density of the NO_2/In_2O_3 system, target gas molecule, and In_2O_3 bulk, respectively.

4.3. RESULTS AND DISCUSSION

4.3.1. INVESTIGATION OF THE SRLS PROCESS

Unlike traditional selective laser sintering (SLS), where the laser is directly applied to the material surface to achieve high-temperature solid-phase transformation, selective reduction laser sintering (SRLS) achieves nanoparticle sintering by finely adjusting the temperature distribution at the edges of the laser scanning path [43]. As shown in Figure 4.1(a), the fabrication of the flexible gas sensors using this technology consists of four main steps: blade coating, laser sintering, surface cleaning, and electron printing. The detailed methodology of this fabrication process is described in the Experimental Section. In the most critical laser sintering process, In_2O_3 NPs serve as both a crucial material for flexible gas sensors and as an essential coating for triggering the photothermal effect. It is well known that polyethylene terephthalate (PET) has a relatively low absorption coefficient for UV lasers. Therefore, when the laser is vertically irradiated onto PET films, most of the laser energy passes through without causing any noticeable physical or chemical reaction. However, when the PET surface is coated with In_2O_3 NPs, the In_2O_3 layer absorbs UV laser energy and rapidly converts it into thermal energy. This conversion triggers a significant pyrolysis reaction on the shallow surface of PET through the photothermal effect. Under UV irradiation, the high energy density of the laser leads to the ablation of the In_2O_3 layer and the underlying PET substrate, forming a laser-ablated region. At the same time, the high temperature generated by the laser-ablated region causes the unirradiated In_2O_3 NPs to undergo rapid thermal sintering at the edge of the laser scanning path, forming a distinct laser-sintered region. In contrast, regions that have not been ablated and sintered can be easily removed by deionized water cleaning (Figure 4.1(b)).

The composition of In_2O_3 nanoparticle (NP) paste, primarily consisting of active and carrier materials, is crucial for the formation of OV defects during the SRLS process. Detailed explanations of the active material and the carrier material are provided in the Supporting Information (Section C.1). Building on this, the thermal properties of In_2O_3 NP paste and its carrier were analyzed using thermogravimetric/derivative thermogravimetric (TG/DTG) and differential scanning calorimetry (DSC) to investigate the formation mechanism of OV defects. After comparative analysis, the thermal weight loss of In_2O_3 NP paste at a low heating rate (10 °C/min) was summarized into three main stages (Figure C.4). The process initiates with the evaporation of organic solvents within the temperature range of 30-170 °C. This is followed by the decomposition of polyvinylpyrrolidone (PVP) side chains, occurring between 170-300 °C. The final stage involves the critical breakdown of the PVP backbone, which occurs from 300-550 °C. In the final stage, reduced macromolecules generated by the decomposition of the PVP main chain partially reduce In_2O_3 to metallic indium (In) while forming OV defects [44]. This provides a certain reference for further understanding the mechanism of the SRLS
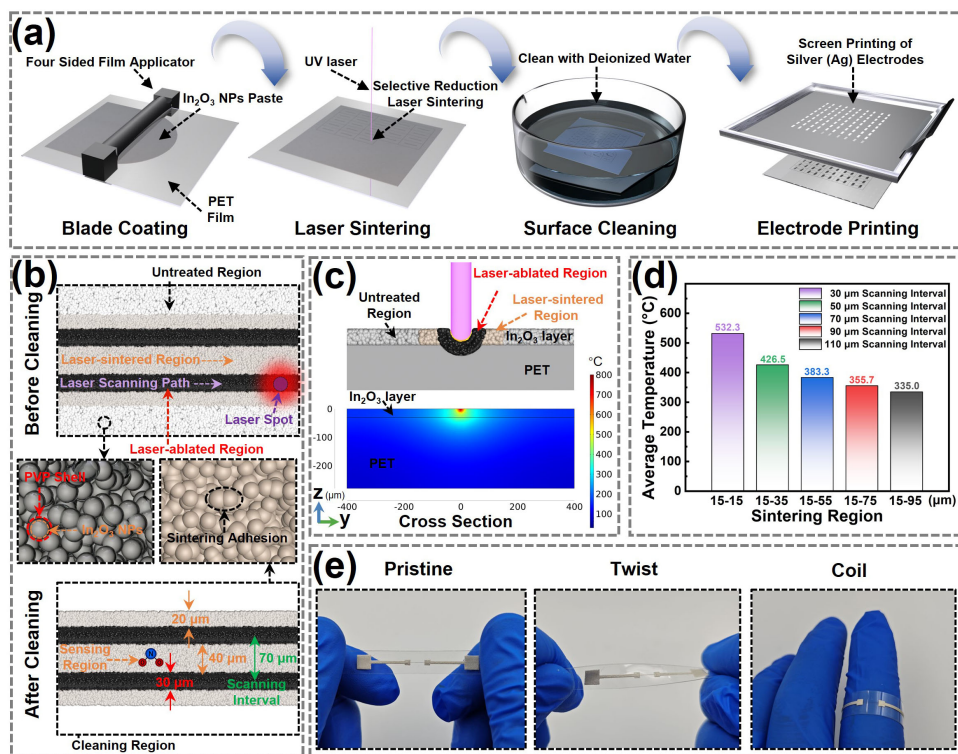
Figure 4.1: The fabrication process of flexible NO₂ gas sensors based on the SRLS technology. (a) Schematic diagram of the sensor fabrication process. (b) Schematic illustration of the structural changes on the surface of In₂O₃ NPs due to laser sintering. (c) Schematic structure and temperature distribution of the sensor cross-section during laser sintering. (d) Histogram of equivalent average sintering temperatures for laser-sintered regions with different scanning intervals. (e) Demonstration of the sensor in different deformation states.

with high temperature gradient. Detailed analyses of the TG/DTG and DSC are presented in the Supporting Information (Section C.2).

To explore the effects of various laser parameters on the SRLS process, a series of experimental optimizations were performed using a UV laser system (Figure C.7). The experiments focused on finely tuning key parameters such as laser scanning speed (V_{ss}), average laser power (P_{avg}), pulse repetition frequency (F_{pr}), and defocus distance (D_{def}), all of which are closely related to the sensor performance and fabrication efficiency. Given the importance of both magnitude and stability in the initial resistance of the sensing region, the optimal laser parameters were set to 10 mm/s for V_{ss}, 0.27 W for P_{avg}, 200 kHz for F_{pr}, and 0 mm for D_{def} (Figure C.10). Detailed parameter optimization and implementation of the SRLS process are provided in the Supporting Information (Section C.3).

To achieve OV defect control, the critical sintering temperature in the SRLS process is precisely controlled by the laser scanning interval. However, the high energy density and rapid scanning speed of UV lasers present significant challenges in monitoring the

real-time temperature during the SRLS process. To further calibrate the influence of the laser scanning interval on the sintering temperature, finite element analysis (FEA) was used to simulate the temperature distribution and evolution within the In_2O_3 layer and PET substrate during the single laser scanning process. The cross-sectional temperature distribution at the midpoint of the linear laser scanning reveals that the photothermal effect of the laser generates a high-temperature region exceeding 800°C at the top center of the model, with a sharp decrease in temperature along the y- and z-axes, as shown in Figure 4.1(c). This temperature distribution radiates outward from the center of the heat source, forming a high-temperature region and temperature diffusion regions on either side of it, corresponding to the laser ablation and laser-sintered regions (70 µm scanning interval). The equivalent average temperatures of the laser-sintered region on one side of the laser scanning are 523.3 °C, 426.5 °C, 383.3 °C, 355.7 °C, and 335.0 °C at various scanning intervals, with corresponding effective sintering close intervals of 15-15 µm, 15-35 µm, 15-55 µm, 15-75 µm, and 15-95 µm (Figure 4.1(d)). Detailed simulation model construction and discussion of the temperature distribution and evolution during linear laser scanning are provided in the Supporting Information (Section C.4).

Benefiting from the high energy density and rapid scanning speed of the laser, the SRLS technology offers more flexible customization while significantly reducing the temperature requirements of the substrate material. This technology enables the rapid fabrication of flexible gas sensors on 0 µm thick PET films, ensuring excellent sensing performance while maintaining stable mechanical properties (Figure 4.1(e)).

4.3.2. CHARACTERIZATION OF OV DEFECTS

To investigate the effect of different laser scanning intervals on the crystal structure and phase transition of In_2O_3 NPs in the SRLS treatment, X-ray diffraction (XRD) patterns were employed to characterize the samples with untreated, 50 µm, 70 µm, and 90 µm scanning intervals (Figure 4.2(a)). The XRD pattern of untreated In_2O_3 NPs indicates characteristic peaks at 30.6°, 35.5°, 51.0°, and 60.7°, corresponding to the (222), (400), (440), and (622) crystal planes (PDF#06-0416). However, the SRLS-treated In_2O_3 NPs exhibit both peaks for In_2O_3 and new peaks for metallic In at 32.9°, 36.3°, 39.2°, and 54.4° (PDF#70-2888). The transition from In_2O_3 to metallic In is clearly evident from the comparison of the overall peak intensities in the XRD spectra. It is noteworthy that the intensities of the metallic In peaks near the (321) and (400) crystal planes increase significantly with decreasing laser scanning intervals in the diffraction angle range from 30° to 40° (Figure 4.2(b)). In addition, normalization of the effective area of the laser scanning region shows that the intensity ratio of diffraction peaks of metal In to In_2O_3 near the (321) crystal plane increases significantly with decreasing scanning intervals (Figure 4.2(c)). These results indicate that the transformation of In_2O_3 to metallic In during the SRLS process is further promoted by the increase in sintering temperature with the decrease in laser scanning interval. Furthermore, local XRD patterns reveal that the diffraction peaks near the (321) crystal plane of In_2O_3 shift to a lower 2θ angle as the sintering temperature increases due to a decrease in the scanning interval (Figure C.17) [45–47]. This shift indicates an expansion of the interplanar spacing in the In_2O_3 crystal, leading to a relaxation of the lattice structure [48]. Notably, this also indicates that indium ions in In_2O_3 have been reduced to lower valence or even metallic states, implying the genera-

tion of OV defects [49, 50]. Detailed discussions and localized XRD spectra of the In$_2$O$_3$ NP paste before and after SLRS treatment are provided in the Supporting Information (Section C.5)
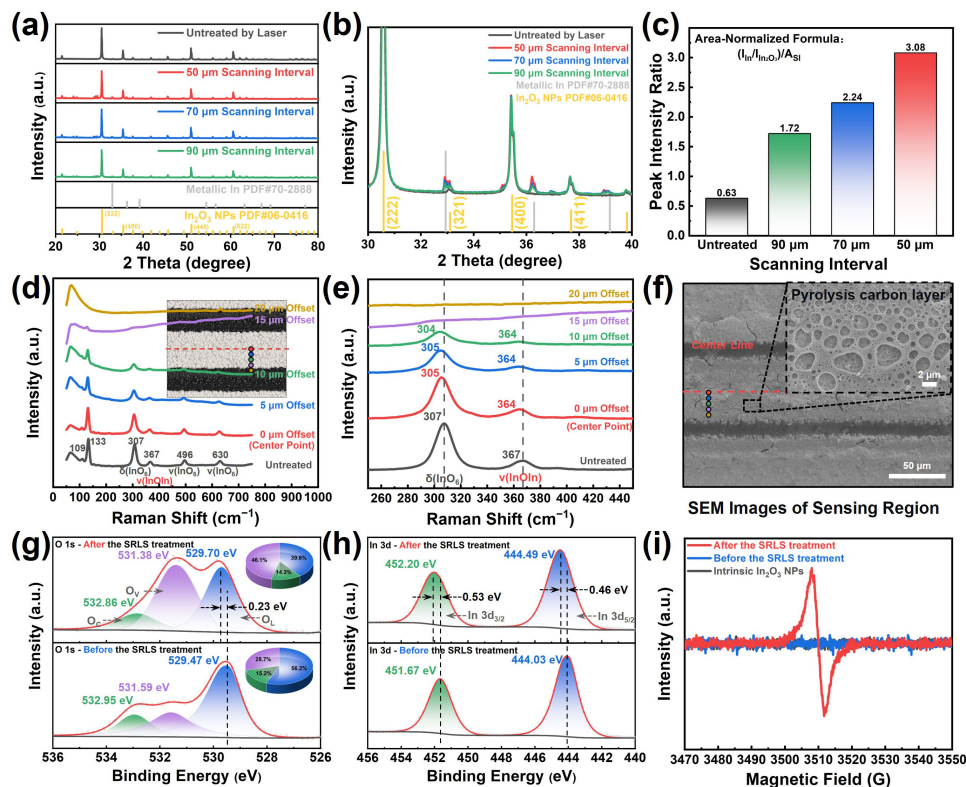

Figure 4.2: Characterization of OV defects in In$_2$O$_3$ NPs. (a) Overall and (b) local XRD patterns of In$_2$O$_3$ before and after the SRLS treatment. (c) Ratio of area-normalized peak intensities in In$_2$O$_3$ XRD patterns at different laser scanning intervals. (d) Overall and (e) local Raman spectra of In$_2$O$_3$ at different points within the laser-sintered region. (f) SEM images of the laser-sintered region.(g) O 1s and (h) In 3d XPS spectra of In$_2$O$_3$ before and after the SRLS treatment. (i) EPR spectra of In$_2$O$_3$ before and after the SRLS treatment.

To analyze the structure and composition of In$_2$O$_3$ NPs after the SRLS treatment (70 μm scanning interval), Raman spectroscopy was employed to characterize different points within the sensing region on the side perpendicular to the scanning direction, as shown in Figure 4.2(d). Raman spectra were collected at five points spaced 5 μm apart from the center of the sensing region within the wavelength range of 50-750 cm^{-1} (Figure C.21). For comparison, the Raman spectra of pure In$_2$O$_3$, PVP, and PET are presented in the Supplementary Information (Figure C.22). Besides the ultra-low frequency peak at 66 cm^{-1} from PET substrates, untreated In$_2$O$_3$ NPs exhibit six prominent peaks at 109 cm^{-1}, 133 cm^{-1}, 307 cm^{-1}, 367 cm^{-1}, 496 cm^{-1}, and 630 cm^{-1}, providing insights into the vibrational modes and properties of In$_2$O$_3$ [51]. In the lower frequency range, the lattice vibrational peaks at 109 cm^{-1} and 133 cm^{-1} indicate large-scale motions involving

the In atoms or the entire lattice structure [52]. The peak at 307 cm^{-1} correlates with the symmetric bending vibrations of δ(InO$_6$) octahedra [53]. Similarly, the peaks at 496 cm^{-1} and 630 cm^{-1} are associated with asymmetric stretching vibrations of ν(InO$_6$) octahedra [50].

Notably, the 367 cm^{-1} scattering feature, identified as ν(InOIn) stretching vibrations, indicates the presence of OV defects in the In$_2$O$_3$ lattice [47, 54]. After the SRLS treatment, the Raman spectra of In$_2$O$_3$ show a slight red shift in characteristic peaks, indicating the formation of OV defects. These defects lead to the expansion and local relaxation of the In$_2$O$_3$ lattice structure and the weakening of the In-O bond. Consequently, the reduced bonding strength alters the vibrational mode of the In-O-In bridge, resulting in a shift of the Raman peak to a lower wavelength (Figure 4.2(e)) [55]. Furthermore, Raman spectra collected at 0, 5, and 10 μm offset points show a gradual decrease in overall relative peak intensity closer to the laser scanning region. Even more, the Raman spectra of the 15 and 20 μm offset points show significant anomaly. Scanning electron microscopy (SEM) characterization reveals that the PET substrate is slightly melted in the laser scanning region due to the photothermal effect (Figure 4.2(f)). The sputtering of molten PET onto In$_2$O$_3$ NPs near the laser-ablated region formed a porous pyrolytic carbon layer, which interferes with Raman spectra analysis [56]. Detailed analyses of Raman spectra, SEM, and energy dispersive X-ray (EDX) of the laser-sintered region are provided in the Supporting Information (Section C.5).

To further determine the chemical composition and defect state of the In$_2$O$_3$ NPs before and after the SRLS process (70 μm scanning interval), the sensing region was analyzed by X-ray photoelectron spectroscopy (XPS). The full XPS survey reveals significant changes in the intensity of the binding energy peaks of In, O, and C elements before and after the SRLS treatment (Figure C.25). After the SRLS treatment, the intensities of the In 3d and O 1s peaks decreased significantly, while the intensity of the C 1s peak increased, demonstrating the formation of pyrolytic carbon on the surface of the laser-sintered region. Furthermore, before the SRLS treatment, the O1s peaks at 529.47 eV, 531.59 eV, and 532.95 eV correspond to different oxygen species in In$_2$O$_3$ NPs: lattice oxygen (O$_L$), oxygen vacancy (O$_V$), and chemisorbed oxygen (O$_C$), respectively (Figure 4.2(g)) [47, 57]. After the SRLS treatment, the O$_L$ peak shifts to 529.70 eV, a positive shift of 0.23 eV. This shift indicates electronic interactions between polyvinylpyrrolidone (PVP) and In$_2$O$_3$, suggesting that the pyrolysis products of PVP contribute to the reduction and removal of lattice oxygen from In$_2$O$_3$, thereby reducing the average oxidation state in the O 1s peak [58]. Specifically, the relative peak area ratio of O$_L$ decreases from 56.2% to 39.6%, reflecting a decrease of 16.6%. Conversely, the OV peak area ratio increases from 28.7% to 46.1%, representing a significant increase of 17.4% (pie chart in Figure 4.2(g)). This directly demonstrates a significant increase in the density of OV defects after the SRLS treatment [50]. Furthermore, compared to the sensing region before the SRLS treatment, the In 3d$_{5/2}$ and 3d$_{3/2}$ XPS peaks of the In$_2$O$_3$ exhibit positive shifts of 0.46 eV and 0.53 eV, respectively (Figure 4.2(h)). This suggests electron transfer from In$_2$O$_3$ to pyrolytic carbon in the PVP pyrolysis product, thus dispersing electron density around In atoms [55].

Additionally, the electron spin resonance (EPR) results reveal that the In$_2$O$_3$ NPs after the SRLS treatment exhibit a signal at a g-value of 2.03, which suggests that the electrons

are trapped in the OV defects generated by the reduction of In$_2$O$_3$ by pyrolysis products during the SRLS process (Figure 4.2(i)). This result further confirms the presence of OV defects in In$_2$O$_3$ after the SRLS treatment [59]. The methodology and process for calculating the g-value are introduced in the Supporting Information (Section C.5).

4.3.3. TESTING OF SENSOR PERFORMANCE

Variations in sintering temperature due to different laser scanning intervals (30, 50, 70, 90, and 110 μm) significantly affect the performance of N-type chemoresistive gas sensors based on In$_2$O$_3$ NPs during the SRLS process. To evaluate this effect, the sensor was exposed to a specific NO$_2$ gas concentration for 30 s at RT (Figure C.30). The relative response of the gas sensor is quantified as $S = \Delta R/R_0 = (R - R_0)/R_0$, where R and R_0 represent the stabilized resistance in the target gas and air environments, respectively. The response (τ_{resp}) and recovery (τ_{reco}) times are defined as the times required to achieve a 90% change in resistance when exposed to NO$_2$ and air [60]. Test results show that sensor resistance spikes sharply when exposed to 10 ppm NO$_2$ and then gradually recovers in the air. Interestingly, as the sintering temperature increases with decreasing laser scanning interval, the sensor response to NO$_2$ decreases significantly with values of 967.62, 802.16, 442.24, 19.69, and 18.27, respectively (Figure 4.3(a)). Higher sintering temperatures lead to an increase in OV defects, which theoretically should enhance the ability of NO$_2$ to capture electrons within the sensing region, thereby promoting a significant increase in sensor resistance change (ΔR) [61, 62]. However, narrower scanning intervals increase the baseline resistance (R_0) of the sensor (Figure C.30 and C.31). Consequently, the sensing gain from the increase in OV defects is counteracted by the increase in baseline resistance, which significantly reduces the sensor response to NO$_2$. On the other hand, a larger scanning interval enlarges the effective adsorption area of the sensor, offering more sites for adsorption but also extending the desorption time, which slows down the recovery ability of the sensor [63, 64]. Additionally, the lower sintering temperature associated with an increased scanning interval reduces the adhesion between the In$_2$O$_3$ NP layer and the PET substrate, challenging the stability and reliability of the sensor [65]. To balance performance and stability, the sensor with a 70 μm scanning interval was selected for further evaluation.

The sensor exhibits rapid response and recovery times of 27 s and 570 s for 10 ppm NO$_2$ at RT, as shown in Figure 4.3(b). Additionally, the sensor also consistently detects 5 ppm NO$_2$ over five cycles, demonstrating high repeatability and reversibility (Figure 4.3(c)). Furthermore, as NO$_2$ concentrations increase from 2 to 10 ppm, the sensor response gradually increases from 9.8 to 460.9, indicating excellent dynamic response capabilities (Figure 4.3(d)). Correspondingly, the linear response of the sensor for NO$_2$ concentrations ranging from 2 to 10 ppm exhibits a slope of 56.91 ppm^{-1} and an R^2 of 0.985, demonstrating stable linear response characteristics (Figure 4.3(e)). Notably, the response of the sensor to 10 ppm NO$_2$ (response ratio > 400) is significantly stronger than its response to 100 ppm of the interfering gases (C$_2$H$_5$OH, CO$_2$, C$_3$H$_6$O, NH$_2$, CH$_4$, and H$_2$S), proving its superior selectivity (Figure 4.3(f)). Compared to other In$_2$O$_3$-based NO$_2$ gas sensors, those fabricated using SRLS technology not only offer flexibility, efficiency, and customization but also demonstrate superior performance (Table C.1).

Considering the practical application of the sensor, the impact of environmental fac-
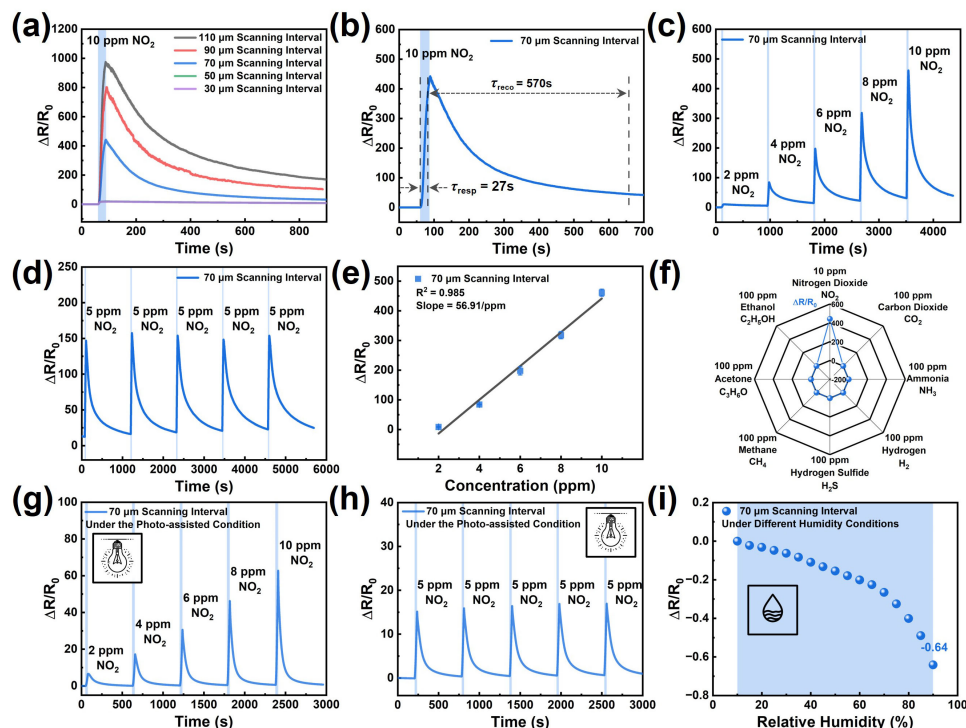
Figure 4.3: Performance testing of sensors based on SRLS technology. (a) Response curves of the sensor to 10 ppm NO₂ with different scanning intervals. (b) Typical response curve of the sensor. (c) Repeatability response curve of the sensor to 5 ppm NO₂ over five consecutive cycles. (d) Dynamic response curve of the sensor to NO₂ from 2 to 10 ppm. (e) Linear fit curve of the sensor response to NO₂ from 2 to 10 ppm with error bars representing three samples. (f) Radar chart of the sensor selectivity for NO₂ compared to other interfering gases. (g) Dynamic response curve of the sensor to NO₂ from 2 to 10 ppm under the photo-assisted condition. (h) Repeatability response curve of the sensor to 5 ppm NO₂ over five consecutive cycles under the photo-assisted condition. (i) Response curve of the sensor to relative humidity from 10% to 90%.

tors such as light and humidity on the sensor performance was further evaluated. Unsurprisingly, flexible gas sensors based on In_2O_3 NPs with OV defects demonstrate excellent NO_2 gas detection performance along with inherent optoelectronic properties [60]. Under the photo-assisted condition (xenon lamp irradiation), the resistance of the sensor decreases due to light-induced electronic excitation. This excitation promotes the transition of electrons from the valence band to the conduction band, leading to the formation of additional electron-hole pairs and enhancing the electrical conductivity of the sensor [65]. Additionally, OV defects in In_2O_3 serve as trapping centers for electrons or holes, stabilizing and extending the lifetimes of photogenerated carriers. This trapping effect reduces the electron-hole recombination rate, further reducing the resistance of the sensor [66]. Under the photon-assisted condition, the sensor demonstrates excellent consistency and reversibility in response to five consecutive 5 ppm NO_2 at RT (Figure 4.3(g)). Meanwhile, the photon-assisted response of the sensor gradually increased from

6.6 to 62.7 as the concentration of NO_2 increased from 2 ppm to 10 ppm, demonstrating its robust dynamic response and recovery under bright light (Figure 4.3(h)). Importantly, although photon assistance significantly reduces the response of the sensor to NO_2, the photon-assisted sensing mechanism enhanced the half-recovery speed by 91.7% in low NO_2 concentration detection (Figure C.32). These properties not only demonstrate the light resistance of the sensor but also further expand its application potential in continuous NO_2 sensing applications.

Given the inherent sensitivity of semiconductor materials to humidity, the response of the sensor to different relative humidity (RH) conditions was further evaluated (Figure 4.3(i)) [66, 67]. As the relative humidity increases, the relative resistance of the sensor decreases, and the sensor response to humidity is only 0.64, even in high-humidity environments (90% RH). Benefiting from the excellent response characteristics of the sensor, the effect of humidity on the sensor is essentially negligible. These features are further evidence of the potential benefits of the sensors in practical applications. Detailed descriptions of the sensing test platform and test details are provided in the Supporting Information (Section C.6).

4.3.4. ANALYSIS OF SENSING MECHANISM

The primary sensing mechanism of NO_2 gas sensors based on In_2O_3 NPs fabricated by SRLS technology is driven by conductivity changes resulting from the adsorption and desorption of gas molecules on the sensor surface. Specifically, the OVs on the surface of In_2O_3 NPs play a crucial role in facilitating this mechanism. These defects enable electrons to transition from the valence band to the conduction band, thereby increasing the concentration of free electrons and enhancing the conductivity of the sensing region [68]. Concurrently, these defects offer active sites in the sensing region, thereby increasing the adsorption of oxygen species [69]. When the sensor is exposed to an air atmosphere, the oxygen (O_2) molecules adsorb onto the surface of In_2O_3 NPs and capture free electrons from the conduction band to form O_2^- (gas) ions with higher chemical activity, as detailed in reaction equations (4.3) and (4.4) [70].

$$O_2(\text{gas}) \leftrightarrow O_2(\text{ads}) \tag{4.3}$$

$$O_2(\text{ads}) + e^- \rightarrow O_2^-(\text{ads}) \tag{4.4}$$
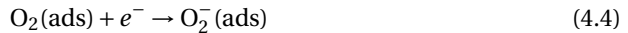
This reaction process depletes the carrier concentration on the surface of In_2O_3, causing the energy bands to bend upwards and forming a surface electron depletion layer (Figure 4.4(a)). When the sensor is exposed to a NO_2 gas atmosphere, the NO_2 molecules interact directly with the electrons in the conduction band of In_2O_3 to form NO_2^-(ads) ions, driven by their high electron affinity [71]. Additionally, these NO_2 molecules can also react with pre-existing O_2^-(ads) ions to form NO_3^- ions, as described in the reaction equations (4.5) and (4.6)[70].

$$NO_2(\text{ads}) + e^- \rightarrow NO_2^-(\text{ads}) \tag{4.5}$$

$$O_2(\text{ads}) + 2NO_2(\text{ads}) \rightarrow 2NO_3^-(\text{ads}) \tag{4.6}$$
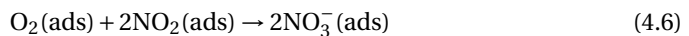
This reaction process further deepens the electron depletion layer on the In_2O_3 surface, which enhances the upward bending of the energy bands and significantly increases the resistance of the In_2O_3 NPs. Furthermore, both of these processes deplete the conduction band electrons in In_2O_3 NPs, resulting in an increased thickness of the electron depletion layer and an elevated potential barrier energy. However, due to its strong oxidizing properties, NO_2 tends to play a dominant role in the reactions at RT, which significantly increases the resistance of the sensor and enables the detection of NO_2 gas [72].
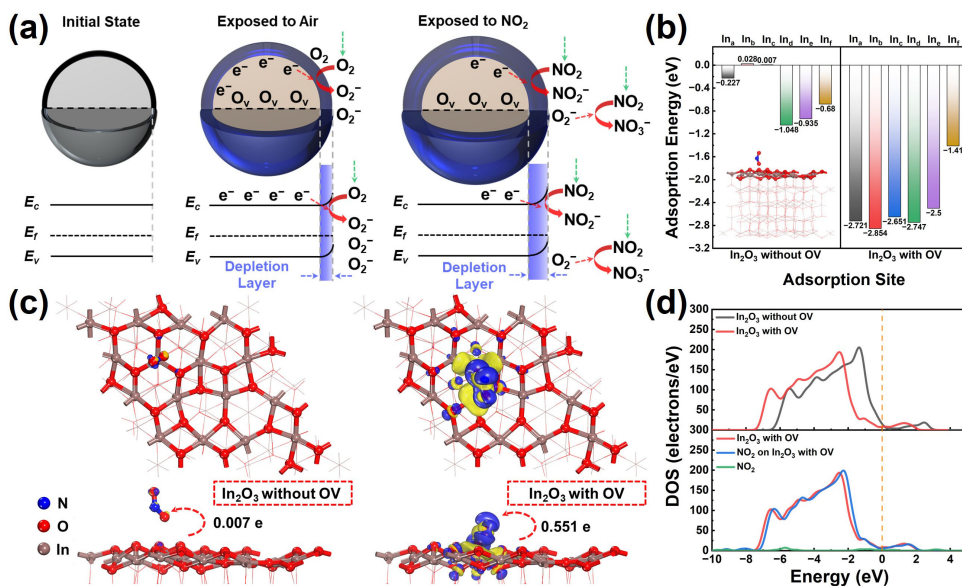
Figure 4.4: Senning mechanisms of NO_2 on In_2O_3 sensors with OV defects. (a) Schematic diagram of the sensing mechanism. (b) Histograms of adsorption energy in different adsorption systems and different adsorption modes. (c) CDD distributions of In_2O_3 with and with OV after NO_2 adsorption (The isosurface is set as 0.01 e/Å^3. The blue region indicates electron accumulation, and the yellow region represents electron depletion. (d) DOS curves of In_2O_3 with and without OV, and DOS curves of In_2O_3 with OV before and after NO_2 adsorption.

To further investigate the adsorption mechanism of NO_2 molecules on In_2O_3 and the role of OVs in enhancing this process, we performed a detailed computational analysis using density functional theory (DFT). Compared to In_2O_3 without OV, In_2O_3 with OV shows a stronger adsorption reaction to NO_2 molecules at various adsorption modes (Figure 4.4(b)). In particular, the presence of OV at the In_{22} site in the Inb adsorption mode significantly enhances its adsorption capacity. This enhancement is thoroughly compared and analyzed using charge density difference (CDD) and density of states (DOS) calculations. The CDD results show that the interaction of the NO_2 molecule in the In_2O_3 adsorption system without OV not only causes a slight electron accumulation of O atoms on the In_2O_3 surface but also leads to a subtle charge rearrangement inside the NO_2 molecule (Figure 4.4(c)). In this process, NO_2 acts as an electron acceptor, receiving 0.07 e from the In_2O_3 as determined by Mulliken charge analysis [73]. The

corresponding adsorption energy of 0.028 eV indicates that the reaction in this adsorption mode (In$_b$) is not spontaneous (Table C.3). This positive adsorption energy further demonstrates the limitations of intrinsic In$_2$O$_3$ in adsorbing NO$_2$ molecules [74]. Conversely, in the In$_2$O$_3$ adsorption system with OV, the CDD results reveal a more intense electronic interaction induced by the adsorption of the NO$_2$ molecule on the In$_2$O$_3$ surface. Specifically, the adsorption of the NO$_2$ molecule leads to the formation of large-volume electron depletion regions between it and three neighboring In atoms of In$_2$O$_3$. Additionally, the N and O atoms of NO$_2$ exhibit distinct electron accumulation regions, while an overall electron depletion region is demonstrated around the N-O bonds. In this process, the NO$_2$ serves as an electron acceptor, receiving 0.551 e from the In$_2$O$_3$, which indicates the formation of chemical solid adsorption between the NO$_2$ and the In$_2$O$_3$ with OV [75]. Moreover, the corresponding adsorption energy of -2.854 eV confirms that the adsorption process is exothermic, indicating its spontaneous nature and highlighting a clear contrast with intrinsic In$_2$O$_3$ (Table C.4).

By comparing the DOS curves of In$_2$O$_3$ with and without OV, it is clear that the introduction of OV shifts the DOS curve toward lower energy levels and flattens the curves near the Fermi level (Figure 4.4(d)). This shift indicates that the introduction of the defect state creates localized states within the band gap of In$_2$O$_3$, which increases the density of electronic states and introduces intermediate energy levels [76, 77]. This enhancement not only reduces the energy required for electron excitation from the valence to the conduction band but also provides additional electrons and transition pathways [78]. Furthermore, when the NO$_2$ molecule is adsorbed on the surface of In$_2$O$_3$ with OV, the DOS curve for the corresponding system shifts slightly to higher energy, and the density of electronic states near the Fermi level decreases. This change confirms that NO$_2$ adsorption promotes electron transfer from the In$_2$O$_3$ surface to the NO$_2$ molecule, resulting in charge redistribution and rearrangement of energy levels [79]. Overall, these results clearly demonstrate the substantial potential of OV in improving the sensitivity of NO$_2$ gas sensors based on In$_2$O$_3$ NPs fabricated by SRLS technology and provide a solid theoretical basis for understanding the sensing mechanism. The classification of different adsorption modes, the corresponding adsorption sites, adsorption energies, adsorption distances, and charge transfer are discussed in the Supporting Information (Section C.7).

4.4. CONCLUSION

In summary, we have successfully developed a selective reduction laser sintering (SRLS) technology based on In$_2$O$_3$ NPs to fabricate flexible NO$_2$ sensors efficiently. This technology employs a UV laser to selectively reduce PVP-coated In$_2$O$_3$ NPs spin-coated on PET substrates to prepare In$_2$O$_3$ sensing regions with oxygen vacancy (OV) defects. These OV defects significantly enhance the active adsorption sites, thereby increasing the NO$_2$ capture rate and introducing additional free electrons, thereby increasing the conductivity of the sensor. Due to the advantages of these properties, In$_2$O$_3$ NPs with OV defects exhibit outstanding NO$_2$ sensor performance at room temperature. These sensors not only demonstrate exceptional response values, fast response/recovery, and superior selectivity, but they also exhibit robust light and humidity resistance. Additionally, the recovery speed of the sensor can be further enhanced under the photo-assisted

condition. This work proposes a new strategy for developing high-performance flexible NO_2 sensors and provides key insights into the mechanism of NO_2 adsorption by In_2O_3 NPs with OVs, paving the way for the development of flexible gas sensors for environmental health monitoring (EHM).

REFERENCES

[1] S. Wang, Q. Zong, H. Yang, Q. Huang, H. Ye, and P. French, "Advanced NO2 gas sensor fabrication through UV laser-induced selective reduction laser sintering", in *2024 IEEE 19th International Conference on Nano/Micro Engineered and Molecular Systems (NEMS)*, IEEE, 2024, pp. 1–4.

[2] S. Wang *et al.*, "Selective reduction laser sintering: A new strategy for NO2 gas detection based on In2O3 nanoparticles", *Advanced Functional Materials*, p. 2 419 057, 2025.

[3] M. Javaid, A. Haleem, S. Rab, R. P. Singh, and R. Suman, "Sensors for daily life: A review", *Sensors International*, vol. 2, p. 100 121, 2021.

[4] A. Sharma, M. Z. Ansari, and C. Cho, "Ultrasensitive flexible wearable pressure/strain sensors: Parameters, materials, mechanisms and applications", *Sensors and Actuators A: Physical*, vol. 347, p. 113 934, 2022.

[5] Q. Li, L.-N. Zhang, X.-M. Tao, and X. Ding, "Review of flexible temperature sensing networks for wearable physiological monitoring", *Advanced healthcare materials*, vol. 6, no. 12, p. 1 601 371, 2017.

[6] Aaryashree, S. Sahoo, P. Walke, S. K. Nayak, C. S. Rout, and D. J. Late, "Recent developments in self-powered smart chemical sensors for wearable electronics", *Nano Research*, vol. 14, pp. 3669–3689, 2021.

[7] Y. Cho, S. Park, J. Lee, and K. J. Yu, "Emerging materials and technologies with applications in flexible neural implants: A comprehensive review of current issues with neural devices", *Advanced Materials*, vol. 33, no. 47, p. 2 005 786, 2021.

[8] F. Gao *et al.*, "Wearable and flexible electrochemical sensors for sweat analysis: A review", *Microsystems & Nanoengineering*, vol. 9, no. 1, pp. 1–21, 2023.

[9] Y. Cheng *et al.*, "Recent progress in intrinsic and stimulated room-temperature gas sensors enabled by low-dimensional materials", *Journal of Materials Chemistry C*, vol. 9, no. 9, pp. 3026–3051, 2021.

[10] B. Rani, U. Singh, A. Chuhan, D. Sharma, and R. Maheshwari, "Photochemical smog pollution and its mitigation measures", *Journal of Advanced Scientific Research*, vol. 2, no. 04, pp. 28–33, 2011.

[11] M. T. Lerdau, J. W. Munger, and D. J. Jacob, "The NO2 flux conundrum", *Science*, vol. 289, no. 5488, pp. 2291–2293, 2000.

[12] K Wetchakun *et al.*, "Semiconducting metal oxides as sensors for environmentally hazardous gases", *Sensors and Actuators B: Chemical*, vol. 160, no. 1, pp. 580–591, 2011.

[13] S. Edginton, D. E. O'Sullivan, W. D. King, and M. D. Lougheed, "The effect of acute outdoor air pollution on peak expiratory flow in individuals with asthma: A systematic review and meta-analysis", *Environmental Research*, vol. 192, p. 110 296, 2021.

[14] N. Yi, M. Shen, D. Erdely, and H. Cheng, "Stretchable gas sensors for detecting biomarkers from humans and exposed environments", *TrAC Trends in Analytical Chemistry*, vol. 133, p. 116 085, 2020.

[15] Y. Wu *et al.*, "NO2 gas sensors based on CVD tungsten diselenide monolayer", *Applied Surface Science*, vol. 529, p. 147 110, 2020.

[16] Y. Sun and Y. Zhang, "Wafer-scale floating-gate field effect transistor sensor built on carbon nanotubes film for ppb-level NO2 detection", *Chemical Engineering Journal*, vol. 473, p. 145 480, 2023.

[17] B. Le Ouay, M. Boudot, T. Kitao, T. Yanagida, S. Kitagawa, and T. Uemura, "Nanostructuration of PEDOT in porous coordination polymers for tunable porosity and conductivity", *Journal of the American Chemical Society*, vol. 138, no. 32, pp. 10 088–10 091, 2016.

[18] Y. Seekaew, D. Phokharatkul, A. Wisitsoraat, and C. Wongchoosuk, "Highly sensitive and selective room-temperature NO2 gas sensor based on bilayer transferred chemical vapor deposited graphene", *Applied Surface Science*, vol. 404, pp. 357–363, 2017.

[19] X. Yan, Z. Han, Y Yang, and B. Tay, "NO2 gas sensing with polyaniline nanofibers synthesized by a facile aqueous/organic interfacial polymerization", *Sensors and Actuators B: Chemical*, vol. 123, no. 1, pp. 107–113, 2007.

[20] C. T. Xuan, C. M. Hung, N. Van Duy, T. M. Ngoc, Q. T. M. Nguyet, and N. D. Hoa, "Arc-discharge deposition of SWCNTs over SnO2 nanowires for highly sensitive NO2 gas sensor", *Advances in Natural Sciences: Nanoscience and Nanotechnology*, vol. 13, no. 3, p. 035 007, 2022.

[21] H. Liu *et al.*, "Physically flexible, rapid-response gas sensor based on colloidal quantum dot solids", *Advanced Materials*, vol. 26, no. 17, pp. 2718–2724, 2014.

[22] T. Stockinger *et al.*, "iSens: A fiber-based, highly permeable and imperceptible sensor design", *Advanced Materials*, vol. 33, no. 37, p. 2 102 736, 2021.

[23] X. Cao, Y. Xiong, J. Sun, X. Zhu, Q. Sun, and Z. L. Wang, "Piezoelectric nanogenerators derived self-powered sensors for multifunctional applications and artificial intelligence", *Advanced Functional Materials*, vol. 31, no. 33, p. 2 102 983, 2021.

[24] P. Chen, X. Yin, M. Que, Y. Yang, X. Liu, and W. Que, "Bilayer photoanode approach for efficient In2O3 based planar heterojunction perovskite solar cells", *Journal of Alloys and Compounds*, vol. 735, pp. 938–944, 2018.

[25] P. Chang, Y. Wang, Y. Wang, and Y. Zhu, "Current trends on In2O3 based heterojunction photocatalytic systems in photocatalytic application", *Chemical Engineering Journal*, vol. 450, p. 137 804, 2022.

[26] T. Waitz, T. Wagner, T. Sauerwald, C.-D. Kohl, and M. Tiemann, "Ordered meso-porous In2O3: Synthesis by structure replication and application as a methane gas sensor", *Advanced Functional Materials*, vol. 19, no. 4, pp. 653–661, 2009.

[27] S. Shah *et al.*, "A review on In2O3 nanostructures for gas sensing applications", *Journal of Environmental Chemical Engineering*, p. 112 538, 2024.

[28] F. Gu, C. Li, D. Han, and Z. Wang, "Manipulating the defect structure (VO) of In2O3 nanoparticles for enhancement of formaldehyde detection", *ACS applied materials & interfaces*, vol. 10, no. 1, pp. 933–942, 2018.

[29] L. Sun *et al.*, "Highly active and porous single-crystal In2O3 nanosheet for NOx gas sensor with excellent response at room temperature", *RSC advances*, vol. 7, no. 53, pp. 33 419–33 425, 2017.

[30] Y.-C. Wang *et al.*, "Sub-ppm acetic acid gas sensor based on In2O3 nanofibers", *Journal of Materials Science*, vol. 54, pp. 14 055–14 063, 2019.

[31] H. Bi *et al.*, "Synthesis of NiO-In2O3 heterojunction nanospheres for highly se-lective and sensitive detection of ppb-level NO2", *Vacuum*, vol. 172, p. 109 086, 2020.

[32] A. Khort *et al.*, "High-performance selective NO2 gas sensor based on In2O3–graphene–Cu nanocomposites", *Scientific Reports*, vol. 13, no. 1, p. 7834, 2023.

[33] Y. Wang *et al.*, "Enhanced NO2 gas sensing properties based on Rb-doped hierar-chical flower-like In2O3 microspheres at low temperature", *Sensors and Actuators B: Chemical*, vol. 332, p. 129 497, 2021.

[34] S. M. Majhi, S. T. Navale, A. Mirzaei, H. W. Kim, and S. S. Kim, "Strategies to boost chemiresistive sensing performance of In2O3-based gas sensors: An overview", *Inorganic Chemistry Frontiers*, vol. 10, no. 12, pp. 3428–3467, 2023.

[35] J. Yeo *et al.*, "Next generation non-vacuum, maskless, low temperature nanopar-ticle ink laser digital direct metal patterning for a large area flexible electronics", 2012.

[36] Y.-L. Zhang, Q.-D. Chen, H. Xia, and H.-B. Sun, "Designable 3D nanofabrication by femtosecond laser direct writing", *Nano Today*, vol. 5, no. 5, pp. 435–448, 2010.

[37] R. Lakraimi, H. Abouchadi, M. T. Janan, A. Chehri, and R. Saadane, "Thermal modeling of polyamide 12 powder in the selective laser sintering process using the discrete element method", *Materials*, vol. 16, no. 2, p. 753, 2023.

[38] L. Papadakis, D. Chantzis, and K. Salonitis, "On the energy efficiency of pre-heating methods in slm/sls processes", *The International Journal of Advanced Manufacturing Technology*, vol. 95, pp. 1325–1338, 2018.

[39] J. Chung, S. Ko, C. P. Grigoropoulos, N. R. Bieri, C. Dockendorf, and D. Poulikakos, "Damage-free low temperature pulsed laser printing of gold nanoinks on poly-mers", *Journal of Heat and Mass Transfer*, 2005.

[40] S. Hong *et al.*, "Nonvacuum, maskless fabrication of a flexible metal grid trans-parent conductor by low-temperature selective laser sintering of nanoparticle ink", *ACS nano*, vol. 7, no. 6, pp. 5024–5031, 2013.

4

[41] M. Al-Hashem, S. Akbar, and P. Morris, "Role of oxygen vacancies in nanostructured metal-oxide gas sensors: A review", *Sensors and Actuators B: Chemical*, vol. 301, p. 126 845, 2019.

[42] B. Zhang *et al.*, "High-performance room temperature NO2 gas sensor based on visible light irradiated In2O3 nanowires", *Journal of Alloys and Compounds*, vol. 867, p. 159 076, 2021.

[43] A. Mazzoli, "Selective laser sintering in biomedical engineering", *Medical & biological engineering & computing*, vol. 51, pp. 245–256, 2013.

[44] C. E. Hoppe, M. Lazzari, I. Pardinas-Blanco, and M. A. López-Quintela, "One-step synthesis of gold and silver hydrosols using poly (N-vinyl-2-pyrrolidone) as a reducing agent", *Langmuir*, vol. 22, no. 16, pp. 7027–7034, 2006.

[45] D. Marrocchelli, S. R. Bishop, H. L. Tuller, and B. Yildiz, "Understanding chemical expansion in non-stoichiometric oxides: Ceria and zirconia case studies", *Advanced Functional Materials*, vol. 22, no. 9, pp. 1958–1965, 2012.

[46] K. Bhattacharyya *et al.*, "The formation and effect of O-vacancies in doped TiO2", *New Journal of Chemistry*, vol. 44, no. 20, pp. 8559–8571, 2020.

[47] W. Wei *et al.*, "Subsurface oxygen defects electronically interacting with active sites on In2O3 for enhanced photothermocatalytic CO2 reduction", *Nature Communications*, vol. 13, no. 1, p. 3199, 2022.

[48] N. Rui, Z. Wang, K. Sun, J. Ye, Q. Ge, and C.-j. Liu, "CO2 hydrogenation to methanol over Pd/In2O3: Effects of pd and oxygen vacancy", *Applied Catalysis B: Environmental*, vol. 218, pp. 488–497, 2017.

[49] Q. Hou *et al.*, "Defect formation in In2O3 and SnO2: A new atomistic approach based on accurate lattice energies", *Journal of Materials Chemistry C*, vol. 6, no. 45, pp. 12 386–12 395, 2018.

[50] J. Gan *et al.*, "Oxygen vacancies promoting photoelectrochemical performance of In2O3 nanocubes", *Scientific reports*, vol. 3, no. 1, p. 1021, 2013.

[51] C. Kranert, R. Schmidt-Grund, and M. Grundmann, "Raman active phonon modes of cubic In2O3", *physica status solidi (RRL)–Rapid Research Letters*, vol. 8, no. 6, pp. 554–559, 2014.

[52] S. Gohil, K. K. Iyer, P Aswathi, S. Ghosh, and E. Sampathkumaran, "Raman study of Ca3Co2O6 single crystals", *Journal of Applied Physics*, vol. 108, no. 10, 2010.

[53] M. Kaur *et al.*, "Room-temperature H2S gas sensing at ppb level by single crystal In2O3 whiskers", *Sensors and Actuators B: Chemical*, vol. 133, no. 2, pp. 456–461, 2008.

[54] A Baszczuk, M Jasiorski, M Nyk, J. Hanuza, M. Mączka, and W. Stręk, "Luminescence properties of europium activated SrIn2O4", *Journal of alloys and compounds*, vol. 394, no. 1-2, pp. 88–92, 2005.

[55] Z. Wang *et al.*, "Carbon-confined indium oxides for efficient carbon dioxide reduction in a solid-state electrolyte flow cell", *Angewandte Chemie*, vol. 134, no. 21, e202200552, 2022.

[56] D. Yoon *et al.*, "Interference effect on raman spectrum of graphene on SiO2/Si", *Physical Review B—Condensed Matter and Materials Physics*, vol. 80, no. 12, p. 125 422, 2009.

[57] Z. Na, R. Yao, Q. Yan, X. Wang, and X. Sun, "Metal-organic frameworks derived in-based nanoparticles encapsulated by carbonaceous matrix for highly efficient energy storage", *Applied Surface Science*, vol. 513, p. 145 894, 2020.

[58] R. Daiyan, X. Lu, W. H. Saputera, Y. H. Ng, and R. Amal, "Highly selective reduction of CO2 to formate at low overpotentials achieved by a mesoporous tin oxide electrocatalyst", *ACS Sustainable Chemistry & Engineering*, vol. 6, no. 2, pp. 1670–1679, 2018.

[59] M. Meng *et al.*, "Boosted photoelectrochemical performance of In2O3 nanowires via modulating oxygen vacancies on crystal facets", *Journal of Alloys and Compounds*, vol. 845, p. 156 311, 2020.

[60] N. Joshi, T. Hayasaka, Y. Liu, H. Liu, O. N. Oliveira, and L. Lin, "A review on chemiresistive room temperature gas sensors based on metal oxide nanostructures, graphene and 2D transition metal dichalcogenides", *Microchimica Acta*, vol. 185, pp. 1–16, 2018.

[61] D. Han, L. Zhai, F. Gu, and Z. Wang, "Highly sensitive NO2 gas sensor of ppb-level detection based on In2O3 nanobricks at low temperature", *Sensors and Actuators B: Chemical*, vol. 262, pp. 655–663, 2018.

[62] H. Ma *et al.*, "Room temperature photoelectric NO2 gas sensor based on direct growth of walnut-like In2O3 nanostructures", *Journal of Alloys and Compounds*, vol. 782, pp. 1121–1126, 2019.

[63] M.-W. Ahn *et al.*, "Gas sensing properties of defect-controlled ZnO-nanowire gas sensor", *Applied physics letters*, vol. 93, no. 26, 2008.

[64] B. Wang *et al.*, "Vertical SnO2 nanosheet@ SiC nanofibers with hierarchical architecture for high-performance gas sensors", *Journal of Materials Chemistry C*, vol. 4, no. 2, pp. 295–304, 2016.

[65] E. Halonen, T. Viiru, K. Ostman, A. L. Cabezas, and M. Mantysalo, "Oven sintering process optimization for inkjet-printed Ag nanoparticle ink", *IEEE Transactions on Components, Packaging and Manufacturing Technology*, vol. 3, no. 2, pp. 350–356, 2012.

[66] N. Liu *et al.*, "Tunable NH4F-assisted synthesis of 3D porous In2O3 microcubes for outstanding NO2 gas-sensing performance: Fast equilibrium at high temperature and resistant to humidity at room temperature", *ACS Applied Materials & Interfaces*, vol. 13, no. 12, pp. 14 355–14 364, 2021.

[67] H. Zhu *et al.*, "A new insight into cross-sensitivity to humidity of SnO2 sensor", *Small*, vol. 14, no. 13, p. 1 703 974, 2018.

[68] S. Yang *et al.*, "Gas sensing performance of In2O3 nanostructures: A mini review", *Frontiers in Chemistry*, vol. 11, p. 1 174 207, 2023.

[69]   N. Wang *et al.*, "Rapid and accurate detection of highly toxic NO2 gas based on catkins biomass-derived porous In2O3 microtubes at low temperature", *Sensors and Actuators B: Chemical*, vol. 361, p. 131 692, 2022.

[70]   Y. Shen *et al.*, "In-situ growth of mesoporous In2O3 nanorod arrays on a porous ceramic substrate for ppb-level NO2 detection at room temperature", *Applied Surface Science*, vol. 498, p. 143 873, 2019.

[71]   Y.-K. Lv, Y.-Y. Li, R.-H. Zhou, Y.-P. Pan, H.-C. Yao, and Z.-J. Li, "N-doped graphene quantum dot-decorated three-dimensional ordered macroporous In2O3 for NO2 sensing at low temperatures", *ACS Applied Materials & Interfaces*, vol. 12, no. 30, pp. 34 245–34 253, 2020.

[72]   J Berkowitz, W. Chupka, and D. Gutman, "Electron affinities of O2, O3, NO, NO2, NO3 by endothermic charge transfer", *The Journal of Chemical Physics*, vol. 55, no. 6, pp. 2733–2745, 1971.

[73]   A. Posada-Borbon and H. Grönbeck, "Hydrogen adsorption on In2O3 (111) and In2O3 (110)", *Physical Chemistry Chemical Physics*, vol. 22, no. 28, pp. 16 193–16 202, 2020.

[74]   G. Henkelman, B. P. Uberuaga, and H. Jónsson, "A climbing image nudged elastic band method for finding saddle points and minimum energy paths", *The Journal of chemical physics*, vol. 113, no. 22, pp. 9901–9904, 2000.

[75]   B. Zhang, R. Shi, W. Duan, Z. Luo, Z.-y. Lu, and S. Cui, "Direct comparison between chemisorption and physisorption: A study of poly (ethylene glycol) by means of single-molecule force spectroscopy", *RSC advances*, vol. 7, no. 54, pp. 33 883–33 889, 2017.

[76]   Y. Liu, J. Li, W. Hou, Q. Zhou, and W. Zeng, "Pristine and Ag decorated In2O3 (110): A gas-sensitive material to selective detect NO2 based on DFT study", *Journal of Materials Research and Technology*, vol. 18, pp. 4236–4247, 2022.

[77]   Y. Ou *et al.*, "Anchoring platinum clusters onto oxygen vacancy-modified In2O3 for ultraefficient, low-temperature, highly sensitive, and stable detection of formaldehyde", *ACS sensors*, vol. 7, no. 4, pp. 1201–1212, 2022.

[78]   D. Xue, Y. Wang, Z. Zhang, and J. Cao, "Porous In2O3 nanospheres with high methane sensitivity: A combined experimental and first-principle study", *Sensors and Actuators A: Physical*, vol. 305, p. 111 944, 2020.

[79]   S.-b. Liu, J.-q. Li, Y.-f. Zhang, X.-l. Xu, and Z.-h. Chen, "Density functional theory study on electronic structure of N-doped In2O3", *Journal of Molecular Structure: THEOCHEM*, vol. 866, no. 1-3, pp. 75–78, 2008.

5

FLEXIBLE TEMPERATURE SENSORS BASED ON NIO-LIG NANOCOMPOSITES UTILIZING UV LASER DIRECT WRITING

In this chapter, a flexible temperature sensor based on nickel oxide and laser-induced graphene (NiO-LIG) nanocomposites was fabricated by ultraviolet (UV) laser direct writing technology. This methodology involved the novel fabrication of a nickel oxide-polyimide (NiO-PI) composite film by dispersing NiO nanoparticles in a PI precursor solution. Subsequently, temperature-sensitive NiO-LIG nanocomposites were rapidly fabricated using UV laser direct writing technology. The sensor demonstrates excellent sensitivity ($-0.075\%\ ^{\circ}C^{-1}$) and outstanding linearity ($R^2 = 0.999$) over the temperature range of 30 to 100 °C, with negligible hysteresis. Additionally, the sensor maintains stable static stability and environmental reliability over time. Notably, the integration of Polydimethylsiloxane (PDMS) packaging technology endows the sensor with exceptional humidity resistance and waterproof performance. The sensor also shows a rapid response to sudden temperature changes and robust long-term monitoring capabilities. These results indicate the potential applications of the proposed temperature sensor in the fields of medical diagnosis, environmental monitoring, and wearable sensing devices.

5.1. INTRODUCTION

TEMPERATURE is a fundamental physical quantity that reflects the thermal state of an object, representing the average kinetic energy of the particles within the object. Temperature sensors, which monitor the temperature of objects and environments, have become one of the most essential measurement tools in scientific research and industrial manufacturing. With continual advancements in technology, high-precision temperature detection techniques have become crucial for enhancing the quality of medical diagnostics and environmental monitoring [2]. Additionally, the rapid development of flexible electronics and the increasing demand for wearable devices have raised the performance standards for flexible temperature sensors [3]. Based on their working mechanisms, flexible temperature sensors can be broadly categorized into three types: resistive [4], thermocouple [5], and thermistor [6].

Among these, resistive-type temperature sensors are valued for their simplicity of fabrication, excellent linear response, and wide temperature measurement range [7]. As a material for resistive temperature sensors, graphene has attracted considerable interest due to its expectational electrical conductivity [8], excellent biocompatibility [9], and outstanding chemical stability [10]. In particular, laser-induced graphene (LIG) technology, which is derived from laser direct writing (LDW) technology, enables the preparation and modulation of graphene through precise non-contact processing at room temperature [11]. The flexibility, controllability, and efficiency of this method accelerate its further development [12]. As reported, Marengo et al. have designed a flexible temperature sensor using LIG technology, which shows a nonlinear negative temperature coefficient (NTC) response within the 20 to 60 °C range, with a sensitivity of 0.1% °C^{-1} (NTC = -0.1% °C^{-1}) [13]. Additionally, Zhang et al. developed a high-performance LIG-based temperature sensor that exhibits a sensitivity of 0.05% °C^{-1} and excellent linearity (R^2 = 0.999) over a temperature range of 30 to 100 °C [14]. These innovative studies demonstrate that using LIG technology to fabricate flexible temperature sensors is a highly effective strategy.

In contrast, thermistor-type temperature sensors, especially those based on negative temperature coefficient (NTC) materials, are known for their high sensitivity, fast response, and low cost. As a material of thermistor temperature sensors, nickel oxide (NiO), as an intrinsic P-type semiconductor material, is widely used due to its good negative temperature coefficient (NTC) [15]. NiO nanoparticles (NPs) show great potential for high precision, high sensitivity, and miniaturization applications due to their high specific surface area and flexible tunability [16]. As reported, Wang et al. combined NiO NPs ink with aerosol jet printing technology to manufacture a miniaturized thermistor sensor [17]. Additionally, Shine et al. developed an integrated monolithic wearable sensor laser reductive sintering technology based on NiO NPs ink [18]. These innovative studies effectively demonstrate the potential application of NiO NPs in temperature detection technology.

Herein, we developed a PI precursor dispersed with NiO NPs and further cured it into a NiO NPs composite PI film using optimized curing parameters. Unlike conventional methods of fabricating LIG composite by surface coating or spraying nanomaterials [19–21], we introduced nanomaterials at the fabrication stage of the PI film. This method not only enhances the uniformity and stability of the composite materials but also facilitates

large-scale production.

Based on this film, flexible temperature sensors using NiO-LIG nanocomposites were designed and fabricated with a UV laser (355 nm). The sensor exhibits excellent sensitivity ($-0.075\% \, °C^{-1}$) and outstanding linear response ($R^2 = 0.999$) over a temperature range of 30 to 100 °C, with a 19.3% improvement in sensitivity compared to conventional LIG-based flexible temperature sensors. The sensor also demonstrates negligible hysteresis, excellent stability, and high environmental stability. Notably, with the integration of polydimethylsiloxane (PDMS) packaging technology, the sensor achieves exceptional humidity resistance and waterproof performance. After packaging, the sensor demonstrates a rapid response to sudden temperature changes, with a response time of 0.67 s for a hot water drop (about 90 °C) and 1.41 s for a cold water drop (about 0 °C). Additionally, the sensor shows reliability in long-term temperature monitoring (hot water cooling over 90 min) under bending conditions. This rapid and scalable temperature sensor fabrication technology is suitable for large-scale production, which not only opens up a new platform for medical diagnosis and environmental monitoring but also further expands the application potential of laser direct writing technology in sensor manufacturing.

5.2. Experimental section

5.2.1. Fabrication of NiO-LIG temperature sensor

NiO-LIG, as a sensing material for temperature sensors, is mainly fabricated from NiO-PI nanocomposite films. The materials and processes for the preparation of NiO-LIG films are discussed in Section D.1 of the Supporting Information. The NiO-LIG temperature sensing region was fabricated by using an ultraviolet (UV) pulsed laser system (Grace X 355-3A, Han's Laser Technology Industry Group Co., Ltd., wavelength 355 nm). The laser movements in the X-Y direction were precisely controlled by software. The distance between the field lens and the NiO-PI nanocomposite film was adjusted by means of a vertical Z-direction translation stage. To ensure high NiO-LIG fabrication quality, the laser scanning speed (V_{ss}), the pulse repetition frequency (F_{pr}), and laser average power (P_{avg}) were set to 10 mm/s, 200 kHz, and 0.9 W, respectively. The optimization processes of the laser parameters and PDMS packaging process are detailed in Section D.2 of the Supporting Information.

5.2.2. Materials characterizations methods

The surface morphology and structure of the NiO-LIG temperature sensor were characterized using scanning electron microscopy (SEM, Regulus 8100, HITACHI) and a 3D laser scanning microscope (VK-X1000, KEYENCE). The elemental distribution analysis of the sensing region was performed using an energy-dispersive X-ray (EDX) spectroscopy integrated with the same SEM equipment. The crystal structure of the material in the sensing region was analyzed using an X-ray diffractometer (XRD, Rigaku SmarLab) with a Cu-Kα radiation source. The chemical composition of the NiO-LIG nanocomposite was analyzed using Raman spectroscopy (LabRAM HR Evolution, HORIBA), employing a 532 nm laser as the excitation source. Additionally, the chemical states of the elements in the sensing region of the sensor were analyzed using X-ray Photoelectron Spectroscopy (XPS, Thermo Scientific K-Alpha).

5.2.3. TEMPERATURE-SENSING MEASUREMENTS

The electrical resistance of the NiO-LIG temperature sensor was measured in the temperature range from 30 to 100 °C, with the ambient relative humidity maintained at 30%. During the measurement, a computer-controlled hotplate (NDK-1A, Asone) was used to control the temperature of the heat source substrate precisely. Furthermore, the resistance of the sensor was continuously and accurately recorded by a high-precision digital source meter (2450, Keithley). Infrared thermal images of the sensors were captured during the measurement process using an infrared thermal imager (UTi384H, UNI-T). The temperature coefficient of resistance (TCR), as a key parameter to measure the sensitivity of the temperature sensors, is defined as:

$$\text{TCR} = \frac{(R_\text{T} - R_0)}{R_0(T - T_0)} \times 100\% = \frac{\Delta R}{R_0 \Delta T} \times 100\% \tag{5.1}$$

where the R_0 and R_T represent the resistance of the sensor at T_0 (30 °C) and the tested temperature of T, respectively.

5.3. RESULTS AND DISCUSSION

5.3.1. FABRICATION PROCESS OF THE NiO-LIG TEMPERATURE SENSOR
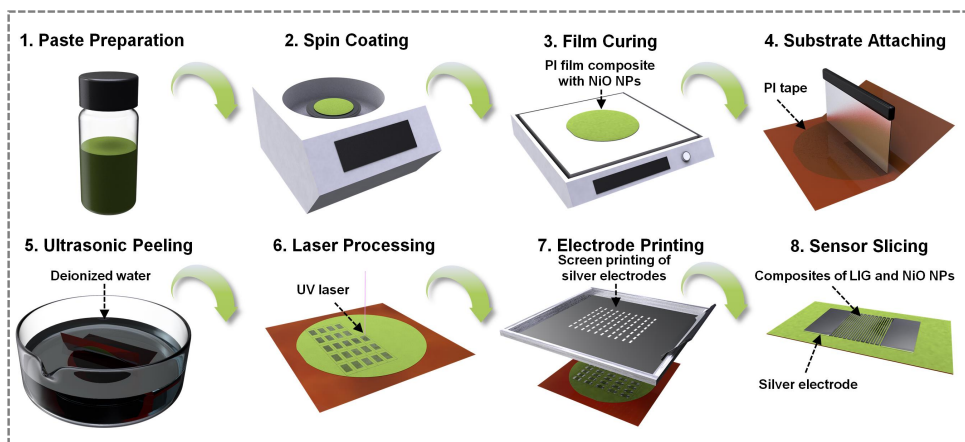
Figure 5.1: Schematic of the fabrication process of NiO-LIG nanocomposite flexible temperature sensor.

Figure 5.1 illustrates the schematic of the fabrication process of the NiO-LIG nanocomposite flexible temperature sensor. The fabrication process consisted of 8 main steps. In step 1, NiO nanoparticles (NPs) were ultrasonically dispersed in DMF solvent, followed by the addition of PI precursor solution. The mixture is thoroughly blended using a planetary mixer to prepare the NiO-PI nanocomposite paste. In step 2, the prepared paste was spin-coated onto a 4-inch silicon wafer pre-coated with a PSSNa sacrificial layer. In step 3, the wafer was heated on a hotplate to cure the paste into a NiO-PI nanocomposite film. In step 4, a layer of PI tape was adhered to the cured NiO-PI film using a scraper to enhance the mechanical stability of the sensor substrate. In step 5,

the NiO-LIG film attached to the PI tape was peeled off using an ultrasonic cleaner with deionized water and then dried in an oven. In step 6, a UV laser system was used to fabricate continuous linear patterns of the NiO-LIG temperature sensing region on the NiO-PI layer. In step 7, silver electrodes were then prepared at both ends of the NiO-LIG sensing region using a screen printing technique and subsequently cured. Finally, in step 8, the fabricated flexible temperature sensor array was diced and packaged.

NiO-LIG nanocomposite flexible temperature sensors, fabricated using UV laser direct writing technology, exhibit significant advantages over conventional fabrication processes. This technology enables the fabrication of the sensing region of an individual sensor in just 46 s, significantly improving fabricating efficiency compared to traditional methods. Furthermore, the high precision of the UV laser-induced graphene fabrication process ensures that the sensor maintains consistent performance and reliability. Moreover, the sensor design is highly customizable, allowing flexibility in adapting both its geometry and substrate material to specific application requirements. Notably, the sensor fabrication process is compatible with conventional thin-film techniques, greatly enhancing commercialization potential.

5.3.2. SURFACE CHARACTERIZATION OF THE NiO-LIG TEMPERATURE SENSOR

Figure 5.2 illustrates the unsliced sensor array, which includes multiple temperature sensor units, each measuring 15 mm × 8 mm. Each sensor has an effective sensing region of 5 mm × 5 mm and silver electrodes measuring 5 mm × 2 mm. As shown in Figure 5.2(b), this interval is defined as the minimum repetition spacing on the longitudinal laser scanning path [22]. This fine control ensures uniformity and repeatability of the NiO-LIG structure, which is essential for efficient and accurate temperature detection. Figure 5.2(c) shows the 3D laser confocal image of the NiO-LIG sensing region. The results indicate that the linear NiO-LIG structure on the NiO-PI film surface after UV laser direct writing exhibits distinct bumps and can be clearly distinguished from the NiO-PI region. This phenomenon is attributed to the thermal expansion characteristics of laser-induced graphene during the high-temperature graphitization process [23].

The scanning electron microscope (SEM) image in Figure 5.2(d) shows the surface morphology and microstructure of NiO-LIG generated by laser treatment. This structure exhibits a porous and foamy shape, attributed to high energy absorption and rapid transformation of the NiO-PI film during laser irradiation [24]. During this transformation, localized regions of the NiO-PI film undergo rapid heating and cooling, which leads to irregular melting and solidification of the surface and the formation of a foam-like porous structure [25]. Figure 5.2(e) illustrates the distinct trench formed along the laser scanning path. The formation of the trench is due to a higher energy density in the laser scanning path compared to the surrounding region, resulting in the partial ablation and removal of the NiO-LIG from the scanning path [26]. Figure 5.2(f) shows a detailed microstructure in the trench. The interior of NiO-LIG demonstrates a complex 3D network composed of dense, irregular, wavy, or curled graphene layers. These graphene layers are interconnected and overlapped on the microscopic scale, forming a complex multi-layer structure consistent with the characterization results in the literature [25, 27]. The energy-dispersive X-ray (EDX) mapping analysis reveals the elemental composition and
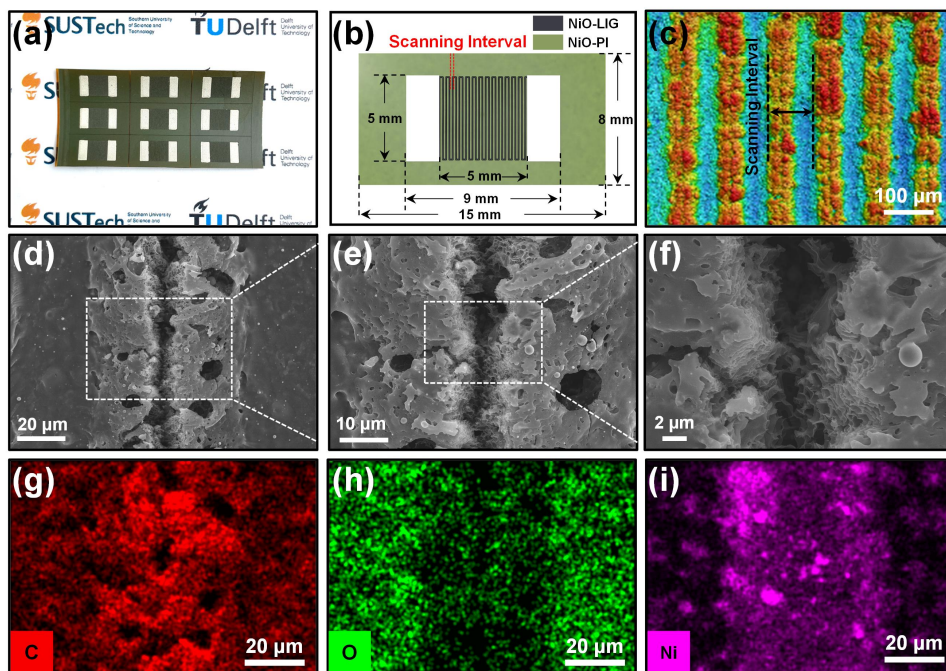
Figure 5.2: Surface characterization of NiO-LIG nanocomposite flexible temperature sensor (a) The illustration of the unsliced temperature sensor array. (b) Schematic of the design size of individual sensors. (c) 3D laser confocal image of NiO-LIG region and NiO-PI region. (d)-(f) SEM images of the porous NiO-LIG surface at different magnifications. (g)-(i) EDS maps of C, O, and Ni distributions.

distribution on the sample surface, as shown in Figure 5.2(g)-(i). After laser treatment, carbon (C) and nickel (Ni) elements are significantly enriched in the NiO-LIG region, while oxygen (O) element is primarily found in the NiO-PI region. These results confirm that the laser-induced high-temperature effect volatilizes the non-carbon elements (e.g., N and O) in polyimide while inducing the rearrangement of carbon atoms to form a graphene structure. Notably, the enrichment of Ni element in the NiO-LIG region implies that NiO NPs undergo a reduction process and are converted to metallic Ni. This conversion not only suggests that the incorporation of NiO introduces a new chemical reaction pathway but also provides an additional pathway for carrier transport within the NiO-LIG nanocomposite.

5.3.3. Material characterization of the NiO-LIG temperature sensor

To further investigate the phase transformations of the materials during the UV laser direct writing process, the surfaces of the Pure-PI, Pure-LIG, NiO-PI, and NiO-LIG samples were analyzed using X-ray diffraction (XRD) patterns. Figure 5.3(a) shows the overall XRD patterns of all samples. In the low diffraction angle region, both Pure-PI and Pure-LIG exhibit distinct broad peaks indicative of amorphous structures. Notably, the amor-

phous structure in Pure-LIG is transformed into a more organized graphene structure by the laser-induced photothermal effect [28, 29]. Additionally, the XRD spectra of NiO-PI and NiO-LIG exhibit distinct peaks characteristic of NiO NPs and metallic Ni. Specifically, as illustrated in Figure 5.3(b), the XRD spectrum of NiO-PI exhibits characteristic peaks of NiO at 37.2°, 43.4°, 62.9°, and 75.4°, corresponding to the (101), (110), (104), and (113) crystal planes of NiO (PDF#44-1159). Interestingly, after the laser treatment, the XRD spectrum of NiO-LIG reveals not only the characteristics peaks of NiO but also the characteristic peaks of metallic Ni at 44.5°, 51.8°, and 76.4°, corresponding to the (111), (200), and (220) crystal planes of Ni (PDF#04-0850). These results clearly demonstrate that the PI in NiO-PI films is converted to LIG, and a small portion of the NiO is reduced to metallic Ni during the laser treatment.

Furthermore, Raman spectroscopy was employed to reveal the structural and compositional differences between the Pure-LIG and NiO-LIG samples, as illustrated in Figure 5.3(c). The spectra of the Pure-LIG and NiO-LIG exhibit three prominent peaks (D, G, and 2D peaks) at approximately 1350, 2580, and 2690 cm^{-1}, respectively. Among these, the D peak indicates a hybridized vibrational mode of the disordered sp^2-hybridized graphitic structure, activated by defects associated with double resonance processes [30]. The G peak, indicative of a graphite-derived structure, results from the vibrations of sp^2-bonded carbon atoms in a hexagonal lattice [31]. The 2D peak arises from the second-order double resonance processes in graphene, evaluating the number of layers and crystallinity of the graphene [32]. Accordingly, the I_D/I_G ratio typically confirms the graphitization degree and the crystalline quality of the LIG after laser treatment [33]. It is noteworthy that the quality of LIG in NiO-LIG fabricated from NiO-PI film composted with NiO NPs is significantly improved, as reflected in the decrease in the I_D/I_G ratio from 0.771 to 0.694. This suggests that the incorporation of NiO NPs promotes an ordered reorganization of carbon atoms within LIG, thereby enhancing its degree of graphitization [34]. Correspondingly, the effects of different average laser powers on the graphitization degree of LIG in NiO-LIG are discussed in Section D.3 of the Supporting Information.

To further investigate the changes in the chemical composition of the NiO-PI and NiO-LIG before and after laser treatment, X-ray photoelectron spectroscopy (XPS) was employed to analyze the surface chemistry of these samples. As shown in Figure 5.3(d), before and after laser treatment, the carbon 1s (C 1s) core levels of NiO-PI and NiO-LIG are fitted with four distinct peaks at binding energies of 284.6, 285.8, 286.5, and 288.5 eV, which corresponded to C-C/C-H, C-N, C-O, and C=O bonds [35, 36]. The peak area ratios of the C-C, C-N, C-O, and C=O bond peaks on the sample surface are shown in the inset pie charts. Compared to Pure-LIG, NiO-LIG exhibits distinct chemical compositional changes after treatment. In Pure-LIG, the peak area ratios of C-C/C-H bonds increase after treatment, whereas those of C-N, C-O, and C=O bonds decrease [37]. Comparatively, in the C1s spectra of NiO-LIG, the peak area ratios of C-O bonds significantly increase from 1.5% to 13.3%, while those of C-C, C-N, and C=O bonds decrease. This suggests that during the conversion from NiO-PI to NiO-LIG, in addition to the release of gases consisting mainly of C, N, and H (e.g., CO_X, NO_X, and H_2O) and the reorganization of the carbon atoms into a honeycomb lattice [38], the carbon from pyrolysis contributes to the reduction of NiO NPs from metallic Ni. This process modifies the chemical reaction
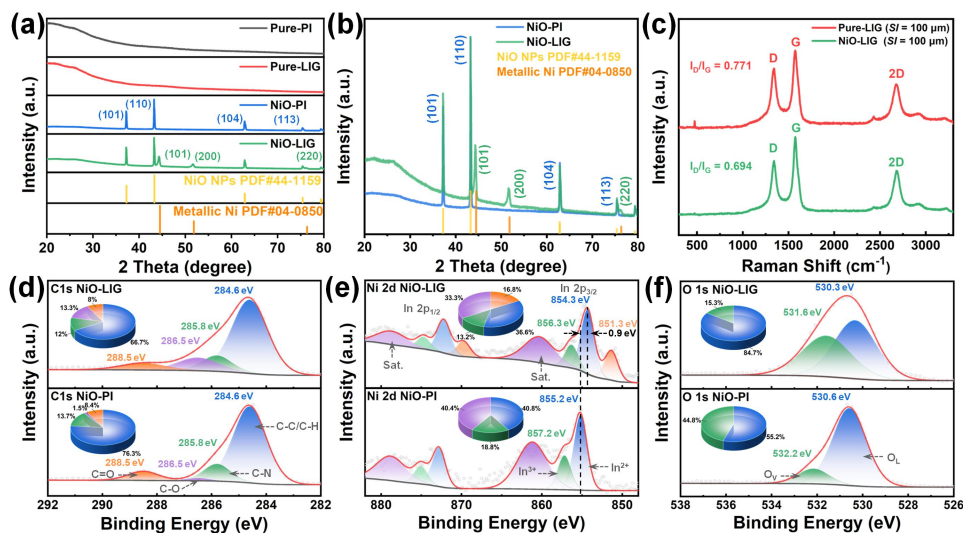
Figure 5.3: Characterization of NiO-LIG nanocomposite. (a) Overall and (b) detailed XRD spectra of Pure-PI, Pure-LIG, NiO-PI, and NiO-LIG. (c) Raman spectra of Pure-LIG and NiO-LIG. (d) C 1s, (e) Ni 2d, and (f) O 1s XPS spectra for NiO-PI and NiO-LIG before and after UV laser treatment (The inset is a pie chart of the corresponding peak area ratios).

pathway from PI laser pyrolysis to LIG to some extent.

The XPS spectra of nickel (Ni) 2p core levels in NiO-PI and NiO-LIG, before and after laser treatment, visually demonstrate the evolution of this process, as illustrated in Figure 5.3(e). The Ni 2p XPS spectrum of NiO-PI is fitted to six peaks, corresponding to the Ni 2p$_{3/2}$ and Ni 2p$_{1/2}$ core levels and their respective satellite peaks [39]. Based on the difference in oxidation states, at the Ni 2p$_{3/2}$ core level, the characteristic peak for the Ni^{2+} state corresponds to a binding energy of 855.2 eV, while that for the Ni^{3+} state corresponds to a binding energy of 857.2 eV [40, 41]. However, after laser treatment, the Ni 2p XPS spectrum of NiO-LIG reveals a new peak corresponding to the core levels of metallic Ni at 851.3 eV. Notably, the peak area ratio of the Ni^{2+} oxidation state decreases from 40.8% to 36.6%, as shown in the pie chart, clearly indicating the reduction of Ni^{2+} to metallic Ni. Additionally, the Ni 2p XPS spectrum of NiO-LIG exhibits an overall significant negative shift of 0.9 eV after calibration. This shift is primarily attributed to carbon contamination introduced during the LIG fabrication process [41]. As shown in Figure 5.3(e), the oxygen (O) 1s core level in the XPS spectra of NiO-PI and NiO-LIG is fitted to identify two different types of oxygen species. The binding energies of lattice oxygen (O$_L$) and vacancy oxygen (O$_V$) are 530.6 eV and 532.2 eV, respectively. After the laser treatment, the O 1s core level in NiO-LIG samples shows the O$_L$ peak at 530.3 eV and the O$_V$ peak at 531.6 eV. Notably, the peak area ratio of O$_L$ decreases from 84.8% to 55.3%. Meanwhile, the peak area ratio of O$_V$ increases from 15.3% to 44.8%. The introduced NiO nanoparticles introduced a 12.3% increase in oxygen vacancy defects even when compared to the 32.9% O$_V$ peak area ratio in Pure-LIG (Figure D.7). Correspondingly, the comparison of the overall XPS survey spectra for NiO-PI and NiO-LIG is detailed in

Section D.4 of the Supporting Information.

5.3.4. PERFORMANCE CHARACTERIZATION OF THE NiO-LIG TEMPERATURE SENSOR

To evaluate the performance of the NiO-LIG flexible temperature sensors, we tested the proposed sensors over a temperature range of 30 to 100 °C. As illustrated in Figure 5.4(a), the temperature responses (relative resistance change percentages) of both Pure-LIG and NiO-LIG temperature sensors demonstrate a decreasing trend with increasing temperature, indicative of a negative temperature coefficient (NTC) characteristic. Notably, both sensors exhibit excellent linear responses over the entire temperature range, with a fitting coefficient (R^2) of 0.999. By reducing the laser scanning interval (SI) from 200 µm to 150 µm and further to 100 µm, the temperature coefficient of resistance (TCR) of the NiO-LIG sensor improves from $-0.069\%\ °C^{-1}$ to $-0.075\%\ °C^{-1}$ and $-0.079\%\ °C^{-1}$, respectively. This improvement is attributed to the reduced scanning interval, which increases the thermal accumulation of laser energy on the NiO-PI film surface and enhances the graphitization quality in NiO-LIG [42]. Specifically, the effects of different average laser powers on sensor sensitivity and linearity are discussed in Section D.5 of the Supporting Information. It is noteworthy that the NiO-LIG sensor, with an SI of 100 µm, has a TCR of $-0.079\%\ °C^{-1}$, which is approximately 23% higher in sensitivity compared to the Pure-LIG temperature sensor ($-0.064\%\ °C^{-1}$). This significant enhancement clearly demonstrates the potential of the NiO-LIG nanocomposite to improve the sensitivity of LIG-based temperature sensors. The performance comparison of the proposed sensor with other LIG-based temperature sensors is shown in Table D.1 of the Supporting Information. Figure 5.4(b) illustrates the response of the NiO-LIG temperature sensor during a single heating and cooling cycle. During the temperature cycling test from 30 to 100 °C, the sensor maintains a stable linear response and exhibits negligible hysteresis. As illustrated in Figure 5.4(c), after exposure to air for 24 h, the sensor exhibits stable electrical characteristics at room temperature, demonstrating the environmental reliability of its sensing material. As shown in Figure 5.4(d), stability testing of the sensor at 10 °C intervals over a temperature range of 30 to 100 °C indicates that the sensor consistently maintained relatively stable resistance over 300 s, demonstrating excellent stability.

Considering the effect of humidity on temperature sensing, we further investigated the response of the NiO-LIG sensor at different relative humidities (RH). As shown in Figure 5.5(e), the response (relative resistance change percentage) of the sensor increases with rising RH, reaching 1.160% in an environment with 100% RH. To mitigate humidity disturbances, the sensor was packaged with a waterproof PDMS film using the spin-coating method. After packaging, the sensor effectively resists changes in RH. Furthermore, the stability tests of the sensor before and after PDMS packaging were further compared, as shown in Figure 5.5(f). The results show that although the packaged sensor maintains overall stability, it exhibits slight resistance fluctuations. These fluctuations are attributed to minor fractures in the NiO-LIG foam structure, resulting from temperature-induced interfacial stress between PDMS and NiO-LIG during the curing process.
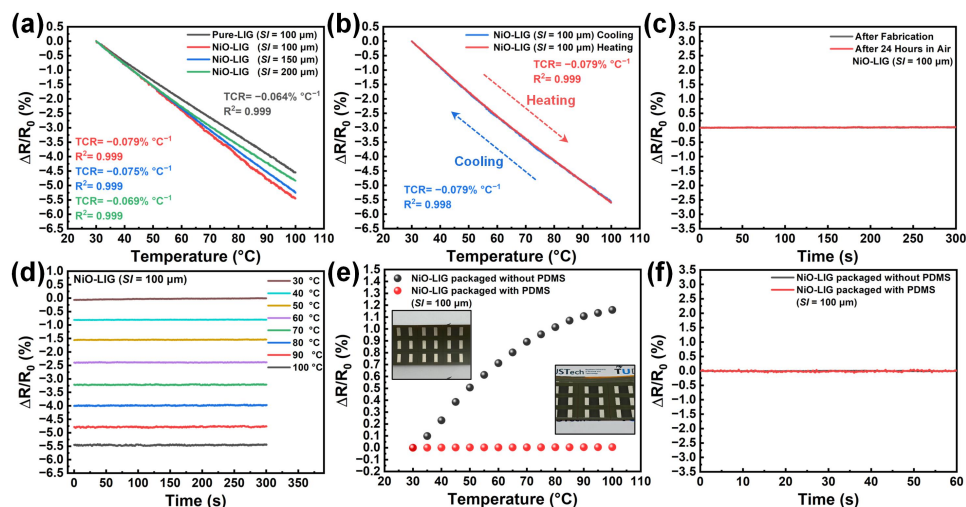
Figure 5.4: Performance characterization of the proposed temperature sensor. (a) Temperature response of NiO-LIG sensors with different scanning intervals (SI) and the Pure-LIG sensor for baseline comparison. (b) The sensor responds during a single heating and cooling cycle at a temperature range of 30 to 100 °C. (c) Comparison of reliability testing of the sensor before and after exposure to air for 24 hours. (d) Comparison of stability testing of the sensor over the temperature range of 30 to 100 °C with intervals of 10 °C. (e) Relative humidity response of the sensor before and after PDMS packaging. (f) Comparison of stability testing of the sensor before and after DMS packaging.

5.3.5. Application demonstrations of the NiO-LIG temperature sensor

To investigate the response time of the PDMS packaged NiO-LIG flexible temperature sensor to sudden temperature changes, we evaluated its performance by dropping water drops of different temperatures into the sensing region of the sensor, as shown in Figure 5.5(a). During the test, water droplets (hot at 90 °C and cold at 0 °C) were precisely dispensed onto the central region of the sensor using a pipette, as shown in Figure 5.5(b) and (c). Benefiting from the waterproof properties of the PDMS packaging, the sensor responds rapidly to sudden temperature changes induced by the droplets, achieving a response time of 0.67 s for hot water and 1.41 s for cold water, demonstrating rapid response capabilities. This result demonstrates that the rapid response of the NiO-LIG sensor significantly surpasses that of other temperature sensors based on LIG or LIG composite nanomaterials [43, 44]. To confirm the stability and accuracy of the NiO-LIG flexible temperature sensor for long-term monitoring, the sensor was attached to a cup surface under bending conditions, and 90 °C hot water was introduced, as illustrated in Figure 5.5(d). The demonstration comprises four stages. In the initial steady state, before introducing hot water, the system comprising the sensor and cup reaches thermal equilibrium with the ambient temperature of 26 °C. Upon the introduction of 90 °C hot water into the cup in the temperature response stage, the sensor immediately detects the rapid temperature increase of the cup wall, demonstrating its excellent response speed. In the temperature drop stage, the temperature of the cup wall aligns with that of the hot wa-

ter, and the heat is gradually transferred to the external environment at 40 °C. The sensor accurately records the slow temperature drop. In the thermodynamic equilibrium stage, the temperature gradually approaches the ambient temperature of 26 °C, indicating that the heat from the hot water has nearly completely transformed, achieving thermal equilibrium. This demonstration further verified the ability of NiO-LIG flexible temperature sensor to monitor temperature changes, demonstrating its potential application in dynamic thermal environments.

5.3.6. SENSING MECHANISM OF THE NIO-LIG TEMPERATURE SENSOR

Although LIG dominates NiO-LIG composites, the introduction of NiO nanoparticles significantly improves the sensitivity of the flexible temperature sensor. The introduction of NiO nanoparticles, on the one hand, improves the graphitization degree of LIG and further reduces the defects in LIG, which reduces the scattering during carrier transport and improves electron mobility. On the other hand, after laser direct writing, part of the nickel oxide is reduced to metallic Ni, and oxygen vacancy defects are generated. When the temperature increases, the conductive network formed by metallic Ni and the defect energy levels introduced by oxygen vacancies significantly promote the carrier hopping transport. As a result, the resistance of NiO-LIG composite decreases significantly when the temperature increases, which further improves the sensitivity of NiO-LIG temperature sensors.

The negative temperature coefficient (NTC) property exhibited by LIG is mainly attributed to its unique carbon nanomaterial structure and charge transport mechanism [45, 46]. However, as a branch of carbon nanomaterials, LIG is known for its complex electronic interactions [45]. The disordered structure of LIG means that the transport of charge carriers does not rely on the traditional band continuity [46]. These carriers (e.g., electrons) usually move between different regions within the material through quantum tunneling effects or variable range hopping [47]. This transport involves crossing energy barriers formed by localized defects, impurities, or interfaces, and the process is strongly influenced by temperature [48]. As the temperature increases, carriers gain more thermal energy and thus can more easily overcome these energy barriers, thus increasing transport efficiency. On the contrary, at lower temperatures, the ability of carriers to cross the barriers is weakened, which leads to lower transport efficiency. In addition, trap states formed by defects and impurities in LIGs further enhance the sensitivity to temperature variations, as these structural irregularities directly affect the kinetic behavior of carriers [49]. During thermal excitation, unhybridized π-electrons in disordered graphene are scattered by thermally generated carriers and phonons, which are temperature-dependent, with variable-range hopping and electron-phonon scattering mechanisms [50].

The mechanisms collectively influencing the performance of the NiO-LIG flexible temperature sensor are well elucidated by the two-dimensional Mott Variable Range Hopping (2D Mott VRH) model. This model describes and analyzes the effects of defects or impurities generated during the fabrication process or functionalization treatments on electron localization and hopping transport in carbon nanomaterials [51–53]. This model explains a theoretical model for electrons to hop between localized energy states to achieve conductivity, which does not rely on the conduction mechanism of the
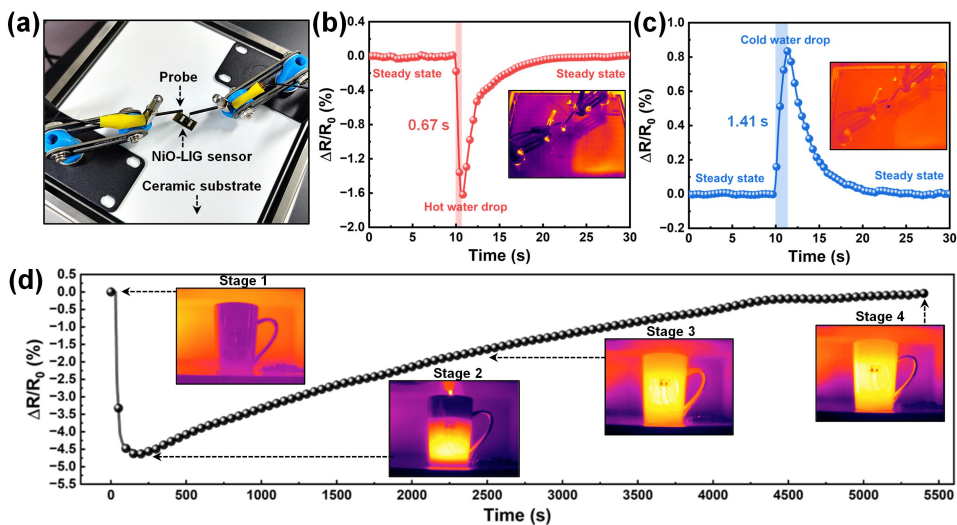
Figure 5.5: (a) The illustration of the NiO-LIG sensor experiment detecting sudden temperature changes. (b) and (c) Real-time sensor response to a drop of hot water and a drop of cold water. (d) Real-time monitoring data on the long-term stability and accuracy of the sensor (Insets are the corresponding infrared thermographs).

continuous movement of electrons in the energy band. The conductivity σ is usually expressed as:

$$\sigma(T) = \sigma_0 \exp\left(-\frac{B}{T^{1/3}}\right) \tag{5.2}$$

where the σ_0 is the pre-exponential factor, representing the maximum conductivity achievable in the absence of temperature constraints [54].

The B is the hopping parameter which is defined as:

$$B = \left(\frac{3}{kN(E_F)L_1^2}\right)^{1/3} \tag{5.3}$$

where k is the Boltzmann constant, and $N(E_F)$ is the density of states at the Fermi energy level E_F, reflecting the number of states near the Fermi energy level available for occupation by electrons. L_1 is the electron localization length, which denotes the average distance over which an electron is confined to a region.

The data points and linear fitting curves of $Ln(\sigma)$ and $T^{-1/3}$ for Pure-LIG and NiO-LIG temperature sensors are shown in Figure D.8, Section D.6 of the Supporting Information. While the fitted curves provide a reasonable approximation over a certain temperature range, the overall transport behavior remains nonlinear, as expected for hopping conduction mechanisms. Although the difference in the slopes of the fitted curves is not significant, the hopping parameter B value of NiO-LIG reaches 5.743 $K^{-1/3}$, which is higher than the 4.610 $K^{-1/3}$ of Pure-LIG. At lower temperatures, the larger B values indicate higher energy barriers that electrons need to overcome, making it more difficult for

electrons to hop and thus reducing conductivity. However, as the temperature rises, the thermal activation effect provides enough energy to help electrons overcome these barriers, significantly improving conductivity at higher temperatures. Therefore, NiO-LIG demonstrates better temperature sensitivity compared to Pure-LIG [55].

5.4. CONCLUSION

In this study, flexible temperature sensors based on the NiO-LIG nanocomposite were fabricated using a UV (355 nm) laser. Sensor performance was enhanced by optimizing the scanning interval and average laser power. Overall, the sensor exhibits excellent sensitivity ($-0.075\%\,°C^{-1}$), linearity ($R^2 = 0.999$), and negligible hysteresis across the temperature range of 30 to 100 °C. Additionally, integrating PDMS packaging technology endows the sensor with exceptional humidity resistance and waterproofing capabilities. Moreover, the sensor rapidly responds to sudden temperature changes and continuously monitors temperature changes over long periods. Compared to the Pure-LIG sensor, the improved sensitivity of the NiO-LIG sensor is attributed to the NiO composite, which provides additional hole carriers and forms an additional conductive network through the reduction of NiO to metallic Ni, verified by the two-dimensional Mott variable-range hopping model. These results demonstrate the potential of NiO-LIG nanocomposite flexible temperature sensors for applications in medical diagnostics and environmental monitoring.

REFERENCES

[1] S. Wang, C. Tan, Q. Zong, A. Sett, H. Ye, and P. French, "NiO-doped laser-induced graphene: A high-performance flexible temperature sensor", in *2024 IEEE SENSORS*, IEEE, 2024, pp. 01–04.

[2] B. A. Kuzubasoglu and S. K. Bahadir, "Flexible temperature sensors: A review", *Sensors and Actuators A: Physical*, vol. 315, p. 112 282, 2020.

[3] Y. Su *et al.*, "Printable, highly sensitive flexible temperature sensors for human body temperature monitoring: A review", *Nanoscale Research Letters*, vol. 15, pp. 1–34, 2020.

[4] H. Qin *et al.*, "Laser-induced graphene-based smart textiles for wireless cross-body metrics", *ACS Applied Nano Materials*, vol. 6, no. 20, pp. 19 158–19 167, 2023.

[5] M. M. Mallick *et al.*, "High-sensitivity flexible thermocouple sensor arrays via printing and photonic curing", *Advanced Functional Materials*, vol. 34, no. 20, p. 2 301 681, 2024.

[6] Z. Peng *et al.*, "Flexible copper-based thermistors fabricated by laser direct writing for low-temperature sensing", *ACS Applied Materials & Interfaces*, vol. 16, no. 8, pp. 10 496–10 507, 2024.

[7] Q. Li, L.-N. Zhang, X.-M. Tao, and X. Ding, "Review of flexible temperature sensing networks for wearable physiological monitoring", *Advanced healthcare materials*, vol. 6, no. 12, p. 1 601 371, 2017.

[8]   Z.-S. Wu *et al.*, "Synthesis of graphene sheets with high electrical conductivity and good thermal stability by hydrogen arc discharge exfoliation", *ACS nano*, vol. 3, no. 2, pp. 411–417, 2009.

[9]   Z. Xiong *et al.*, "Harnessing the 2D structure-enabled viscoelasticity of graphene-based hydrogel membranes for chronic neural interfacing", *Small Methods*, vol. 6, no. 5, p. 2 200 022, 2022.

[10] R. Stine, W.-K. Lee, K. E. Whitener Jr, J. T. Robinson, and P. E. Sheehan, "Chemical stability of graphene fluoride produced by exposure to XeF2", *Nano letters*, vol. 13, no. 9, pp. 4311–4316, 2013.

[11] Z. Li, L. Huang, L. Cheng, W. Guo, and R. Ye, "Laser-induced graphene-based sensors in health monitoring: Progress, sensing mechanisms, and applications", *Small Methods*, p. 2 400 118, 2024.

[12] L. Huang, J. Su, Y. Song, and R. Ye, "Laser-induced graphene: En route to smart sensing", *Nano-micro letters*, vol. 12, pp. 1–17, 2020.

[13] Y. Houeix *et al.*, "Laser-synthesis of conductive carbon-based materials from two flexible commercial substrates: A comparison", *Applied Surface Science*, vol. 634, p. 157 629, 2023.

[14] Y. Zhang *et al.*, "High-linearity graphene-based temperature sensor fabricated by laser writing", *Journal of Materials Science: Materials in Electronics*, vol. 35, no. 2, p. 109, 2024.

[15] C. Wu *et al.*, "Work function tunable laser induced graphene electrodes for Schottky type solar-blind photodetectors", *Applied Physics Letters*, vol. 120, no. 10, 2022.

[16] M. Carbone, "NiO-based electronic flexible devices", *Applied Sciences*, vol. 12, no. 6, p. 2839, 2022.

[17] C. Wang, G.-Y. Hong, K.-M. Li, and H.-T. Young, "A miniaturized nickel oxide thermistor via aerosol jet technology", *Sensors*, vol. 17, no. 11, p. 2602, 2017.

[18] J. Shin *et al.*, "Sensitive wearable temperature sensor with seamless monolithic integration", *Advanced Materials*, vol. 32, no. 2, p. 1 905 527, 2020.

[19] L. Wang, M. Liu, A. Yadav, Y. Wu, and H. Zheng, "A method for preparing and investigating anti-/de-icing surface by integration of laser-induced graphene (LIG) with a silica sol adhesive (SMP@ M-SiO2)", *Surface and Coatings Technology*, vol. 474, p. 130 111, 2023.

[20] H. Yang *et al.*, "Stretchable strain sensor based on HfSe2/LIG composite with high sensitivity and good linearity within a wide range", *Applied Surface Science*, vol. 636, p. 157 772, 2023.

[21] A. Chhetry *et al.*, "Black phosphorus@ laser-engraved graphene heterostructure-based temperature–strain hybridized sensor for electronic-skin applications", *Advanced Functional Materials*, vol. 31, no. 10, p. 2 007 661, 2021.

[22] S. Wang *et al.*, "Rapid fabrication of high-performance flexible pressure sensors using laser pyrolysis direct writing", *ACS applied materials & interfaces*, vol. 15, no. 34, pp. 41 055–41 066, 2023.

[23] S. Movaghgharnezhad and P. Kang, "Laser-induced graphene: Synthesis advances, structural tailoring, enhanced properties, and sensing applications", *Journal of Materials Chemistry C*, 2024.

[24] A. Sarkar, H.-w. Noh, I. C. Nlebedim, and P. Shrotriya, "Magnetic functionalization and catalytic behavior of magnetic nanoparticles during laser photochemical graphitization of polyimide", *APL Materials*, vol. 12, no. 3, 2024.

[25] Y. Chen *et al.*, "UV laser-induced polyimide-to-graphene conversion: Modeling, fabrication, and application", *Small Methods*, vol. 3, no. 10, p. 1 900 208, 2019.

[26] Y. Guo, C. Zhang, Y. Chen, and Z. Nie, "Research progress on the preparation and applications of laser-induced graphene technology", *Nanomaterials*, vol. 12, no. 14, p. 2336, 2022.

[27] S. Hong, J. Kim, S. Jung, J. Lee, and B. S. Shin, "Surface morphological growth characteristics of laser-induced graphene with UV pulsed laser and sensor applications", *ACS Materials Letters*, vol. 5, no. 4, pp. 1261–1270, 2023.

[28] H. Yu, M. Gai, L. Liu, F. Chen, J. Bian, and Y. Huang, "Laser-induced direct graphene patterning: From formation mechanism to flexible applications", *Soft Science*, vol. 3, no. 1, N–A, 2023.

[29] N.-K. Yang *et al.*, "Exploring graphene structure, material properties, and electrochemical characteristics through laser-induced temperature analysis", *Micro and Nano Systems Letters*, vol. 12, no. 1, p. 8, 2024.

[30] L. G. Cançado *et al.*, "Quantifying defects in graphene via Raman spectroscopy at different excitation energies", *Nano letters*, vol. 11, no. 8, pp. 3190–3196, 2011.

[31] T. Kuila, S. Bose, A. K. Mishra, P. Khanra, N. H. Kim, and J. H. Lee, "Chemical functionalization of graphene and its applications", *Progress in Materials Science*, vol. 57, no. 7, pp. 1061–1105, 2012.

[32] A. C. Ferrari *et al.*, "Raman spectrum of graphene and graphene layers", *Physical review letters*, vol. 97, no. 18, p. 187 401, 2006.

[33] L. Cançado *et al.*, "General equation for the determination of the crystallite size la of nanographite by Raman spectroscopy", *Applied physics letters*, vol. 88, no. 16, 2006.

[34] N. F. Santos *et al.*, "IR and UV laser-induced graphene: Application as dopamine electrochemical sensors", *Advanced Materials Technologies*, vol. 6, no. 6, p. 2 100 007, 2021.

[35] S. F. Ahmed, K.-R. Lee, J.-i. Yoon, and M.-W. Moon, "Nanoporous structures of polyimide induced by Ar ion beam irradiation", *Applied Surface Science*, vol. 258, no. 8, pp. 3841–3845, 2012.

[36] A. K. Thakur, B. Lin, F. H. Nowrin, and M. Malmali, "Comparing structure and sorption characteristics of laser-induced graphene (LIG) from various polymeric substrates", *ACS ES&T Water*, vol. 2, no. 1, pp. 75–87, 2021.

[37] H. Li, J. Yang, S. Dong, F. Tian, and X. Li, "Low dielectric constant polyimide obtained by four kinds of irradiation sources", *Polymers*, vol. 12, no. 4, p. 879, 2020.

5

[38]   S. Y. Kim, J. H. Kim, K. N. Kim, H. Oh, S. Myung, and D. H. Kim, "Highly conduc-
        tive, conformable ionic laser-induced graphene electrodes for flexible iontronic
        devices", *Scientific Reports*, vol. 14, no. 1, p. 4599, 2024.

[39]   N. Kitchamsetti *et al.*, "DFT and experimental investigations on the photocat-
        alytic activities of nio nanobelts for removal of organic pollutants", *Journal of Al-
        loys and Compounds*, vol. 855, p. 157 337, 2021.

[40]   C. Alex, G. Shukla, and N. S. John, "Introduction of surface defects in NiO with
        effective removal of adsorbed catalyst poisons for improved electrochemical urea
        oxidation", *Electrochimica Acta*, vol. 385, p. 138 425, 2021.

[41]   D. R. Baer *et al.*, "XPS guide: Charge neutralization and binding energy referenc-
        ing for insulating samples", *Journal of Vacuum Science & Technology A*, vol. 38,
        no. 3, 2020.

[42]   J. de la Roche, I. López-Cifuentes, and A. Jaramillo-Botero, "Influence of las-
        ing parameters on the morphology and electrical resistance of polyimide-based
        laser-induced graphene (LIG)", *Carbon Letters*, vol. 33, no. 2, pp. 587–595, 2023.

[43]   R. Han *et al.*, "Facile fabrication of rGO/LIG-based temperature sensor with high
        sensitivity", *Materials Letters*, vol. 304, p. 130 637, 2021.

[44]   T. Q. Trung, H. S. Le, T. M. L. Dang, S. Ju, S. Y. Park, and N.-E. Lee, "Freestanding,
        fiber-based, wearable temperature sensor with tunable thermal index for health-
        care monitoring", *Advanced healthcare materials*, vol. 7, no. 12, p. 1 800 074, 2018.

[45]   J. Zhu, X. Huang, and W. Song, "Physical and chemical sensors on the basis
        of laser-induced graphene: Mechanisms, applications, and perspectives", *ACS
        nano*, vol. 15, no. 12, pp. 18 708–18 741, 2021.

[46]   B. Kulyk *et al.*, "Laser-induced graphene from paper by ultraviolet irradiation:
        Humidity and temperature sensors", *Advanced Materials Technologies*, vol. 7,
        no. 7, p. 2 101 311, 2022.

[47]   Abid, P. Sehrawat, C. Julien, and S. Islam, "WS2 quantum dots on e-textile as a
        wearable uv photodetector: How well reduced graphene oxide can serve as a
        carrier transport medium?", *ACS applied materials & interfaces*, vol. 12, no. 35,
        pp. 39 730–39 744, 2020.

[48]   S. Gandla *et al.*, "Highly linear and stable flexible temperature sensors based on
        laser-induced carbonization of polyimide substrates for personal mobile moni-
        toring", *Advanced Materials Technologies*, vol. 5, no. 7, p. 2 000 014, 2020.

[49]   P. Sehrawat, S. Islam, P. Mishra, *et al.*, "Reduced graphene oxide based temper-
        ature sensor: Extraordinary performance governed by lattice dynamics assisted
        carrier transport", *Sensors and Actuators B: Chemical*, vol. 258, pp. 424–435, 2018.

[50]   X.-Y. Fang, X.-X. Yu, H.-M. Zheng, H.-B. Jin, L. Wang, and M.-S. Cao,
        "Temperature-and thickness-dependent electrical conductivity of few-layer
        graphene and graphene nanosheets", *Physics Letters A*, vol. 379, no. 37, pp. 2245–
        2251, 2015.

[51]   M. Park *et al.*, "Electrical and thermoelectric transport by variable range hopping
        in reduced graphene oxide", *Applied Physics Letters*, vol. 111, no. 17, 2017.

[52] A. B. Kaiser, C. Gómez-Navarro, R. S. Sundaram, M. Burghard, and K. Kern, "Electrical conduction mechanism in chemically derived graphene monolayers", *Nano letters*, vol. 9, no. 5, pp. 1787–1792, 2009.

[53] S. Baek, J. Kim, P. Pujar, H.-J. Kwon, S. Kim, and S. Gandla, "Sub-zero temperature sensor based on laser-written carbon", *Advanced Electronic Materials*, vol. 8, no. 7, p. 2 101 252, 2022.

[54] N. F. Mott and E. A. Davis, *Electronic processes in non-crystalline materials.* OUP Oxford, 2012.

[55] D. Yu, C. Wang, B. L. Wehrenberg, and P. Guyot-Sionnest, "Variable range hopping conduction in semiconductor nanocrystal solids", *Physical review letters*, vol. 92, no. 21, p. 216 802, 2004.

5

6

CONCLUSION AND FUTURE PERSPECTIVE

6.1. CONCLUSIONS

THIS thesis demonstrates the significant potential of laser direct writing (LDW) technology in designing and fabricating flexible sensors. Employing innovative technologies and materials, these studies highlight the capabilities of UV laser direct writing technology in fabricating high-performance sensors, demonstrating its extensive potential in health monitoring and environmental detection. The results not only illustrate the versatility of laser technology in creating high-performance flexible sensors but also promote its widespread application in the field of flexible electronics. Specifically, this research has made significant progress in the following four key areas:

Design Freedom: LDW technology allows for precise control over sintering, pyrolysis, and material modification on a microscopic scale, offering a broad degree of design freedom in the development of flexible sensors with complex geometries and customized material properties.

Fabrication Efficiency: Compared to traditional methods, LDW technology dramatically enhances efficiency, reducing both time and material waste by directly writing patterns onto target materials and substantially accelerating the development cycle from concept to product.

Material Versatility: LDW technology is compatible with different types of materials (polymers, metals, oxide, and composites) to optimize the performance and functionality of flexible sensors for specific applications.

Integration and Composite Functionality: LDW technology facilitates the integration of multiple functions into a single flexible sensor, simplifying the production process, enhancing performance and reliability, and offering the possibility of miniaturizing and smartening complex sensing systems.

In terms of the specific contribution to the fabrication of flexible sensors, the following work was carried out in this thesis:

Novel Fabrication Technologies: The development of laser pyrolysis direct writing (LPDW) and laser transmission pyrolysis (LTP) technologies has expanded the potential for creating flexible mechanical sensors based on polymer microstructures. The introduction of selective reduction laser sintering (SRLS) and UV laser direct writing (UV-LDW) technologies has improved the fabrication efficiency and performance of flexible gas and temperature sensors through micro- and nanomaterial modifications.

Material and Process Innovations: The exploration of novel materials and composite manufacturing techniques in this study has expanded the functionalities and potential application fields of flexible sensors, paving the way for future technological developments and applications.

Innovative Sensor Applications: The developed sensors demonstrate potential application value in the field of health monitoring and environmental detection and confirm the feasibility and effectiveness of these sensors in practical applications.

These results not only promote the development of flexible sensor technology but also provide valuable insights and references for future research in related fields.

6.2. FUTURE PERSPECTIVE

In this thesis, we have successfully developed and enhanced flexible sensors using laser direct writing (LDW) technology, leading to significant advancements in sensor design, material preparation, and functional applications. Considering the future trajectory of LDW technology, there are several key areas that need to be focused on to further enhance the development and application of these technologies.

Technology Improvement: Future research will prioritize further enhancing the precision and efficiency of LDW technologies to enable more intricate and smaller-scale applications. This includes refining control over laser parameters and exploring new laser types.

Material Innovation: Ongoing exploration of new materials and composites suitable for use in LDW will expand the functionality and applicability of flexible sensors. Efforts may include synthesizing materials that are both more environmentally friendly and cost-effective.

Application Expansion: There is potential to broaden the application areas of these sensors, particularly into emerging fields such as wearable technology and intelligent textiles. This expansion involves integrating sensors with wireless technologies to improve user interaction and data integration.

Commercialization: Advancing the commercialization of these developed technologies will be crucial. This includes scaling up production processes and ensuring that the sensors comply with industry standards and regulations for various applications.

ACKNOWLEDGEMENTS

Time passes swiftly, and as my four-year doctoral journey draws to a close, I am filled with both excitement and melancholy. These years have been marked by numerous challenges and setbacks, each pushing me closer to my goals and reshaping my expectations for the future. I have come to deeply appreciate that without the support of my mentors, colleagues, and friends, I would not have been able to face these challenges alone. Here, I express my sincerest gratitude to the outstanding individuals who have accompanied me on this journey.

First and foremost, I extend my heartfelt gratitude to my promotor, Prof. Dr. Paddy French, for the opportunity to pursue my doctoral degree under his guidance. His expertise, patience, and invaluable advice have illuminated my research path. Over the past four years, his thoughtful and wise mentorship inspired me to persevere and advance boldly in the realm of scientific inquiry. I am equally grateful to my co-promotor and supervisor, Prof. Dr. Huaiyu Ye, who provided essential equipment and resources for my research. His generous support and guidance were crucial in shaping my research direction.

My thanks also go to Prof. Dr. Guoqi Zhang, whose support was invaluable throughout my academic journey. He offered numerous opportunities for engaging in discussions and exchanges, enriching my research experience and aiding in my professional growth. Additionally, I owe a great deal of gratitude to Dr. Chunjian Tan, who has been a mentor since my master's studies. His guidance in both my professional and personal life has been a cornerstone of my growth.

I must also express my heartfelt gratitude to my outstanding colleagues Huiru Yang, Qianming Huang, Shizhen Li, and Chenshan Gao in Research Group Ye at the Southern University of Science and Technology. Their passion for research and commitment to knowledge have profoundly influenced me. Our discussions were always enlightening and inspiring. I am also thankful for Binlu Yu and Yumeng Luo from Research Group Li at the same institution. Their valuable feedback and suggestions significantly aided my experimental work. Our exchanges were always enriching and motivating.

I would like to express my sincere gratitude to Xu Liu, Leiming Du, Shanliang Deng, and Zihan Zhang, my friends from the ECTM group at Delft University of Technology. Their companionship was a cornerstone of my life overseas, providing not only academic collaboration but also personal support that helped me navigate the challenges of living and studying in a foreign country.

Lastly, my deepest appreciation goes to my family, whose unwavering support and love have sustained me through the long days and nights of my doctoral journey.

Dare to dream, dare to try, dare to fail, dare to succeed.

A

SUPPORTING INFORMATION CHAPTER 2

A.1. REALIZATION CONDITIONS OF LPDW TECHNOLOGY
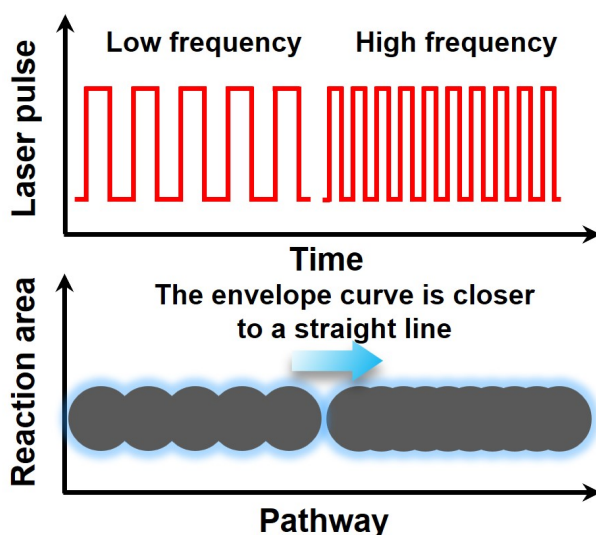
Figure A.1: Schematic illustration of continuous laser pyrolysis surface reaction morphology at different pulse repletion frequencies (low and high frequency).

The laser beam, due to its high energy density, rapidly heats the powder (6H-SiC NPs) to extremely high temperatures when interacting with the target material. This high temperature can cause the surface of the powder, or portions close to the surface, to rapidly evaporate or melt. When a portion of the surface of the powder material is rapidly heated

A

by the laser to the point of evaporation, this portion of the material suddenly becomes gaseous and expands rapidly in the form of an explosion. The gases produced by this evaporation process spread rapidly in all directions, creating powerful pressure waves. These pressure waves are strong enough to push the surrounding unevaporated powder particles away [1]. This is the reason why continuum laser pyrolysis cannot be triggered at the focal plane.
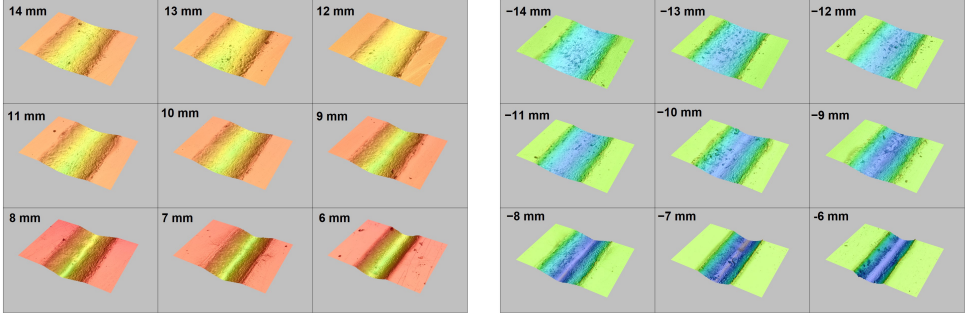
Figure A.2: 3D laser confocal images of microchannel structures on PDMS surface at different focal distances.
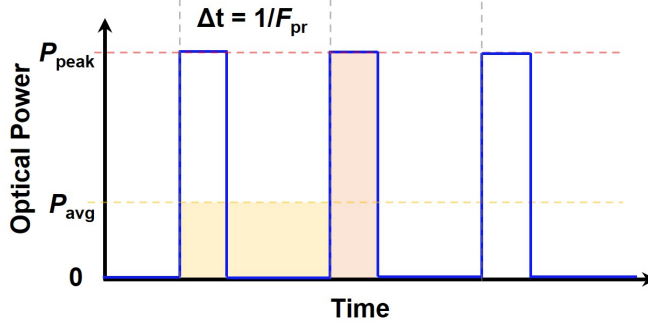
Figure A.3: Schematic illustration of the relationship between the laser average power (P_{avg}), laser peak power (P_{peak}), and pulse repetition frequency (F_{pr}).

In detail, increasing the average power (P_{avg}) of the laser at the fixed repetition frequency (F_{pr}) and scanning speed (V_{ss}) did not effectively improve the aspect ratio of the microchannels, which remained stable at around 1.55, as shown in Table A.1. On the other hand, the width and depth of the microchannels increased simultaneously with the laser power. It is worth noting that the final morphology of the microchannel is jointly determined by the critical pyrolysis temperature of continuous laser pyrolysis and the morphology of SiC pyrolysis products. The overall temperature during laser pyrolysis significantly increases as the laser power increases. However, heat conduction in the medium remains isotropic [2]. The temperature distribution in the system formed by the PDMS substrate and SiC pyrolysis products still follows the Gaussian temperature distribution. As the laser power increases, the temperature of the laser-irradiated SiC py-
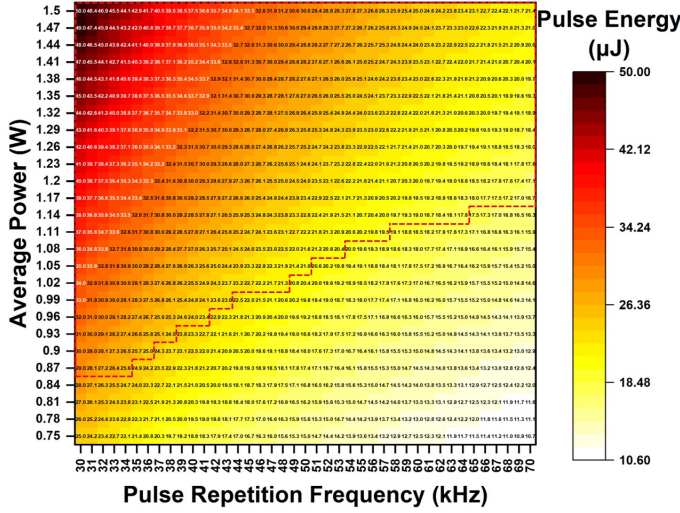
Figure A.4: The detailed heat map of critical realization conditions for continuous laser pyrolysis (CLP) reaction.

rolysis product also rises. Due to the constant thermal conductivity of the SiC pyrolysis product, its overall temperature increases and maintains isotropic conduction. However, the critical temperature for laser pyrolysis remains unchanged. Therefore, while the laser moves, the cross-section of the PDMS microchannel expands uniformly in all directions. Consequently, increasing the laser power leads to an increase in the depth and width of the SiC pyrolysis product morphology, which also keeps the aspect ratio of the microchannel unchanged. In contrast, increasing the number of laser scans gradually increases the etching depth of laser scanning due to the high temperature and stress generated during the pyrolysis process, as shown in Figure A.5. As the etching depth increases, the depth of the PDMS microchannels after laser pyrolysis increases, which leads to an increase in the aspect ratio of the microchannels.

Table A.1: The average width and depth of the microchannel with different average power at fixed pulse repetition frequency.

Conditions	Average Depth	Average Width	Aspect Ratio
$P_{avg} = 1.50$ W, $F_{pr} = 30$ kHz	39.2 µm	258.1 µm	0.152
$P_{avg} = 1.35$ W, $F_{pr} = 30$ kHz	37.0 µm	237.5 µm	0.155
$P_{avg} = 1.20$ W, $F_{pr} = 30$ kHz	33.8 µm	226.1 µm	0.149
$P_{avg} = 1.05$ W, $F_{pr} = 30$ kHz	31.0 µm	205.6 µm	0.151
$P_{avg} = 0.90$ W, $F_{pr} = 30$ kHz	28.7 µm	192.5 µm	0.149

In detail, Figure A.6 and Figure A.7 show the roughness results and 3D laser confocal images of the microchannel sidewalls with different numbers of laser scans. To avoid measurement errors resulting from the groove-like shape of the microchannel
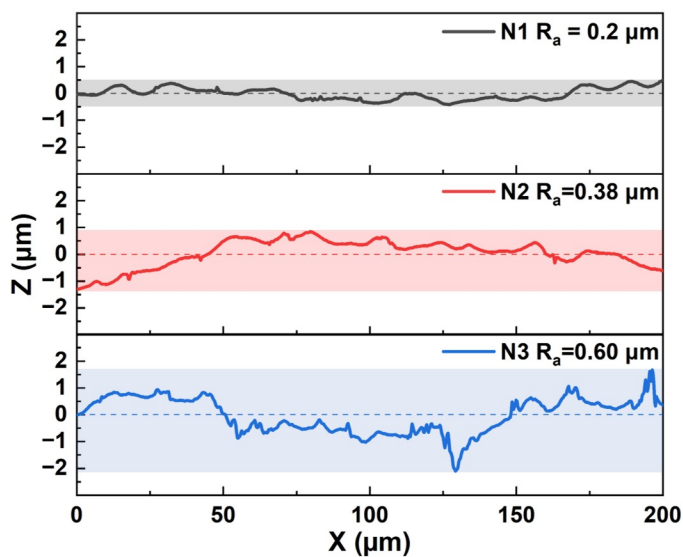
Figure A.5: The corresponding scanning electron microscopy (SEM) images of the surface topography under the different numbers of laser scans (N1, N2, and N3).
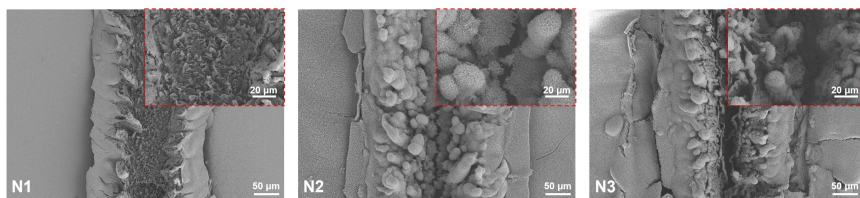
Figure A.6: Roughness results of PDMS microchannel sidewall under different laser scanning times (N1, N2, and N3).

cross-section, line roughness analysis was conducted on the roughest position of the microchannel sidewall for varying numbers of laser scans. The average roughness (R_a) of the microchannel sidewall increased from 0.2 μm to 0.38 μm and 0.60 μm with an increase in the number of scanning times. Meanwhile, the average roughness depth ((R_z)) also increased from 0.92 μm to 1.94 μm and 3.78 μm, respectively. These results clearly show that the microchannel roughness increases with multiple laser scans compared to a single laser scan. This is because as the number of laser scans increases, the 3C-SiC pyrolysis product extends further into the PDMS, leading to an increase in thermal expansion and interfacial stress between the PDMS substrate and the 3C-SiC pyrolysis product. As a result, the interlayer dislocation between the 3C-SiC pyrolysis products and PDMS results in an increase in the surface roughness of the PDMS microchannels.
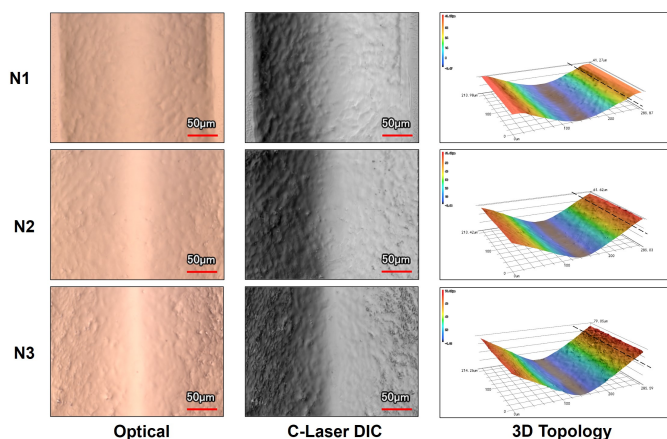
Figure A.7: Optical, DIC, and 3D topological figures of PDMS microchannels under different numbers of laser scans (N1, N2, and N3).

A.2. MECHANISM ANALYSIS OF LPDW TECHNOLOGY

The schematic diagram of the pyrolysis mechanism under high and low heating rate conditions is illustrated in Figure A.8. In fact, the conversion mechanism of PDMS to 3C-SiC through continuous laser pyrolysis is influenced by various physical conditions. Burn et al. reported on the conversion of siloxane polymers to silicon carbide, which provided a general theory for the pyrolysis of polysiloxane-based materials through a two-step successive pyrolysis [3]. Although their research mainly focuses on siloxane polymers rather than PDMS, it is still informative. Subsequently, Camino et al. conducted further investigations on the pyrolysis of PDMS through experiments and simulations, which revealed two competing mechanisms of molecular (Low heating rate pyrolysis route) and radical mechanisms (High heating rate pyrolysis route) in the pyrolysis behavior of PDMS at different heating rates [4, 5]. Based on the above, Shin et al. proposed a reaction path for laser pyrolysis of PDMS that directly converted it into SiC at low temperature [6].

However, the comparative studies on laser pyrolysis products and processes still need to be clarified. Therefore, we compared and summarized the low-heating-rate and high-heating-rate pyrolysis routes. When the heating rate is lower than 50 °C/min, PDMS is pyrolyzed into various cyclic oligomers at around 500 °C. In this phase, the molecular mechanism dominates and causes the breaking and reforming of Si-O bonds on PDMS chains to form cyclic oligomers. This further induces tight cross-linking of PDMS chains, leading to an increase in thermal stability. Subsequently, under conditions of low chain flexibility, the cyclic oligomers decompose into SiC with a further increase in temperature. When the heating rate is higher than 100 °C/min, PDMS is pyrolyzed into more stable carbide or oxycarbide of silicon in the low-temperature range of 600 °C to 700 °C. The radical mechanism dominates and inhibits the molecular mechanism in this phase, inducing the breaking and reforming of Si-CH3 bonds on PDMS chains to increase the additional cross-linking of PDMS further. This mechanism also leads to the condensation of the remaining main chains, resulting in the derivation of silicon oxides. Finally,
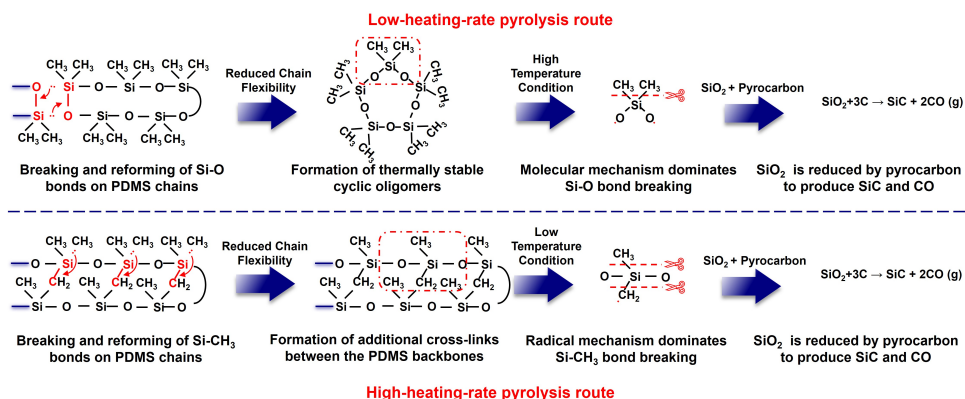
Figure A.8: The pyrolysis mechanisms of PDMS under low-heating-rate pyrolysis and high-heating-rate pyrolysis routes.

the oxides of silicon are reduced by the pyrocarbon in the absence of oxygen to produce silicon carbide (SiC) and carbon monoxide (CO).

A.3. THERMAL AND MECHANICAL EFFECTS OF LPDW TECHNOLOGY
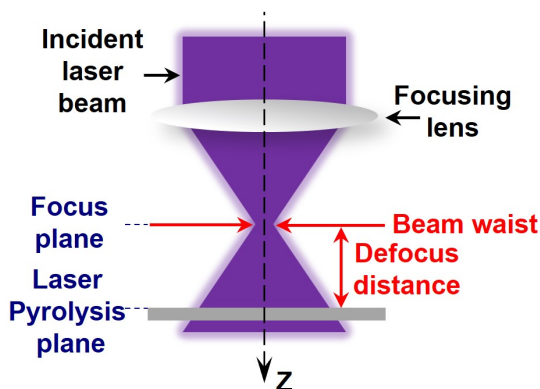
Figure A.9: Schematic illustration of laser pyrolysis parameters in the defocused condition.

During laser scribing, the pyrolysis reaction occurs in a time sequence. Above all, the 6H-SiC NPs at the initial point induce the pyrolysis of PDMS via the photothermal effect, resulting in the generation of 3C-SiC products. Subsequently, the 3C-SiC pyrolysis product absorbs the laser energy and induces the continuous pyrolysis reaction of PDMS in laser moving direction. Consequently, the pyrolysis reaction can be categorized into two different models: the continuous laser pyrolysis process and the initial laser pyroly-
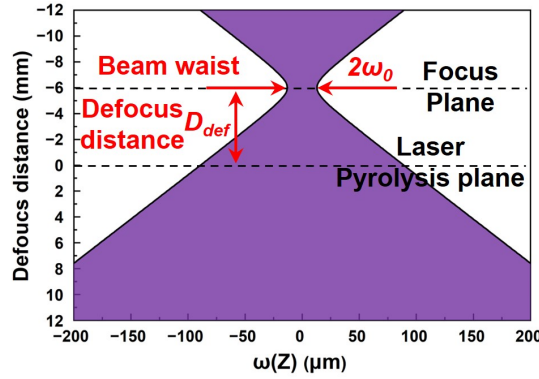
Figure A.10: The functional relationship between the spot radius $\omega(z)$ and the defocus distance (D_{def}) in the defocused state.

sis process. After making some trade-offs between calculation accuracy and calculation time, certain assumptions were applied to FEM (Finite Element Method) calculations, as follows:

(1) The UV laser beam was assumed to follow the Gaussian distribution and was vertically incident on the surface of the SiC pyrolysis product.

(2) The surface morphology of SiC pyrolysis products was assumed to be flat.

(3) The absorption of laser energy on the surface of SiC pyrolysis products was assumed to follow the Beer-Lambert law and was considered a volume heat source.

(4) The heat transfer direction between SiC pyrolysis products and PDMS was assumed to be isotropic.

(5) The heat loss due to phase transition during laser pyrolysis was assumed to be negligible.

After considering the reflection loss and absorption coefficient of the Gaussian light source in the application of the Beer-Lambert law, the heat source density per unit volume at a position (x, y, z) transformed by the photo-thermal effect of the UV laser can be expressed as follows in the Spatial Cartesian coordinate system:

$$q(x, y, z) = \alpha(1 - R) \frac{2P_{\text{avg}}}{\pi \omega_{\text{def}}^2} \exp\left(-\frac{2(x^2 + y^2)}{\omega(z)^2}\right) \exp(-\alpha z) \tag{A.1}$$

$$\alpha = \frac{4\pi\kappa}{\lambda_0} \tag{A.2}$$

$$R = \frac{(n-1)^2 + \kappa^2}{(n+1)^2 + \kappa^2} \tag{A.3}$$

$$\omega(z) = \omega_0 \sqrt{1 + \left(\frac{z + D_{\text{def}}}{z_R}\right)^2} \tag{A.4}$$

$$z_R = \frac{\pi \omega_0^2}{\lambda_0} \tag{A.5}$$

where the parameters of α and R are absorption and reflectivity coefficients of material at the incident wavelength, respectively [7, 8]. These parameters can be calculated according to the complex refractive index in formulas (A.2) and (A.3). Furthermore, P_{avg} and ω_{def} denote the average power of the incident laser and the beam radius at the defocused plane, respectively [9].

In the equation (A.4) and (A.5), $\omega(z)$ is a function of the spot radius size along the direction of beam incidence at different positions, while ω_0 is the beam waist of the incident laser beam. The parameter z_R represents the distance along the incident direction of the beam from the waist to a section where the cross-sectional area is twice that of the waist [10].

Meanwhile, the parameter D_{def} is defined as the vertical distance between the focal plane and the laser pyrolysis plane in the defocused state, which is consistent with the definition above, as shown in Figure A.9. The value of D_{def} can be set to zero (when the laser pyrolysis plane coincides with the focal plane), positive (when the laser pyrolysis plane is above the focal plane), or negative (when the laser pyrolysis plane is below the focal plane). When D_{def} is set to -6.0 mm, the corresponding function curve is shown in Figure A.10. Finally, $\exp(-\alpha z)$ is the relative intensity given by the Beer-Lambert law at the different positions inside the 3C-SiC pyrolysis product [11].

As the incident laser energy is absorbed and partially converted into heat, transient heat equation for the spatial distribution(x,y,z)of temperature T(x,y,z,t) at time t as define-difference form:

$$\rho C_p \frac{\partial T}{\partial t} - \nabla \cdot (k \nabla T) = q(x, y, z) \tag{A.6}$$

the corresponding initial condition is written as:

$$T(x, y, z, t = 0) = T_{\mathrm{ext}} = 293.15\,\mathrm{K} \tag{A.7}$$

the boundary conditions are formulated as:

$$\begin{cases} \vec{n} \cdot \vec{q} = h(T_{\mathrm{ext}} - T) \\ \vec{n} \cdot \vec{q} = \varepsilon \sigma (T_{\mathrm{amb}}^4 - T^4) \\ \vec{n} \cdot \vec{q} = 0 \end{cases} \tag{A.8}$$

where the ρ, C_p, and k are density, heat capacity, and thermal conductivity of the material in the heat conduction system, respectively. T_{ext} and T_{amb} are the external temperature and ambient temperature, respectively, in the equation (A.7) and (A.8). Additionally, h, ϵ, and σ are the heat transfer coefficient, emissivity, and Boltzmann constant [12, 13]. The heat transfer coefficients for the top and bottom surfaces of the material are determined using empirical formulas, resulting in values of 17.9 W/m^2/K and 9.0 W/m^2/K, respectively [14]. These coefficients are used to characterize the heat exchange process between the material and the surrounding air during natural convection process.

In addition, much attention has been paid to investigating the deformation and stress resulting from the photothermal effect during continuous laser pyrolysis. Therefore, we conducted a thermomechanical coupling analysis of continuous laser pyrolysis. To simulate changes in stress and deformation using the finite element method (FEM), certain assumptions were applied in the computational model, as follows:
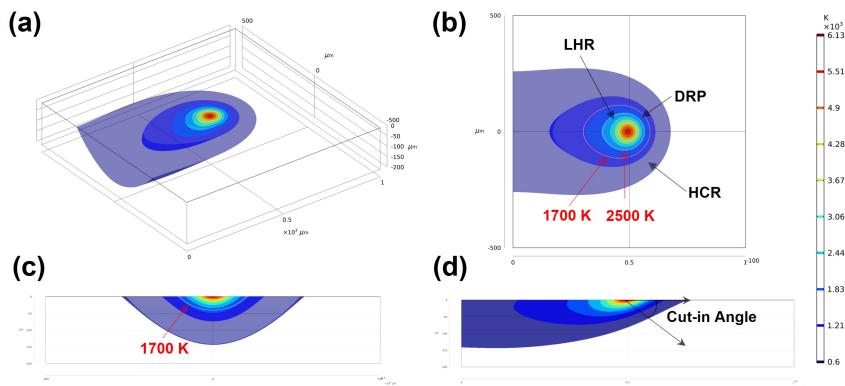
Figure A.11: (a) 3D isothermal surface distribution of the initial pyrolysis process and corresponding top view (b) and cross-sectional views (c) and (d) (Y = 0 µm and X = 500 µm).
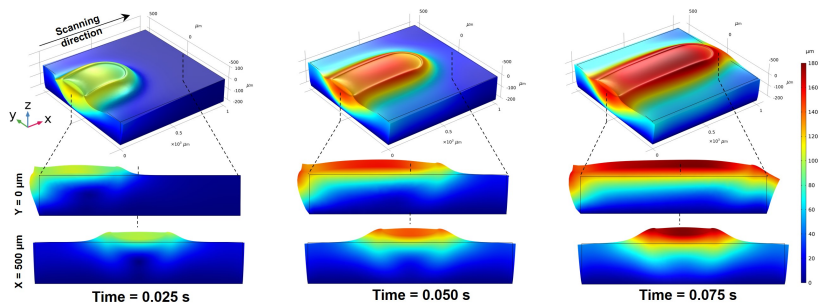
Figure A.12: 3D and cross-sectional distributions of the deformation evolution of PDMS and SiC during continuous laser pyrolysis (Time = 0.025, 0.050, and 0.075 s).
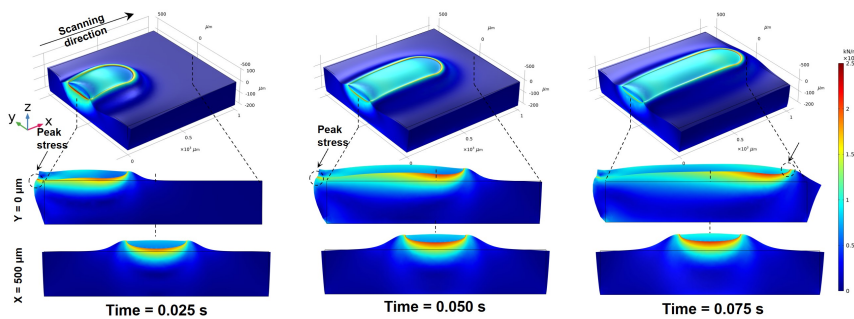

Figure A.13: 3D and cross-sectional distributions of the stress evolution of PDMS and SiC during continuous laser pyrolysis (Time = 0.025, 0.050, and 0.075 s).

(1) The mechanical properties, stress, and strain of the material changed linearly during a small-time increment.

(2) In the plastic zone, the material followed the hardening rule and flow rule.

(3) The material underwent plastic deformation following the law of constant volume.

(4) The yield deformation process of the material followed the Von Mises yield criterion.

When implementing thermomechanical coupling using finite element simulation, it is necessary to analyze and define the elastic-plastic deformation of materials induced by thermodynamics. The elastic strain is determined according to isotropic Hooke's law with temperature-dependent Young's modulus E and Poisson's ratio v. The thermal strain is obtained from the coefficient of thermal expansion α. Plastic strains are obtained through elastoplastic constitutive equations, which consider the von Mises yield criterion, isotropic hardening rules, and temperature-dependent mechanical properties. The relationship between stress and strain can be expressed as follows:

$$\{d\sigma\} = [D]\{d\varepsilon\} - \{C\}dT \tag{A.9}$$

where $[D]$ is elastic-plastic stiffness matrix, $\{C\}$ is vector matrix related to temperature T, dT is temperature increment [15].

Figure A.12 shows the 3D and cross-sectional distributions of the deformation evolution during continuous laser pyrolysis. It was evident that both the 3C-SiC and PDMS underwent significant thermal expansion due to the laser photothermal effect, and their morphology was consistent with experimental results. Due to the different coefficients of thermal expansion, there was an apparent interlayer mismatch between the 3C-SiC and PDMS. The maximum deformation values at different time stages were 117.0 μm, 155.3 μm, and 180.0 μm, respectively. Interestingly, the maximum deformation occurred behind the position of the laser spot, as indicated by the 2D deformation distribution parallel to the laser scanning direction. This phenomenon is because the deformation of the 3C-SiC pyrolysis product at the center of the spot is limited by the half-surrounding PDMS in the forward direction.

Figure A.13 shows the 3D and cross-sectional distributions of the stress evolution during continuous laser pyrolysis. Obviously, the stress distribution at the interface of PDMS and 3C-SiC was much larger than that in other regions. Meanwhile, the 2D stress distribution parallel to the laser scanning direction showed that the maximum stress positions occurred in the edge region of the PDMS substrate. Correspondingly, the maximum stress values at different time stages were 2213.4 kN/m^2, 1675.2 kN/m^2, and 2466.92 kN/m^2, respectively. This also indicated that the stress distribution in the intermediate stage was more uniform and stable than in the initial and final stages, during the continuous laser pyrolysis process. The two-dimensional stress distribution perpendicular to the laser scanning direction demonstrated that the stress distribution was most concentrated in the area directly below the SiC. This further explains why the SiC pyrolysis products can be easily peeled off from the PDMS substrate. The principal stress line distribution can more intuitively display the stress distribution between PDMS and 3C-SiC, as shown in Figure A.14.
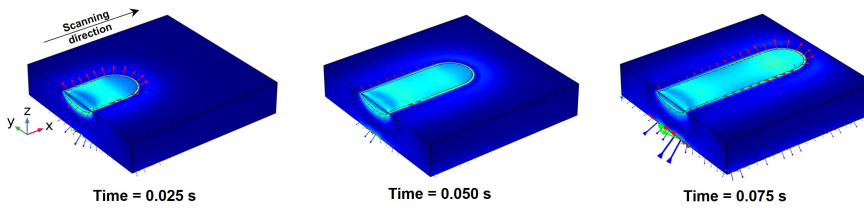
Figure A.14: The principal stress line distributions of PDMS and SiC during continuous laser pyrolysis (Time = 0.025, 0.050, and 0.075 s).

REFERENCES

[1] K. Dongfang *et al.*, "Effect of laser powder bed fusion process parameters on the microstructures, mechanical properties, and conductivity of CuCrZr alloy", *Journal of Materials Engineering and Performance*, pp. 1–14, 2024.

[2] F Moufekkir, M. Moussaoui, A Mezrhab, H Naji, and D Lemonnier, "Numerical prediction of heat transfer by natural convection and radiation in an enclosure filled with an isotropic scattering medium", *Journal of Quantitative Spectroscopy and Radiative Transfer*, vol. 113, no. 13, pp. 1689–1704, 2012.

[3] G. T. Burns, R. B. Taylor, Y. Xu, A. Zangvil, and G. A. Zank, "High-temperature chemistry of the conversion of siloxanes to silicon carbide", *Chemistry of materials*, vol. 4, no. 6, pp. 1313–1323, 1992.

[4] G. Camino, S. Lomakin, and M. Lazzari, "Polydimethylsiloxane thermal degradation. Part 1. Kinetic aspects", *Polymer*, vol. 42, no. 6, pp. 2395–2402, 2001.

[5] G. Camino, S. Lomakin, and M Lageard, "Thermal polydimethylsiloxane degradation. Part 2. The degradation mechanisms", *Polymer*, vol. 43, no. 7, pp. 2011–2015, 2002.

[6] J. Shin *et al.*, "Monolithic digital patterning of polydimethylsiloxane with successive laser pyrolysis", *Nature Materials*, vol. 20, no. 1, pp. 100–107, 2021.

[7] J. I. Larruquert, A. P. Pérez-Marín, S. García-Cortés, L. Rodríguez-de Marcos, J. A. Aznárez, and J. A. Méndez, "Self-consistent optical constants of SiC thin films", *JOSA A*, vol. 28, no. 11, pp. 2340–2345, 2011.

[8] X. Zhang, J. Qiu, X. Li, J. Zhao, and L. Liu, "Complex refractive indices measurements of polymers in visible and near-infrared bands", *Applied optics*, vol. 59, no. 8, pp. 2337–2344, 2020.

[9] G. Poulain, D. Blanc, A. Kaminski, B. Semmache, and M. Lemiti, "Modeling of laser processing for advanced silicon solar cells", in *Excerpt from the Proceedings of the COMSOL Conference*, 2010.

[10] B. E. Saleh and M. C. Teich, "Fundamentals of photonics john wiley & sons", *Inc., Hoboken NJ*, vol. 2, 1991.

[11] W. J. Marshall, "Two methods for measuring laser beam diameter", *Journal of Laser Applications*, vol. 22, no. 4, pp. 132–136, 2010.

[12]   M. Darif, N. Semmar, and F. Orléans Cedex, "Numerical simulation of si nanosecond laser annealing by COMSOL multiphysics", in *Proceedings of the COMSOL Conference 2008 Hannover*, 2008, pp. 567–571.

[13]   W. Wang *et al.*, "Controlling the laser induction and cutting process on polyimide films for kirigami-inspired supercapacitor applications", *Science China Technological Sciences*, vol. 64, no. 3, pp. 651–661, 2021.

[14]   X. Ruan, R. Wang, J. Luo, Y. Yao, and T. Liu, "Experimental and modeling study of CO2 laser writing induced polyimide carbonization process", *Materials & Design*, vol. 160, pp. 1168–1177, 2018.

[15]   Q.-h. Zhang, Y. Ma, C. Cui, X.-y. Chai, and S.-h. Han, "Experimental investigation and numerical simulation on welding residual stress of innovative double-side welded rib-to-deck joints of orthotropic steel decks", *Journal of Constructional Steel Research*, vol. 179, p. 106 544, 2021.

B

SUPPORTING INFORMATION
CHAPTER 3

B.1. SENSOR FABRICATION PROCESS

| After Cutting | After Spin-coating | After Patterning | After Cleaning |
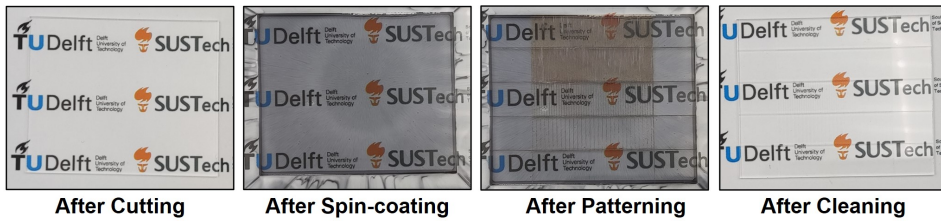
Figure B.1: PDMS surface microstructure fabrication process based on laser transmission pyrolysis.

Sputtering Process
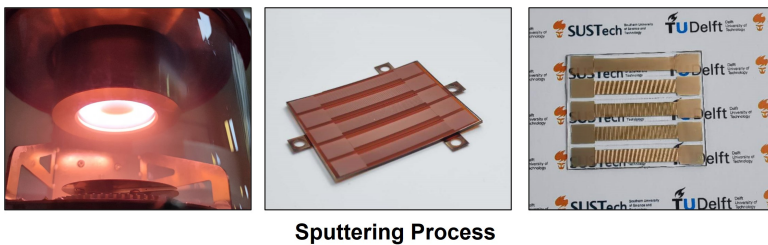
Figure B.2: Metal sputtering process of PDMS with surface microstructure.

B.2. SENSOR TEST PLATFORM
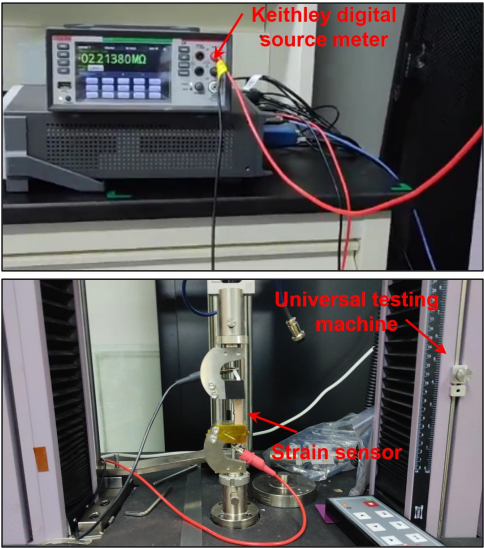
Figure B.3: Performance test platform of flexible strain sensor.
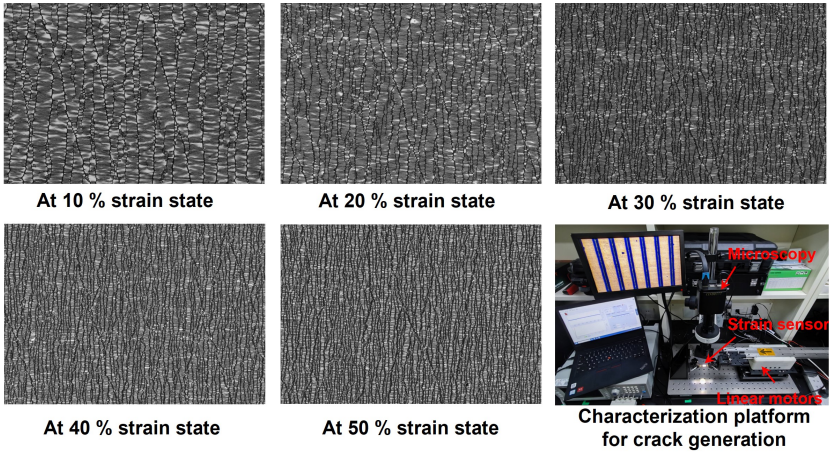
Figure B.4: Generation and expansion of metal cracks on PDMS surface under different strain states.

C

SUPPORTING INFORMATION
CHAPTER 4

C.1. MATERIAL COMPOSITION OF In$_2$O$_3$ NP PASTE
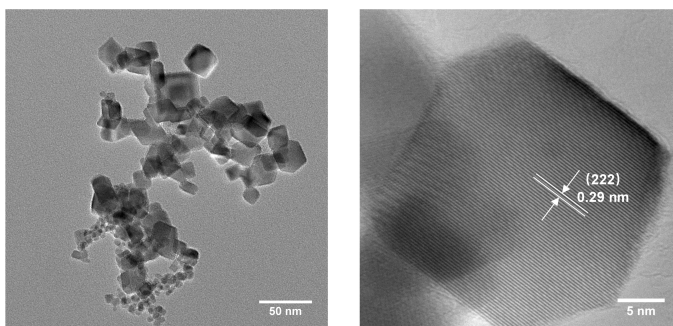
Figure C.1: High resolution transmission electron microscopy (HR-TEM) images of In$_2$O$_3$ NPs.

Indium oxide (In$_2$O$_3$) nanoparticles are renowned across various domains for their unique physical and chemical properties. These nanoparticles are highly valued for their exceptional electrical conductivity and transparency, which are crucial for electronics and touchscreen applications. Additionally, In$_2$O$_3$ demonstrates superior catalytic performance in photocatalysis and electrocatalysis thanks to the synergistic effects of its distinctive optical properties, large specific surface area, oxygen vacancies, and doping effects. These attributes enhance the efficacy of In$_2$O$_3$ in sensing, catalysis, and electronic device applications. Their robust environmental stability and biocompatibility further extend their utility into environmental and biomedical fields. The versatile and multifaceted nature of In$_2$O$_3$ nanoparticles makes them a valuable material for cutting-edge research and diverse applications in electronics, energy, environmental science, and biomedicine. In this study, all chemicals were sourced from commercial suppli-
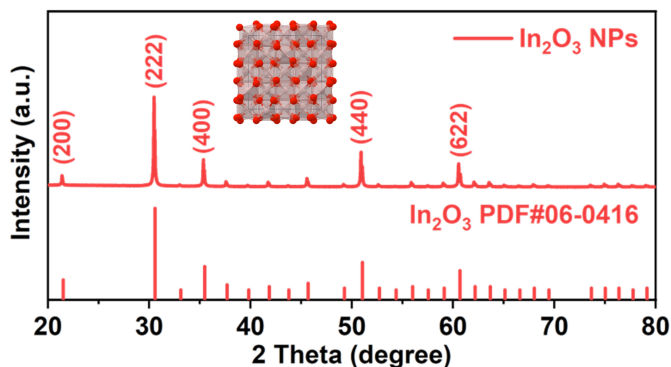
Figure C.2: X-ray diffraction (XRD) pattern of In_2O_3 NPs.
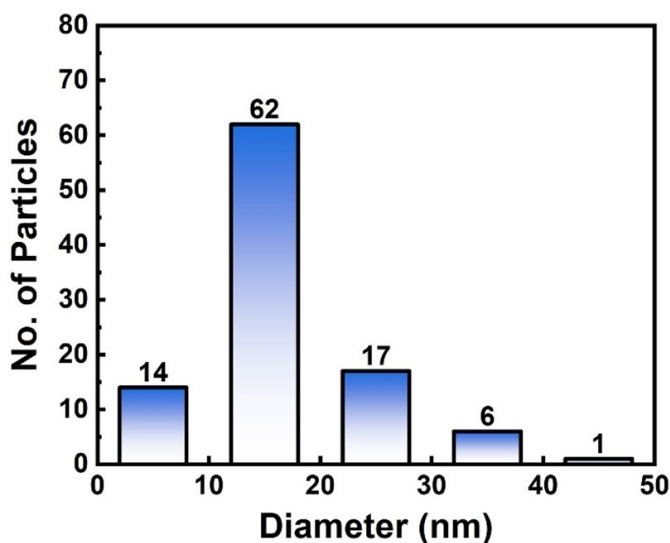
Figure C.3: Statistical distribution of In_2O_3 NP sizes.

ers and required no further purification. To further elucidate the microstructure and morphological characteristics of the In_2O_3 nanoparticles, comprehensive characterization was conducted. The 0.29 nm spacing observed in the high-resolution transmission electron microscope (HR-TEM) image confirmed the (222) lattice plane of the cubic In_2O_3 crystalline phase, as evidenced by Fast Fourier Transform (FFT) patterns showing diffraction along the [111] axis (Figure C.1). The crystal structure was analyzed using powder X-ray diffraction (XRD), with all peaks corresponding to the standard In_2O_3 PDF card (JCPDS card number 06-0416) (Figure C.2) [1]. Additionally, a statistical distribution analysis of the nanoparticle sizes (Figure C.3) revealed that the diameter of the In_2O_3 nanoparticles predominantly falls within the 10-20 nm range. The smaller size of these

particles posed notable challenges in achieving an even dispersion in the paste.

Cetyltrimethylammonium bromide (CTAB), a cationic surfactant, plays a critical role in enhancing the dispersion and stability of solutions. It optimizes the application of nanomaterials by reducing the aggregation of nanoparticles and effectively maintaining their uniform dispersion [2, 3].

Ethylcellulose (EC), serving as a thickener, not only increases the viscosity of the paste but also provides necessary structural stability. Post-sintering, EC is integral to achieving firm adhesion to the PET surface, thereby improving the viscosity of the paste and film-forming properties. In the selective reduction laser sintering (SRLS) process, EC is crucial for stable fixation [4].

Polyvinylpyrrolidone (PVP), also used as a thickener, coats the surface of nanoparticles to enhance inter-particle repulsion through interactions of its polar groups with the nanoparticle surfaces. This enhances the dispersion of nanoparticles in the paste and prevents their adhesion and agglomeration [5]. Furthermore, PVP serves as a binder in the paste, improving both the adhesion of the paste and its adherence to the substrate during the coating process. Most importantly, during the SRLS process, PVP undergoes pyrolysis, producing reducing agents that facilitate the selective reduction of nanoparticles [6].

1-Pentanol, utilized as a solvent, plays a pivotal role in regulating the viscosity and flowability of pastes and in facilitating the homogeneous mixing of ingredients. Due to its relatively low polarity compared to solvents like ethanol, 1-pentanol is particularly effective in dispersing indium oxide nanoparticles. With a boiling point of approximately 137 °C, 1-pentanol evaporates more slowly than ethanol, which boils at 78 °C. This slower evaporation rate helps prevent crack formation in the In$_2$O$_3$ layer during the drying of the paste. Therefore, 1-pentanol is the ideal solvent choice for preparing In$_2$O$_3$ pastes [7].

C.2. THERMAL ANALYSIS OF IN$_2$O$_3$ NP PASTE

To preliminarily explore the physical and chemical changes of In$_2$O$_3$ NP paste during the SRLS process, we conducted thermogravimetric (TG) and derivative thermogravimetry (DTG) analyses on both the paste and the carrier materials. For the carrier material, using polyvinylpyrrolidone (PVP) as the main thickener component, the mass loss process under increasing temperature can be categorized into three distinct stages (Figure C.4(a)). In the first stage (30-190 °C), a mass reduction (9.98%) is mainly due to the volatilization of the solvent (1-pentanol). In the second stage (190-390 °C), the mass reduction (29.39%) is primarily attributed to the cleavage of the pyrrolidone rings in PVP and the decomposition of its side chains [8]. In the third stage (390-640 °C), the significant mass reduction (58.66%) is mainly attributed to the reductive macroradicals formed by the scission of the main chain in PVP, which is subsequently further oxidized [9].

Similarly, the thermal weight loss process of In$_2$O$_3$ NP paste also progresses through three stages. In the first stage (30-170 °C), the mass reduction (1.79%) is mainly due to the volatilization of the organic solvent. In the second stage (170-300 °C), the mass reduction (2.86%) occurs from the decomposition of PVP side chains. In the final stage (300-550 °C), the primary mass loss (14.13%) can be attributed to the decomposition of the PVP mainchain and the reduction of In$_2$O$_3$ to metallic In, which resulted in the
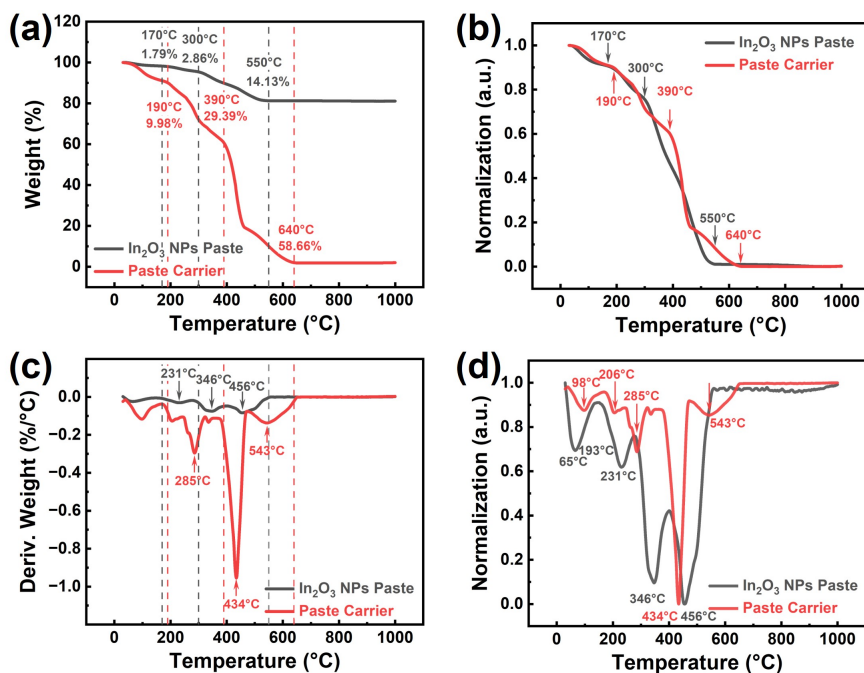
Figure C.4: (a) Thermogravimetric (TG) and (b) normalized TG analysis curves for In$_2$O$_3$ paste and its carrier materials. (c) Derivative thermogravimetric (DTG) and (d) normalized DTG analysis curves for In$_2$O$_3$ paste and its carrier materials (Under air conditions, a heating rate of 10 °C/min).

formation of OV defects in In$_2$O$_3$. The corresponding DTG curves have the same trend as the slope of the TG curves described above, except for differences in the vertical axis due to the difference in effective content (Figure C.4(c)). Overall, the addition of In$_2$O$_3$ NPs reduces the thermal stability of the paste and accelerates the rate of thermal weight loss in the carrier material system. A significant change in the trend of these curves is clearly observed in the comparison of normalized TG and DTG curves (Figure C.4(b) and C.4(d)).

The addition of In$_2$O$_3$ NPs increases the porosity among the carrier materials, which accelerates the volatilization of organic solvents. Furthermore, the high thermal conductivity of In$_2$O$_3$ leads to an overall shift in the peak of the DTG curve [10]. Notably, the DTG peaks of the In$_2$O$_3$ NP paste at 346 °C and 456 °C suggest these are the critical temperatures where the reduction reaction is most intense, corresponding to the third stage of PVP decomposition in the carrier material, which occurs over the temperature range of 300-500 °C with a mass loss of 14.13%. However, it remains challenging to determine the predominant temperature at which the reduction of In$_2$O$_3$ NPs occurs, as the correspondence between the DTG peaks of the paste and its carrier material is not clear.

To further investigate the dominant temperature at which the reduction reaction of In$_2$O$_3$ NPs occurs, we conducted a series of calcination experiments under controlled
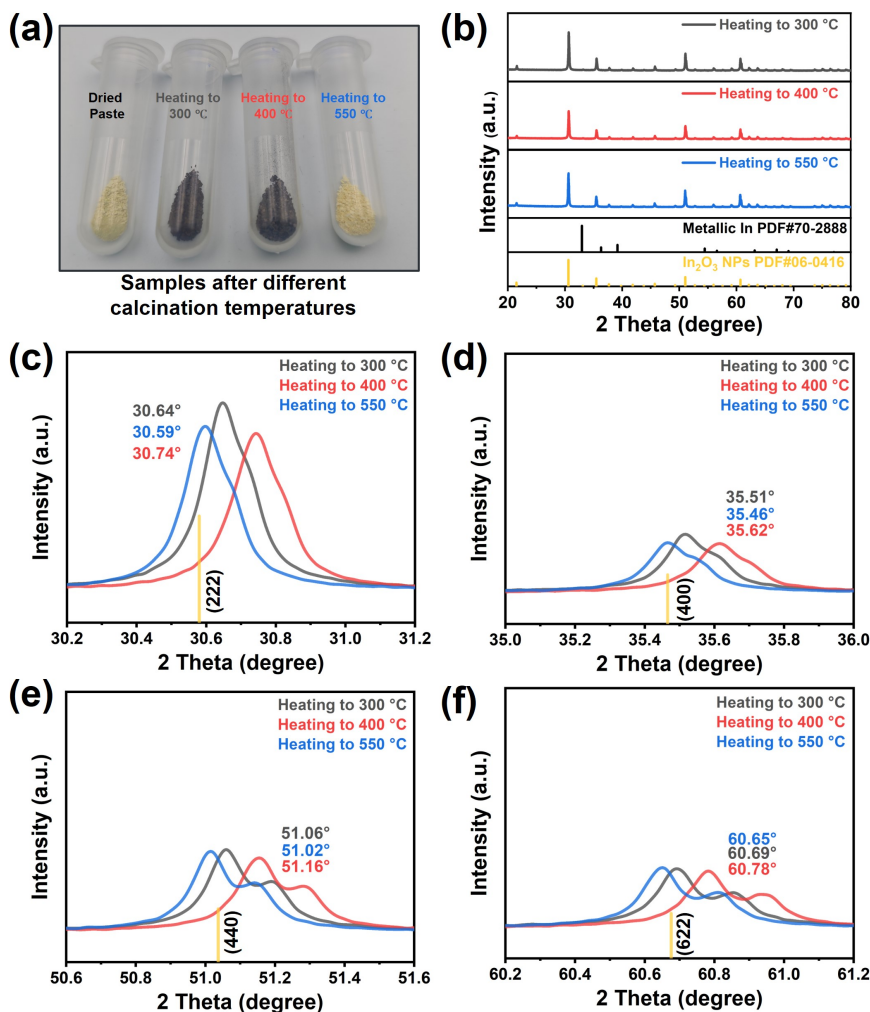
Figure C.5: (a) Images of In_2O_3 NP paste before and after calcination. (b) X-ray diffraction (XRD) patterns and (c)-(f) local patterns of In_2O_3 NP paste under different calcination temperatures (300, 400, and 550 °C).

conditions (Equipment: Muffle furnace; Atmosphere: Air; Heat-up rate: 10 °C/min; Final temperatures: 300, 400, and 550 °C). After calcination, we performed X-ray diffraction (XRD) analysis to examine changes in the crystal structure of the In_2O_3 NP pastes and recorded the changes in the color of its samples (Figure C.5(a)).

At a calcination temperature of 300 °C, the paste turns black, implying that the PVP coating on the surface of In_2O_3 decomposes under high temperatures into residual black pyrolysis products. As the temperature increases to 400 °C, the color of the slurry powder changes to dark brown, indicating that the pyrolytic carbon layer begins to oxidize.

When the temperature reaches 550 °C, the black pyrolysis product layer is completely ox-
idized, leading to re-oxidation of the reduced In_2O_3 in the paste. As a result, the color of
the paste powder returns to a creamy white color with a brighter luster than the original
paste powder, indicating that In_2O_3 has regained its original crystal structure.

The X-ray diffraction (XRD) patterns of In_2O_3 NP paste at varying calcination temper-
atures were further analyzed (Figure C.5(b)). Compared to the high-temperature gradi-
ent brought about by the SRLS, the low and uniform heating of calcination is still limited
for the modification of In_2O_3 NP paste. Therefore, we performed further analyses of the
enlarged XRD patterns of In_2O_3 powders on (222), (400), (440), and (622) crystal planes
at different calcination temperatures (Figure C.5(c)-(f)). Focusing on the (222) crystal
plane, at a lower calcination temperature of 300 °C, the diffraction peaks (black line)
shifted to a higher 2θ angle, showing enhanced intensity and reduced crystal spacing.
This indicates a lattice contraction, which is even more pronounced after calcination at
400 °C, where the diffraction peaks (red line) undergo significant shifts, further decreas-
ing lattice constants and tightening lattice spacings. However, the peak position (30.59°)
of the diffraction peak (blue line) after calcination at 550 °C is highly consistent with the
typical XRD peak position (30.58°) of In_2O_3, confirming that the high-temperature treat-
ment at 550 °C restores the In_2O_3 paste powders to their intrinsic crystalline state. These
observations suggest that the reduction of In_2O_3 NPs to metallic In and the formation of
oxygen vacancy (OV) defects predominantly occur at 456 °C. This specific temperature
is associated with the main decomposition temperature of the third stage of the paste
carrier (434 °C).
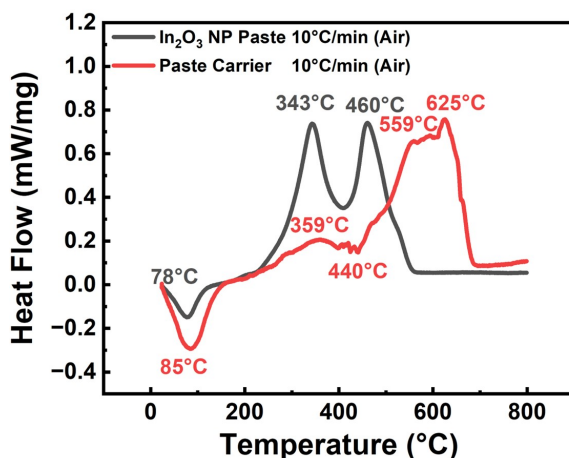
Figure C.6: Differential scanning calorimetry (DSC) of In_2O_3 NP paste and carrier at 10 °C/min heating rate in
air.

To further clarify the thermal reaction mechanism of In_2O_3 NP paste and its carrier,
differential scanning calorimetry (DSC) was employed to analyze the heat flow changes
in air conditions (Figure C.6). In the low-temperature range (0 °C to about 200 °C), the
DSC curves for both samples display similar endothermic peaks at 78 °C and 85 °C, pri-

marily due to the volatilization of the solvent in the paste and carrier. However, beyond 200 °C, the thermal behavior of the two samples diverged significantly. For the carrier paste (red line), a minor exothermic peak observed at 359 °C is primarily attributed to the cleavage or decomposition of the five-membered ring structures within the PVP side chains. As the temperature increases to 440 °C, an endothermic peak occurs, indicating that the backbone of PVP begins to undergo random chain scission. This is followed by another exothermic peak at 559 °C, which signals further decomposition of PVP into smaller organic molecules or gases. The most significant thermal event is recorded at 625 °C, where a major exothermic peak represents the vigorous reaction between the decomposition products of PVP and oxygen, generating considerable heat. In comparison, the In_2O_3 NP paste (black line) exhibits two significant exothermic peaks at 343 °C and 460 °C. The peak at 343 °C corresponds to the further decomposition of PVP, involving the cleavage of PVP side chains and the breakage of cross-linked structures. Notably, the exothermic peak at 460 °C is attributed to the breakdown of PVP backbones and other structural macromolecules. This suggests that In_2O_3 promotes more complex chemical activities, leading to the complete combustion or deep oxidation of organic substances. These thermal event sequences are consistent with previous TG/DTG analysis results, illustrating a comprehensive thermal degradation profile of In_2O_3 NP paste and paste carrier.

C.3. PARAMETER OPTIMIZATION OF SRLS
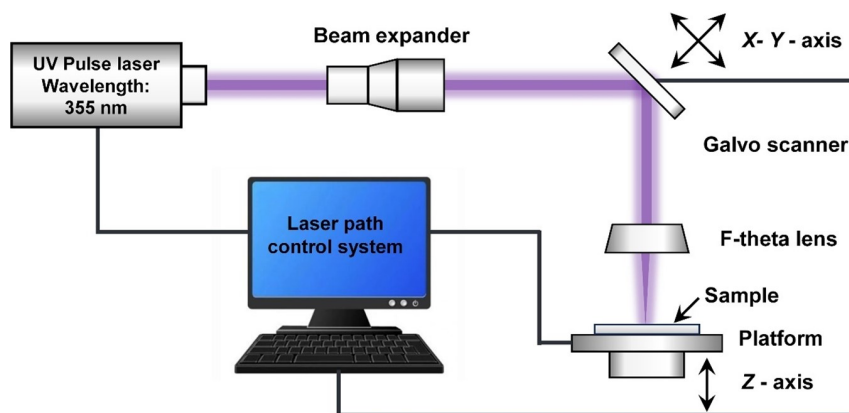
Figure C.7: Schematic diagram of the UV laser system (Wavelength: 355 nm).

To investigate the effects of different laser parameters on the SRLS process, we conducted a series of comprehensive optimization experiments. Through experimental design, we adjusted the laser scanning speed (V_{ss}), average laser power (P_{avg}), pulse repetition frequency (F_{pr}), and defocus distance (D_{def}), which are closely related to the sensor performance and fabrication efficiency.

The V_{ss} regulates the scanning speed of the laser over the surface of the In_2O_3 NP paste, which ensures efficient heat accumulation while preventing excessive damage to
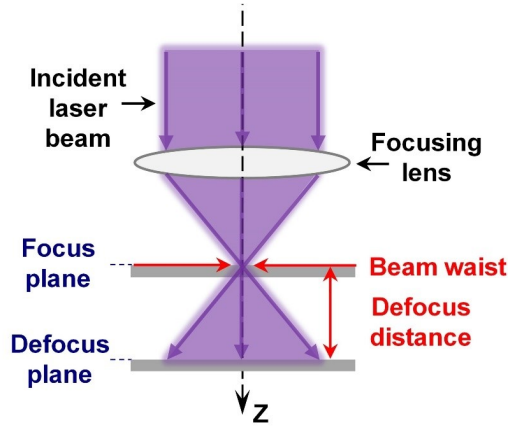
Figure C.8: Schematic representation of laser under focused and defocused conditions.

the PET substrate. The P_{avg} influences the amount of energy delivered to the In_2O_3 NP paste, which directly affects the intensity and range of the thermal effects in the laser ablation and sintering regions. The F_{pr} adjusts the degree of overlap of the pulsed laser on the In_2O_3 NP paste, which affects the smoothness and uniformity of the laser ablated region as well as the microstructural characteristics of the laser sintered region. The D_{def} determines the alignment accuracy between the laser focus and the In_2O_3 NP paste, which affects the energy distribution of the laser spot during the SRLS process (Figure C.8).

In the initial phase of optimization, we focused on fine-tuning the parameters in the SRLS process in order to optimize the quality of the linear laser scanning region. The main challenges are the variability of the laser parameter settings and the adhesion of the sintered region to the substrate.

The SRLS technology requires fine control of several key parameters that are essential to achieve accurate sintering results. The complexity of managing these different parameters adds significantly to the complexity of the experimental setup. In addition, ensuring effective adhesion between the sintered region and the PET substrate after sintering is also a serious challenge. This adhesion is crucial for the long-term stability of the sensor and is essential for the practical application of the device. Notably, the presence of ethyl cellulose (EC) in the paste plays an important role in enhancing this stability, greatly improving the overall integrity and functionality of the flexible gas sensor [11]. In addition, a higher pulse repetition frequency (F_{pr} = 200 kHz) has a significant positive effect on improving the quality of laser sintering [12]. On this basis, we further fixed the laser scanning speed (V_{ss} = 10 mm/s) to verify other laser parameters.

With the fixed V_{ss} and F_{pr}, we investigated the effects of P_{avg} and D_{def} on the surface morphology of In_2O_3 NP pastes using scanning electron microscopy (SEM) (Figure C.9). An increase in the P_{avg} (from left to right) leads to more pronounced particle rearrangement and eutectic fusion in the laser scanning region, which exacerbates the sintering and melting of particles. This is mainly attributed to the increase in sintering tempera-
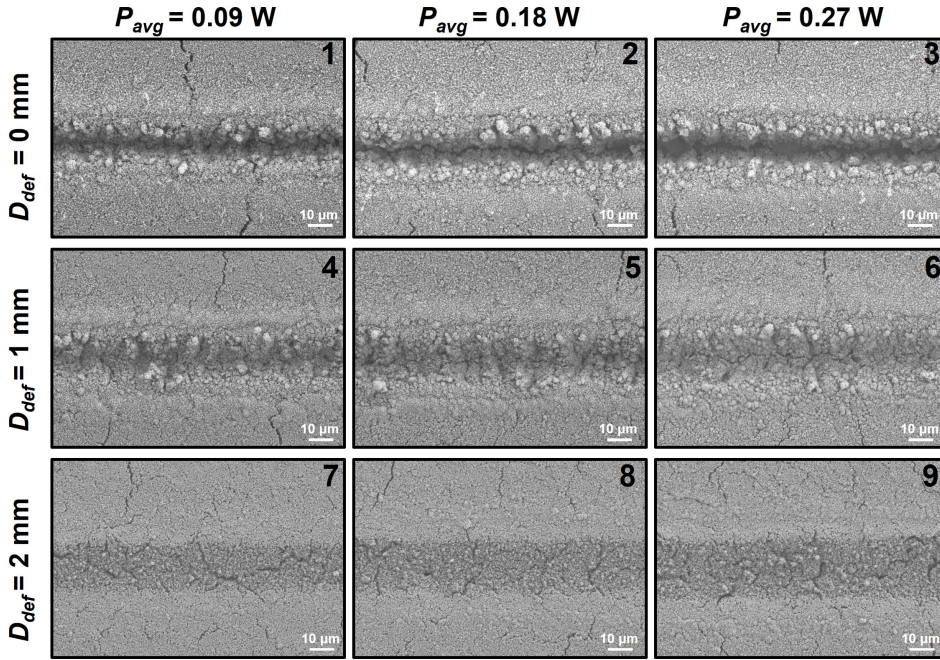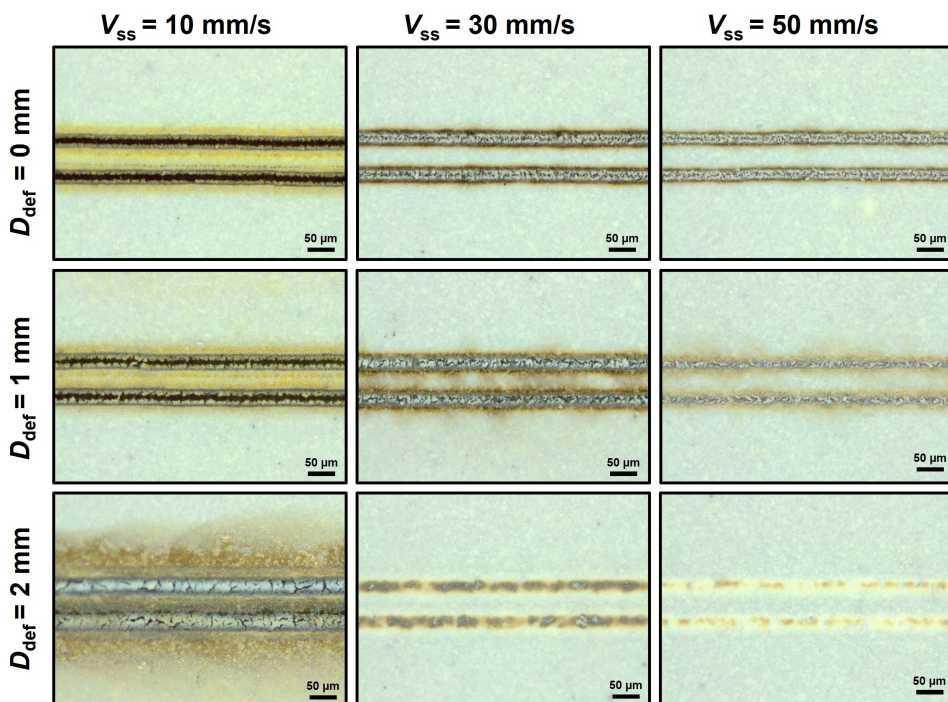
Figure C.9: Scanning electron microscope (SEM) images of the surface morphology of In_2O_3 NP paste after laser scanning at different laser average power (P_{avg}) and defocus distances (D_{def}).

ture due to the increase in laser power. Correspondingly, a decrease in the D_{def} (bottom to top) leads to a significant increase in the ablation depth within the laser scanning region. This is attributed to the increase in energy density due to the reduction of the laser spot area [13].

We further evaluated the linear resistance of the sintered regions over a 5 mm length after the SRLS process (Figure C.10). The analysis reveals notable variations in linear resistance influenced by different settings of average laser power (P_{avg}) and defocus distance (D_{def}). The horizontal axis categorizes the settings by laser average power: 0.09 W (Nos. 1, 4, 7), 0.18 W (Nos. 2, 5, 8), and 0.27 W (Nos. 3, 6, 9), which correspond to the labeling of their SEM images. At defocus distances of 0 mm and 1 mm, the linear resistance of the sintering regions remains consistently low, indicating effective sintering. Moreover, an increase in P_{avg} generally results in a decrease in line resistance, suggesting that higher laser powers enhance the quality of sintering [14]. In contrast, at a D_{def} of 2 mm, the line resistance significantly increases along with instability. This rise in line resistance is due to the uneven distribution of laser energy density caused by increased defocusing, which compromises the quality of the sintering process. This resistance instability is unacceptable for applications such as gas sensors that rely on resistance changes for detection.

Through the scanning electron microscopy (SEM) analysis of the laser scanning region, we found that SEM can clearly reflect the morphological changes of selective laser
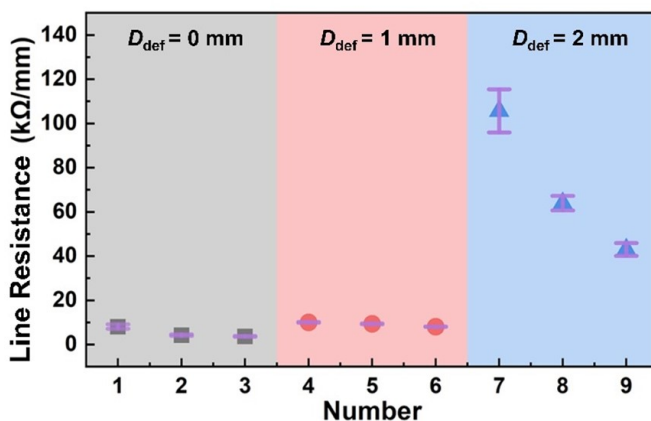
Figure C.10: Statistical data on the line resistance of In_2O_3 NPs at different laser average powers (P_{avg}) with different defocused distances (D_{def}).

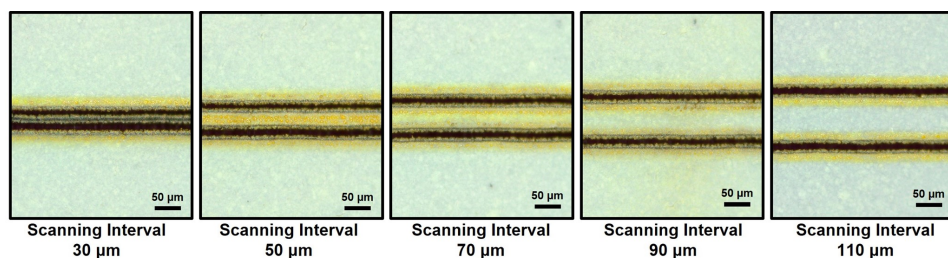

Figure C.11: Optical microscope (OM) images of the surface morphology of In_2O_3 NP paste after laser scanning at different laser scanning speeds (V_{ss}) and defocus distances (D_{def}).

sintering. However, for the topographic characterization of the laser scanning region, optical microscopy (OM) has a significant advantage because it can clearly distinguish

the color change of the sintered region after the SRLS process.

With a fixed P_{avg} of 0.27 W (Figure C.11), we investigated the effects of V_{ss} and D_{def} on the surface morphology of In_2O_3 paste after SRLS by optical microscope (OM). As the V_{ss} increases (from left to right), the destructiveness of the laser to the laser scanning region gradually decreases. However, the heat accumulation in the sintered region decreases considerably, which is unfavorable for the fabrication of the gas sensing region. Especially on PET substrates, it is difficult to ensure the stability and consistency of the fabricated sensor region during the deionized water cleaning process. As the D_{def} decreases (from top to bottom), the laser energy density in the scanning region gradually decreases, which leads to the formation of a smoother direct sintered surface of the In_2O_3 NP paste in the laser scanning region. Correspondingly, the sintering temperature in the sintered region near the laser scanning region decreases. This not only reduces the density of OV defects but also poses a challenge to the adhesion properties between the In_2O_3 layer and the PET substrate.

| Scanning Interval 30 μm | Scanning Interval 50 μm | Scanning Interval 70 μm | Scanning Interval 90 μm | Scanning Interval 110 μm |

Figure C.12: Optical microscope (OM) images of the surface morphology of In_2O_3 NP paste after laser scanning using different laser scanning intervals.

In addition, we also found that the sintering temperature of the laser-sintered region and the effective area of the sensing region can be effectively controlled by adjusting the laser scanning interval (Figure C.11). It is worth noting that when the scanning interval is gradually increased from 30 μm to 110 μm, the width of the laser-sintered regions gradually decreases, and the color of the sintered In_2O_3 NP paste gradually changes from black-brown to yellow and finally transitions to milky white. This color change is consistent with the trend of powder color change after different calcination temperatures in the previous thermal analysis of In_2O_3 NP pastes (Figure C.5(a)). Meanwhile, this change directly reflects the decrease in sintering temperature with increasing scanning interval, which is consistent with the simulation results (Figure 4.1(d)). In addition, this is the key strategy to achieve sensitive regulation of NO_2 gas by regulating the OV defects in the SRLS process.

C.4. Finite element simulation of laser sintering

During the SRLS process, the In_2O_3 NP paste coating on the PET surface acts as an absorber layer to achieve selective sintering through laser-induced photothermal effects. After referring to the literature on the construction of sintering and ablating models for nanoparticles and polymers, we used a heat transfer model to simulate the temperature

distribution between the In_2O_3 paste layer and the PET substrate layer during the laser sintering process [15, 16].

The finite element method (FEM) calculations were conducted under certain assumptions to balance computational accuracy with computational time effectively:

(1) It is assumed that the ultraviolet laser exhibits a Gaussian distribution and is perpendicularly incident on the surface of the In_2O_3 NP paste.

(2) The surface of the In_2O_3 NP paste is presumed to be flat.

(3) It is assumed that the absorption of laser energy by the In_2O_3 NP paste surface follows the Beer-Lambert Law and is considered a volumetric heat source.

(4) The In_2O_3 NP paste and PET substrate material are assumed to be completely uniform internally and to follow Fourier's Law of Heat Conduction.

(5) During the laser sintering process of In_2O_3 NP paste and PET substrate, it is assumed that the heat loss due to phase transitions is negligible.

After considering the reflection loss and absorption coefficient of the Gaussian light source in the application of the Beer-Lambert law, the heat source density per unit volume at a position (x, y, z) transformed by the photothermal effect of the UV laser can be expressed as follows in the Spatial Cartesian coordinate system:

$$q(x, y, z) = (1 - R)F_\eta \exp\left(-\frac{2(x^2 + y^2)}{\omega(z)^2}\right)\exp(-\alpha z) \tag{C.1}$$

$$F_\eta = F(1 + \gamma) = \frac{2P_{avg}}{\pi\omega(z)^2}(1 + \gamma) \tag{C.2}$$

$$\alpha = \frac{4\pi\kappa}{\lambda_0} \tag{C.3}$$

$$R = \frac{(n-1)^2 + \kappa^2}{(n+1)^2 + \kappa^2} \tag{C.4}$$

$$\omega(z) = \omega_0\sqrt{1 + \left(\frac{z + D_{def}}{z_R}\right)^2} \tag{C.5}$$

$$z_R = \frac{\pi\omega_0^2}{\lambda_0} \tag{C.6}$$

where the parameters of R and $1 - R$ are the reflectivity and absorptivity coefficients of material at the incident wavelength, respectively [17]. These parameters can be calculated according to the complex refractive index in formulas (C.3) and (C.4). Meanwhile, F and F_η are the laser flux and effective laser flux, respectively; γ is the over-lapping factor. Furthermore, P_{avg} and ω_{def} denote the average power of the incident laser and the beam radius at the defocused and focused plane, respectively [18].

In the equation (C.5) and (C.6), $\omega(z)$ is a function of the spot radius size along the direction of beam incidence at different positions, while ω_0 is the beam waist of the incident laser beam. The parameter z_R represents the distance along the incident direction of the beam from the waist to a section where the cross-sectional area is twice that of the waist [19].

Correspondingly, the parameter D_{def} is defined as the vertical distance between the focal plane and the laser pyrolysis plane in the defocused state. The value of D_{def} can be set to zero (when the laser sintering plane coincides with the focal plane), positive (when the laser sintering plane is above the focal plane), or negative (when the laser sintering plane is below the focal plane). Finally, $\exp(-\alpha z)$ is the relative intensity given by the Beer-Lambert law at the different positions inside the In_2O_3 NP paste layer [20].

As the incident laser energy is absorbed and partially converted into heat, transient heat equation for the spatial distribution (x, y, z) of temperature $T(x, y, z, t)$ at time t as define-difference form:

$$\rho C_p \frac{\partial T}{\partial t} - \nabla \cdot (k \nabla T) = q(x, y, z) \tag{C.7}$$

the corresponding initial condition is written as:

$$T(x, y, z, t = 0) = T_{ext} = 293.15 \, \text{K} \tag{C.8}$$

the boundary conditions are formulated as:

$$\begin{cases} \vec{n} \cdot \vec{q} = h(T_{ext} - T) \\ \vec{n} \cdot \vec{q} = \varepsilon \sigma (T_{amb}^4 - T^4) \\ \vec{n} \cdot \vec{q} = 0 \end{cases} \tag{C.9}$$

where the ρ, C_ρ, and k are density, heat capacity, and thermal conductivity of the material in the heat conduction system, respectively. T_{ext} and T_{amb} are the external temperature and ambient temperature, respectively, in the equation (S8) and (S9). Additionally, h, ε, and σ are the heat transfer coefficient, emissivity, and Boltzmann constant [21, 22]. The heat transfer coefficients for the top, and bottom surfaces of the material are determined using empirical formulas, resulting in values of 9.0, and 17.9 W/m^2/K, respectively [15, 23]. These coefficients are used to characterize the heat exchange process between the material and the surrounding air during natural convection process.

As the laser spot moves, there are obvious differences in the temperature distribution between the In_2O_3 layer and the PET substrate (Figure C.13). At the moments of 0.15 s and 0.30 s, the heat source caused by the photothermal effect is concentrated on the laser spot and shows a rapid heating effect of the laser on the material system. At the moments of 0.45 s and 0.60 s, the heat energy generated by the laser begins to spread out, showing that heat is transferred from the central region to the boundaries of the material system. This diffusion process is controlled by both the thermal conductivity properties of the material and boundary conditions. At the moments of 0.7 s and 0.9 s, the heat distribution within the model becomes more balanced. As the heat spreads to a wider region, the overall temperature distribution becomes more uniform and tends to reach a temperature equilibrium state. In the corresponding model, the maximum temperature change curves of the In_2O_3 layer and PET substrate clearly demonstrate the trend of temperature evolution (Figure C.14).

Further, we analyzed the temperature distribution model at the midpoint of linear laser scanning (Figure C.15). It can be found that the high temperature is concentrated in the central region of the laser spot, and the heat spreads along the center of the material to the outside through heat conduction. In the top view, we can clearly observe
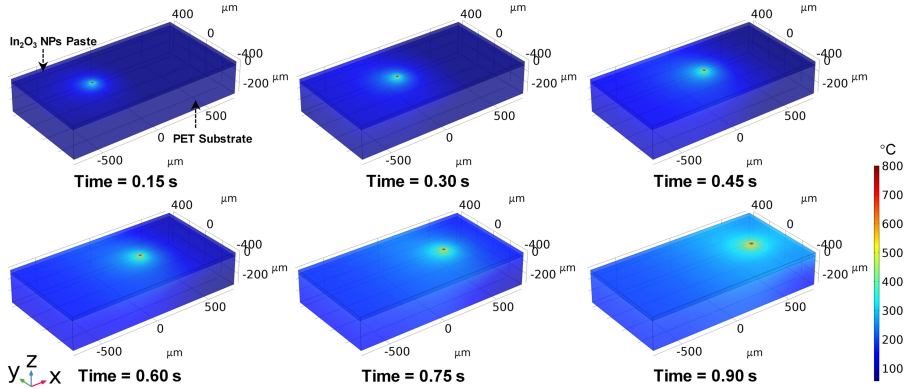
Figure C.13: Evolution of the temperature distribution of the In_2O_3 layer and PET substrate during the SRLS (Time = 0.15, 0.30, 0.45, 0.60, 0.75, and 0.90 s).
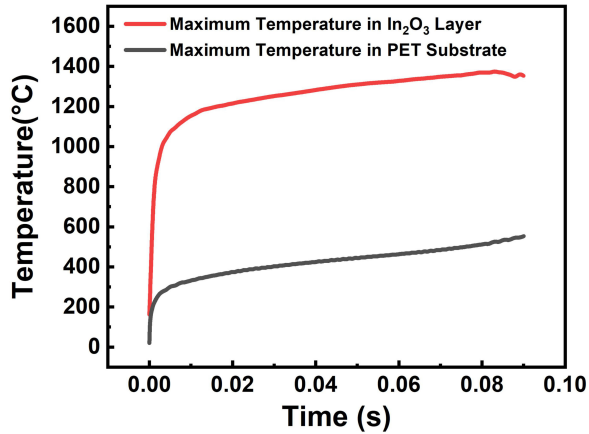

Figure C.14: Curves of the maximum temperature of In_2O_3 with PET layer as a function of time during a single linear laser scanning process.

that the highest temperatures are concentrated in the central region and diminish radially outward, forming distinct concentric isotherms. Additionally, from the side view, it is evident that the temperature decreases gradually from the surface to the bottom, showing a horizontally distributed isothermal layer, indicating that the efficiency of heat propagation is lower in the vertical direction compared to the horizontal direction. The isotherms in the top view further show that most of the heat accumulates around the vertical centerline of the model and spreads around from that center.

At the intermediate moments of the linear laser scanning process of the SRLS, the temperature distributions at different depths perpendicular to the scanning direction $(0, -5, -10, -15,$ and -20 μm) were statistically analyzed in detail (Figure C.16). The re-
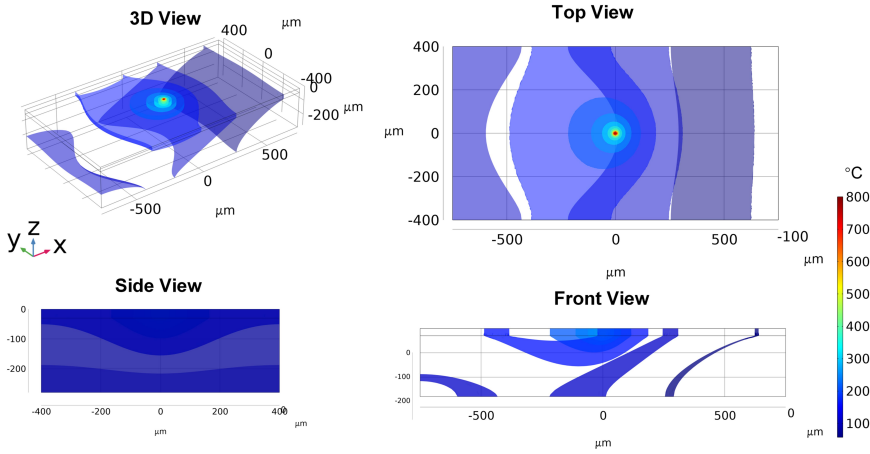
Figure C.15: Three-dimensional isothermal surface distribution of selective reduction laser sintering and the corresponding top view, side view, and front view (Time = 0.45 s).
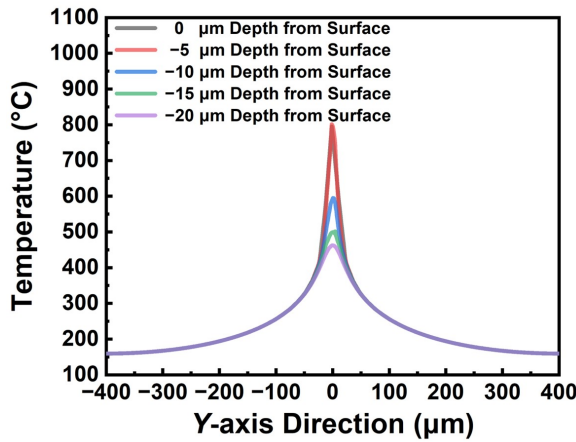
Figure C.16: Temperature distribution statistics for different surface depths (0, −5, −10, −15, and −20 μm) perpendicular to the scanning direction at intermediate moments of linear laser sintering (Time = 0.45 s).

sults clearly show that the temperature decreases exponentially with increasing distance from the center of the laser spot. It is noteworthy that the highest temperature does not occur at the surface of the In_2O_3 layer during linear laser scanning sintering. Instead, the highest temperature actually occurs below the In_2O_3 NP layer. The main reason for this phenomenon is that the simulation model takes into account the heat exchange with the environment, resulting in rapid heat dissipation from the surface layer, with the final peak temperature occurring underneath the laser-irradiated region rather than at the

surface.

However, it should be noted that heat loss due to material phase change and model size effects are not considered in the model, which would result in an overestimation of the maximum temperature trend over time. Despite these limitations of the model, the analysis of the temperature change and distribution still provides a valuable reference for accurate temperature control in the SRLS processes.

C.5. CHARACTERIZATION OF OV DEFECTS IN SENSORS
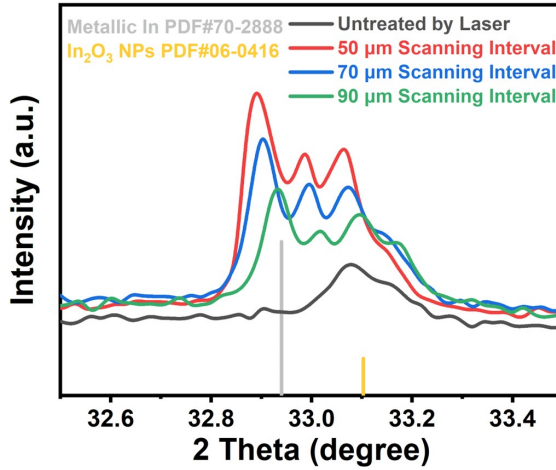
Figure C.17: Local X-ray diffraction (XRD) diffraction pattern of the sensing material after SLRS treatment (2θ range from 32.5° to 33.5°).

As the laser scanning interval decreases, the corresponding average sintering temperature increases. Then, the sintering temperature rises, and the X-ray diffraction (XRD) characteristic peaks of In_2O_3 move towards lower 2θ angles. This phenomenon can be further explained using Bragg's law, which is formulated as:

$$n\lambda = 2d\sin\theta \qquad (C.10)$$

where n is the diffraction order, λ is the wavelength of the X-rays, d is the distance between neighboring crystal planes, and θ is the diffraction angle [24]. Therefore, when the XRD characteristic peaks of In_2O_3 shift to lower 2θ angles, it indicates that the diffraction angle θ is decreasing. If the wavelength λ remains constant, a decrease in the diffraction angle θ implies an increase in the distance d between the crystal planes.

Through detailed observation by scanning electron microscopy (SEM), we noticed that the flexible gas sensor formed porous pyrolytic carbon layers at the edge of the laser-sintered region (Figure C.23) [25]. The main reason for the formation of these pyrolytic carbon layers is the sputtering of part of the PET substrate during the SRLS process. Further energy dispersive X-ray (EDX) analysis confirms that the main composition of these layers is elemental carbon (Figure C.24).
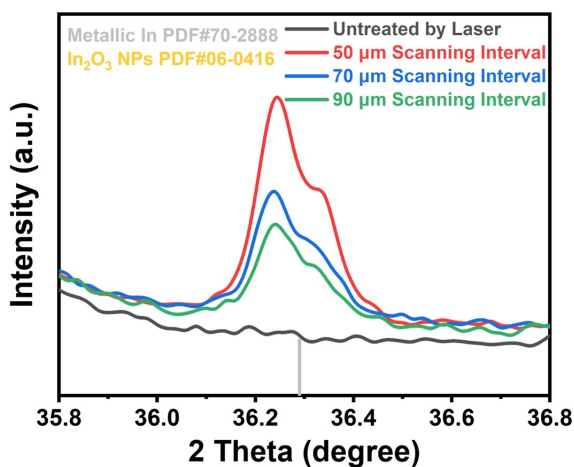
Figure C.18: Local X-ray diffraction (XRD) diffraction pattern of the sensing material after SLRS treatment (2θ from 35.8° to 36.8°).
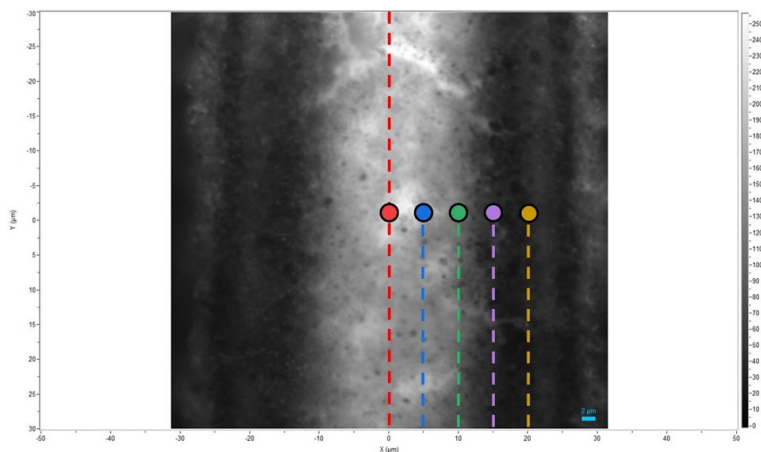

Figure C.19: Selection of Raman spectrum test points at different locations in the laser-sintered region after the SRLS treatment.

Considering the composition of the In_2O_3 NP paste, the primary source of nitrogen is identified as the PVP-$(C_6H_9NO)_n$, which serves as a thickening and reducing agent [8, 26]. During the SRLS process, PVP undergoes thermal decomposition at high temperatures to produce reducing macromolecules (Figure C.25). At the same time, the high temperature also induces the pyrolysis of PET to produce pyrolytic carbon, which is sputtered on the surface of the laser-sintered region. These results lead to an increase in the content of C species and a decrease in the content of In and O species in the sensing region. In detail, before the SRLS treatment, the C 1s peaks at 284.8 eV, 285.88 eV, and 288.60 eV detected within the In_2O_3 NP paste are attributed to the chemical bonding en-
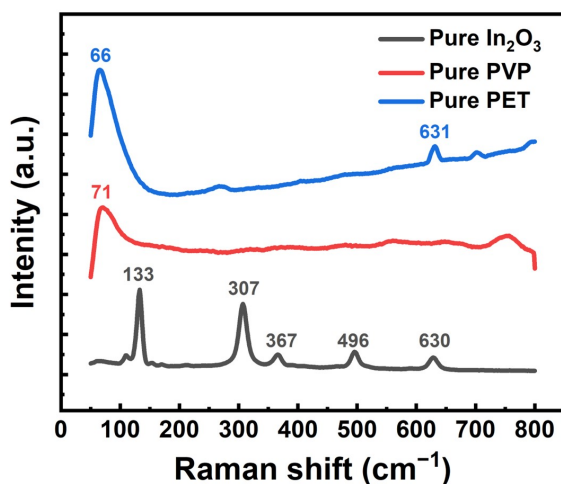
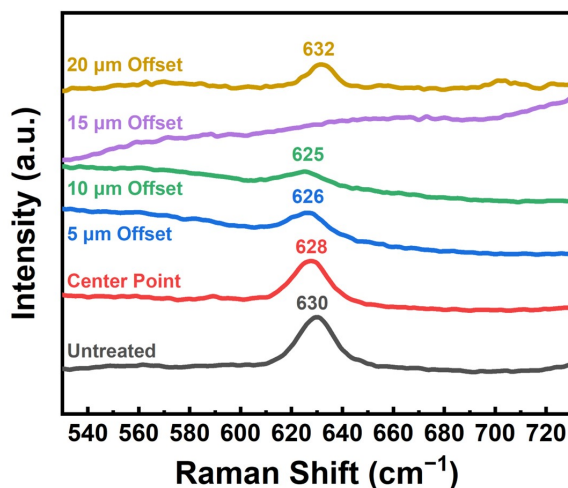Figure C.20: Overall Raman spectra of pure In_2O_3, PVP, and PET.
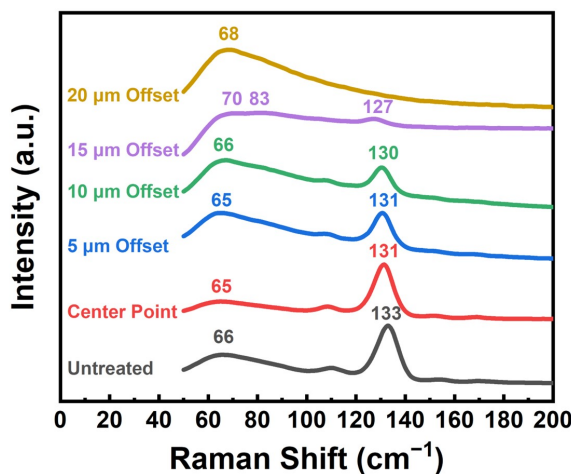
Figure C.21: Local Raman spectra (50-200 cm-1) of In_2O_3 at different points of the sintering region perpendicular to the laser scanning direction.

vironments of C-C/C-H, C-O, and C=O in PVP, respectively (Figure C.26) [27]. After the SRLS treatment, the XPS spectrum indicates that the C-C/C-H related C 1s peak remains at 284.8 eV, indicating that the saturated carbon environment is unaffected. The significant difference appears in the C 1s peak associated with C-O, which exhibits a negative shift to 285.55 eV and a notable increase in peak intensity. Combined with the results of the previous thermal analysis of the In_2O_3 NP paste, these differences are attributed to the pyrolysis of PVP during the SRLS treatment, mainly due to PVP side-chain breaks and C-O bond formation. Moreover, the thermal decomposition of the PVP main chain

Figure C.22: Local Raman spectra (550-720 cm-1) of In$_2$O$_3$ at different points of the sintering region perpendicular to the laser scanning direction.
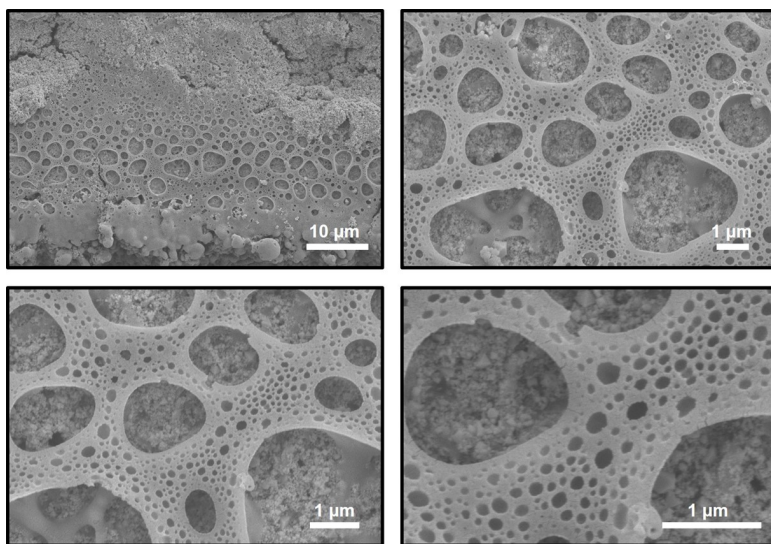

Figure C.23: Scanning electron microscope (SEM) images of the laser-sintered region of the sensor at different magnifications.

forms macroradicals that reduce In$_2$O$_3$ to metallic In while inducing oxygen vacancy defects and further forming more C-O bonds. Meanwhile, the C 1s peak associated with C=O bonding slightly shifts downward from 288.60 to 288.56 eV after the SRLS treatment, accompanied by a decrease in peak intensity, implying a decrease in the ketone group content in PVP. The negative shift and intensity enhancement of the C 1s peak further suggests that electron redistribution occurs between the pyrolysis products of PVP and
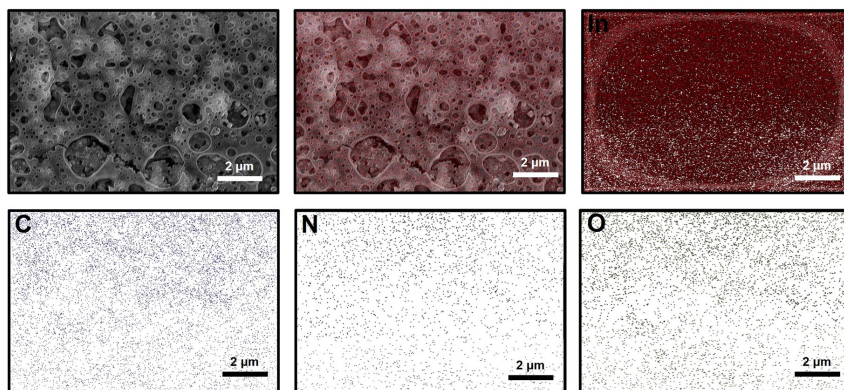
Figure C.24: Energy dispersive X-ray (EDX) spectroscopy characterization of surface porous carbon layer in sintering region.
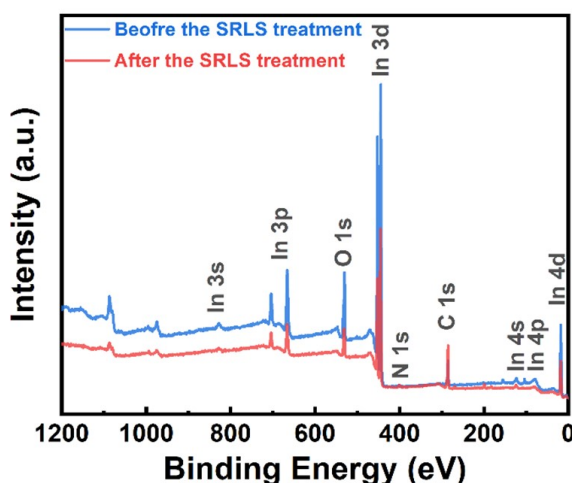

Figure C.25: The full XPS survey of the sensing material surface before and after the SRLS treatment.

In_2O_3 as well as the reduced metalized In during the SRLS treatment, matching with the electron transfer trend of In 3d and O 1s.

In the electron paramagnetic resonance (EPR) study, the samples before and after treatment with the SRLS process exhibit significant spectral changes. The first derivative of the EPR signal typically represents the line shape of the resonance. In this derivative form, the location of the resonance absorption peak is indicated by the zero-crossing point of the differential spectral lines. In the sensing region of the sensor, the resonance absorption peak is located at a magnetic field strength of 3510 G. It is essential for the calculation of the g-factor, which reflects the actual energy difference between the magnetic energy levels of the unpaired electrons. The corresponding formula is as follows:
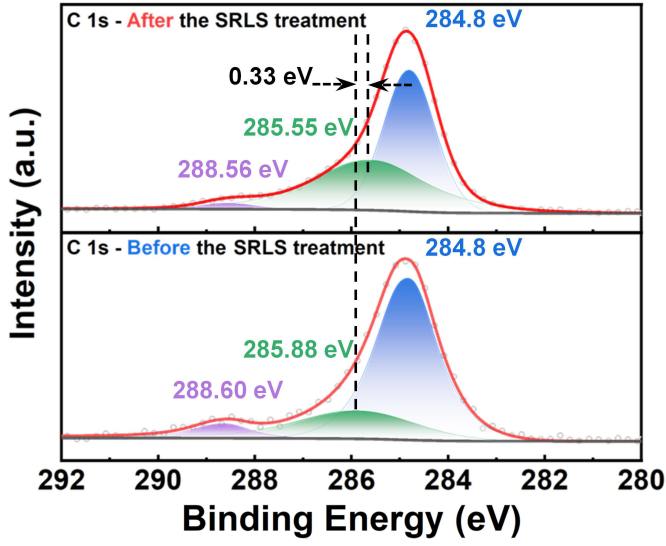
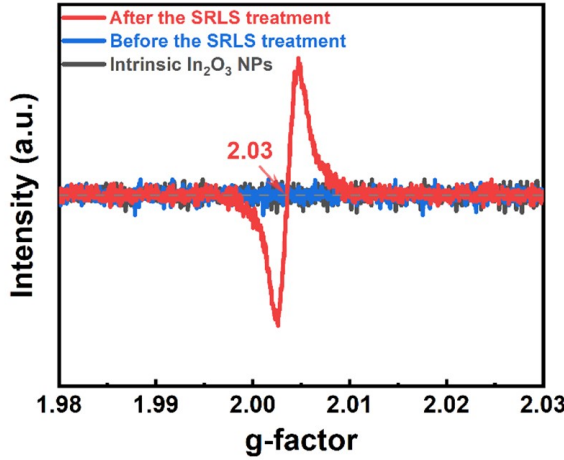Figure C.26: C 1s XPS spectra of In_2O_3 before and after the SRLS treatment.

Figure C.27: EPR spectrum of In_2O_3 NPs. Spectra showing the intrinsic EPR signal of In_2O_3 NPs (black), the signal before the SRLS treatment (blue), and the signal after the SRLS treatment (red).

$$g = \frac{h\nu}{\mu_B B} \tag{C.11}$$

where h represents Planck's constant, ν denotes the microwave frequency, μ_B is the Bohr magneton, and B corresponds to the magnetic field strength at the resonance absorption peak. The final g-factor is calculated to be 2.03 (Figure C.27) [28].

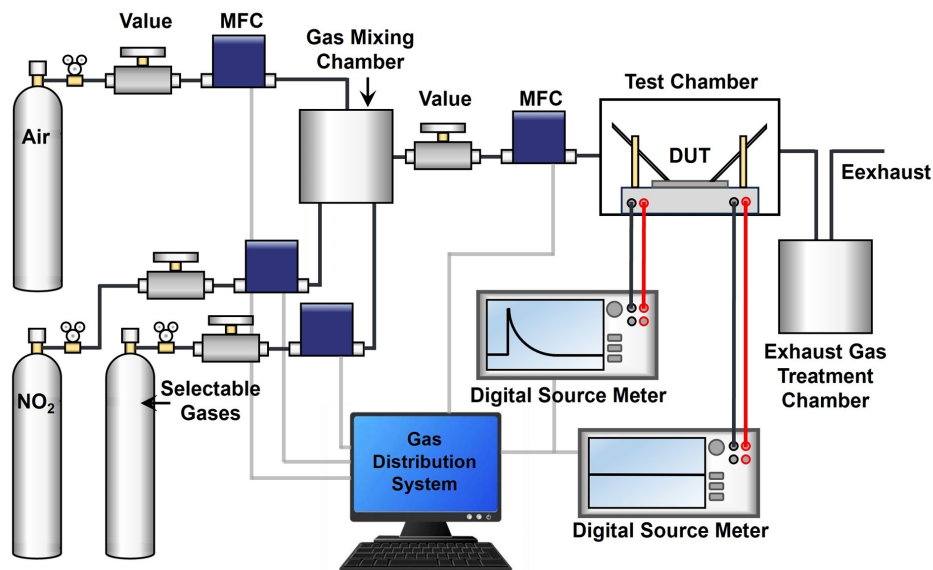## C.6. PERFORMANCE TESTING OF SENSORS

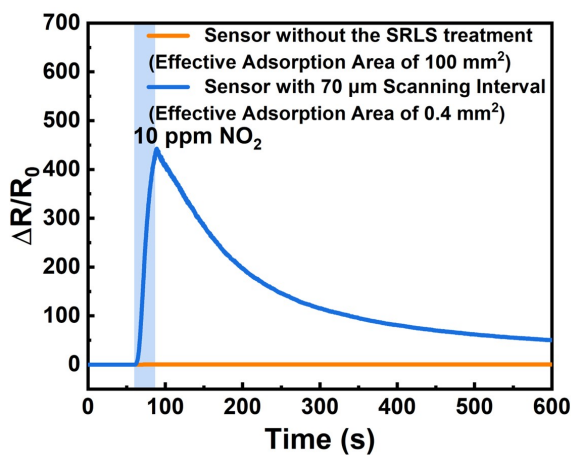Figure C.28: Schematic diagram of the gas sensor test system.

Figure C.29: Response curves to 10 ppm for samples with and without the SRLS treatment.

Before evaluating the effect of different laser scanning intervals on NO$_2$ sensing performance, we first confirmed the influence of OV defects on the adsorption capability of the sensor (Figure C.29). By comparing the response curves of SRLS-treated and untreated samples exposed to 10 ppm NO$_2$ for 30 s, it is observed that the untreated samples exhibited a negligible response despite their lower initial resistance and larger effec-

Table C.1: Summary of gas sensor performance data.

Num.	Sensing Material	OT(°C)	GC(ppm)	Res.	τ_{resp}(s)	τ_{reco}(s)
1	Nanorod clusters In_2O_3 [29]	150	0.5	41	50	30
2	rGO-In_2O_3 [30]	150	0.5	22.3	170	280
3	Nanorod-flowers In_2O_3 [31]	145	1.0	132	60	30
4	In_2O_3/ZIF-8 [32]	140	1.0	16.4	80	133
5	Nanospheres In_2O_3 [33]	120	1.0	371.9	148	72
6	Ni-doped In_2O_3 [34]	120	1.0	6.46	30	120
7	Bundle-like In_2O_3 [35]	100	1.0	87	177	152
8	Brick-like In_2O_3 [36]	50	0.5	402	114	49
9	Zn-In_2O_3 nanofiber [37]	50	5.0	130	600	2218
10	Walnut-like In_2O_3 [38]	25	1.0	3.6	89	80
11	This work	25	10.0	442	27	570

Note: OT - Operating Temperature; GC - Gas Concentration; Res. - Response; τ_{resp} - Response Time; τ_{reco} - Recovery Time.

tive adsorption area. In contrast, the SRLS-treated samples demonstrate a significantly enhanced NO_2 detection performance.
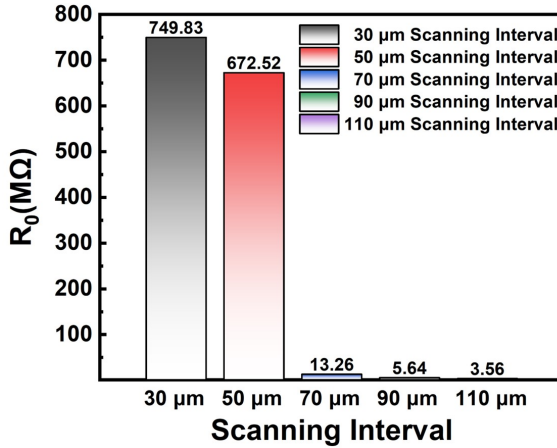

Figure C.30: Histogram of the baseline resistance (R0) of the sensors with different laser scanning intervals (In Air).

Building on these findings, we further investigated the effect of the laser scanning interval on the sensing adsorption performance. The relative response of the gas sensor is quantified as $S = \Delta R/R_0 = (R - R_0)/R_0$, with a bias voltage of 1.0 V, where R and R_0 represent the stabilized resistance in the target gas and air environments, respectively. The experimental results show that increasing the laser scanning interval can reduce the initial resistance of the sensor and increase the effective adsorption area of the sensor, thus
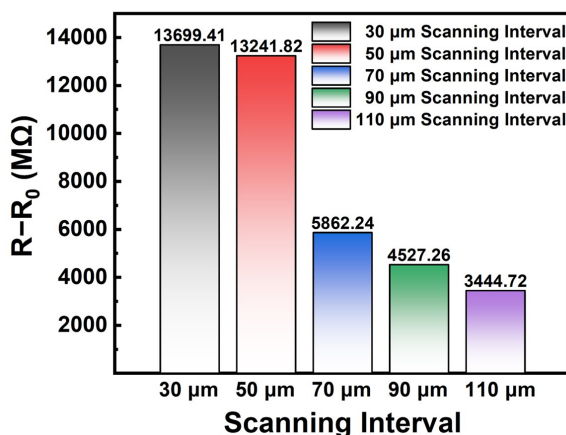
Figure C.31: Histogram of the change resistance ($\Delta R = R - R_0$) of the sensors with different laser scanning intervals (In NO_2).

improving the sensor response to NO_2 . However, there are limitations to this approach: on the one hand, increasing the scanning interval leads to a lower laser sintering temperature and reduces the generation of oxygen vacancy defects, which are crucial for flexible NO_2 sensors fabricated based on the SRLS technology; on the other hand, although increasing the effective adsorption area is favorable for improving the response, it may also lead to a lower desorption efficiency of NO_2 gas after adsorption on the sensor surface, thus affecting the recovery speed of the sensor.

Importantly, even at lower effective adsorption areas (30 µm scanning interval), the change in sensor resistance to NO_2 is much higher than that of the sensor under other conditions due to the high density of OV defects. This finding highlights the importance of optimizing the laser scanning interval and sintering temperature to modulate OV defects in improving the performance of gas sensors.

To more visually analyze the effect of xenon lamp irradiation on the recovery speed of the gas sensor, we further calculated the half-recovery time of the sensor under the different NO_2 concentrations (Figure C.32). It can be noticed that there is a huge difference between the half recovery time of the sensor at high and low concentrations. This is mainly due to the fact that at high gas concentrations, the sensor surface is more likely to reach a saturated adsorption state, where potential adsorption sites are filled with target gas molecules. Therefore, when the target gas is removed, the desorption process occurs more rapidly due to the saturation of the adsorption sites, thereby enhancing the recovery speed [39].

The photon-assisted condition dramatically reduces the half-recovery time of the NO_2 gas sensor compared to standard test conditions. In particular, at lower NO_2 concentrations, the half-recovery time of the sensor is drastically reduced from 791.6 to 65.7 s, which is a 91.7% improvement in recovery speed. This remarkable effect can be attributed to the photogenerated conductivity effect of the In_2O_3 NPs with OV defect, which produces photogenerated carriers that cancel out the conductivity change due
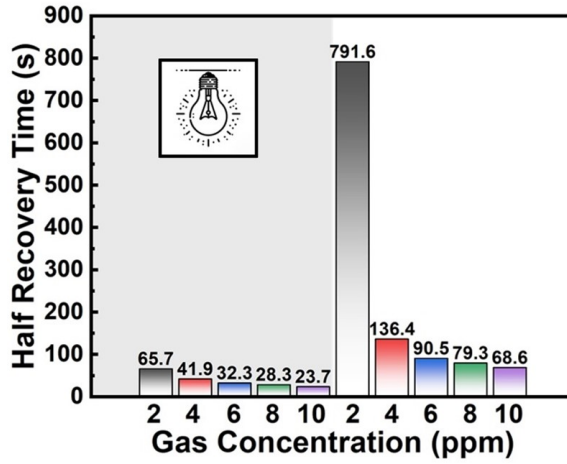
Figure C.32: Statistical histogram of the half-recovery time of the sensor for different concentrations of NO_2 gas with and without xenon lamp irradiation.
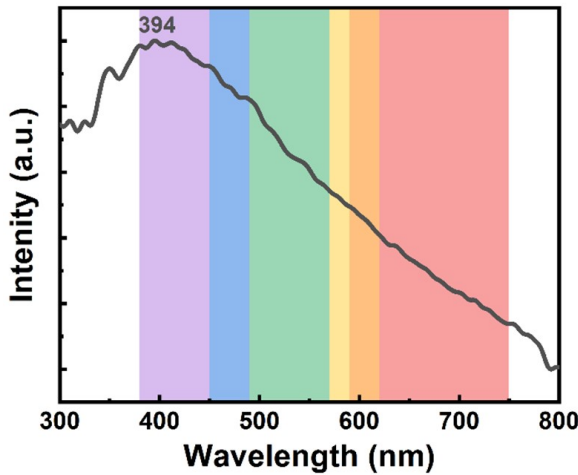

Figure C.33: Photoresponse curves of the sensor to different wavelengths of visible light.

to gas adsorption. This reduces the response of the sensor to NO_2 gas but dramatically increases its recovery speed [40]. Correspondingly, we also tested the photoresponse curve of the sensor to visible light (Figure C.33). The results show that the In_2O_3 gas sensor with OV defects shows a more significant response to violet light located at 394 nm. These photoelectric properties further demonstrate the potential application of this type of sensor in the field of photosensitive gas sensing.

C.7. Theoretical calculation of the sensor with OV defect

The top and front views of the In$_2$O$_3$ (222) show the layered structure, which is arranged according to a fixed stoichiometric ratio (In:O = 2:3), and each layer consists of an O-In-O triple-layer structure (Figure C.34). To highlight its triple-layer structure, the first triple-layer in the model is detailed using a ball-and-stick model. The surface has three slightly different geometric terminations, which are energetically equivalent, and there is no significant difference in stability among the terminations [41].

In these layers, the middle In layer contains 16 In atoms, and each O layer contains 12 O atoms. The top 12 O atoms are each connected to three In atoms, presenting a three-coordination. Correspondingly, the 12 O atoms (Figure C.35) in the top layer and the 16 In atoms (Figure C.36) in the middle layer of In$_2$O$_3$ were labeled according to their respective row and column positions. To further subdivide the adsorption sites of gas molecules on In atoms, In atoms can be classified into six different adsorption modes according to the number of O atoms bonded to the In atoms and the corresponding difference in coordination number (Table C.2).
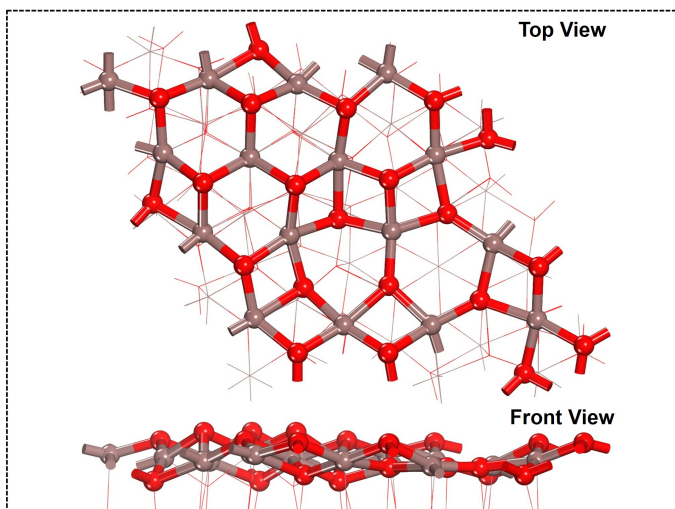

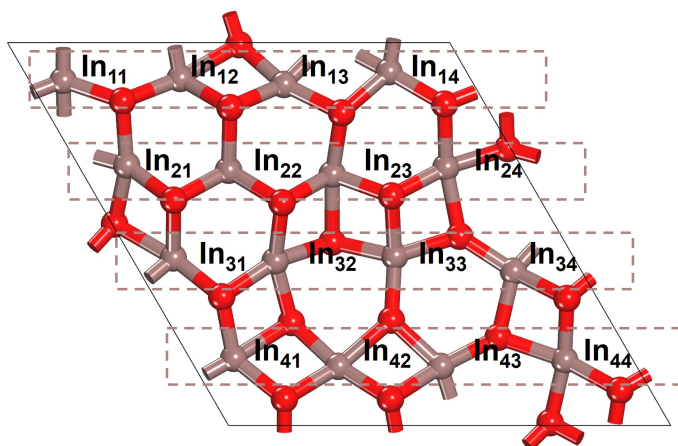Figure C.34: Top and front views of the In$_2$O$_3$ unit cell structure.

Figure C.35: The 16 indium (In) atoms in the middle layer of In_2O_3 were labeled according to their respective row and column positions.
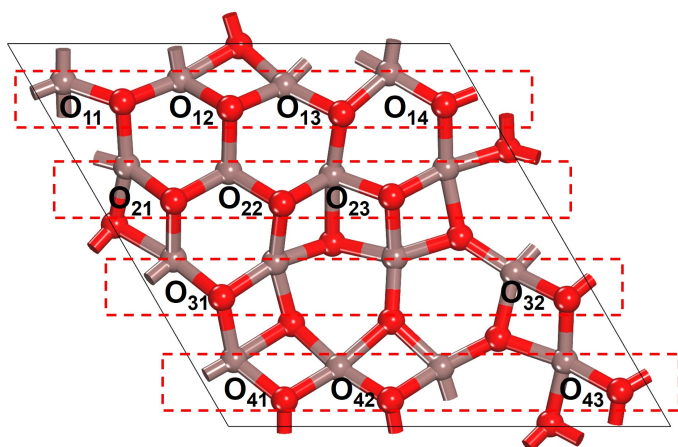

Figure C.36: The 12 oxygen (O) atoms in the top layer of In_2O_3 were labeled according to their respective row and column positions.

After geometry optimization of the unit cell of the In_2O_3 bulk, the adsorption energies, adsorption distances, and charge transfers were calculated according to the adsorption modes of the different In atoms for the NO_2 gas molecule (Table C.3). Based on the Gibbs free energy definition of whether the gas adsorption process proceeds spontaneously or not [42]. We can find that the adsorption processes of In_a and Inc are not spontaneous and require external energy to drive them. In contrast, all other adsorption modes (In_a, In_d, In_e, and In_f) proceed spontaneously. Among them, the NO_2 gas molecule acts as an electron acceptor to capture electrons from the In atoms at the adsorption sites (Figure C.37 and Table C.3).

Table C.2: The classification of adsorption modes is based on the number of oxygen atoms (O) bonded to indium atoms (In) and the number of bonds to the corresponding oxygen atoms.

Adsorption Mode	Position of the O-atom	Coordination Number of In-atom	Number of Bonds of Coordinated O-atoms
In$_a$	In$_{11}$	5	333-4-4
	In$_{14}$	5	333-4-4
	In$_{41}$	5	333-4-4
In$_b$	In$_{22}$	6	333-444
In$_c$	In$_{12}$	6	333-44-4
	In$_{23}$	6	333-44-4
	In$_{31}$	6	333-44-4
In$_d$	In$_{13}$	5	33-444
	In$_{21}$	5	33-444
	In$_{32}$	5	33-444
In$_e$	In$_{24}$	5	33-44-4
	In$_{42}$	5	33-44-4
	In$_{44}$	5	33-44-4
In$_f$	In$_{33}$	5	3-444-4
	In$_{34}$	5	3-444-4
	In$_{43}$	5	3-444-4

Note: Taking **333-44-4** as an example, **333** represents the **three** top-layer oxygen atoms, each with a coordination number of **3** in the O-In-O structure; **44** denotes the **two** bottom-layer oxygen atoms, each with a coordination number of **4**; and **4** refers to another top-layer oxygen atom with a coordination number of **4** in a corresponding layer within the same periodic O-In-O structure.
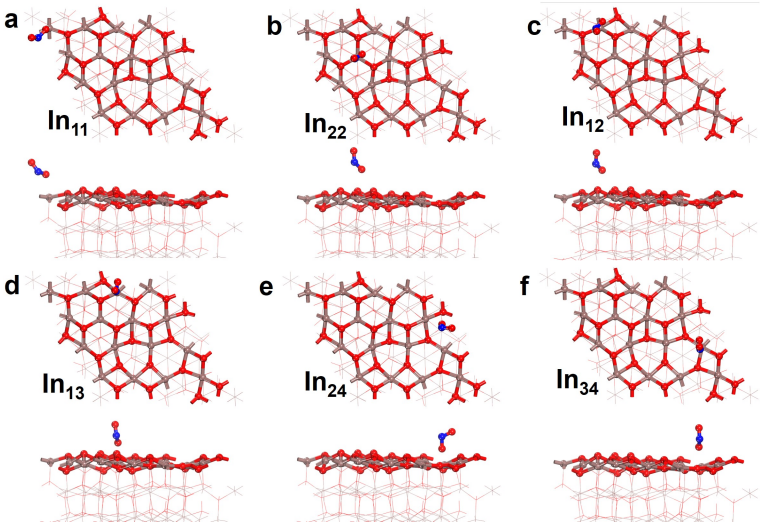

Figure C.37: Top and front views of In$_2$O$_3$ in different In$_2$O$_3$ adsorption modes without OV.

Table C.3: The adsorption energy, adsorption distance, and charge transfer of the NO_2 molecules in different In_2O_3 adsorption site systems without OV.

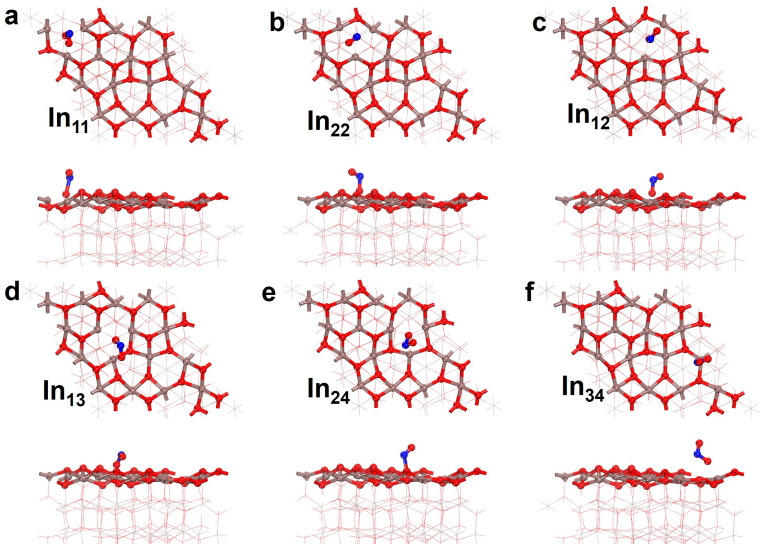| Adsorption Model	The Coordination Number of In	Adsorption Energy (eV)	Adsorption Distance (Å)	Charge Transfer (e)	Style (NO_2 as an Object)
In_a (In_{11})	5	−0.227	2.508 (O-In)	−0.207	Acceptor
In_b (In_{22})	6	0.028	3.192 (O-In)	−0.007	Acceptor
In_c (In_{12})	6	0.007	3.306 (O-In)	−0.045	Acceptor
In_d (In_{13})	5	−1.048	2.486 (O-In)	−0.491	Acceptor
In_e (In_{24})	5	−0.935	2.384 (O-In)	−0.479	Acceptor
In_f (In_{34})	5	−0.711	2.282 (O-In)	−0.360	Acceptor

Figure C.38: Top and front views of In_2O_3 in different In_2O_3 adsorption modes with OV

After geometry optimization of the In_2O_3 unit cell with OV, we performed calculations by placing the NO_2 gas molecule at the same adsorption positions as the intrinsic In_2O_3 surface. The results clearly show that the adsorption energy on the In_2O_3 surface with OV is significantly increased. In particular, the adsorption energy is significantly enhanced from 0.028 eV to −2.854 eV at the In_{22} adsorption site (Figure C.38 and Table C.4). These results further confirm the critical role of oxygen vacancy defects in enhancing NO_2 gas adsorption.

Table C.4: The adsorption energy, adsorption distance, and charge transfer of the NO_2 molecules in different In_2O_3 adsorption site systems without OV.

Adsorption Model	The coordination Number of In	Adsorption Energy (eV)	Adsorption Distance (Å)	Charge Transfer (e)	Style (NO_2 as an Object)
In_a (In_{11})	4	−2.721	2.230 (O-In)	−0.631	Acceptor
In_b (In_{22})	5	−2.854	2.596 (O-In)	−0.551	Acceptor
In_c (In_{12})	5	−2.651	2.474 (O-In)	−0.545	Acceptor
In_d (In_{13})	4	−2.747	2.568 (O-In)	−0.570	Acceptor
In_e (In_{24})	4	−2.500	2.148 (O-In)	−0.768	Acceptor
In_f (In_{34})	4	−1.410	2.150 (O-In)	−0.353	Acceptor

REFERENCES

[1] M. Hafeez, T. Zhai, A. S. Bhatti, Y. Bando, and D. Golberg, "Oxygen vacancy driven modulations in In2O3 pyramidal beaded nanowires", *Crystal growth & design*, vol. 12, no. 10, pp. 4935–4943, 2012.

[2] T. Schmutzler *et al.*, "Concentration dependent morphology and composition of n-alcohol modified cetyltrimethylammonium bromide micelles", *Journal of Physics: Condensed Matter*, vol. 30, no. 49, p. 495 001, 2018.

[3] G. Palazzo, L. Carbone, G. Colafemmina, R. Angelico, A. Ceglie, and M. Giustini, "The role of the cosurfactant in the CTAB/water/n-pentanol/n-hexane system: Pentanol effect on the phase equilibria and mesophase structure", *Physical Chemistry Chemical Physics*, vol. 6, no. 7, pp. 1423–1429, 2004.

[4] S. Murakami *et al.*, "Effects of ethyl cellulose polymers on rheological properties of (La, Sr)(Ti, Fe) O3-terpineol pastes for screen printing", *Ceramics International*, vol. 40, no. 1, pp. 1661–1666, 2014.

[5] S. Yokoyama, J. Nozaki, K. Motomiya, N. Tsukahara, and H. Takahashi, "Strong adhesion of polyvinylpyrrolidone-coated copper nanoparticles on various substrates fabricated from well-dispersed copper nanoparticle inks", *Colloids and Surfaces A: Physicochemical and Engineering Aspects*, vol. 591, p. 124 567, 2020.

[6] H. Lee and M. Yang, "Effect of solvent and PVP on electrode conductivity in laser-induced reduction process", *Applied Physics A*, vol. 119, pp. 317–323, 2015.

[7] Y.-S. Cho, H.-M. Kim, J.-J. Hong, G.-R. Yi, S. H. Jang, and S.-M. Yang, "Dispersion stabilization of conductive transparent oxide nanoparticles", *Colloids and Surfaces A: Physicochemical and Engineering Aspects*, vol. 336, no. 1-3, pp. 88–98, 2009.

[8] Y. Du, P Yang, Z. Mou, N. Hua, and L Jiang, "Thermal decomposition behaviors of PVP coated on platinum nanoparticles", *Journal of Applied Polymer Science*, vol. 99, no. 1, pp. 23–26, 2006.

[9]   C. E. Hoppe, M. Lazzari, I. Pardinas-Blanco, and M. A. López-Quintela, "One-step synthesis of gold and silver hydrosols using poly (N-vinyl-2-pyrrolidone) as a reducing agent", *Langmuir*, vol. 22, no. 16, pp. 7027–7034, 2006.

[10] W. Xu, Y. Liu, B. Chen, D.-B. Liu, Y.-H. Lin, and A. Marcelli, "Nano-inclusions: A novel approach to tune the thermal conductivity of In2O3", *Physical Chemistry Chemical Physics*, vol. 15, no. 40, pp. 17 595–17 600, 2013.

[11] J. W. Phair, "Rheological analysis of concentrated zirconia pastes with ethyl cellulose for screen printing SOFC electrolyte films", *Journal of the American Ceramic Society*, vol. 91, no. 7, pp. 2130–2137, 2008.

[12] F. Zacharatos *et al.*, "Selective laser sintering of laser printed Ag nanoparticle micropatterns at high repetition rates", *Materials*, vol. 11, no. 11, p. 2142, 2018.

[13] S. Wang *et al.*, "Rapid fabrication of high-performance flexible pressure sensors using laser pyrolysis direct writing", *ACS applied materials & interfaces*, vol. 15, no. 34, pp. 41 055–41 066, 2023.

[14] V. B. Nam, T. T. Giang, S. Koo, J. Rho, and D. Lee, "Laser digital patterning of conductive electrodes using metal oxide nanomaterials", *Nano Convergence*, vol. 7, no. 1, p. 23, 2020.

[15] X. Ruan, R. Wang, J. Luo, Y. Yao, and T. Liu, "Experimental and modeling study of CO2 laser writing induced polyimide carbonization process", *Materials & Design*, vol. 160, pp. 1168–1177, 2018.

[16] Y. Yang, Z. Li, S. Yang, Y. Li, and J. Huang, "Multiscale simulation study of laser sintering of inkjet-printed silver nanoparticle inks", *International Journal of Heat and Mass Transfer*, vol. 159, p. 120 110, 2020.

[17] S. Wang *et al.*, "Facile fabrication and enhanced gas sensing properties of In2O3 nanoparticles", *New Journal of Chemistry*, vol. 38, no. 10, pp. 4879–4884, 2014.

[18] G. Poulain, D. Blanc, A. Kaminski, B. Semmache, and M. Lemiti, "Modeling of laser processing for advanced silicon solar cells", in *Excerpt from the Proceedings of the COMSOL Conference*, 2010.

[19] B. E. Saleh and M. C. Teich, "Fundamentals of photonics john wiley & sons", *Inc., Hoboken NJ*, vol. 2, 1991.

[20] W. J. Marshall, "Two methods for measuring laser beam diameter", *Journal of Laser Applications*, vol. 22, no. 4, pp. 132–136, 2010.

[21] M. Darif, N. Semmar, and F. Orléans Cedex, "Numerical simulation of si nanosecond laser annealing by COMSOL multiphysics", in *Proceedings of the COMSOL Conference 2008 Hannover*, 2008, pp. 567–571.

[22] W. Wang *et al.*, "Controlling the laser induction and cutting process on polyimide films for kirigami-inspired supercapacitor applications", *Science China Technological Sciences*, vol. 64, no. 3, pp. 651–661, 2021.

[23] G. Colangelo, N. F. Diamante, M. Milanese, G. Starace, and A. de Risi, "A critical review of experimental investigations about convective heat transfer characteristics of nanofluids under turbulent and laminar regimes with a focus on the experimental setup", *Energies*, vol. 14, no. 18, p. 6004, 2021.

[24] T. Gruene, J. J. Holstein, G. H. Clever, and B. Keppler, "Establishing electron diffraction in chemical crystallography", *Nature Reviews Chemistry*, vol. 5, no. 9, pp. 660–668, 2021.

[25] A. Sharma, S. B. Eadi, H. Noothalapati, M. Otyepka, H.-D. Lee, and K. Jayaramulu, "Porous materials as effective chemiresistive gas sensors", *Chemical Society Reviews*, 2024.

[26] K. M. Koczkur, S. Mourdikoudis, L. Polavarapu, and S. E. Skrabalak, "Polyvinylpyrrolidone (PVP) in nanoparticle synthesis", *Dalton transactions*, vol. 44, no. 41, pp. 17 883–17 905, 2015.

[27] W.-y. Huang and G.-c. Xu, "Characterization of nano-Ag/PVP composites synthesized via ultra-violet irradiation", *Journal of Coal Science and Engineering (China)*, vol. 16, pp. 188–192, 2010.

[28] M. Meng *et al.*, "Boosted photoelectrochemical performance of In2O3 nanowires via modulating oxygen vacancies on crystal facets", *Journal of Alloys and Compounds*, vol. 845, p. 156 311, 2020.

[29] X. Xu *et al.*, "Synthesis and NO2 sensing properties of indium oxide nanorod clusters via a simple solvothermal route", *RSC advances*, vol. 6, no. 52, pp. 47 083–47 088, 2016.

[30] C. W. Na *et al.*, "Highly selective and sensitive detection of NO2 using rGO-In2O3 structure on flexible substrate at low temperature", *Sensors and Actuators B: Chemical*, vol. 255, pp. 1671–1679, 2018.

[31] X. Xu *et al.*, "Hierarchical nanorod-flowers indium oxide microspheres and their gas sensing properties", *Sensors and Actuators B: Chemical*, vol. 227, pp. 547–553, 2016.

[32] Y. Liu, R. Wang, T. Zhang, S. Liu, and T. Fei, "Zeolitic imidazolate framework-8 (ZIF-8)-coated In2O3 nanofibers as an efficient sensing material for ppb-level NO2 detection", *Journal of colloid and interface science*, vol. 541, pp. 249–257, 2019.

[33] B. Xiao, Q. Zhao, D. Wang, G. Ma, and M. Zhang, "Facile synthesis of nanoparticle packed In2O3 nanospheres for highly sensitive NO2 sensing", *New Journal of Chemistry*, vol. 41, no. 16, pp. 8530–8535, 2017.

[34] S. Hambir and S. Jagtap, "NO2 sensing behavior of Ni-doped In2O3 microcubes based chemiresistive gas sensors", *Journal of Materials Science: Materials in Electronics*, vol. 34, no. 24, p. 1716, 2023.

[35] X. Li *et al.*, "Vitamin C-assisted synthesis and gas sensing properties of coaxial In2O3 nanorod bundles", *Sensors and Actuators B: Chemical*, vol. 220, pp. 68–74, 2015.

[36] D. Han, L. Zhai, F. Gu, and Z. Wang, "Highly sensitive NO2 gas sensor of ppb-level detection based on In2O3 nanobricks at low temperature", *Sensors and Actuators B: Chemical*, vol. 262, pp. 655–663, 2018.

[37] K. Chen *et al.*, "Surface functionalization of porous In2O3 nanofibers with Zn nanoparticles for enhanced low-temperature NO2 sensing properties", *Sensors and Actuators B: Chemical*, vol. 308, p. 127 716, 2020.

[38] H. Ma *et al.*, "Room temperature photoelectric NO2 gas sensor based on direct growth of walnut-like In2O3 nanostructures", *Journal of Alloys and Compounds*, vol. 782, pp. 1121–1126, 2019.

[39] S.-W. Fan, A. K. Srivastava, and V. P. Dravid, "UV-activated room-temperature gas sensing mechanism of polycrystalline ZnO", *Applied Physics Letters*, vol. 95, no. 14, 2009.

[40] H. Tabata, H. Matsuyama, T. Goto, O. Kubo, and M. Katayama, "Visible-light-activated response originating from carrier-mobility modulation of NO2 gas sensors based on MoS2 monolayers", *ACS nano*, vol. 15, no. 2, pp. 2542–2553, 2021.

[41] A. Posada-Borbon and H. Gronbeck, "Hydrogen adsorption on In2O3 (111) and In2O3 (110)", *Physical Chemistry Chemical Physics*, vol. 22, no. 28, pp. 16 193–16 202, 2020.

[42] Y. Yang, C. Shen, K. Sun, D. Mei, and C.-j. Liu, "Enhanced surface charge localization over nitrogen-doped In2O3 for CO2 hydrogenation to methanol with improved stability", *ACS Catalysis*, vol. 13, no. 9, pp. 6154–6168, 2023.

C

D.1. PREPARATION OF NIO-PI NANOCOMPOSITE FILMS

During the experimental process, all chemicals were sourced commercially and used without further purification. Thermoset polyimide poly solution (PI precursor solution, Mw = 50000 with a 20% solids content) was obtained from Dongguan Zhanyang Polymer Materials Co., Ltd. Nickel oxide nanoparticles (grain size 100 nm) were provided by ZhouNuo Advanced Material Technology Co., Ltd. N,N-Dimethylformamide (C_3H_7NO, 99.5% AR, DMF) and Poly(sodium-p-styrenesulfonate) (($C_8H_7NaO_3S)_n$, Mw = 1000000, PSSNa) were procured from Shanghai Macklin Biochemical Co., Ltd. Polyimide tape (PI tape, 3M-92#) was obtained from 3M Company. Low-temperature curing silver paste (01L-2211D) was purchased from Shenzhen Sryeo Electronic Paste Co., Ltd. Polydimethylsiloxane (PDMS Sylgard 184) was obtained from Dow Corning Company.

Under ice bath conditions, 1.5 g of NiO NPs were first dispersed ultrasonically in 2.12 ml of DMF (about 2.0 g) solvent for 30 min. Subsequently, 6.5 g of PI precursor solution was added to the mixture. Afterward, a planetary vacuum mixer was used to homogenize the mixture at a speed of 2000 rpm for 120 s to fabricate the NiO-PI nanocomposite paste. After that, the paste was spin-coated onto a silicon-based wafer (4 inch) coated with a PSSNa sacrificial layer at a speed of 1000 rpm for 30 s. Next, the wafer was placed on a hot plate for a multi-temperature curing process.

In the film curing process, the polyimide precursor solution utilizes DMF as the primary solvent, which has a boiling point of approximately 153°C. The curing process focuses on two pivotal aspects: the gradual volatilization of DMF and the imidization reaction of polyimide. Both processes are critical in ensuring the superior performance of the final film [1, 2]. The corresponding curing process is shown in Figure D.1.

From 30°C to 50°C: This temperature range is employed for gentle heating, which promotes the slow evaporation of DMF. This helps prevent rapid shrinkage or bubble formation in the film during the curing process.
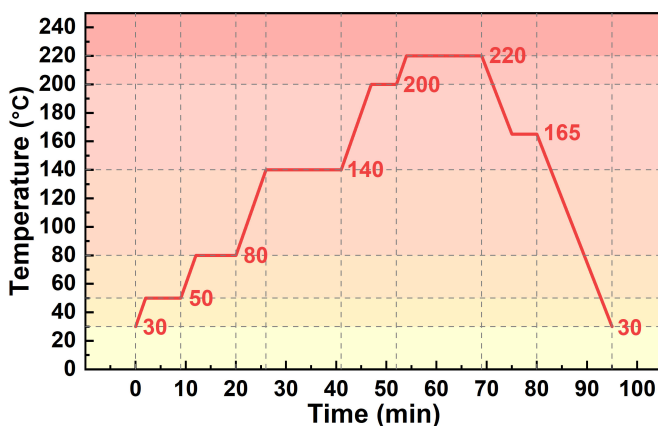
Figure D.1: Temperature profile of NiO-PI films during curing.

From 50°C to 80°C: During this stage, the evaporation rate of DMF accelerates, preparing for subsequent curing and cross-linking reactions.

From 80°C to 140°C: This range continues to advance the evaporation of DMF and marks the effective initiation of the imidization reaction. Here, the polyimide precursor begins to transform into a more stable structure as carboxyl (-COOH) and amine (-NH−2) groups undergo dehydration condensation to form stable amide bonds (-CONH-).

From 140°C to 200°C: At this stage, the temperature well exceeds the boiling point of DMF, ensuring its complete evaporation. This phase intensifies the imidization reaction, where increased cross-linking between polymer chains forms a highly cross-linked network, substantially boosting mechanical stability.

From 200°C to 220°C: This final high-temperature treatment stage involves final chemical cross-linking and molecular alignment of the polyimide chains. These reactions not only further enhance the chemical stability of polyimide but also optimize its mechanical properties.

After curing, a scraper was used to attach the PI tape to the cured NiO-PI nanocomposite film. Then, the wafer was sonicated in deionized water for 120 min to strip the NiO-PI nanocomposite film. Finally, the film was dried in an oven at 60 °C for 20 min.

D.2. Optimization of UV Laser parameters and PDMS packaging process

During the laser direct writing process, parameters such as laser scanning speed (V_{ss}), laser average power (P_{avg}), pulse repetition frequency (F_{pr}), and defocus distance (D_{def}) have a decisive influence on the LIG fabrication results.

Under fixed D_{def} (0 mm) and F_{pr} (200 kHz) conditions, we investigated the effects of different V_{ss} and P_{avg} on the morphology and linear resistance changes of NiO-LIG. As shown in Figure D.2, the images are arranged in a matrix format, showing the variation of
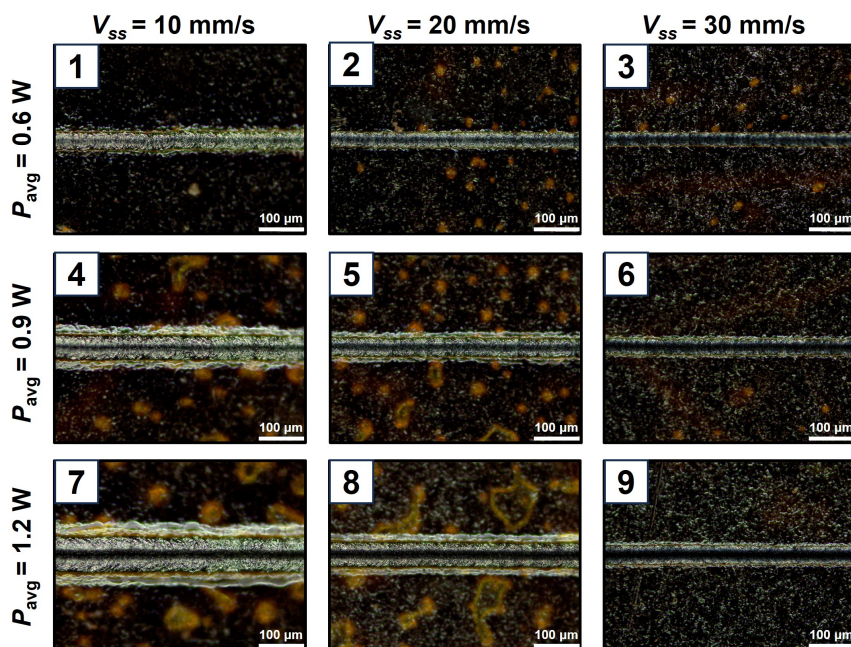
Figure D.2: Effect of different laser scanning speeds and laser average powers on the NiO-LIG surface morphology.

NiO-LIG morphology under different conditions. The top rows (images 1, 2, and 3) used a low power setting of 0.6 W and scanning speeds of 10, 20, and 30 mm/s. The middle rows (images 4, 5, and 6) increased the power to 0.9 W, and the bottom rows (images 7, 8, and 9) used 1.2 W. As V_{ss} increases, the heat accumulated on the NiO-PI surface per unit length further decreases, significantly reducing the linewidth of the fabricated NiO-LIG at the same P_{avg}. Correspondingly, at a V_{ss}, an increase in P_{avg} not only broadens the linewidth of NiO-LIGs but also results in more significant heat accumulation due to the photothermal effect. This further enhances the ablation effect of the laser on the NiO-LIG surface, resulting in the formation of an obvious trench.

As shown in Figure D.3, the histogram of the average value of line resistance of NiO-LIG (based on 10 sets of test data) for different V_{ss} and P_{avg} conditions. The results show that under the condition of fixed P_{avg}, the line resistance of NiO-LIG increases with the increase of V_{ss}. Comparatively, under the condition of fixed V_{ss}, the resistance of NiO-LIG decreases with the increase of P_{avg}. These phenomena further reveal the effect of V_{ss} and P_{avg} on the degree of graphitization of LIG in the NiO-LIG nanocomposite. The same trend is also observed in the treatment of Pure-PI films, as shown in Figure D.4. Unexpectedly, under the same laser parameters, the line resistance of LIG after composite NiO NPs is generally much higher than that of Pure-LIG. This phenomenon is attributed to the fact that NiO, as a semiconductor material, has a much higher intrinsic resistivity than LIG.

Considering the linewidth of the laser-induced NiO-LIG and the compromise effect
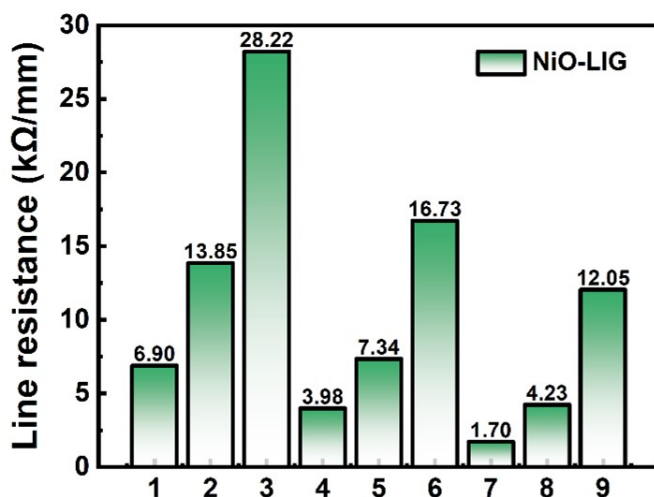
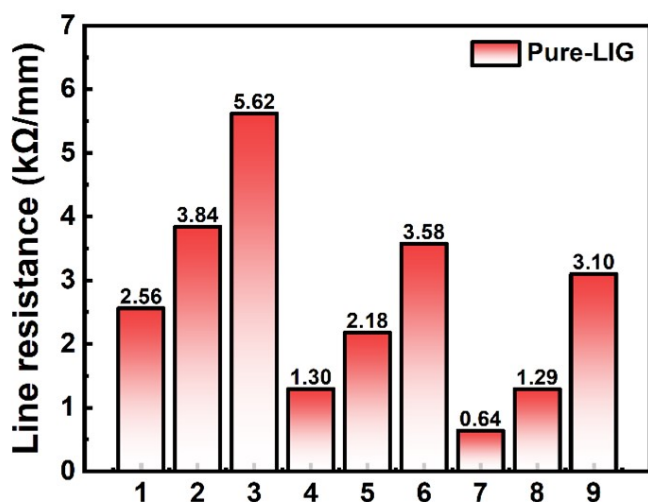Figure D.3: Effect of different laser scanning speeds and average laser power on NiO-LIG line resistance.

Figure D.4: Effect of different laser scanning speeds and average laser power on Pure-LIG line resistance.

of resistance, the laser scanning speed (V_{ss}), the pulse repetition frequency (F_{pr}), and laser average power (P_{avg}) were set to 10 mm/s, 200 kHz, and 0.9 W, respectively.

A linear square wave pattern of NiO-LIG for temperature sensing was fabricated on the NiO-PI nanocomposite film by linear movement of a UV laser. Wherein the linear scanning interval was set to 100 μm. Subsequently, silver electrodes were printed on both ends of the sensors using the screen printing technique and placed in an oven at 60 °C for 30 min for curing. Finally, the flexible temperature sensor array was diced and

tested.

In addition, PDMS was used as a waterproof coating for flexible NiO-LIG temperature sensors. The PDMS base and curing agent were mixed at a weight ratio of 10:1, then degassed and spin-coated onto the surface of the NiO-LIG sensors. The primary spin-coating parameters were set to 1000 rpm for 20 s. Subsequently, the coated sensors were cured in an oven at 80 °C for 2 h.

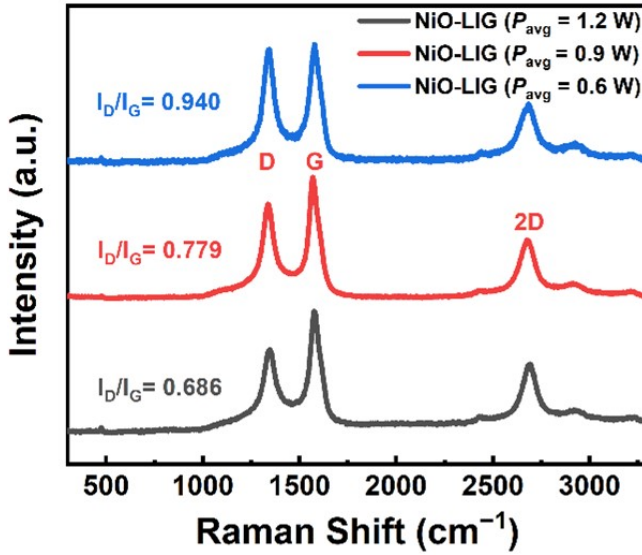## D.3. EFFECT OF P_{avg} ON THE DEGREE OF GRAPHITIZATION

Figure D.5: Effect of different laser average powers on the degree of LIG graphitization in NiO-LIG (SI = 150 μm).

As shown in Figure D.5, with fixed V_{ss}, F_{pr}, and D_{def}, we compare the NiO-LIG Raman spectra across different P_{avg}. The spectrum reveals three significant peaks: the D peak at 1350 cm^{-1}, the G peak at 2580 cm^{-1}, and the 2D peak at 2690 cm^{-1}. Specifically, the G peak reflects the vibration mode of sp² hybridized carbon atoms in graphene and is usually used to indicate the integrity of the graphene structure. The D peak is used to evaluate defects and disorders in the carbon-based material [3]. A high I$_D$/I$_G$ ratio indicates that there are more defects and disorders in the structure of the LIG material. In contrast, a low I$_D$/I$_G$ ratio indicates that the LIG material has higher crystal structure integrity and fewer structural defects. These results show that with the increase of P_{avg}, the I$_D$/I$_G$ ratio gradually decreases, indicating a reduction in internal defects and an increase in the graphitization degree within NiO-LIG. This trend is consistent with the analysis of existing literature [4, 5].
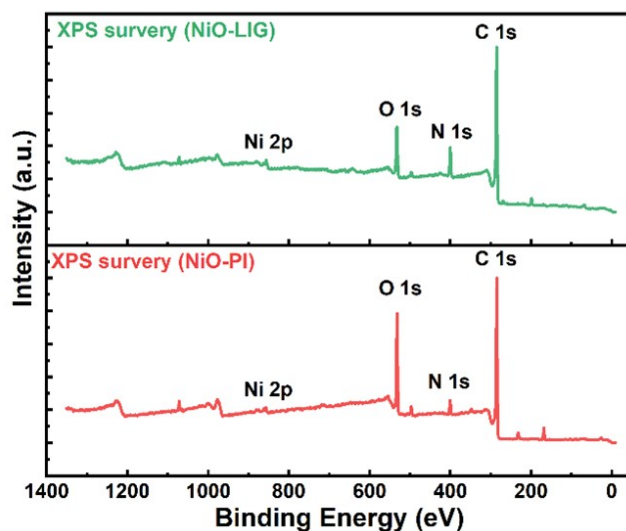
Figure D.6: Comparison of the XPS survey spectrum of NiO-PI and NiO-LIG before and after laser treatment.

D.4. XPS ANALYSIS BEFORE AND AFTER LASER TREATMENT

In the XPS spectrum of NiO-PI without laser directly writing treatment, the peaks of C 1s, N 1s, O 1s, and Ni 2p further explain the elemental composition and chemical state in NiO-PI, as shown in Figure D.6. Among them, due to the low content of NiO nanoparticles, the peak intensity of Ni 2p is not apparent. Laser treatment induces a high-temperature environment, which leads to the breakage and thermal decomposition of polyimide molecular chains and then releases oxygen-containing gas molecules (such as CO_X, NO_X, and H_2O), which reduces the peak intensity of O 1s relatively. Meanwhile, part of the NiO is reduced to metallic Ni after laser treatment, which increases the relative peak intensity of Ni 2p. It is worth noting that the peak of N 1s is significantly enhanced after laser treatment, which may be caused by laser-induced surface functionalization [6].

D.5. EFFECT OF P_{avg} ON SENSOR PERFORMANCE

In fact, adjusting the laser average power (P_{avg}) can more effectively tune the sensitivity of LIG-based temperature sensors [17]. However, the composite of NiO particles significantly improves the performance of the LIG-based temperature sensor and further intensifies the impact of different P_{avg} on the trade-off relationship between sensor sensitivity and linearity. The effects of different laser powers on the sensitivity and linearity of Pure-LIG and NiO-LIG temperature sensors are shown in Figure D.8 and Figure D.9. By reducing the average laser power from 1.2 W to 0.9 W and further to 0.6 W, the TCR of the NiO-LIG sensor increased from -0.065% °C^{-1} (R^2 = 0.995) to -0.074%°C^{-1} (R^2 = 0.999) and to -0.095% °C^{-1} (R^2=0.998), respectively. In contrast, the Pure-LIG sensor showed almost no change in performance. Although higher average laser power can
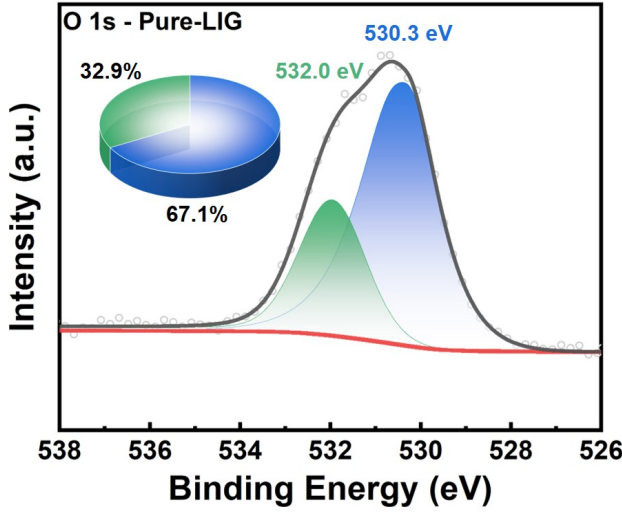
Figure D.7: O 1s XPS spectra of Pure-PI after the UV laser treatment (The inset is a pie chart of the corresponding peak area ratios).
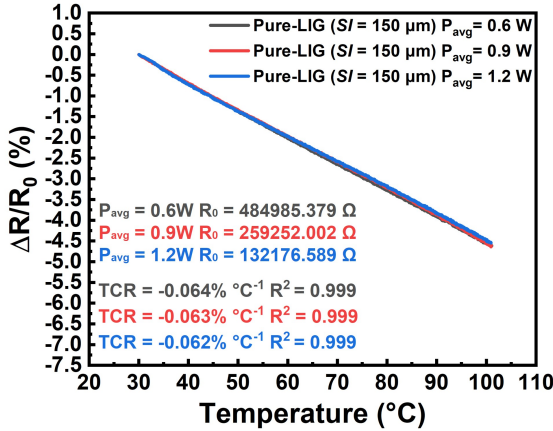

Figure D.8: Temperature response of Pure-LIG sensors with different laser average powers (P_{avg}).

achieve a higher degree of graphitization and better conductivity in LIG, excessive carbonization can lead to internal structural inconsistencies, such as cracks or localized charring, which can affect the linearity of the sensor response. Conversely, lower laser power can result in insufficient graphitization and incomplete internal structures within the LIG, which will also affect the linear response of the sensor [18]. Therefore, this fine scanning interval adjustment can achieve effective adjustment of the sensitivity of the
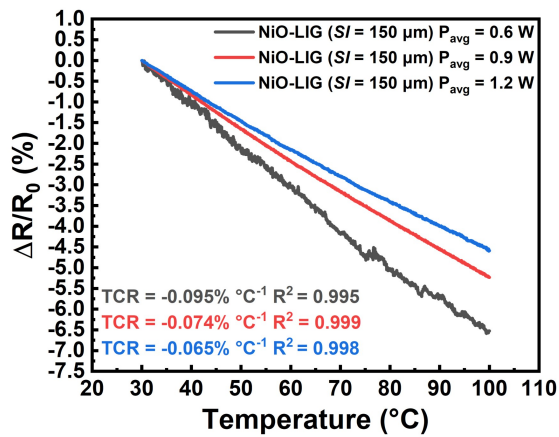
Figure D.9: Temperature response of NiO-LIG sensors with different laser average powers (P_{avg}).

Table D.1: Performance comparison of LIG-based flexible temperature sensors.

Num.	Materials	Laser type	Temp. range (°C)	Sensitivity (°C^{-1})	Linearity (R^2)
1	Polyimide [7]	CO_2 (10.6 μm)	30-100	−0.05%	Linear (0.999)
2	Polyimide [8]	CO_2 (10.6 μm)	30-40	−0.04145%	Linear (N/A)
3	Polyimide (Kapton) [9]	CO_2 (10.6 μm)	20-60	−0.11%	Nonlinear
4	Polyimide (Kapton) [10]	CO_2 (10.6 μm)	30-50	−0.06%	Linear (N/A)
5	Polyimide [11]	CO_2 (10.6 μm)	20-100	−0.25%	Linear (0.980)
6	Polyimide [12]	CO_2 (10.6 μm)	18-40	−0.057%	Linear (N/A)
7	Polyimide (Kapton) [13]	Nd: YAG (1064 nm)	−150-0	−0.026%	Linear (0.992)
8	Polyimide (Kapton) [14]	Nd: YAG (1064 nm)	−10-60	−0.14%	Linear (0.999)
9	Cellulose filter paper [15]	UV (355 nm)	10-60	−0.28%	Linear (N/A)
10	Polyimide with nanosilver [16]	UV (355 nm)	24-85	−0.58%	Linear (N/A)
11	Polyimide with NiO NPs This work	UV (355 nm)	30-100	−0.075%	Linear (0.999)

temperature sensor while ensuring linearity.

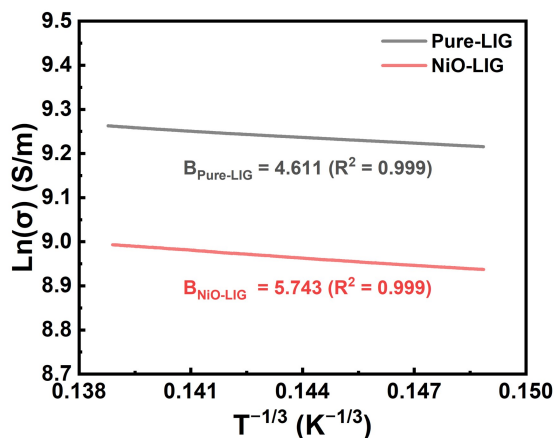## D.6. FITTING OF THE 2D MOTT VRH MODEL FOR SENSOR

Figure D.10: Fitting curves for the experimental data of NiO-LIG and Pure-LIG flexible temperature sensors using the 2D Mott VRH model.

REFERENCES

[1] J. H. Jou and P. T. Huang, "Effect of thermal curing on the structures and properties of aromatic polyimide films", *Macromolecules*, vol. 24, no. 13, pp. 3796–3803, 1991.

[2] C. Li *et al.*, "A comprehensive study of pyrazine-contained and low-temperature curable polyimide", *Polymer*, vol. 228, p. 123 963, 2021.

[3] F. M. Vivaldi *et al.*, "Three-dimensional (3D) laser-induced graphene: Structure, properties, and application to chemical sensing", *ACS Applied Materials & Interfaces*, vol. 13, no. 26, pp. 30 245–30 260, 2021.

[4] S. Bai *et al.*, "Investigation of micro/nano formation mechanism of porous graphene induced by CO2 laser processing on polyimide film", *Journal of Manufacturing Processes*, vol. 84, pp. 555–564, 2022.

[5] K. Mikheev, R. Zonov, A. Syugaev, D. Bulatov, and G. Mikheev, "The effect of line-by-line laser scanning on the properties of laser-induced graphene", *Physics of the Solid State*, vol. 64, no. 5, 2022.

[6] T. Kato, Y. Yamada, Y. Nishikawa, T. Otomo, H. Sato, and S. Sato, "Origins of peaks of graphitic and pyrrolic nitrogen in N1s x-ray photoelectron spectra of carbon materials: Quaternary nitrogen, tertiary amine, or secondary amine?", *Journal of Materials Science*, vol. 56, pp. 15 798–15 811, 2021.

[7]   Y. Zhang *et al.*, "High-linearity graphene-based temperature sensor fabricated by laser writing", *Journal of Materials Science: Materials in Electronics*, vol. 35, no. 2, p. 109, 2024.

[8]   H. Kun, L. Bin, M. Orban, Q. Donghai, and Y. Hongbo, "Accurate flexible temperature sensor based on laser-induced graphene material", *Shock and Vibration*, vol. 2021, no. 1, p. 9 938 010, 2021.

[9]   M. Marengo, G. Marinaro, and J. Kosel, "Flexible temperature and flow sensor from laser-induced graphene", *IEEE SENSORS*, pp. 1–3, 2017.

[10]   H. Qin *et al.*, "Laser-induced graphene-based smart textiles for wireless cross-body metrics", *ACS Applied Nano Materials*, vol. 6, no. 20, pp. 19 158–19 167, 2023.

[11]   J. Guo *et al.*, "An intelligent dual-sensing e-skin system for pressure and temperature detection using laser-induced graphene and polydimethylsiloxane", *Materials & Design*, vol. 238, p. 112 640, 2024.

[12]   A. Kaidarova, M. Marengo, N. R. Geraldi, C. M. Duarte, and J. Kosel, "Flexible conductivity, temperature, and depth sensor for marine environment monitoring", in *2019 IEEE SENSORS*, IEEE, 2019, pp. 1–4.

[13]   S. Baek, J. Kim, P. Pujar, H.-J. Kwon, S. Kim, and S. Gandla, "Sub-zero temperature sensor based on laser-written carbon", *Advanced Electronic Materials*, vol. 8, no. 7, p. 2 101 252, 2022.

[14]   S. Gandla *et al.*, "Highly linear and stable flexible temperature sensors based on laser-induced carbonization of polyimide substrates for personal mobile monitoring", *Advanced Materials Technologies*, vol. 5, no. 7, p. 2 000 014, 2020.

[15]   B. Kulyk *et al.*, "Laser-induced graphene from paper by ultraviolet irradiation: Humidity and temperature sensors", *Advanced Materials Technologies*, vol. 7, no. 7, p. 2 101 311, 2022.

[16]   Q. Li, R. Bai, L. Guo, and Y. Gao, "All laser direct writing process for temperature sensor based on graphene and silver", *Frontiers of Optoelectronics*, vol. 17, no. 1, p. 5, 2024.

[17]   R. Han *et al.*, "Facile fabrication of rGO/LIG-based temperature sensor with high sensitivity", *Materials Letters*, vol. 304, p. 130 637, 2021.

[18]   M. Liu, J. Wu, and H. Cheng, "Effects of laser processing parameters on properties of laser-induced graphene by irradiating CO2 laser on polyimide", *Science China Technological Sciences*, vol. 65, no. 1, pp. 41–52, 2022.

CURRICULUM VITÆ

Shaogang WANG

26-10-1993   Born in Henan, China.

EDUCATION

2020–2024   PhD. in Microelectronic
                Delft University of Technology
                Delft, the Netherlands
Thesis: UV Laser Direct Writing Technology for the Fabrication of Flexible Sensors
Promotor: Prof. dr. P. J. French
Copromotor: Prof. dr. H. Ye

2016–2019   Master of Mechanical Engineering
                Guilin University of Electronic Technology
                Guangxi, China

2012–2016   Bachelor of Mechanical Design, Manufacturing and Automation
                North China University of Water Resources and Electric Power
                Henan, China

WORK AND INTERNSHIP EXPERIENCE

2017–2019   Assistant Power Semiconductor Device Design Engineer
                China Resources Microelectronics Limited
                Chongqing, China

2019–2020   Power Semiconductor Device Design Engineer
                China Resources Microelectronics Limited
                Chongqing, China

LIST OF PUBLICATIONS

JOURNAL PAPERS

1. **S. G. Wang,** C. J. Tan, Q. H. Zong, S. Z. Li, C. S. Gao, A. Sett, G. Q. Zhang, P. J. French, H. Y. Ye*, *Flexible temperature sensors based on NiO-LIG nanocomposites utilizing UV laser direct writing*, ACS Applied Nano Materials (2025). (Under Review)

2. **S. G. Wang,** C. J. Tan, Q. H. Zong, S. Z. Li, C. S. Gao, H. R. Yang, Q. M. Huang, G. Q. Zhang, P. J. French, H. Y. Ye*, *Selective Reduction Laser Sintering: A New Strategy for NO$_2$ Gas Detection Based on In$_2$O$_3$ Nanoparticles*, Advanced Functional Materials (2025). (DOI: 10.1002/adfm.202419057)

3. **S. G. Wang,** H. R. Yang, Q. H. Zong, Q. M. Huang, C. J. Tan, C. S. Gao, S. Z. Li, H. Y. Ye, G. Q. Zhang, P. French*, *High-performance flexible strain sensor fabricated using laser transmission pyrolysis*, IEEE Sensors Journal **24**, 7521 (2024). (DOI: 10.1109/JSEN.2023.3337233)

4. **S. G. Wang,** Q. H. Zong, H. R. Yang, C. J. Tan, Q. M. Huang, G. Q. Zhang, P. French, H. Y. Ye*, *Rapid fabrication of high-performance flexible pressure sensors using laser pyrolysis direct writing*, ACS Applied Materials & Interfaces **34**, 41055 (2023). (DOI: 10.1021/acsami.3c04290)

5. K. Liu, C. J. Tan, S. Z. Li, W. C. Yuan, X. Liu, G. Q. Zhang, P. French, H. Y. Ye*, **S. G. Wang*,** *Reverse recovery optimization of multiepi superjunction MOSFET based on tunable doping profile*, Electronics **12**, 13 (2023). (DOI: 10.3390/electronics12132977)

6. **S. G. Wang,** J. Jiang, X. Liu, J. H. Liu, J. Li, D. X. Zhou, G. Q. Zhang*, H. Y. Ye, C. J. Tan*, *Electron-Irradiation-Induced Degradation of Transfer Characteristics in Super-Junction VD-MOSFET*, Electronics **11**, 13 (2022).

7. Q. M. Huang, H. R. Yang, **S. G. Wang,** X. Liu, C. J. Tan, Q. H. Zong, C. S. Gao, S. Z. Li, P. French, H. Y. Ye*, *Chitosan oligosaccharide laser lithograph: a facile route to porous graphene electrodes for flexible on-chip microsupercapacitors*, ACS Applied Materials & Interface **16**, 35651 (2024). (DOI: 10.1021/acsami.4c02139)

8. H. R. Yang, **S. G. Wang,** Q. M. Huang, C. J. Tan, C. S. Gao, S. Y. Xu, H. Y. Ye*, G. Q. Zhang, *Stretchable strain sensor based on HfSe$_2$/LIG composite with high sensitivity and good linearity within a wide range*, Applied Surface Science **636**, 15772 (2023). (DOI: 10.1016/j.apsusc.2023.157772)

9. Q. M. Huang, H. R. Yang, **S. G. Wang,** X. Liu, C. J. Tan, A. x. Luo, S. Y. Xu, G. Q. Zhang, H. Y. Ye*, *Laser-induced graphene formation on chitosan derivatives toward ecofriendly electronics*, ACS Applied Nano Materials **6**, 10453 (2023). (DOI: 10.1021/acsanm.3c01408)

10. C. J. Tan, **S. G. Wang,** H. R. Yang, Q. M. Huang, S. Z. Li, X. Liu, H. Y. Ye*, G. Q. Zhang*, *Understanding the interaction of nucleotides with UVC light: An insight from quantum chemical calculation-based findings*, Physical Chemistry Chemical Physics **25**, 3270 (2022). (DOI: 10.1039/D2CP05054D)

11. C. J. Tan, **S. G. Wang,** H. R. Yang, Q. M. Huang, S. Z. Li, X. Liu, H. Y. Ye*, G. Q. Zhang*, *Hydrogenated Boron Phosphide THz-Metamaterial-Based Biosensor for Diagnosing COVID-19: A DFT Coupled FEM Study,* Nanomaterials **12**, 22 (2022). (DOI: 10.3390/nano12224024)

CONFERENCE PAPERS

1. **S. G. Wang,** Q. H. Zong, H. R. Yang, Q. M. Huang, H. Y. Ye, P. French*, *Flexible high-sensitivity strain sensor fabricated with PDMS micro-channel array using laser transmission pyrolysis technology,* IEEE 37th International Conference on Micro Electro Mechanical Systems (MEMS) **(**2024). (DOI: 10.1109/MEMS58180.2024.10439302)

2. **S. G. Wang,** Q. H. Zong, H. R. Yang, Q. M. Huang, H. Y. Ye, P. French*, *Advanced NO_2 gas sensor fabrication through UV laser-induced selective reduction laser sintering,* IEEE 19th International Conference on Nano/Micro Engineered and Molecular Systems (NEMS) **(**2024). (DOI: 10.1109/NEMS60219.2024.10639835)

3. S. Z. Li, C. S. Gao, **S. G. Wang,** H. Y. Ye, G. Q. Zhang, S. H. Wu*, *Multi physics simulation of wafer bonding with nano copper paste,* 25th International Conference on Thermal, Mechanical and Multi-Physics Simulation and Experiments in Microelectronics and Microsystems (EuroSimE) **,** (2024). (DOI: 10.1109/EuroSimE60745.2024.10491552)

4. **S. G. Wang,** C. J. Tan, Q. H. Zong, A. Set, H. Y. Ye, P. French*, *NiO-doped laser-induced graphene: a high-performance flexible temperature sensor,* 2023 IEEE SENSORS (2024).

5. **S. G. Wang,** Y. L. Tan, X. Liu, S. Z. Li, K. Liu, W. C. Yuan, T. Lin, G. Q. Zhang, P. French, H. Y. Ye, C. J. Tan*, *Investigation on transient failure mode of asymmetric trench gate SiC MOSFET under single-pulse avalanche stress,* 24th International Conference on Electronic Packaging Technology (ICEPT) **,** (2023). (DOI: 10.1109/ICEPT59018.2023.10492291)

6. X. Liu, **S. G. Wang,** D. Hu, C. S. Gao, Q. M. Huang, H. Y. Ye, P. French, G. Q. Zhang*, *Reliability analysis of Cu sintered die-attach for SiC power devices: mechanical, electrical, and thermal evaluation,* IEEE 74th Electronic Components and Technology Conference (ECTC) **(**2024). (DOI: 10.1109/ECTC51529.2024.00180)

7. C. J. Tan, **S. G. Wang,** X. Liu, J. Jiang, G. Q. Zhang, H. Y. Ye*, *High-Voltage and High-Current IGBT Press-pack Module for Power Grid,* 23rd International Conference on Thermal, Mechanical and Multi-Physics Simulation and Experiments in Microelectronics and Microsystems (EuroSimE) **,** (2022). (DOI: 10.1109/EuroSimE54907.2022.9758878)

8. W. C. Yuan, K. Liu, **S. G. Wang,** C. J. Tan, H. Y. Ye*, *A TCAD simulation study on the short-circuit performance of 650V super-junction MOSFET,* 23rd International Conference on Electronic Packaging Technology (ICEPT) **,** (2022). (DOI: 10.1109/ICEPT56209.2022.9873366)

9. K. Liu, W. C. Yuan, **S. G. Wang,** C. J. Tan, H. Y. Ye*, *Study on reverse recovery characteristics of P-pillar tunable super-junction MOSFET,* 23rd International Conference on Electronic Packaging Technology (ICEPT) **,** (2022). (DOI: 10.1109/ICEPT56209.2022.9873366)